Computational Modelling of Instability and Transition Using High-Resolution Methods

Sanjay Patel

Submitted for the Degree of Ph.D.

Fluid Mechanics and Computational Science Group
School of Engineering
Cranfield University
Cranfield, UK

2007

Abstract

This thesis concerns the numerical investigation of suddenly expanded flows featuring separation, instabilities and transition, in the context of Implicit Large Eddy Simulation (ILES). The study of separated flows through suddenly expanded geometries is a classic yet complex area of research. These types of flows feature instabilities which may lead to bifurcation. Non-linear bifurcation is of great importance when considering hydrodynamic stability and the mechanism of laminar to turbulent flow transition.

A detailed numerical investigation of various high-resolution methods and their ability to correctly predict the flow through a suddenly expanded and contracted geometry demonstrates that the choice of the particular numerical method employed can lead to an incorrect solution of the flow. The key difference between the various high-resolution methods employed is in the calculation of the nonlinear wave-speed dependent term. It is shown that the nonlinearity of this term provides an asymmetric dissipation to the flow which triggers symmetry-breaking bifurcation in a fully symmetric computational set-up. High-resolution simulations of three-dimensional flow through a plane suddenly expanded channel at low Reynolds numbers show that this type of flow is characterised by a symmetric separation of the fluid which is nominally two-dimensional in the spanwise direction. Increasing the Reynolds number reveals a symmetry-breaking bifurcation of the fluid flow which becomes three-dimensional as Reynolds number is further increased. Simulations confirm that it is this three-dimensional disturbance which leads to the onset of time-dependent flow characterised by the periodic shedding of vortices from the upstream recirculation zones.

Preconditioning techniques which aim to alleviate stiffness in the calculation of the advective fluxes for low Reynolds number flows are shown to be unsuitable for flows featuring instabilities. The added dissipation to the flow causes the prediction of an incorrect stable solution or to an improper estimation of the size of the separation bubbles.

Simulations of a synthetic jet issuing into quiescent air using various slope limiters manage to capture the flow physics relatively well. Limiters are used to avoid a scheme from being oscillatory and provide non-linear dissipation in the region of excessively large gradients. The various limiters differ with regards to the amount of dissipation they provide to the flow, hence the solution obtained is dependent on the limiter used.

Acknowledgements

First and foremost I would like to sincerely thank my supervisor Professor Dimitris Drikakis, for the advice and support which he has given me over the past few years. His guidance throughout the course of this thesis and the wealth of knowledge he has passed onto me is greatly appreciated.

Special thanks must go to my girlfriend, Joanna, whose unwavering support throughout my PhD has kept me both sane and focused on the task at hand.

I hope that the friendships I have made during the course of this PhD last beyond my time at Cranfield. Considerable thanks go to: Marco Hahn, Marco Kalweit, Ben Thornber, Stephen Carnduff, Sunil Mistry, Jason Bennett, Simon Croucher, Ian Cowling, John Murphy, Adam Ruggles, Edouard Berrocal, and Dmitry Churmakov. I would especially like to thank Marco Hahn and Ben Thornber for the many insightful discussions about numerical methods and flow physics.

Last but by no means least I am extremely grateful to my parents for their love, support and encouragement throughout my life. My older brother, Milan, has been an inspirational figure in my life to whom I have always looked up to. He has been a constant source of advice and support especially during the many arduous times encountered over the course of this PhD.

Sanjay Patel

Contents

List of Figures

List of Tables

Nomenclature

Acronyms

AC Artificial Compressibility

CB Characteristics-Based Riemann Solver

CFL Courant-Friedrichs-Levy

DD Drikakis

DNS Direct Numerical Simulation

ENO Essentially Non-Oscillatory

FCT Fluc-Corrected Transport

FD Finite Difference

FE Finite Element

FV Finite Volume

HLL Harten, Lax and van Leer Riemann Solver

HLLE Harten, Lax and van Leer, Einfeldt Riemann Solver

ILES Implicit Large Eddy Simulation

KK5 Kim and Kim fifth order

LES Large Eddy Simulation

MB Minbee

MUSCL Monotone Upstream-centred Schemes for Conservation Laws

PPM Piecewise Parabolic Method

RANS Reynolds Averaged Navier-Stokes

RK Runge-Kutta

SB Superbee

TVB Total Variation Bounding

TVD Total Variation Diminishing

VA van Albada

VL van Leer

WENO Weighted Essentially Non-Oscillatory

Greek Symbols

α Preconditioning parameter

β Artificial compressibility parameter

γ Ratio of specific heats

λ Eigenvalue

μ Dynamic viscosity

ν Kinematic viscosity

ω Vorticity

$\phi(r)$ Limiting function

ψ Stream function

ρ Density

τ Pseudo-time

φ Potential

ξ, η, ζ Curvilinear coordinates

Latin Symbols

$\mathbf{A}$ Flux jacobian

a Speed of sound

C CFL number

c Artificial speed of sound

E Inviscid flux vector

e Total energy per unit volume

$\mathbf{E}^{a}_{i+1/2}$ Averaged part of the Godunov flux

$\mathbf{E}^{cb}_{i+1/2}$ Reconstructed part of the Godunov flux

H Total enthalpy

$\mathbf{I}$ Unit diagonal tensor

J Jacobian

M Mach number

$\mathcal{P}$ Projection operator

p Pressure

$\mathbf{q}$ Heat flux

R Restriction operator

R Specific gas constant

Re Reynolds number

S Wave speed

T Temperature

t time

u Particle speed

u, v, w Velocity components in the x, y, z cartesian directions, respectively

U_{cg} Steady state coarse grid solution

U_{ig} Steady state intermediate grid solution

$\mathbf{u}$ Velocity component vector

$\bar{V}_{cg}$ Coarse grid function

$\bar{V}_{ig}$ Intermediate grid function

V_{fg} Current fine grid solution

V_{ig} Current intermediate grid solution

x, y, z Cartesian directions

CHAPTER 1

Introduction

The purpose of this Chapter is to review some of the fundamental concepts of Computational Fluid Mechanics and to provide a foundation for the remaining Chapters of this thesis. This Chapter starts by giving a few examples of everyday fluid mechanics followed by a brief description of the physical relevance of the non-linear equations solved during the solution procedure. Three different techniques for numerical discretisation will be briefly discussed before moving on to a discussion on the various approaches used in Computational Fluid Dynamics. A discussion of the flow physics behind the phenomena of flow separation, instabilities and the transition to turbulence will be presented followed by the outline of the thesis and the resulting publications from the work carried out during the course of the thesis.

1.1 Everyday Life Fluid Mechanics

'THE flow of a river never ceases to go past, nevertheless it is not the same water as before. Bubbles floating along on the stagnant water now vanish and then develop but have never remained'. Stated by Chohmei Kamo, a thirteenth century Japanese essayist, in the prologue of *Hohjohki*. The movement of gas or liquid (collectively called fluid) is referred to as the 'flow', and the study of this is called 'fluid mechanics'. Natural fluid flows such as the flow of the air and the water of rivers and seas would be the first thoughts of typical everyday life fluid mechanics. Figure 1.1 shows a powerful example of natural fluid mechanics, hurricane Dean approaching the Yucatan Peninsula. The flow of water, sewage and gas in pipes, in irrigation canals, and around rockets, aircraft, express trains, automobiles and boats are more industrial examples of fluid mechanics which also exist in everyday life. The science of fluid dynamics can be subdivided into three areas: Hydrodynamics, which study the flow of liquids; Gas dynamics, which study the flow of gases and Aerodynamics, which concerns the flow of air. These three areas are by no means mutually exclusive and often coincide with one another. The study of fluid mechanics from a numerical point of view is referred to as Computational Fluid Dynamics.

Computational Fluid Dynamics has been a constantly developing field of science since

Figure 1.1: Hurricane Dean, powerful natural fluid mechanics.

the advent of the digital computer, and will continue to develop for many many years to come. The attraction of the subject is twofold. Firstly, the desire to be able to model physical fluid phenomena that cannot be easily simulated or measured with a physical experiment, for example weather systems or hypersonic aerospace vehicles. Secondly, the desire to be able to investigate physical fluid systems more cost effectively and more rapidly than with experimental procedures.

There has been considerable growth in the development and application of Computational Fluid Dynamics to all aspects of fluid dynamics. Commercial CFD programs are now considered to be a standard numerical tool in the design and development area of industry. As a consequence there is a considerable demand for specialists in the subject, to apply and develop CFD methods throughout engineering companies and research organisations. As the demand for CFD increases in conjunction with the capabilities to model more and more complex flows, the need for faster, more accurate, more stable and robust numerical methods becomes pertinent to the forward progression of CFD.

Understanding the physical events that occur in the flow of fluids around and within designated objects is an integral part of Computational Fluid Dynamics. These events are related to the action and interaction of phenomena such as, and by no means limited to, dissipation, diffusion, convection, shock waves, slip surfaces, boundary layers, and turbulence. These phenomena are governed by the Navier-Stokes equations which are inherently non-linear and hence have no analytic solution. This means that the equations need to be solved numerically. How this is carried out is a whole subsection of Computational Fluid Mechanics and will be briefly discussed later in this Chapter. The Reynolds number of the particular flow in question plays in important part in deciding whether the flow is laminar or turbulent. At low Reynolds numbers the flow is laminar characterised by a smooth flow. As Reynolds number increases, the flow becomes transitional and eventually becomes fully turbulent. A turbulent flow field is extremely complex and features a large range of different scales structures. The process of laminar transition to turbulence is usually due to some type of instability which triggers the flow to become turbulent. Unstable perturbations grow as viscous effects decrease with increasing Reynolds number. The growth of these perturbations effects the flow field as it's 'energy' is passed to the different length scales, with the large scales passing on to smaller scales until this 'energy' is small enough to be damped out by the viscosity effects.

The equations governing the fluid flow problem are the continuity (conservation of mass), the Navier-Stokes (conservation of momentum) and the energy equations. These equations form a system of coupled non-linear partial differential equations (PDEs). These equations can only be solved analytically in closed form by making the PDEs linear. This can only be true if the non-linear terms naturally drop out for example in a fully developed flow through a duct or for flows that are inviscid and irrotational everywhere. In the case that the nonlinear terms are small compared to other terms they can often be neglected for example, creeping flows or small amplitude sloshing of liquids. If the non-linearities in the governing PDEs cannot be neglected, which is usually the case for most engineering flows, then solutions need to be obtained by solving the equations numerically. Computational Fluid Dynamics replaces the differential equations governing the fluid flow, with a set of algebraic equations. This process is called discretisation, and the resulting equations can be solved using computers to obtain an approximate solution. The most commonly used discretisation methods in CFD are the Finite Difference Method (FDM), Finite Volume Method (FVM), Finite Element Method (FEM), and Boundary Element Method (BEM).

The use of numerical methods to solve partial differential equations introduces an approximation that alters the form of the basic partial differential equations themselves. The new equations, which are the ones actually being solved, are often referred to as the modified partial differential equations. Since they are not precisely the same as the original equations, they will never give exactly the same solution as an exact solution to the unmodified original partial differential equation. These differences are mathematically referred to as truncation errors.

Numerical analysis of fluid mechanics has shown that these errors have a physical meaning and contribute to the flow being simulated. Depending on the characteristics of the truncation error terms methods are said to have a lot of "artificial viscosity" or said to be highly dispersive. This means that the truncation errors which were caused by the numerical approximation, result in a modified partial differential equation having additional terms. These terms can either be identified with the physics of dissipation or dispersion. There is nothing wrong, with designing a numerical method to be physically dissipative or dispersive depending on the flow under investigation, as long as the error remains in some engineering sense "small", and does not destroy or substantially alter the actual physics of the flow situation. Most numerical methods used in solving the non-dissipative Euler equations are created with a modified partial differential equation that will produce some degree of dissipation. Regardless of the specific characteristics of the error term, if their effects are not thoroughly understood and controlled, they can lead to serious difficulties, producing answers that have little, if any, physical reality. On the other hand, even if the errors are kept small enough that they can be somewhat neglected from an engineering perspective, the resulting simulation can still be of little practical use if inappropriate numerical algorithms are used. This motivates studying the concepts of stiffness and numerical algorithm characteristics in general.

1.2 Numerical Discretisation

1.2.1 The Finite Difference Method

As discussed above, the governing equations of unsteady fluid flow contain partial derivatives with respect to both space and time. The spatial derivatives can be first approximated resulting in a system of ordinary differential equations. Next the time derivatives are approximated which leads to a time-marching method producing a set of difference equations. Finite difference approximations can be applied to either the spatial derivatives or time derivatives. The finite difference method has been shown to be the easiest method to implement if the geometry being investigated is simple. By considering the conservation equation in differential form and creating a structured mesh over the geometry under investigation the differential equation is approximated by replacing the partial derivatives by approximations in terms of the nodal values of the functions. This results in a single algebraic equation for each grid node. The variable value at that node and also at other nodes around are unknown. Using Taylor series expansion or polynomial fitting, approximations to the first and second derivatives of the variables with respect to the coordinates are obtained. Due to the simplicity of obtaining high-order schemes on structured grids, an increase in accuracy can often be achieved with little complication to the numerical method. The main disadvantage to finite difference methods is that conservation is not enforced unless special care is taken. The problems associated with using a structured grid for complex flow geometries can be overcome by using finite volume methods which will be discussed next.

1.2.2 The Finite Volume Method

The finite volume method is probably the most popular of the three discretisation methods used in CFD. This method, in some ways, is similar to the finite difference method discussed above. The finite volume method was primarily developed to solve the equations of heat transfer and fluid flow and is described in detail by Patanker [126]. The advantages of finite volume methods over finite difference methods are that they ensure that the discretisation is conservative, mass, momentum and energy are conserved in a discrete sense. Although this can be obtained using finite difference equations, conservation is obtained naturally with the use of finite volume methods as long as the surface integral representing the convective and diffusive flux are the same for the control volumes sharing the boundary. Since finite volume methods do not require a coordinate transformation in order to be used on irregular meshes, three-dimensional unstructured meshes using arbitrary polyhedra can be generated for use in complex flow geometries. Finite volume methods make use of the governing equations in an integral form to satisfy the conservation law to some degree of approximation for each of the control volumes covering the domain of interest. At the centre of each of the control volumes lies a computational node at which the variable values are calculated. Interpolation is used in order to express the variable value on the volume face in terms of the central nodal value. The surface and volume integrals are approximated using suitable quadrature formulae, which results in an algebraic equation for each control volume, which in turn consists of neighbouring nodal values. A time-marching method can then be applied to find the values of the variables in each cell at the next time step. The finite volume approach ensures that a 'balance' of some physical quantity is made on the control volume in the neighbourhood of a grid point. The discrete nature of the problem domain is always accounted for in the finite volume approach ensuring that the physical law is satisfied over a finite region rather than at a point as is the case with finite difference methods.

1.2.3 The Finite Element Method

The finite element method is similar to the finite volume method in a way that both methods make use of finite volumes or elements to decompose to computational domain. With finite elements the decomposition is usually unstructured. The finite element method came about from computational techniques used to predict stress and strain in solid structures and is now a standard computational technique in the area of structural engineering. The finite element technique has been developed into a more general computational technique used to solve a wide variety of partial differential equations and is suitable for many physical problems. The feature which distinguishes finite element methods from the two previous methods is that in finite element methods the equations are multiplied by a 'weight function' before being integrated over the entire domain. Over each element a simple variation of the dependent variables is assumed and this piecewise description is used to build up a picture of how the variables vary over the whole domain. The discretisation process is far more complex than that of the finite volume and finite difference methods and for a more in depth discussion of this approach the reader is referred to the text of Zienkiewicz and Taylor [195]. Finite element methods have the advantage of being able to accommodate arbitrary geometries.

1.3 Numerical Approaches in CFD

There exist several numerical approaches used in computational fluid dynamics, with the majority concerning the simulation of turbulent flows. A brief description of three of these methods namely: Direct Numerical Simulation, Large Eddy Simulation and Implicit Large Eddy Simulation will now be discussed.

1.3.1 Direct Numerical Simulation (DNS)

DNS is the most simple approach from a conceptual point of view in the simulation of transitional and turbulent flows. In DNS, the Navier-Stokes system of equations is solved directly with refined meshes resolving all length scales ranging from large scale features down to the smallest scale features at the Kolmogorov dissipation scale. Figure 1.2 shows the wide range of length scale typical of a turbulent flow. The largest eddies in this flow are the spanwise rollers with a length scale L. It is clear to see a wide range of small scale eddies present with the smallest being the Kolmogorov scales η. The DNS approach does not average or approximate the Navier-Stokes equations apart from numerical discretisation in which the errors can be estimated and controlled. DNS make it possible to compute and visualise any quantity of interest, including some that are difficult or impossible to measure experimentally and also to obtain detailed insight into the kinematics and dynamics of turbulent eddies. There are various limitations to DNS; firstly the use of very high-order schemes is desirable in order to limit dispersion and dissipation errors, these schemes have little flexibility in handling complex geometries and general boundary conditions. Secondly, the problem associated with the resolving of all length scales requires grid resolutions with the number of grid points is proportional to the 9/4 power of the Reynolds number, $Re^{9/4}$. Due to the extremely fine grids employed in such simulations the numerical cost of the computations scales like Re^3. For wall bounded flow the number of grid points required for DNS increases further due to the resulting flow physics in the near wall region. These are the main reasons as to why DNS have been limited to simple flow configurations at low Reynolds numbers. It's application to industrial engineering flows where often the Reynolds number is in the turbulent regime is unlikely to be practically possible even with the rapid evolution of computing technologies.

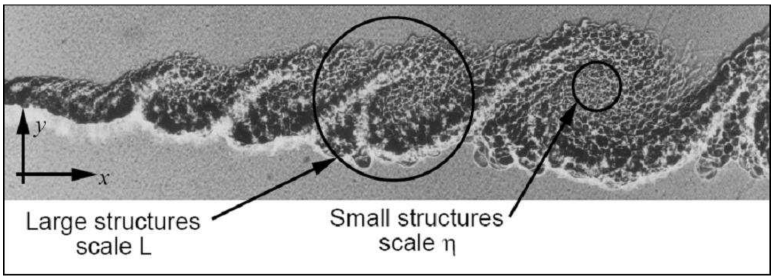

Figure 1.2: Visualisation of the flow in a mixing layer (from Brown and Roshko [23]).

1.3.2 Large-Eddy Simulation (LES)

Large-eddy simulations are a technique intermediate between DNS and Reynolds-Averaged-Navier-Stokes (not discussed here). As the name suggests LES computes the contribution of the large, energy carrying structures and the smallest scale turbulence is modelled. LES are similar to DNS in that they both provide a three-dimensional, time-dependent solution of the Navier-Stokes equations. Hence, they still require fairly fine meshes but not to the extent of DNS. The general concept of LES can be described with the use of Figure 1.3, showing a plot of energy spectrum verses wave number space. LES aims to resolve all of the energy containing scales as well as some of the inertial subrange. The remaining inertial subrange and the energy dissipation range scales are modelled. This is done by applying low pass filtering to the Navier-Stokes equations, introducing subgrid stresses which account for the interaction between the resolved turbulent structures and the subgrid scales. The subgrid scale (SGS) terms are modelled explicitly by the addition of extra terms to close out the system of equations. Since the dissipative scales of motion are poorly resolved in LES, the main role of SGS models is to remove energy from the resolved scales, essentially mimicking the energy cascade drain. Thus these SGS models do not actually represent the exact SGS at each point in both space and time, instead accounting for the global effect. This often leads to excessive dissipation in the flow field. A wide range of SGS models exit and it is not the intention of this thesis to give an in depth discussion of these models. Instead the reader is referred to various books including the book by Sagaut [149] and references therein. Since most of the turbulent energy is contained within the large scale eddies, modelling the high wave number part of the spectrum seems to be a much better approach than full Reynolds stress modelling or DNS. However, if the flow in question was wall bounded then the computational cost of performing LES is approximately only one order of magnitude 'cheaper' than DNS. The physics at the wall become complex as large eddies decrease in size, hence the grid resolution in the near wall region must be close to that of a DNS grid. The main drawback to conventional LES are the difficulties in constructing the SGS models for complex wall bounded high Reynolds number flows. This has led to the development of alternative methods such as Implicit LES.

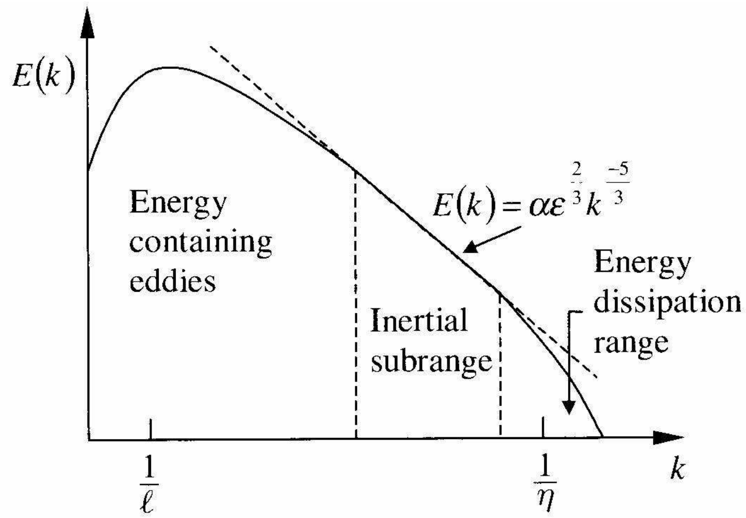

Figure 1.3: Energy spectrum vs. wave number space (log-log scales).

1.3.3 Implicit Large Eddy Simulation (ILES)

The concept behind Implicit Large Eddy Simulation is that the equations are solved in their original form without any filtering (hence the commutation error can be dropped) or explicit modelling leaving the embedded numerical viscosity inherent to the numerical methods used to resolve the small scales. These methods are implicitly based on the hypothesis; *The action of subgrid scales on the resolved scales is equivalent to a strictly dissipative action*, as written by Sagaut [149]. Simulations using these methods most commonly use dissipation terms introduced in the framework of upwind schemes for the convection term. This diffusive term adapts itself to the nature of the local solution in order to obtain a solution that is both accurate and has some physical meaning. There are several types of numerical methods used in the context of ILES; Godunov (Yan and Knight [190]), PPM (Colella and Woodward [37]), TVD (Cousteix [38]), FCT (Boris and Book [17]), MPDATA (Margolin et al. [109, 108]) among others.

In order to further understand the ILES methodology it is important to outline the differences between standard LES, and ILES, with some referencing to DNS. In DNS the dissipation needed in order to maintain numerical stability is provided by the physical viscosity. As discussed in the previous subsection, in LES a SGS model is provided to the solver in order to represent the effects of the unresolved scales. An essential part of these SGS models are that they must provide sufficient dissipation to the flow else the resulting build up of energy in the smallest resolved scales grows unboundedly, until the numerical solution breaks down. The SGS models and filtering of the equations in LES should ensure that the flow is smooth accordingly without having to worry about added dissipation from the numerical algorithm which should be kept to a minimum. Figure 1.4 shows the similarities between standard LES and ILES methodologies. In LES subgrid models are defined by applying physical theories of homogeneous isotropic turbulence in Kolmogorov's framework. These models are then coupled to the ideal (zero dissipation) Euler equations to provide a representation of reality. In the case of ILES the model and the numerics are merged together. The models have theoretical foundations in vanishing viscosity used in the selection of entropy satisfying weak solutions. High-resolution and non-linear stability is achieved via extensions to the numerics such as monotonicity, TVD, TVB, ENO and other such physical/mathematical principles. These extensions are a key to the ILES approach and allow at least second order of accuracy in smooth areas of the flow. Without these extensions the vanishing viscosity approach produces first-order results which are not considered as 'high-resolution'.

High-resolutions scheme have been built upon circumventing Godunov's theorem (Godunov [66]) which stated that: *if an advection scheme preserves the monotonicity of the solution it is at most first-order accurate*. Non-linear discretisation of the advection equation allows higher orders of accuracy and forms the basis of high-resolution methods. The history behind the discovery of these schemes will not be presented here and the reader is referred to the text of Drikakis and Rider [50]. The non-linearity of these methods differentiates them from classical techniques and guarantees numerical stability and physical results. It is this connection between the numerics and flow physics that makes these methods attractive in the simulation of a wide variety of flows. There has been an increasing amount of evidence to suggest that high-resolution methods have an embedded turbulence model (Boris et al. [18]; Drikakis [45]; Drikakis and Geurts [49]; Fureby and Grinstein [63, 62]; Linden et al. [97]; Margolin and Rider [107]; Margolin et al. [108]; Oran and Boris [124]; Porter et al. [131]; Youngs [193, 194, 192]). High-resolution methods have been accepted as powerful and efficient methods in simulating laminar flows and there extension to turbulent flows require no further changes to the numerical methods employed. The user does not need to decide whether the flow is laminar or turbulent leaving the numerics to make the decision themselves. This makes for simple and flexible numerical codes.

Modified Equation Analysis (MEA) can be used to shed light on the embedded similarities between standard LES and ILES. MEA derives the effective differential equation of a numerical algorithm as a basis to analyse the numerical algorithms behaviour (Griffiths and Sanz-Serna [69]; Knoll et al. [86]; Warming and Hyett [188]). MEA can be applied to examine several LES models two of which (Smagorinky and Bardina) will be now discussed (for a complete analysis see the text of Drikakis and Rider [50]). The general form of the numerical/modelled solution is:

$$U_t + \nabla \cdot E(U) = \nabla \cdot \tau(U), \tag{1.3.1}$$

where the subscript t represents the time derivative and $\tau(U)$ the subgrid scale stress. The left hand side is the idealised inviscid equation and the right hand side is the subgrid model. The model by Smagorinsky [159] can be defined by

$$\tau(U) \sim C\Delta^2 \parallel \nabla U \parallel \nabla U, \tag{1.3.2}$$

where C is a constant and Δ is the cell size.

Bardina et al. [13] proposed a model based on filtering, which uses the difference in the subgrid term evaluated at two different filter sizes, and can be defined by

$$\tau(U) \sim \overline{E(\bar{U})} - \overline{\overline{E(U)}} \approx E''(U)\Delta^2 \nabla U \nabla U. \tag{1.3.3}$$

Evaluating the differential form of the Smagorinsky model in one spatial direction is a simple process since the form presented in Eqn. 1.3.2 can be directly used, giving

$$\tau(U) = C\Delta^2 \mid U_x \mid U_x, \tag{1.3.4}$$

For the Bardina model which is based on filtering, MEA is needed to produce the differential forms. Using a box filter at 2Δ and 4Δ gives,

$$\tau(U) = C\Delta^2 (U_x)^2. \tag{1.3.5}$$

It should be noted that the constant C is different for each of the two models. Also the Smagorinsky model has been found to be explicitly dissipative whereas the Bardina model is unstable without additional dissipation. This additional dissipation is provided by adding the Smagorinsky model. Now it will be shown that ILES can produce the same effect naturally including the same differential terms as the self similar Bardina model, producing a mixed model through the nonlinear regularisation associated with nonoscillatory differencing. Analysis of spatial errors in a one-dimensional high-resolution algorithm can be carried out by considering the following form,

$$U_j^{n+1} = U_j^n - \frac{\Delta t}{\Delta x}\left[E(U_{j+1/2}) - E(U_{j-1/2})\right]. \tag{1.3.6}$$

A high-resolution Godunov method based on a reconstruction procedure employing limited slopes, $S_j(U)$, produces two edge values in each cell.

$$U_{j\pm 1/2;L/R} = U_j \pm -\frac{1}{2}S_j. \tag{1.3.7}$$

The two values at each node can be resolved by employing a linearised Riemann solver:

$$E(U_{j+1/2}) = \frac{1}{2}\left[E_{j+1/2;L} + E_{j+1/2;R}\right] - \frac{|E'|}{2}(U_{j+1/2;R} - U_{j+1/2;L}), \tag{1.3.8}$$

where $E' \equiv \partial E/\partial U$.

The effective subgrid stress $\tilde{\tau}$ from the general form of the modified equation from (1.3.6), at an order of Δ^2 is

$$\tilde{\tau}_2(U) = c_1 E'(U)U_{xx} + c_2 E''(U)(U_x)^2. \tag{1.3.9}$$

The subgrid stress τ_2 is a second order approximation and the constants c_1 and c_2 depending on the specific differencing scheme employed. Margolin and Rider [107] have shown that the term $E''(U)(U_x)^2$ is a consequence of the conservation form and is not present if the differencing is not in conservation form. Furthermore, this term is identical to the leading order term for the self similar model with standard LES shown in Equation 1.3.5. Hence, with the use of MEA one can show that high-resolution methods used for solving ILES have embedded similar subgrid stresses as explict models used for LES.

Further information in Chapter 2 regarding high-resolution methods is presented together with various Riemann solvers used during this thesis as well as two different interpolation procedures, one of which incorporates various slope limiting schemes.

1.4 Flow Separation

The term separation is used in fluid mechanics to describe the situation, where part of a flow has a direction opposite to the mean flow. Separated flows are extremely common in external flows, examples of which would be flow over cars, trains, planes, ships or submarines. Internal separated flows are much less obvious and everyday examples would be suddenly expanded or contracted pipe flows found in various industrial applications such as environmental instruments and fluid machineries. The separation of

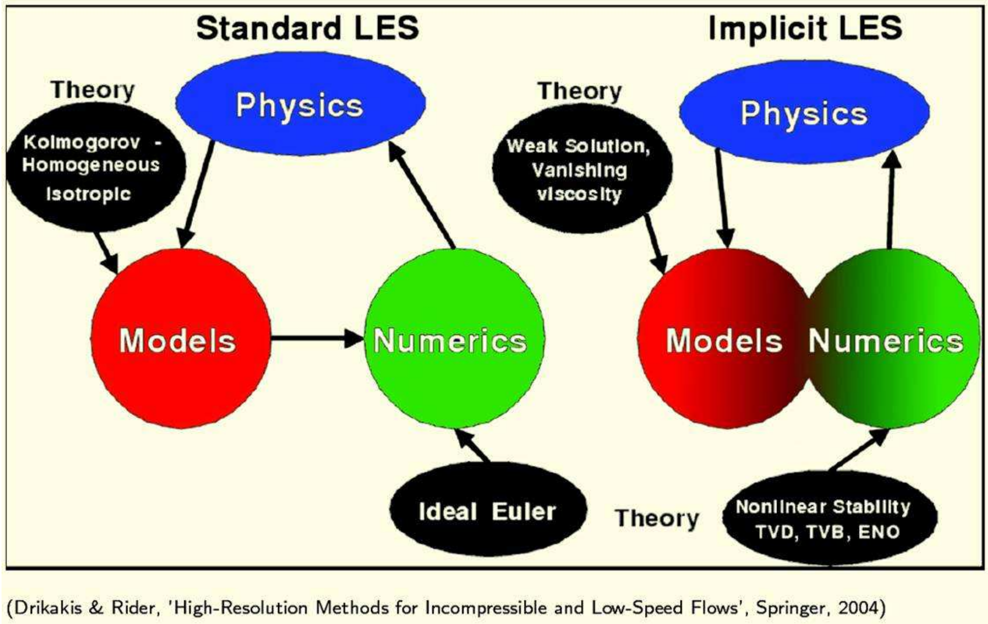

Figure 1.4: Fundamental similarities between LES and ILES. Figure taken from Drikakis and Rider [50]

a fluid can be either geometric or dynamic. Geometric separation occurs due to the fluid flow passing over a sharp edge such such as the corner of a sudden expansion. The fluid detaches from the sharp edge regardless of how much the fluid velocity has been reduced by frictional effects.

Separation in a boundary layer occurs where the tangential flow velocity changes sign and recirculation occurs. Similarly, a separated flow may reattach where the tangential velocity changes sign in the opposite direction. Alternatively, separation/reattachment can be defined to occur where the streamwise shear stress at the boundary changes sign. Dynamic separation is caused by a positive pressure gradient in the streamwise direction, resulting in a force opposing the flow with a retarding effect. If the opposing pressure force is strong enough over a sufficiently long time, the tangential velocity may change sign and separation will occur.

Figure 1.5 illustrates the steady separation process for a given pressure distribution p. The interface that occurs due to the separation rolls up into one or more vortices. The reverse flow close to the wall causes a thickening in the boundary layer indicted by the streamline portrait of the boundary layer flow close to the separation position A. The wall streamlines departs the wall at a certain angle at the point of separation. The position of the point of separation is that point on the wall where the velocity gradient perpendicular to the wall vanishes, i.e., the point where the wall shear stress τ_w becomes zero:

$$\tau_w = \mu \cdot \left. \frac{\partial u}{\partial y} \right|_w = 0 \tag{1.4.1}$$

In industry one attempts to avoid a separation of the flow in spite of the pressure rise,

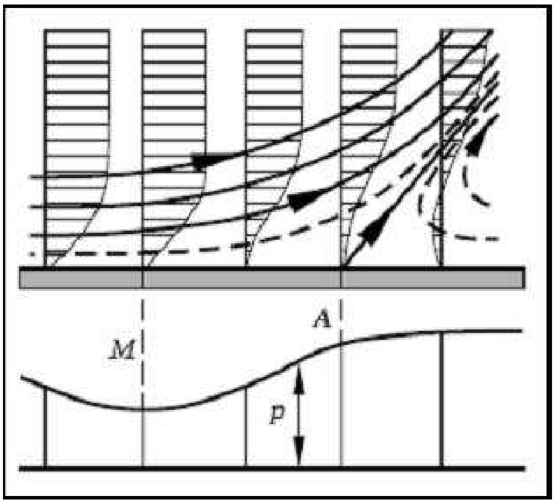

Figure 1.5: Schematic of the separation process, reproduced from Prandtl [132].

in order to keep flow losses small. This is achieved by permitting channels to expand only gradually, or by designing the shape of bodies sufficiently narrow so that the acceleration of the outer flow prevails over the pressure rise. This concept is generally successful when the boundary layer in the decelerated part is turbulent. In a flow featuring a pressure increase such as the flow past a body, the flow can remain laminar up to the point of separation subject to the surface being smooth and the approach flow free of turbulence. Just in front of the separation point, the boundary-layer profile has a turning point. This is a sufficient criterion for the onset of the instability in the boundary layer. The laminar to turbulent transition begins, leading to a reattachment of the turbulent boundary-layer flow downstream, if the Reynolds number is large enough. An example of laminar flow separation with turbulent reattachment is the flow over thin wing profiles with sharp nose curvature and sufficiently large angles of attack.

Flow separation can be influenced via several mechanisms such as rotation, blowing, suction, and oscillatory suction and blowing. The study of flow control has attracted a significant interest especially in the aviation industry by reducing drag via the manipulation of the boundary layer over the wing surface. Boundary layer separation can be delayed by sucking the fluid in the boundary layer into the interior of the body, usually through small pores in the wall of the body. The suction is implemented in the region where the flow is reversed. If the suction is significantly strong, the accumulation of the decelerated fluid is avoided and boundary layer separation can be avoided. Tangential blowing is an alternative to flow control from suction. Fluid is blown into the boundary layer through a slit parallel to the main flow direction. This extra fluid can impart enough kinetic energy to the boundary layer to prevent separation. Tangential blowing onto a wing can significantly increase the maximum lift although this would be at the cost of a substantial increase in drag. Combining suction with blowing has been introduced to the world of flow control via synthetic jet actuators. Fluid is periodically expelled and sucked back through a small slot. A piezoelectric actuator is the most common device used to generate the expulsion and suction cycle. The most desirable aspect of synthetic jet actuators are that there is zero net mass flux across the slot boundary. This means that no complicated fluidic piping is needed to provide a constant source of fluid as in the case of tangential blowing. During the expulsion phase a pair of counter rotating vortices are generated from the edges of the slot and move away into the downstream region under a self-induced velocity. The suction phase imparts a stabilising effect onto the flow before the next expulsion cycle begins. The vortices generated on the expulsion phase impart a finite momentum into the surrounding fluid and the interaction of these vortices with the surrounding fluid can cause large scale global modifications to the base flow. Synthetic jets have been used in a variety of applications such as; active flow control, jet vectoring, and triggering turbulence in boundary layers.

1.5 Transition to Turbulent Flows

From a qualitative point of view the transition from laminar to turbulent flow occurs if the momentum exchange by molecular transport cannot compete sufficiently effectively with the transport due to macroscopic fluctuations in the flow velocity. Turbulence can only develop in rotational flows and it is due to shear in a basic flow that small perturbation will develop, through various instabilities, and eventually degenerate into turbulence. Reynolds [138, 139] proposed that the transition from laminar to turbulent flow occurs at some critical Reynolds number. This has been found to work for flow through a pipe, however for other flow situations the critical Reynolds number depends on a number of other factors such as initial disturbances. The growth of instabilities are an important factor in most industrial flows and can often be the deciding factor as to whether a flow stays stable (laminar) or transitions to an unstable turbulent flow. Some important instabilities related to the types of flow investigated in this thesis are briefly discussed in the following subsection.

1.5.1 Instabilities

The property of stability is a criterion to determine whether a flow retains or alters its state. A fluid-mechanical instability can initiate the transition to a turbulent flow and is therefore an important criterion for the temporal and spatial pattern formation of transitional and turbulent flows.

Consider the example of a glowing cigarette and the consequent smoke rising from the lit end. If the surrounding air is assumed to be at rest, the smoke initially moves in smooth straight path close to the cigarette. After a certain height has been reached, these smoke paths suddenly disintegrate into an obviously disordered, temporally and spatially irregular fluctuation structure. The flow carrying the smoke particles is said to have passed over from the laminar to the turbulent state. In many flow problems, this laminar to turbulent transition is initiated by instabilities inherently present in the flow in question or from some external disturbance on the particular flow. The laminar flow regime becomes increasingly influenced by small perturbations with increasing Reynolds number, eventually become unstable and then fully turbulent.

Various types of instabilities exist in everyday life and it would be too exhaustive a task to consider them all. Shear flow instabilities occur when the amplitude of a local perturbation in a shear flow is amplified and the transition from laminar to turbulent flow initiated. Examples of shear flow instabilities are the Kármán vortex street in wakes and the Tollmien-Schlichting waves in boundary layers. The Kármán vortex street occurs in the wake of a body flow when the critical Reynolds number is exceeded as a consequence of shear instabilities leading to temporally and spatially separating vortices. Figure 1.6 shows the typical patterns formed in a Kármán vortex street. Tollmien-Schlichting waves are caused by the laminar to turbulent transition in boundary layers. The state of fully developed turbulence is reached via several intermediate states in the transition regime. Tollmien-Schlichting waves initially become unstable to cross-wave perturbations above some second critical Reynolds number. Lambda structures are formed downstream with local shear layers in the boundary layer as shown in Fig. 1.7. The turbulent boundary layer flow is fully developed only once these shear layers decay. Instabilities in boundary layers are not usually initiated with plane harmonic waves, instead being caused by local perturbations such as surface roughness. It should be noted that in free-shear flows, such as mixing layers, jets or wakes, primary instabilities leading to the formation of coherent vortices are inviscid, i.e. they are not affected by molecular viscosity, if it is small enough. In wall bounded flows such as boundary layers, pipe flows or channel flows the linear instabilities depend critically upon the viscosity and tend to vanish in the Euler case.

Figure 1.6: Kármán vortex street from a shipwreck.

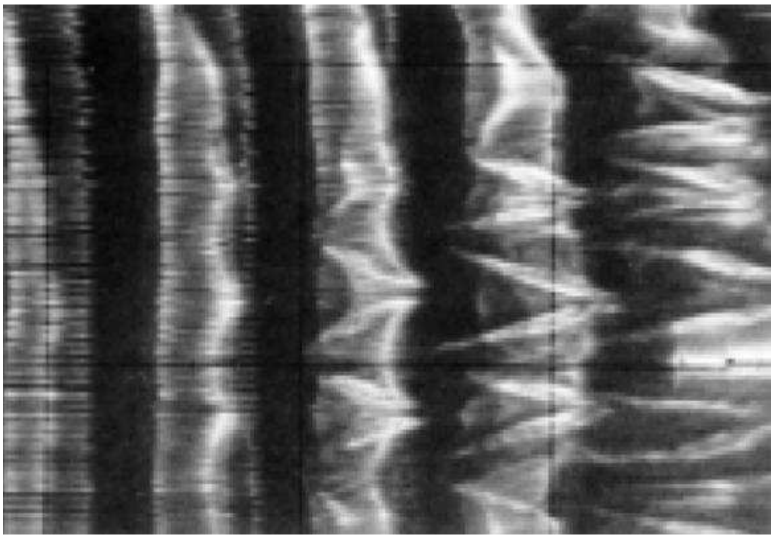

Figure 1.7: Lambda structures in the transition regime of the plate boundary-layer flow, Saric [150].

1.6 Thesis Outline

The outline of this thesis is as follows:

- Chapter 2 provides a full description of the numerical methods employed throughout this thesis including various methods for solving incompressible flows, the mutigrid approach, mutiblock decomposition. Further discussion on high-resolution methods is presented together with various Riemann solvers and high-order reconstruction methods. Finally some different time-integration methods are presented.

- The first of five results Chapters, Chapter 3, concerns the effect of preconditioning of the incompressible advective flux equations using a pre-existing method from Turkel [177]. The preconditioning method is applied to two different suddenly expanded geometries in which instabilities are manifested in the form of an asymmetric separation of the fluid flow.

- Chapter 4 investigates various Riemann solvers and their ability to simulate flow through a suddenly expanded and contracted channel. The effect of the order of accuracy in the reconstruction of the flux on the cell face is investigated for grid independent simulations. Experimental flow visualisations have been used as a comparison for the computational results obtained.

- The investigation of flow through a suddenly expanded channel both in two-dimensions and three-dimensions is presented in Chapter 5. The effect of expansion ratio on flow through a two-dimensional geometry is first discussed. In three-dimensions the effect of the aspect ratio in stabilising the flow is presented including an in-depth study of the topology of the flow. The results have been compared to available experimental data. The transition from steady flow to unsteady flow is discussed and results are presented for higher Reynolds number flows.

- Chapter 6 concerns the analysis of high-resolution Godunov-type methods and their ability to accurately model flows featuring symmetry breaking bifurcation in a perfectly symmetric computational setup. The nonlinear terms are analysed and it is believed that these terms act as a trigger mechanism for symmetry breaking.

- The final results Chapter, Chapter 7, presents the numerical investigation of a synthetic jet issuing into quiescent air. An investigation into several slope limiters has been carried out and the results have been compared to experimental data from a workshop held on CFD validation for flows featuring separation, instabilities and transition to turbulence.

- Chapter 8 provides conclusions to the thesis summarising the key results and highlights work that could be carried out in the future.

1.7 Journal and Conference Publications

During the course of this thesis several journal and conference papers have been written.

- S. Patel and D. Drikakis, "On the symmetry-breaking mechanism in suddenly-expanded flow computations", (submitted to Computers and Fluids).

- S. Patel and D. Drikakis, "Effects of preconditioning on the accuracy and efficiency of incompressible flows", International Journal for Numerical Methods in Fluids, **47**:963–970, 2005.

- D. Drikakis, M.Hahn, S. Patel, E. Shapiro, "High-resolution methods for incompressible, compressible and variable density flows", ERCOFTAC Bulletin, n. 62, 2004.

- S. Patel and D. Drikakis, "Large eddy simulation of transitional and turbulent flows in synthetic jet actuators", Proceedings of the IUTAM Symposium on Flow Control with MEMS, held in London, UK, 19-22nd September 2006, Springer.

- S. Patel and D. Drikakis, "Flux limiting schemes for implicit large eddy simulation of synthetic jets", In Proceedings of The Fourth International Conference on Computational Fluid Dynamics, Ghent, Belgium, 2006.

- S. Patel and D. Drikakis, “Large eddy simulation of bifurcating and transitional suddenly expanded flows”, In proceedings of ECCOMAS CFD 2006, Netherlands.
- S. Patel and D. Drikakis, “Prediction of flow instabilities and transition using high-resolution methods”, In Proceedings of ECCOMAS Congress, Finland, 2004.

CHAPTER 2

Mathematical Model

This chapter concerns the numerical background employed throughout the course of this thesis. Both incompressible and compressible flow solvers have been available for use within the High-Resolution and Computing (HIRECOM) library of codes used by the Fluid Mechanics and Computational Science (FMaCS) group, at Cranfield University. The numerical idealogies behind both solvers are the same with both making use of high-resolution numerical methods. The chapter will be broken down into several sections covering; the fundamental equations governing fluid flow namely the Navier-Stokes equations; methods of solving the incompressible Navier-Stokes equations; high-resolution methods; multigrid and multiblock methods; preconditioning and flux-limiting within the compressible flow solver.

2.1 Governing Equations

The physics of (Newtonian) fluid flow is governed by the Navier-Stokes equations. These equations can be solved by considering the coupled generalised conservation laws, namely the continuity, momentum and energy equations. The governing equations outlined in this section will be presented for a compressible flow. Differences between the compressible and incompressible equations used in the respective codes will be highlighted in the text.

2.1.1 Mathematical Modelling

The Navier-Stokes equations for a compressible fluid can be written in conservation form as,

$$\frac{\partial \rho}{\partial t} + \nabla \cdot (\rho \mathbf{u}) = 0, \tag{2.1.1}$$

$$\frac{\partial \rho \mathbf{u}}{\partial t} + \nabla \cdot (\rho \mathbf{u}\mathbf{u}) = -\nabla \cdot \mathbf{P}, \tag{2.1.2}$$

$$\frac{\partial e}{\partial t} + \nabla \cdot (e\mathbf{u}) = -\nabla \cdot (\mathbf{P} \cdot \mathbf{u}) - \nabla \cdot \mathbf{q}, \tag{2.1.3}$$

where $\mathbf{u}$, ρ, e, and $\mathbf{q}$ stand for the velocity components (u, v, w), density, total energy per unit volume and the heat flux, respectively. The volume forces may account for inertial forces, gravitational forces or electromagnetic forces. The tensor $\mathbf{P}$ for a Newtonian fluid is defined by

$$\mathbf{P} = p(\rho, T)\mathbf{I} + \frac{2}{3}\mu(\nabla \cdot \mathbf{u})\mathbf{I} - \mu\left[(\nabla\mathbf{u}) + (\nabla\mathbf{u})^T\right], \tag{2.1.4}$$

where $p(\rho, T)$ is the scalar pressure, $\mathbf{I}$ is a unit diagonal tensor, T is the temperature and μ is the dynamic viscosity coefficient. The above system of equations is completed by an equation of state. For a perfect gas the equation of state is given by: $p = \rho RT$, where R is the gas constant.

For an incompressible fluid the density remains constant and hence changes the Navier-Stokes equations to:

$$\nabla \cdot \mathbf{u} = 0 \tag{2.1.5}$$

$$\frac{\partial \mathbf{u}}{\partial t} + \nabla \cdot (\mathbf{uu}) = -\frac{1}{\rho}\nabla p + \mu\nabla^2\mathbf{u} \tag{2.1.6}$$

It should be noted that the pressure used in Eq. 2.1.6 is an incompressible one and not the thermodynamic pressure. The heuristic notion is that the thermodynamic pressure is constant in the domain where the incompressible flow equations are valid. Another difference between the incompressible and compressible solvers used during the course of the PhD is that the energy equation is not solved for incompressible flows and all computed cases have isothermal conditions.

Generalised Co-ordinates Formulation

The three-dimensional compressible flow equations can be written in a matrix form as

$$\frac{\partial \bar{\mathbf{U}}}{\partial \tau} + \frac{\partial \bar{\mathbf{E}}}{\partial \xi} + \frac{\partial \bar{\mathbf{F}}}{\partial \eta} + \frac{\partial \bar{\mathbf{G}}}{\partial \zeta} = \frac{\partial \bar{\mathbf{R}}}{\partial \xi} + \frac{\partial \bar{\mathbf{S}}}{\partial \eta} + \frac{\partial \bar{\mathbf{L}}}{\partial \zeta}, \tag{2.1.7}$$

where,

$$\begin{aligned}
\bar{\mathbf{U}} &= JU \\
\bar{\mathbf{E}} &= J(E\xi_x + F\xi_y + G\xi_z) \\
\bar{\mathbf{F}} &= J(E\eta_x + F\eta_y + G\eta_z) \\
\bar{\mathbf{G}} &= J(E\zeta_x + F\zeta_y + G\zeta_z) \\
\bar{\mathbf{R}} &= J(R\xi_x + S\xi_y + L\xi_z) \\
\bar{\mathbf{S}} &= J(R\eta_x + S\eta_y + L\eta_z) \\
\bar{\mathbf{L}} &= J(R\zeta_x + S\zeta_y + L\zeta_z)
\end{aligned}$$

where **E, F** and **G** denote the inviscid Cartesian fluxes and **R, S** and **L** denote the viscous Cartesian fluxes in the $x-, y-, z-$directions, respectively. The three-dimensional

Cartesian fluxes are written in a matrix form as

$$\mathbf{U} = \begin{pmatrix} \rho \\ \rho u \\ \rho v \\ \rho w \\ e \end{pmatrix},$$

$$\mathbf{E} = \begin{pmatrix} \rho u \\ \rho u^2 + p \\ \rho vu \\ \rho wu \\ (e+p)u \end{pmatrix}, \qquad \mathbf{F} = \begin{pmatrix} \rho v \\ \rho uv \\ \rho v^2 + p \\ \rho wv \\ (e+p)v \end{pmatrix}, \qquad \mathbf{G} = \begin{pmatrix} \rho w \\ \rho uw \\ \rho vw \\ \rho w^2 + p \\ (e+p)w \end{pmatrix},$$

$$\mathbf{R} = \begin{pmatrix} 0 \\ \tau_{xx} \\ \tau_{xy} \\ \tau_{xz} \\ u\tau_{xx} + v\tau_{xy} + w\tau_{xz} - \dot{q}_x \end{pmatrix}, \qquad \mathbf{S} = \begin{pmatrix} 0 \\ \tau_{yx} \\ \tau_{yy} \\ \tau_{yz} \\ u\tau_{yx} + v\tau_{yy} + w\tau_{yz} - \dot{q}_y \end{pmatrix},$$

$$\mathbf{L} = \begin{pmatrix} 0 \\ \tau_{zx} \\ \tau_{zy} \\ \tau_{zz} \\ u\tau_{zx} + v\tau_{zy} + w\tau_{zz} - \dot{q}_z \end{pmatrix}.$$

The Jacobian and metrics for a three-dimensional grid are defined by

$$J = x_\xi(y_\eta z_\zeta - y_\zeta z_\eta) + x_\eta(y_\zeta z_\xi - y_\xi z_\zeta) + x_\zeta(y_\xi z_\eta - y_\eta z_\xi), \tag{2.1.8}$$

$$\xi_x = \frac{y_\eta z_\zeta - y_\zeta z_\eta}{J}, \qquad \xi_y = \frac{-x_\eta z_\zeta + x_\zeta z_\eta}{J}, \qquad \xi_z = \frac{x_\eta y_\zeta - x_\zeta y_\eta}{J}, \tag{2.1.9}$$

$$\eta_x = \frac{-y_\xi z_\zeta + y_\zeta z_\xi}{J}, \qquad \eta_y = \frac{x_\xi z_\zeta - x_\zeta z_\xi}{J}, \qquad \eta_z = \frac{-x_\xi y_\zeta + x_\zeta y_\xi}{J}, \tag{2.1.10}$$

$$\zeta_x = \frac{y_\xi z_\eta - y_\eta z_\xi}{J}, \qquad \zeta_y = \frac{-x_\xi z_\eta + x_\eta z_\xi}{J}, \qquad \zeta_z = \frac{x_\xi y_\eta - x_\eta y_\xi}{J}. \tag{2.1.11}$$

The discretisation of the viscous terms of the Navier-Stokes equations is fairly straightforward since these terms do not encompass any nonlinearities if the fluid under consideration is Newtonian. Both the incompressible and compressible flow solvers discretise the viscous terms using central differencing and a complete description is given in the text of Drikakis and Rider [50].

2.2 Computing Incompressible Flow

The range of flows modelled by the Incompressible Navier-Stokes equations encompasses a large number of industrially important applications for which the Mach number is less than 0.3. This includes use in the automobile industry, architectural flows, and sub-sea applications to name but a few. All of these applications require accurate numerical solutions to the Navier-Stokes equations that can be obtained in a realistic time scale using high performance computing facilities. However, the solution of the incompressible Navier-Stokes equations still presents a significant numerical challenge. The reason for this is that there is a lack of coupling between the velocity and the pressure fields. This means that the equations themselves provide no way of explicitly updating pressure as velocity is advanced. It should be noted that in an incompressible flow the absolute pressure is of no significance and that only the gradient of the pressure (pressure difference) affects the flow. Several schemes have been developed to solve this problem, and they can be divided into two categories: primitive variable and non-primitive variable.

The non-primitive variable formulation is based on the introduction of dependent variables other than velocity and pressure. Examples of methods in this category are: the vorticity/stream function method (section 2.3), the vorticity/vector-potential method, and the vorticity-velocity method (Fasel [58]). All these present problems such as boundary conditions, amount of data that must be stored and inefficiency.

Methods for solving the incompressible Navier-Stokes equations in primitive variables can be grouped into two broad categories. The first can be referred to as the pressure correction method approach (also refer to sections 2.4 and 2.5). This approach is discussed in detail in the texts of Harlow and Welch [74]; Patanker [126]; Raithby and Scheider [134]. The distinguishing feature of this method is the use of a derived equation to determine the pressure. Typically, the momentum equations are solved for the velocity components independently. This produces linearised equations by using values lagged in iteration level for the other unknowns, including pressure. Since the velocity components have been obtained without the using the continuity equation as a constraint, a Poisson equation is usually developed for the pressure that will alter the velocity field in a direction such as to satisfy the continuity equation.

The second category is a coupled approach where the discretised conservation equations are solved, treating all dependent variables as simultaneous unknowns. The method referred to is called the artificial compressibility method (Chorin [35]; Kwak et al. [91]; Choi and Merkle [34]). A detailed discussion of the artificial compressibility formulation is given in section 2.6.

2.3 Vorticity/Stream-Function Formulation

In order to avoid the presence of pressure for a two-dimensional incompressible flow one can introduce the vorticity and stream function as dependent variables in the governing equations. The vorticity is defined by

$$\omega = \text{curl}\,\mathbf{u} = \nabla \times \mathbf{u} \tag{2.3.1}$$

This approach is best suited for a two-dimensional case as vorticity is transformed to a vector quantity in three dimensions. In two-dimensional flows, the vorticity vector is orthogonal to the plane of flow and Eq. 2.3.1 reduces to Eq. 2.3.2.

$$\omega = \frac{\partial u}{\partial y} - \frac{\partial v}{\partial x} \tag{2.3.2}$$

The principle reason of introducing the stream function is that, for flows in which density and dynamic viscosity are constant, the continuity equation is identically satisfied and does not need to be dealt with explicitly. Writing the two-dimensional momentum equations in expanded Cartesian co-ordinate system (x, y) (Eq.2.3.3 and Eq.2.3.4) and differentiating , with respect to y and x, respectively, and subsequently subtracting the latter from the former we obtain Eq. 2.3.5

$$\frac{\partial u}{\partial t} + \frac{\partial u^2}{\partial x} + \frac{\partial uv}{\partial y} = -\frac{1}{\rho}\frac{\partial p}{\partial x} + \nu\left(\frac{\partial^2 u}{\partial x^2} + \frac{\partial^2 u}{\partial y^2}\right) \tag{2.3.3}$$

$$\frac{\partial v}{\partial t} + \frac{\partial uv}{\partial x} + \frac{\partial v^2}{\partial y} = -\frac{1}{\rho}\frac{\partial p}{\partial y} + \nu\left(\frac{\partial^2 v}{\partial x^2} + \frac{\partial^2 v}{\partial y^2}\right) \tag{2.3.4}$$

$$\frac{\partial \omega}{\partial t} + u\frac{\partial \omega}{\partial x} + v\frac{\partial \omega}{\partial y} = \nu\left(\frac{\partial^2 \omega}{\partial x^2} + \frac{\partial^2 \omega}{\partial y^2}\right), \tag{2.3.5}$$

where

$$\omega = \frac{\partial u}{\partial y} - \frac{\partial v}{\partial x}. \tag{2.3.6}$$

Using the continuity equation, Eq.2.3.5 can be written as

$$\frac{\partial \omega}{\partial t} + \frac{\partial u\omega}{\partial x} + \frac{\partial v\omega}{\partial y} = \nu\left(\frac{\partial^2 \omega}{\partial x^2} + \frac{\partial^2 \omega}{\partial y^2}\right), \tag{2.3.7}$$

The velocities (u, v) can be calculated via the introduction of the stream function ψ where

$$u = \frac{\partial \psi}{\partial y} \qquad v = -\frac{\partial \psi}{\partial x} \tag{2.3.8}$$

By substituting Eq.2.3.8 into Eq.2.3.6 we obtain a Poisson equation for the stream function subject to the given vorticity, (Eq.2.3.9)

$$\frac{\partial^2 \psi}{\partial x^2} + \frac{\partial^2 \psi}{\partial y^2} = \omega. \tag{2.3.9}$$

Equations 2.3.7, 2.3.8 and 2.3.9 are the three equations that make up the vorticity/stream function formulation and can be used for solving both steady and unsteady flows. It should be noted that the velocities u and v in Eq.2.3.7 can also be replaced by the stream function in Eq.2.3.8.

Equation 2.3.9 can be replaced by a pseudo-transient approach providing a coupled approach (Eq. 2.3.10) for solving the vorticity (Eq.2.3.7) and stream function (Eq. 2.3.8) equations.

$$\frac{\partial \psi}{\partial \tau} - \left(\frac{\partial^2 \psi}{\partial x^2} + \frac{\partial^2 \psi}{\partial y^2} - \omega \right) = 0. \tag{2.3.10}$$

The main problem with this approach is in the implementation of boundary conditions. For a two-dimensional case the derivatives of the stream function can be calculated from Eq. 2.3.8 only if the velocity components are known e.g. at inflow and far-field boundaries. No boundary condition is required for the vorticity. At the surface of solid boundaries and symmetry planes the stream function is constant and the following boundary conditions need to be implemented.

$$\psi = 0, \qquad \frac{\partial \psi}{\partial n} = 0, \tag{2.3.11}$$

where n denotes the normal direction to the boundary.

The pressure is calculated using the following equation,

$$\frac{\partial^2 p}{\partial x^2} + \frac{\partial^2 p}{\partial y^2} = 2\left[\frac{\partial^2 \psi}{\partial x^2}\frac{\partial^2 \psi}{\partial y^2} - \left(\frac{\partial^2 \psi}{\partial x \partial y} \right)^2 \right], \tag{2.3.12}$$

Neumann boundary conditions for the pressure p are obtained by the momentum equations.

The vorticity/stream function approach is less popular due to its complicated extension to three-dimensional flows. Both the vorticity and stream function become three component vectors in three dimensions so one ends up with six partial differential equations in place of the four that are necessary in a velocity-pressure formulation. It also inherits the difficulties associated with two-dimensional flows regarding variable fluid properties, compressibility and boundary conditions. Two alternative formulations can be applied for three-dimensional flows; The vorticity/vector potential formulation and the vorticity/velocity formulation. These two methods will not be described here instead refereing the reader to the book by Drikakis and Rider [50].

2.4 Pressure-Poisson Method

The pressure-Poisson formulation derives an explicit equation for the pressure by applying the continuity equation (divergence constraint) to the equation of motion. The equation is typically simplified by using the explicit knowledge that the divergence of velocity and its time derivative is zero. Taking the divergence of the non-conservative form of the momentum equation gives,

$$\nabla \cdot \left[\frac{\partial \mathbf{u}}{\partial t} + \mathbf{u} \cdot \nabla \mathbf{u} + \frac{1}{\rho} \nabla \mathbf{p} - \nu \nabla^2 \mathbf{u} \right] = 0 \tag{2.4.1}$$

$\nabla \cdot \mathbf{u} = 0$ holds at all times, hence, $\nabla \cdot \partial \mathbf{u}/\partial t = 0$, a time-invariant form of the equation can be formed. Rearranging and simplifying Eq. 2.4.1 gives the pressure Poisson equation presented for a pure incompressible flow as,

$$\nabla^2 p = -\rho \nabla \cdot \left[\mathbf{u} \cdot \nabla \mathbf{u} - \nu \nabla^2 \mathbf{u} \right]. \tag{2.4.2}$$

The LHS is the pressure-Poisson operator, and the RHS is the divergence of the remainder of the equation of motion without the time derivative. The inclusion of boundary conditions, completes the pressure Poisson equation.

2.5 Projection Formulation

Similar to the pressure Poisson approach the projection formulation ultimately produces a Poisson equation that is solved for the "pressure" in the incompressible flow. This pressure can be viewed as a potential field used to enforce a divergence-free velocity.

The principle behind projection methods is to advance a vector (velocity) field, $\mathbf{V} = (V^x, V^y, V^z)^T$ by some convenient means disregarding the solenoidal nature of $\mathbf{V}$, then recover the desired solenoidal vector field, $\mathbf{V}^d$ i.e. $\left(\nabla \cdot \mathbf{V}^d = 0\right)$. The notation $\mathbf{V}$ is used to either denote the velocity $\mathbf{u}$ or its time derivative $\partial \mathbf{u}/\partial t$ since the projection can be carried out using either form. In order to recover the solenoidal field a projection $\mathcal{P}$ operation is carried out which has the effect, $\mathbf{V}^d = \mathcal{P}(\mathbf{V})$. The projection uses Hodge or Helmholtz decomposition (Chorin and Marsden [36]) to decompose the velocity field into divergence-free and curl-free parts. If one denotes the curl-free portion of the velocity as the gradient of a potential, $\nabla \varphi$, the decomposition can be written as,

$$\mathbf{V} = \mathbf{V}^d + \nabla \varphi. \tag{2.5.1}$$

Taking the divergence of the above equation gives,

$$\nabla \cdot \mathbf{V} = \nabla \cdot \mathbf{V}^d + \nabla \cdot \nabla \varphi \rightarrow \nabla \cdot \mathbf{V} = \nabla^2 \varphi. \tag{2.5.2}$$

Once φ is known, the solenoidal vector field can be found through,

$$\mathbf{V}^d = \mathbf{V} - \nabla \varphi. \tag{2.5.3}$$

The projection operator can be written as, $\mathcal{P} = \mathbf{I} - \nabla (\nabla \cdot \nabla)^{-1} \nabla$. After the application of $\mathcal{P}$ to a vector field, $\mathbf{V}$, this field will be divergence free. An important aspect of projections are that they are idempotent, i.e. $\mathcal{P}^2 = \mathcal{P}$, thus repeated application of the operator will not change the result.

In the context of incompressible flow, the equations are used in a manner such that the divergence-free velocity constraint is firstly ignored then imposed via the above Helmholtz decomposition. Detailed descriptions of approximate and exact projection methods is presented in Drikakis and Rider [50].

2.6 Artificial Compressiblity Formulation

Methods for solving the compressible flow equations have attracted a significant interest resulting in a number of different methods being developed. Ideally one would like to be able to use existing compressible methods to solve the incompressible flow equations. This cannot be carried out directly due to the inherent mathematical character of the compressible equations. The compressible flow equations are hyperbolic which means that they have real characteristics on which signals travel at finite propagation speeds; this reflects the ability of compressible fluids to support sound waves. On the other hand, the incompressible flow equations have a mixed parabolic-elliptic character. Hence, in order to use numerical methods originally developed for solving the compressible flow equations, the character of the incompressible flow equations needs to be modified.

The difference in character between the compressible and incompressible flow equations lies in the lack of the time derivative term in the incompressible continuity equation. Hence the simplest way to give the incompressible equations a hyperbolic character is to include a time derivative in the continuity equation. The compressible continuity equation contains the time derivative of the density but since density is constant for the incompressible equations one cannot use this approach. Time derivatives of the velocity appear in the incompressible momentum equations and hence are not logical choices. That leaves the time derivative of the pressure as the clear choice.

The addition of a time derivative of the pressure to the incompressible continuity equation means that the equations being solved are no longer truly incompressible. A result of this is that the time history generated is no longer accurate and the extension of the equations to unsteady incompressible flow needs further consideration and will be discussed later.

For steady flows, Chorin [35] introduced the auxiliary system of equations,

$$\frac{1}{\beta}\frac{\partial p}{\partial \tau} + \frac{\partial u_j}{\partial x_j} = 0, \tag{2.6.1}$$

$$\frac{\partial u_i}{\partial t} + \frac{\partial u_i \partial u_j}{\partial x_j} = -\frac{1}{\rho}\frac{\partial p}{\partial x_i} + \nu \frac{\partial^2 u_i}{\partial x_j^2}, \tag{2.6.2}$$

where β is the artificial compressibility parameter, u_i are the velocity components, p is the pressure, ρ is the density, ν the kinematic viscosity and t is the time. The indices $i, j = 1, 2, 3$ refer to the space coordinates x, y, z. For the case of steady flow $\tau \equiv t$. The artificial compressibility parameter, which has dimensions of a velocity, is a disposable parameter, which enables the above system of equations to converge to a solution that satisfies the incompressibility condition as the steady state is approached (Chang and Kwak [28]). The value chosen for β is a key parameter to the performance of this method. It is clear that the larger the value of β the more "incompressible" the equations become. This is an undesired effect leading to the inviscid terms of the equations becoming very stiff numerically. The choice of the artificial compressibility parameter will be discussed further later in this section.

Equations 2.6.1 and 2.6.2 also have similarities with low Mach number compressible flow equations, hence the artificial compressibility parameter can be related to an artificial speed of sound.

$$c = \sqrt{\beta} \tag{2.6.3}$$

The artificial compressibility approach transforms the incompressible flow equations to fully hyperbolic and hyperbolic-parabolic for inviscid and viscous flows, respectively. The artificial compressibility approach has been found to be less computationally expensive in comparison to solving the elliptic equations and has be used extensively by various researchers. (Temam [170]; Steger and Kutler [169]; Peyret and Taylor [129]; Chang and Kwak [28]; Choi and Merkle [34]; Rizzi and Eriksson [141]; Kwak et al. [91]).

Chorin [35] originally designed the artificial compressibility approach for steady flow problems because the solutions had to be iterated to time convergence for the artificial term to vanish. It has now been well documented (Merkle and Athavale [112]; Soh and Goodrich [166]; Rogers and Kwak [144]; Rogers et al. [145]; Breuer and Hänel [22]; Kim and Menon [85]; Drikakis [45] that by adding a pseudo-time derivative to the momentum equation the artificial compressibility approach can be extended to unsteady flows. The system of equations become;

$$\frac{1}{\beta}\frac{\partial p}{\partial \tau} + \frac{\partial u_j}{\partial x_j} = 0 \tag{2.6.4}$$

$$\frac{\partial u_i}{\partial \tau} + \frac{\partial u_i u_j}{\partial x_j} = -\frac{\partial u_i}{\partial t} - \frac{1}{\rho}\frac{\partial p}{\partial x_i} + \nu\frac{\partial^2 u_i}{\partial x_j^2} \tag{2.6.5}$$

The above set of equations are iterated to pseudotime τ convergence where the divergence free flow field is satisfied, (i.e., $\partial p/\partial \tau = 0$ and $\partial u_i/\partial \tau = 0$) at each real time step. This procedure is a dual-time stepping technique and can be commonly found in the solution of the compressible equations for both steady and unsteady flows.

2.6.1 Estimation of the Artificial Compressibility Parameter

The estimation of the artificial compressibility parameter β can affect the convergence in both steady and unsteady problems. The optimum value is problem dependent, although some authors have suggested an automatic procedure for choosing it. Chang and Kwak [28] derived a criterion for a simple channel flow in which they considered the interaction of upstream propagating waves with vorticity spreading. With the requirement that the upstream propagating waves must propagate much faster than the spread of vorticity the following criterion was derived,

$$\frac{\beta}{u_{ref}} \gg \left(1 + \frac{4L}{\delta Re}\right)^2 - 1, \tag{2.6.6}$$

where L is the length of the channel and δ is the half-width. The parameter u_{ref} is a reference velocity used in the calculation of the Reynolds number ($Re = u_{ref}L/\nu$). A more complete derivation is given in Chang and Kwak [28] and Drikakis and Rider [50]. Chang and Kwak [28] pointed out that the choice of the artificial compressibility parameter β, is more important for internal flows with respect to the rate of convergence.

2.7 Multigrid Method

Multigrid methods have long been established as a powerful tool for accelerating the numerical convergence and thus reducing computing time. Brandt [21] wrote the "golden rule" for multigrid methods *"The amount of computational work should be proportional to the amount of real physical changes in the computed system"*. The first pioneer of multigrid methods was Fedorenko [60] who formulated a multigrid algorithm for the standard five-point finite difference discretisation of the Poisson equation on a square, proving that the work required to reach a given precision is $O(N)$, where N represents the number of unknowns. Bakhvalov [12] generalised this to central difference discretisation of the general elliptic partial differential equations with variable smooth coefficients. Brandt [20] presented the first practical results and then published another paper (Brandt [19]) outlining the main principles and the practical utility of multigrid methods. These papers were the beginning of a rapid development in multigrid methods. The multigrid method was discovered independently by Hackbusch [72], who laid firm mathematical foundations and provided reliable methods (Hackbush [73]). It is important to note that most multigrid methods have been developed for elliptic systems of equations. Very little work has been done using multigrid methods in conjunction with an artificial compressibility formulation. Farmer et al. [57] developed a multigrid algorithm combining the artificial compressibility formulation with the Euler equations to enforce the incompressibility constraint for the bulk flow in reference to free surface flows. The development of a three-level V-cycle multigrid algorithm in conjuction with the artificial compressibility approach was carried out by Lin and Sotiropoulos [96]. They used first order upwind differencing for the discretisation of the convection terms during the coarse grid iterations and investigated several other schemes for discretisation of the convection terms on the fine grid. Lin and Sotiropoulos [96] used the Full Approximation Storage (FAS) scheme proposed by Brandt [19], providing an estimation of the solution on the finest grid and performing a fixed number of iterations on the coarser grid levels. A multigrid algorithm for the simulation of three-dimensional incompressible turbulent flows in conjunction with the artificial compressibility approach and Newton relaxation methods was developed by Sheng et al. [157]. Two different approaches for building coarse grid equations were reported. The influence of implicit correction smoothing on increasing the stability of the scheme was also investigated. It was found that fast convergence rates for the case of external flows was obtained with relative ease, but the multigrid efficiency appeared to deteriorate in the case of complex internal flows. The above multigrid method was similar to that of Jameson [80, 81, 82] whom originally developed multigrid procedures for the solution of the compressible Euler equations which were later applied to the compressible Navier-Stokes equations by Liu and Jameson [98] and Kuerten and Geurts [90].

Drikakis et al. [52] combined Full Multigrid (FMG) and Full Approximation storage (FAS) to solve the artificial compressibility formulation of the incompressible Navier-Stokes equations. The main differences between the method of Drikakis et al. [52] and the other methods described above are:

- A combination of Full Multigrid (FMG) and Full Approximation storage (FAS) was used. FMG not only provides an initial approximation before the V-cycles are performed but also calculates basic coarse grid functions which are used in the FAS procedure.
- A third-order upwind characteristics-based method developed by Drikakis et al. [51] and Drikakis [47] was used in conjunction with the FMG-FAS procedure to discretise the convective terms at all grid levels.
- Various prolongations operators were developed to be used in conjunction with the FMG-FAS procedure.

Drikakis et al. [52] opted to use a three-level multigrid (V-cycle) approach justifying their choice of a “short-multigrid” by pointing out that in order for the multigrid to work efficiently coarser grid level should provide a good correction to the finer grid levels. This requires coarse grid levels to have a sufficient number of grid points. A multiple level multigrid algorithm may not be able to satisfy this condition and would need to create a fine grid fine enough to make sure that the coarsest grid level has a sufficient number of grid points. This may often lead to a loss of efficiency. Several grid levels can increase the complexity of the computer code and the associated memory requirements. Also shorter-multigrid algorithms are more efficient in parallel computing rather than using several grids.

2.7.1 Full Multigrid (FMG)

For steady flow cases the Full Multigrid approach can be utilised. The equations are solved on a series of coarser grid levels to provide a good initial guess for the finest grid. Once this initial guess has been computed the three-level multigrid procedure is initialised. Figure 2.1 shows the main stages of the three-level multigrid algorithm.

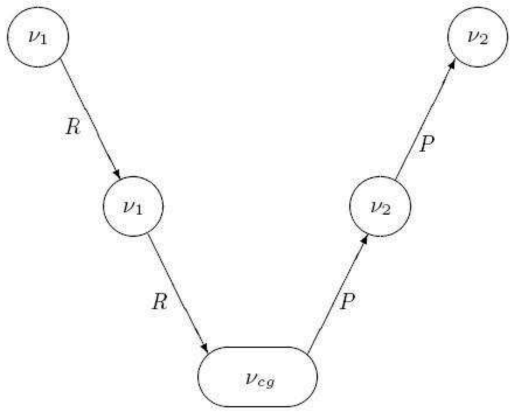

Figure 2.1: Schematic of the V-cycle for a three-grid multigrid algorithm (Drikakis and Rider [50]).

For a detailed description outlining the solution procedure please refer to Drikakis et al. [52] and Drikakis and Rider [50]. A brief description will be given here for completeness. Once the equations have been computed on the finest grid level (pre-smoothing iterations), the fine grid defect is computed. This defect is restricted to the intermediate grid level where the RHS is computed and the correction equation is solved. The intermediate grid defect is then computed and is restricted to the coarse grid. The RHS is computed on the coarse grid and the coarse grid approximate solution is obtained. The coarse grid correction is then calculated and is prolongated to the intermediate grid. Post smoothing iterations are carried out followed by computing the correction on the intermediate grid. This is then prolongated to the finest grid and the solution is corrected on the finest grid followed by post smoothing iterations. This cycle is repeated until a steady state solution is reached on the finest grid level.

It should be noted that the Navier-Stokes solver used on the intermediate and coarse grids is slightly different than that of a single grid solver. This is due to the fact that for a single grid solver the Navier-Stokes equations have a RHS equal to zero in the domain. For the multigrid method the RHS of the equations on intermediate and coarse grids levels is not zero, due to additional terms arising from the FAS linearisation procedure, which will be discussed further in the following section. The multigrid method outlined above can be extended to unsteady flows by performing V-cycles at each time step. The FMG procedure is no longer utilised in this case and iterations begin on the finest grid without any pre-smoothing on the coarser grid levels.

2.7.2 Full Approximation Storage (FAS)

The Full Approximation Storage (FAS) scheme was first described by Brandt [19]. This scheme forms the coarse-grid equations in a manner that can be successful for nonlinear problems. For linear equations the “correction” multigrid scheme is sufficient. The correction of the solution on the fine grid can be directly computed on coarser grids using the same solution matrix with the right-hand sides of the equations being the restricted defect. For nonlinear problems the multigrid corrections are formed as differences between some basic, reference solution and the currently computed approximation of this solution. The discrete problems at each grid level are solved as in a single grid case but coupled to each other by the FAS prescription in order to obtain improved convergence of the fine-grid iterations. The three level multigrid requires the calculation of the *coarse-grid* functions which need to be defined for the coarsest grid $\bar{V}_{cg}$ and intermediate grid $\bar{V}_{ig}$ respectively. According to Brandt's original algorithm these functions were computed as projections of the current intermediate and finest grid solutions onto the coarsest and intermediate grids, respectively,

$$\bar{V}_{cg} = RV_{ig} \qquad \bar{V}_{ig} = RV_{fg} \tag{2.7.1}$$

where R is the restricted operator. The approach used by Drikakis et al. [52] computed the steady state coarsest and intermediate grid solutions via FMG, U_{cg} and U_{ig} and used these values as coarsest and intermediate grid functions in Brandt's FAS algorithm to obtain;

$$\bar{V}_{cg} = U_{cg} \qquad \bar{V}_{ig} = U_{ig}. \tag{2.7.2}$$

Drikakis et al found that using the above coarsest and intermediate grid functions improved the performance of the multigrid algorithm in the case of fine grids.

The relaxation and prolongation procedures will not be discussed here and the reader is referred the paper of Drikakis et al. [52] for a detailed explanation.

2.8 Multiblock Method

There are many physical problems that exhibit multiple length and time scales in the form, for example, high velocity and temperature gradients, recirculating zones, and phase change fronts, as well as geometric complexities due to irregular shapes of the flow domain. There are many techniques available for generating complex grid geometries to handle such characteristics. These techniques include unstructured, hybrid, chimera, and structured multiblock just to name a few. In the field of Computational Fluid Dynamics (CFD), the methods used to calculate the flow field, and the flow characteristics themselves, place some rather stringent requirements on the computational grid. For most CFD applications, the structured multiblock technique is usually preferred over the others for its ability to both resolve the desired characteristics of the flow and provide for a fair amount of computational efficiency.

The multiblock method is an approach which can break a complicated geometry into sub domains (blocks) with simple shapes. Structured grids can then be generated within each block independently. It is not always required for the grid lines to be continuous across the block interface. This is dependent on the numerical algorithm. There are certain advantages of using multiblock methods:

- Multiblock methods can reduce the topological complexity of a single structured grid system by employing several grid blocks, permitting each individual grid block to be generated independently so that both geometry and resolution in the boundary region can be treated more satisfactorily;

- More freedom is allowed in the generation of grid lines, since grid lines can be discontinuous across the block interface, and local grid refinement can be conducted more easily to accommodate different physical length scales present in different regions. More grid lines can be put in high gradient region without wasting computational resource in other zones.

- With structural grids used in each block, standard structured flow solvers can be used, which greatly obviate the needs of complicated data structure, book keeping and algorithm design.

- This approach provides a natural routine for parallel computing.

Multiblock structured grids can be broadly classified as either patched grids (Rai [133]) or overlapping grids (Steger [168]). Patched grids are individual grid blocks of which any two neighbouring blocks are joined together at a common grid line without overlap. With overlapping grids, the grid blocks can be arbitrarily superimposed on each other to cover the domain of interest. Figure 2.2 shows various types of multiblock configurations.

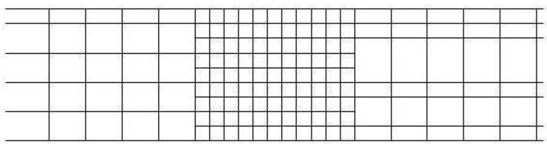

(a) Patched grid.

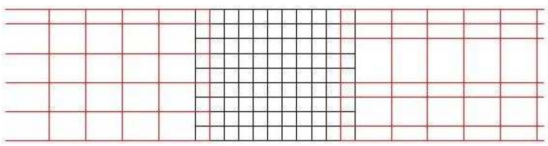

(b) Overlapping grid with discontinuous grid lines.

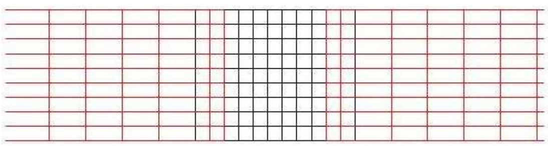

(c) Overlapping grid with continuous grid lines.

Figure 2.2: Various multiblock grid configurations.

The primary issue of concern for any multiblock solution technique is the transfer of information in the vicinity of the internal block boundaries. The details of the interface setup for "abutting" grids can be described as follows. For ease of information transfer, the ratio of the resolutions of the abutting grids is restricted to 1:1. Therefore, if a fine block was matched up to a coarse block the coarse block would have the same number of nodes as the fine block along the common interface. Also grid connectivity is required between every grid line in the coarse block and every grid line in the fine block. This way a compromise between the flexibility of the variation of grid density between two neighbouring blocks and the ease of maintaining flux conservation across the interface is reached. To facilitate the exchange of information between the two blocks, two layers of extended control volumes in each block are constructed at the common interface. These control volumes extend two layers deep into the neighbouring block. Once constructed using the neighbouring block grid, they are treated as part of the parent block, which now has extended dimensions (compared to its original dimensions). The spacing of the extended lines along the multiblock interface is the same as that of the parent block whereas the spacing in the direction normal to the interface is that of the neighbouring block grid lines. To illustrate the construction of the extended lines a two block grid is used, as shown in Fig. 2.3. The two layers of extended control vol-

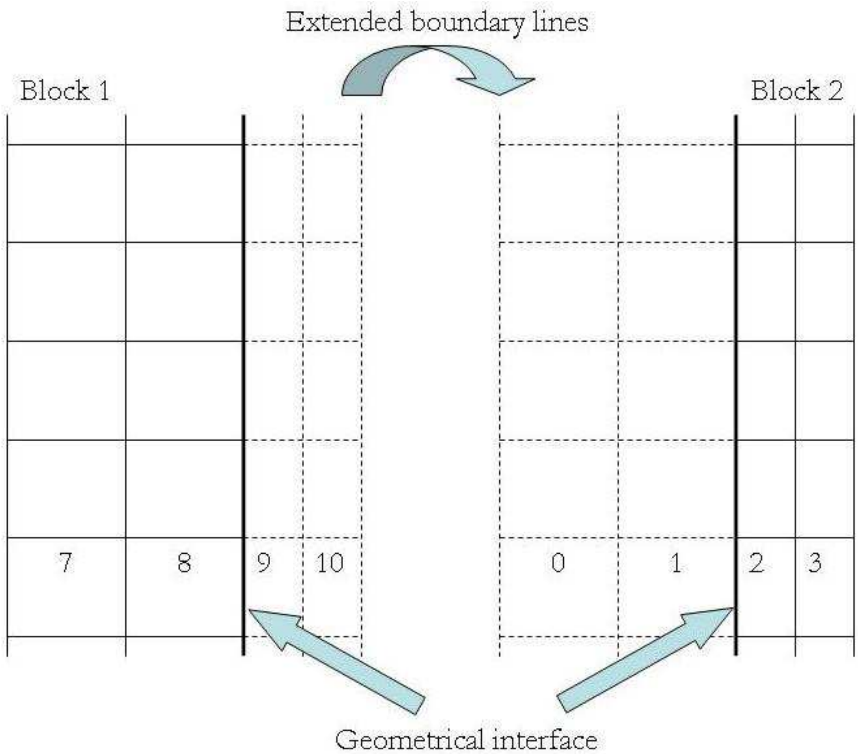

Figure 2.3: Illustration of the multiblock method using abutting grids and extended lines.

umes in each of the two parent blocks are constructed from appropriate interpolations of the coordinates of the two grid lines next to the interface in the neighbouring block. For the left block (block 1) shown in Fig. 2.3, the extended lines 9 and 10 correspond to the lines 2 and 3 respectively, of the right block (block 2). Likewise, the extended lines 0 and 1, of the right block correspond to the lines 7 and 8, respectively, of the left block. The height of any extended control volume (physical dimension) is the same as the corresponding control volume of the neighbouring block. The variable values from the neighbouring block are stored in these extended control volumes and are used in the computation of the fluxes at or near the interface.

There are some disadvantages with fully boundary-fitted multiblock grids:

- The blocking requires a great deal of user effort, especially for complex configurations. A complex configuration may need many blocks with different grid structures hence increasing the difficulty in generating the grid.
- Changes of geometry in one block can cause changes to many other blocks.
- Changes in the grid point distribution in one block, e.g. adding points near a sharp feature on an object, will generally cause changes in other blocks if grid point continuity is to be maintained.
- Requiring grid point continuity makes it difficult to increase resolution in one block without (unnecessarily) increasing the resolution in other block.

2.9 Preconditioning

The aim of preconditioning techniques is to try and overcome stiffness in the solution of the Euler and Navier-Stokes equations (Turkel [177, 179]). These techniques can be categorised into two main streams of research. Firstly, the development of preconditioning for low Mach number and incompressible flows (Choi and Merkle [34]; Turkel [178, 179]; Hirsch and Hakimi [79]; van Leer et al. [187]). The artificial compressibility method proposed by Chorin [35] can also be viewed as a type of preconditioning technique since the artificial compressibility parameter, β, acts in a similar way in preconditioning the flow equations. The second category are methods that aim to alleviate discrete stiffness in the Euler and Navier-Stokes equations. These include clustering high frequency eigenvalues away from the origin, thus providing rapid damping by a multi-stage scheme, directional coarsening multigrid and alternating direction implicit preconditioners. Preconditioning methods for the compressible equations have been investigated by several researchers; see Turkel [179] for a review on this topic. They present generalisations of the incompressible artificial compressibility formulation to compressible equations. Turkel's approach modifies the transient behaviour of the Navier-Stokes equation in such a way that the stiffness is removed from the eigenvalues. Lee and van Leer [95] preconditioner uses a minimum range in the characteristic speeds and a minimum variation from the associated eigenvectors. Lynn [101] further developed the idea of Lee and van Leer [95] and found that at stagnation points the preconditioner produced instabilities which could not be fixed.

The steady-state incompressible Navier-Srokes equations in their pseudo-compressibility (artificial compressibility) formulation are written as in Eqns. 2.6.1 and 2.6.2.

Turkel's preconditioning approach[1] replaces the momentum equation with

$$\frac{(\alpha+1)}{\beta}u_i\frac{\partial p}{\partial \tau}+\frac{\partial u_i}{\partial \tau}+\frac{\partial u_i u_j}{\partial x_j}=-\frac{\partial p}{\partial x_i}+\frac{1}{Re}\frac{\partial^2 u_i}{\partial x_j^2}\ , \tag{2.9.1}$$

in conservative form[2], or

$$\frac{(\alpha u_i)}{\beta}\frac{\partial p}{\partial \tau}+\frac{\partial u_i}{\partial \tau}+u_j\frac{\partial u_i}{\partial x_j}=-\frac{\partial p}{\partial x_i}+\frac{1}{Re}\frac{\partial^2 u_i}{\partial x_j^2}\ , \tag{2.9.2}$$

in non-conservative form.

α is yet another parameter controlling the attenuation of the flow divergence towards zero.

Equations 2.6.1 and 2.9.2 can be written in matrix form as

$$\mathbf{P}^{-1}\frac{\partial \mathbf{U}}{\partial t}+\boldsymbol{A}\frac{\partial \mathbf{U}}{\partial x}+\boldsymbol{B}\frac{\partial \mathbf{U}}{\partial y}=0 \tag{2.9.3}$$

where $\mathbf{U}=(p,u,v)^T$ and

$$\mathbf{P}^{-1}=\begin{pmatrix} 1/\beta & 0 & 0\\ \alpha u/\beta & 1 & 0\\ \alpha v/\beta & 0 & 1\end{pmatrix} \tag{2.9.4}$$

$$\boldsymbol{A}=\begin{pmatrix} 0 & 1 & 0\\ 1 & u & 0\\ 0 & 0 & u\end{pmatrix} \tag{2.9.5}$$

$$\boldsymbol{B}=\begin{pmatrix} 0 & 0 & 1\\ 0 & v & 0\\ 1 & 0 & v\end{pmatrix} \tag{2.9.6}$$

Multiplying Eq.2.9.3 with $\mathbf{P}$ yields,

$$\frac{\partial \mathbf{U}}{\partial t}+\boldsymbol{A}\mathbf{P}\frac{\partial \mathbf{U}}{\partial x}+\boldsymbol{B}\mathbf{P}\frac{\partial \mathbf{U}}{\partial y}=0 \tag{2.9.7}$$

The system of equations is hyperbolic since its eigenvalues are real. For example, the eigenvalues associated with the momentum flux in the $x-$direction (in a Cartesian system) are given by

$$\lambda_0=u\ ,\quad \lambda_{1,2}=\frac{(1-\alpha)u\pm\sqrt{(1-\alpha)^2u^2+4\beta}}{2}\ . \tag{2.9.8}$$

[1]Note that in Turkel [177] the derivation was presented for the inviscid incompressible equations, but it can also be formally applied to the system of the Navier-Stokes equations.

[2]For time-dependent flows this system is only truly conservative once the steady state has been reached

The choice of β needs to be optimised to minimise the largest possible ratio of wave speeds. Turkel proposed the calculation of β as:

$$\beta^2 = \begin{cases} \max[(2-\alpha)(u^2+v^2), \varepsilon] & \alpha < 1 \\ K\max[\alpha(u^2+v^2), \varepsilon] & \alpha \geq 1 \end{cases} \tag{2.9.9}$$

where β is a function of the fluid speed $(u^2 + v^2)$. The value of ε should be a fraction of $(u^2 + v^2)_{\max}$ and the value of K should be chosen slightly larger than one. It should be noted that the original artificial compressibility formulation in conservative form can be obtained by selecting $\alpha = -1$ in Eq. 2.9.1, in conjunction with the continuity equation (Eq. 2.6.1). For the case that $\alpha = 1$ the acoustic sound speed is isotropic and independent of the flow velocity.

2.10 High-Resolution Methods

High-resolution methods employ some sort of nonlinear "recipe" to control oscillations in the solution. High-resolution methods differ from linear methods, which use the same differencing stencil everywhere regardless of the local solution, by using the local solution to adapt the stencil used for the differencing and also to use the nonlinearity to control oscillations. The inherent nonlinearity of high-resolution methods means that even if the equations being solved are linear high-resolution methods are still nonlinear. This means that high-resolution methods are both a function of space and time as well as being dependent upon the nature of the local solution. Another property which must be satisfied in order for a numerical method to be classed as high-resolution is that the nonlinear principle used must remove spurious oscillations as well as allowing at least second-order accuracy in areas where the solution is smooth.

The above discussion leads to a more general definition of high-resolution. High-resolution methods select the "best" technique for approximating the solution given the evidence provided by the local solution. Thus, high-resolution methods adapt themselves to their circumstances so that the solution obtained is accurate and has some physical meaning.

In 1959, Godunov suggested an approach for the numerical solution of fluid flows (Godunov [66]). In this work Godunov states that *There are no monotone, linear schemes for the linear advection equation of second or higher order of accuracy*. This suggest that second order accuracy and monotonicity are contradictory requirements. Godunov's first approach involved solving a general flow field by implementing directly a numerical solution of the Euler equations written in partial differential equation form (discretised by the finite difference approach). Godunov suggested that exact solutions of the Euler equations for a local region of the flow be pieced together to synthesise the general flow field. The concept here is that you are constructing a general flow field from elements that are themselves solutions to the Euler equations in a local region of the flow. In order to construct the general flow field you are piecing together local solutions of a smaller problem, rather than visualising a widely sweeping solution of the governing partial differential equations or integral equations over the whole space of the flow. The evolution of flow to the next time step results from the wave interactions originating at the boundaries between adjacent cells. The resulting local interaction can be resolved using an approximate Riemann solver. Riemann solvers are a key to high-resolution methods and are explained in further detail in section 2.11. The basic Godunov algorithm is explained graphically in Fig. 2.4.

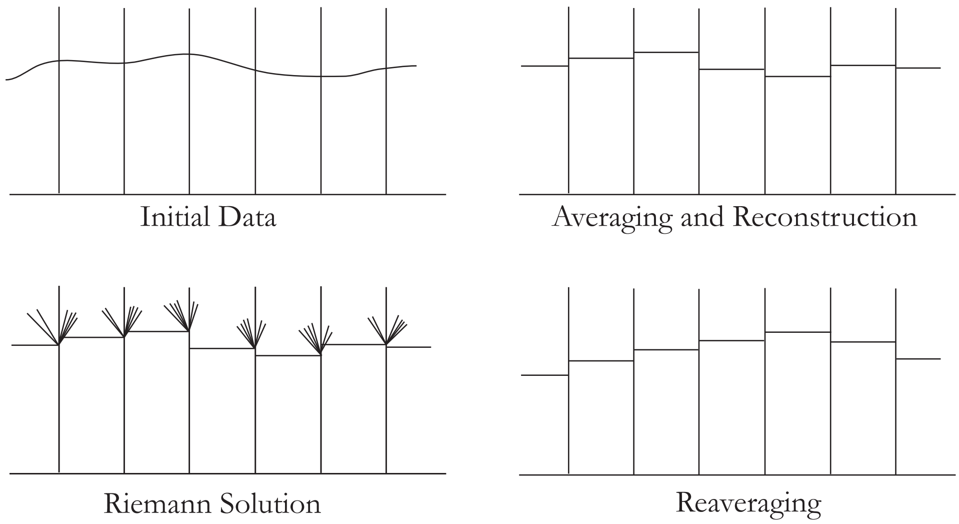

Figure 2.4: The basic geometric picture of Godunovs method showing the steps of the algorithm. The piecewise constant reconstruction, the evolution via the Riemann solution and the averaging associated with the finite volume update (figure taken from Drikakis and Rider [50]).

The key to circumventing Godunov's theorem lies in the assumption made by Godunov that the schemes are linear. Thus, in order to design schemes that are higher than first-order accurate and still preserve monotonicity, nonlinear methods need to be developed. The development of high-resolution methods needs to be carried out in a one-dimensional context due to the lack of adequate theory in multi-dimensions. It should be noted that even though a numerical method can be designed to be second-order accurate for one-dimensional problems, its accuracy in multi-dimensions is not guaranteed to be second-order. High-order flux methods can be derived by using a finite difference approach where the dependent variables are point values. If the dependent variables are viewed as averages over a cell then a mean preserving high-order interpolation can produce high-order methods. Note, that the description of the extension to high-order methods is equivalent to that of those for linear problems. Many non-linear problems develop discontinuities and as such the solution is nominally first-order accurate (Majda and Osher [103]).

Other methods of interest which have built upon high-resolution Godunov-type methods are: total variation diminishing (TVD), essentially nonoscillatory (ENO), total variation bounding (TVB) and weighted ENO (WENO). For further information of these numerical methods refer to the text of Drikakis and Rider [50] and Toro [174].

High-resolution Godunov-type methods all have a general form of the intercell Godunov-flux;

$$E_{i+1/2} = \frac{1}{2}(E_L + E_R) - \frac{1}{2}|A|(U_R - U_L) \tag{2.10.1}$$

where A approximates $\partial E/\partial U$ (the entries of the Jacoby matrix, in general), $E_L = E_L(U_L)$ and $E_R = E_R(U_R)$ denote the left and right states of the flux respectively, at the cell face and U_L and U_R are the left and right states, respectively, of the vector of the primitive variables $U = (p, u, v)^T$ at the cell face of the computational volume. The second term on the right hand side is the wave-speed dependent term, which, is a function of the local wave speeds and flow data. It is essentially acting as a nonlinear numerical viscosity that adjusts the amount of numerical dissipation locally, at the cell faces, in order to maintain monotonicity and conservation.

2.11 Riemann solvers

The solution of the flow field in the shock tube is frequently called the Riemann problem, named after the German mathematician G.F. Bernhard Riemann who first attempted its solution in 1858. The Riemann problem lends itself to a direct analytic solution of the unsteady, one dimensional Euler equations. Details of the Riemann or shock tube problem will not be presented here and the reader is referred to the text of Anderson [8] for a detailed explanation.

Approximate Riemann solvers are preferred to exact Riemann solvers due to the high computational expense of exact Riemann solvers. Moreover, approximate Riemann solvers are more reasonable for general circumstances (complicated physics, equations of state) encountered in most applications. A number of approaches have been developed concerning the purpose of computing the Godunov flux. Harten et al. [76] presented a novel approach for solving the Riemann problem approximately. The resulting Riemann solvers have been known as the HLL Riemann solvers. In this approach an approximation for the intercell numerical flux is obtained directly. The central idea is to assume a wave configuration for the solution that consists of two waves separating three contact states. Assuming that the wave speeds are given by some algorithm, application of the integral form of the conservation laws gives a closed-form, approximate expression for the flux. The approach produced practical schemes after the contributions of Davis [43] and Einfeldt [56], who independently proposed various ways of computing the wave speeds required to completely determine the intercell flux. The resulting Riemann solvers form the bases of very efficient and robust approximate Godunov-type methods.

2.11.1 HLL Scheme (Harten et al. [76])

Harten, Lax and van Leer [76] proposed a novel approach for approximately solving the Riemann problem which became known as the HLL Riemann Solver. The HLL scheme considers only the left S_L, and the right S_R, wave speeds by ignoring the contact discontinuity (see Fig. 2.5) and assuming a single intermediate ("star") region. The solver is defined as:

$$\tilde{U}(x,t) = \begin{cases} U_L & \text{if} \quad \frac{x}{t} \leq S_L, \\ U^{hll} & \text{if} \quad S_L \leq \frac{x}{t} \leq S_R, \\ U_R & \text{if} \quad \frac{x}{t} \geq S_R \end{cases} \tag{2.11.1}$$

where U^{hll} is the constant state vector given by

$$U^{hll} = \frac{S_R U_R - S_L U_L + E_L - E_R}{S_R - S_L} \tag{2.11.2}$$

where E_L and E_R are the physical flux functions at the left and right respectively. The speeds S_L and S_R are assumed to be known. The corresponding flux E^{hll} is given by

$$E^{hll} = \frac{S_R E_L - S_L E_R + S_L S_R (U_R - U_L)}{S_R - S_L} \tag{2.11.3}$$

The intercell flux for the HLL approximate Godunov method is given by

$$E^{hll}_{i+1/2} = \begin{cases} E_L & \text{if} \quad 0 \leq S_L, \\ \frac{S_R E_L - S_L E_R + S_L S_R (U_R - U_L)}{S_R - S_L} & \text{if} \quad S_L \leq 0 \leq S_R, \\ E_R & \text{if} \quad 0 \geq S_R \end{cases} \tag{2.11.4}$$

The above can be combined into a single formula (Harten et al. [76])

$$E^{hll}_{i+1/2} = \frac{S_R^- - S_L^-}{S_R - S_L} E_R + \frac{S_R^+ - S_L^+}{S_R - S_L} E_L - \frac{1}{2} \frac{S_R |S_L| - S_L |S_R|}{S_R - S_L} (U_R - U_L) \tag{2.11.5}$$

where $S^-_{L,R} = \min(0, S_{L,R})$ and $S^+_{L,R} = \max(0, S_{L,R})$.

There are various ways of estimating the wave speeds for the minimum and maximum signal velocities present in the solution of the Riemann problem for compressible flows (Davis [43]; Toro et al. [175]; Einfeldt [56]). The most well known is to directly apply the wave speeds S_L and S_R. Davis [43] suggested the simple estimates

$$S_L = u_L - a_L \qquad S_R = u_R + a_R$$

$$S_L = \min\{u_L - a_L, u_R - a_R\} \qquad S_R = \max\{u_L + a_L, u_R + a_R\}$$

where, u and a are the particle speed and the speed of sound respectively. These estimates for the wave speeds makes use of data values only.

The HLLE scheme proposed by Einfeldt [56] provides an alternative approach to the above and can be applicable to incompressible flows.

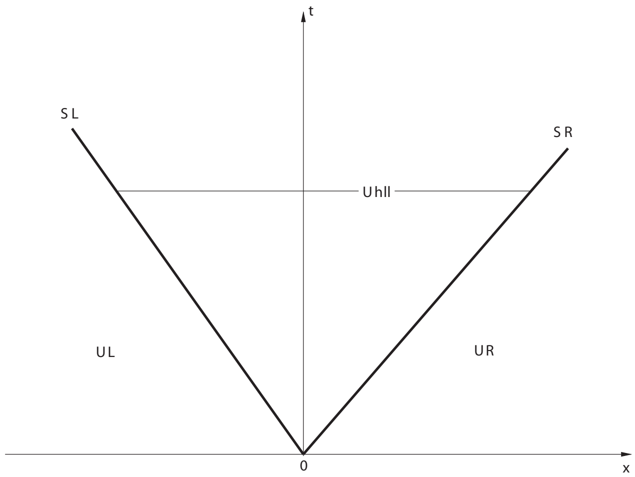

Figure 2.5: Approximate HLL Riemann solver. Solution in the *Star Region* consists of a single state $\mathbf{U}^{hll}$ separated from data states by two waves of speed S_l and S_R. Figure taken from Toro [174]

2.11.2 Einfeldt's Scheme (Einfeldt [56])

Einfeldt's HLLE scheme is an extension of the Harten-Lax-van Leer (HLL) scheme (Harten et al. [76]). In contrast to the HLL scheme and other Riemann solvers, where a numerical approximation for velocities and pressure at contact discontinuities is computed, Einfeldt derived a numerical approximation for the largest and smallest signal velocity in the Riemann problem. Using the numerical signal velocities, he used theoretical results of Harten et al. [76] to obtain the numerical flux.

The difference between the original HLL scheme and the HLLE version lies in the way that the wave speeds are calculated. According to the HLLE scheme, the intercell flux $E_{i+1/2}$ is defined by

$$E_{i+1/2} = \frac{b^+_{i+1/2}E_L - b^-_{i+1/2}E_R}{b^+_{i+1/2} - b^-_{i+1/2}} + \frac{b^+_{i+1/2}b^-_{i+1/2}}{b^+_{i+1/2} - b^-_{i+1/2}}(U_R - U_L), \tag{2.11.6}$$

where $b^+_{i+1/2} = \max((\lambda_1)_i, (\lambda_1)_{i+1})$, and $b^-_{i+1/2} = \min((\lambda_2)_i, (\lambda_2)_{i+1})$. In the context of the artificial compressibility approach, the eigenvalues λ_1 and λ_2 are given by

$$\lambda_1 = u + \sqrt{u^2 + \beta}, \qquad \lambda_2 = u - \sqrt{u^2 + \beta}. \tag{2.11.7}$$

2.11.3 Rusanov Scheme (Rusanov [148])

The Rusanov flux at a cell face $(i + 1/2)$ is given by

$$E_{i+1/2} = \frac{1}{2}(E_L + E_R) - \frac{1}{2}S^+(U_R - U_L) \tag{2.11.8}$$

$E_L = E_L(U_L)$ and $E_R = E_R(U_R)$ denote the left and right states of the flux respectively at the cell face of the computational volume. Similarly, U_L and U_R are the left and right states, respectively, of the vector of the primative variables $U = (p, u, v)^T$ at the cell face of the computational volume. The second term on the right-hand side of Eq.2.11.8 is the wave-speed dependent term (WST). Davis [43] defined this parameter as the maximum wave speed, i.e.,

$$S^+ = \max(|u_L - s_L|, |u_R - s_R|, |u_L + s_L|, |u_R + s_R|), \tag{2.11.9}$$

where, in the context of the artificial compressibility approach, $s = \sqrt{u^2 + \beta}$.

2.11.4 Lax-Friedrichs Scheme (Lax [93])

The Lax-Friedrichs scheme can be directly related to the Rusanov scheme above. If one defines the maximum wave speed in Eq. 2.11.9 by imposing the CFL stability condition, i.e., $S^+ = S_{max} = C\Delta x/\Delta t$, where C is the CFL number, then for $C = 1$, one obtains the Lax-Friedrichs flux:

$$E_{i+1/2} = \frac{1}{2}(E_L + E_R) - \frac{1}{2}\frac{\Delta x}{\Delta t}(U_R - U_L) \tag{2.11.10}$$

2.11.5 Characteristics-Based Scheme (Drikakis et al. [51])

The Characteristics-based scheme is a Riemann solver which defines the conservative variables along the characteristics as functions of their characteristic values. The method was firstly presented by Eberle [55] for the compressible Euler equations and was extended by Drikakis et al. [51] and Drikakis [47] to solve the incompressible Navier-Stokes equations. The method will be presented in the sequence of reconstruction steps firstly for the incompressible Navier-Stokes equations and secondly for the compressible equations. For a more detailed explanation of the numerical scheme please refer to the work of Drikakis et al. [51], Drikakis [47] and Eberle [55].

Incompressible flows

The calculation of the advective flux is summarised as:

1. The three eigenvalues λ_l for $l = 0, 1, 2$ are calculated using the velocities u, v, and w from the previous timestep.

2. The left and right, states of the characteristic variables are calculated by high-order reconstruction from the variables in the neighbouring cells, for example,

third-order reconstruction:

$$\begin{aligned} U_{i+\frac{1}{2},R} &= \frac{1}{6}(5U_{i+1} - U_{i+2} + 2U_i), \\ U_{i+\frac{1}{2},L} &= \frac{1}{6}(5U_i - U_{i-1} + 2U_{i+1}). \end{aligned} \tag{2.11.11}$$

It should be noted that the reconstruction in Eq. 2.11.11 is not strictly third-order accurate, but assures third-order accuracy of the term $(U_R - U_L)$ in Eq. 2.10.1 (Drikakis et al. [51])

3. For each characteristic (denoted by $l = 0, 1, 2$), the variables U_l are calculated using an upwind Godunov scheme

$$U_{l,_{i+1/2}} = \frac{1}{2}[(1 + sign(\lambda_l))U_{i+1/2,L} + (1 - sign(\lambda_l))U_{i+1/2,R}], \tag{2.11.12}$$

where

$$sign(\lambda_l) = \begin{cases} -1 & \text{for} \quad \lambda_l > 0 \\ 1 & \text{for} \quad \lambda_l < 0 \end{cases} \tag{2.11.13}$$

4. Using information from above (U_l) the new characteristic reconstructed variables $\tilde{U}$ are calculated. The variables $\tilde{U}$ associated with the advective flux E (in Cartesian co-ordinates) are given by

$$\tilde{U} = \begin{pmatrix} \tilde{p} \\ \tilde{u} \\ \tilde{v} \\ \tilde{w} \end{pmatrix} = \begin{pmatrix} \frac{1}{2s}(\lambda_1 k_2 - \lambda_2 k_1) \\ R\tilde{x} + u_0(\tilde{y}^2 + \tilde{z}^2) - v_0\tilde{x}\tilde{y} - w_0\tilde{x}\tilde{z} \\ R\tilde{y} + v_0(\tilde{x}^2 + \tilde{z}^2) - w_0\tilde{z}\tilde{y} - u_0\tilde{x}\tilde{y} \\ R\tilde{z} + w_0(\tilde{y}^2 + \tilde{x}^2) - v_0\tilde{z}\tilde{y} - u_0\tilde{x}\tilde{z} \end{pmatrix}, \tag{2.11.14}$$

where

$$R = \frac{1}{2s}\left[p_1 - p_2 + \tilde{x}(\lambda_1 u_1 - \lambda_2 u_2) + \tilde{y}(\lambda_1 v_1 - \lambda_2 v_2) + \tilde{z}(\lambda_1 w_1 - \lambda_2 w_2)\right],$$

$$\begin{aligned} k_1 &= p_1 + \lambda_1(u_1\tilde{x} + v_1\tilde{y} + w_1\tilde{z}), \\ k_2 &= p_2 + \lambda_2(u_2\tilde{x} + v_2\tilde{y} + w_2\tilde{z}). \end{aligned}$$

5. Finally the reconstructed variables are used to calculate the intercell advective flux, $\bar{E}_{i+1/2} \equiv [\bar{E}(\tilde{U})]_{i+1/2}$.

The above steps are also performed for the calculation of the advective fluxes in η and ζ directions. The discretised flux derivatives are then added (including the viscous fluxes in the case of the Navier-Stokes equations) and the system of the equations is integrated in time using a time integration scheme.

Compressible flows

The general approach for computing the incompressible equations using the characteristics based scheme is employed for computing compressible flows and again will be outlined in a sequence of reconstruction steps.

1. The three eigenvalues λ_l for $l = 0, 1, 2$ are calculated using the velocities u, v, and w from the previous timestep.

2. The left and right states of the conservative variables at the cell faces are calculated using a MUSCL-type high order interpolation of the neighbouring cell centred data. The left state (and accordingly the right state) is given by
$$\bar{U}_{L,i-1/2} = U_{i-1} + S_L[(0.5 - S_L)\Delta_{i-3/2} + (0.5 + S_L)\Delta_{i-1/2}], \tag{2.11.15}$$
where S_L is the smoothing function
$$S_L = 0.5 - (0.5 + nA_L)(1 - 2A_L)^n,$$
A_L is a modified van Albada limiter defined by
$$A_L = \frac{\Delta_{i-1/2}\Delta_{i-3/2}}{\Delta^2_{i-1/2} + \Delta^2_{i-3/2} + \epsilon},$$
ϵ is a small positive value preventing division by zero and Δ is the vector of slopes of conserved variables at the corresponding cell face. Sensor functions are applied to detect strong discontinuities, e.g., shocks in hypersonic flows, and limit A_L in order to obtain a more dissipative (low-order) interpolation scheme.

3. For each characteristic (denoted by $l = 0, 1, 2$), the variables U_l are calculated using an upwind Godunov scheme
$$U_{l,i-1/2} = (0.5 + \phi_l)\bar{U}_{L,i-1/2} + (0.5 - \phi_l)\bar{U}_{R,i-1/2}, \tag{2.11.16}$$
where the function ϕ_l is defined as,
$$\phi_l = 0.5\frac{\lambda_{L,l} + \lambda_{R,l}}{|\lambda_{L,l}| + |\lambda_{R,l}| + \epsilon}.$$
The parameter ϵ averts division by zero and $\lambda_{L,l}$, $\lambda_{R,l}$ are the left and right eigenvalues at the cell face, respectively. Using the Godunov-type up-winding scheme in Eq. 2.11.16, three sets of characteristic variables are calculated, i.e., for $l = 0, 1, 2$.

4. Using information from above ($U_{l,i-1/2}$) the new characteristic reconstructed variables $\tilde{U}_{i-1/2}$ are calculated. The variables $\tilde{U}_{i-1/2}$ associated with the advective flux E (in Cartesian co-ordinates) are given by
$$\tilde{U}_{i-1/2} = \begin{pmatrix} \tilde{\rho} \\ \widetilde{\rho u} \\ \widetilde{\rho v} \\ \widetilde{\rho w} \\ \tilde{e} \end{pmatrix} = \begin{pmatrix} \rho_0 + r_1 + r_2 \\ (\rho u)_0 + (u+s)r_1 + (u-s)r_2 \\ (\rho v)_0 + vr_1 + vr_2 \\ (\rho w)_0 + wr_1 + wr_2 \\ e_0 + (H + s\lambda_0)r_1 + (H - s\lambda_0)r_2 \end{pmatrix}, \tag{2.11.17}$$

where

$$r_1 = \frac{1}{2s^2}\Big[(\rho_0 - \rho_1)(s\lambda_0 - \frac{\gamma-1}{2}q^2) + ((\rho u)_0 - (\rho u)_1)((\gamma-1)u - s)$$
$$+ ((\rho v)_0 - (\rho v)_1)(\gamma-1)v$$
$$+ ((\rho w)_0 - (\rho w)_1)(\gamma-1)w - (e_0 - e_1)(\gamma-1)\Big],$$

$$r_2 = \frac{1}{2s^2}\Big[- (\rho_0 - \rho_2)(s\lambda_0 + \frac{\gamma-1}{2}q^2) + ((\rho u)_0 - (\rho u)_2)((\gamma-1)u + s)$$
$$+ ((\rho v)_0 - (\rho v)_2)(\gamma-1)v$$
$$+ ((\rho w)_0 - (\rho w)_2)(\gamma-1)w - (e_0 - e_2)(\gamma-1)\Big],$$

and the total enthalpy is given by

$$H = \frac{s^2}{\gamma - 1} + 0.5q^2.$$

The velocities u, v, w and the speed of sound s are the average values of their left and right states and $q^2 = u^2 + v^2 + w^2$. Finally the advective flux $E_{i-1/2}$ for the characteristics-based scheme is calculated using the variables $\tilde{U}_{i-1/2}$, i.e.,

$$E_{i-1/2} = E(\tilde{U}_{i-1/2}) \qquad (2.11.18)$$

2.12 High-Order Reconstruction and Slope Limiting

Higher-order spatial accuracy can be achieved by introducing more upwind points in the scheme. The following description is based on an extension of the Godunov type approach by van Leer [185]. The projection stage whereby the solution is projected in each cell $(i - 1/2, i + 1/2)$ on piecewise constant states, is the cause of the first-order accuracy of the Godunov schemes. This stage is completely decoupled from the physical stage where the Riemann problems are solved at the interfaces of the cells. This means that the first projection stage can be modified without modifying the Riemann solver, in order to generate higher than first-order spatial approximations. The state variables at the interfaces are thereby obtained from an interpolation between the neighbouring cell averages.

Two interpolation procedures are presented for the high-order reconstruction. Firstly a Lagrangian interpolation scheme and secondly a MUSCL interpolation scheme (van Leer [183]).

2.12.1 Largangian interpolation

Consider the one-dimensional stencil shown in Fig. 2.6. Two states, left and right, for the intercell characteristic variables can be defined as follows

$$U_{i+1/2,L} = aU_i - bU_{i-1} + cU_{i+1} + dU_{i+2}, \tag{2.12.1}$$

for the left state, and

$$U_{i+1/2,R} = aU_{i+1} - bU_{i+2} + cU_i + dU_{i-1}, \tag{2.12.2}$$

for the right state. The coefficients a, b, c and d need to be determined.

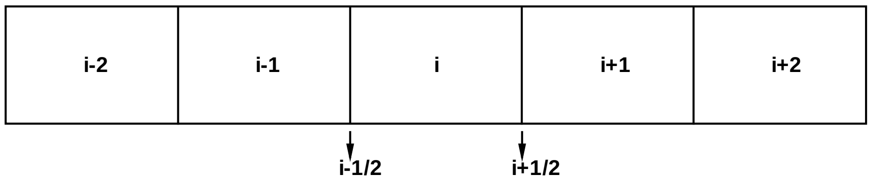

Figure 2.6: One-dimensional stencil used to define the high-order interpolation. Figure taken from Drikakis and Rider [50].

By taking the derivative of the characteristic variable at the cell centre for the case of a positive eigenvalue and developing all variables in a Taylor series expansion around the cell centre i, yields

$$\begin{aligned}\left(\frac{\partial U}{\partial \xi}\right)_i &= (a - b + c + d)U^{(1)} + \Big[c - a + 3(b + d)\Big]U^{(2)} \\ &\quad + \Big[c + a + 7(d - b)\Big]U^{(3)} + \Big[c - a + 15(b + d)\Big]U^{(4)}.\end{aligned} \tag{2.12.3}$$

Using 2.12.3 schemes of different orders of accuracy can be derived.

- First-order upwind scheme:
  The right and left states of the variables at the cell face are defined as:

$$\begin{aligned}U_{i+\frac{1}{2},R} &= U_{i+1}, \\ U_{i+\frac{1}{2},L} &= U_i.\end{aligned} \tag{2.12.4}$$

- Second-order scheme:

$$\begin{aligned}U_{i+\frac{1}{2},R} &= \frac{1}{2}(3U_{i+1} - U_{i+2}), \\ U_{i+\frac{1}{2},L} &= \frac{1}{2}(3U_i - U_{i-1}).\end{aligned} \tag{2.12.5}$$

- Third-order scheme:

$$
\begin{aligned}
U_{i+\frac{1}{2},R} &= \frac{1}{6}(5U_{i+1} - U_{i+2} + 2U_i), \\
U_{i+\frac{1}{2},L} &= \frac{1}{6}(5U_i - U_{i-1} + 2U_{i+1}).
\end{aligned}
\tag{2.12.6}
$$

The interpolation formulae 2.12.4, 2.12.5 and 2.12.6 can be used for calculating the characteristic variables p_l, u_l, v_l and w_l $(l = 0, 1, 2)$ for each of the three eigenvalues. The decision on the selection of the left or right state can be made according to the sign of the local (intercell) eigenvalue according to the formula

$$
U_{l,i+1/2} = \frac{1}{2}\left\{[1 + sign(\lambda_l)]U_{i+1/2,L} + [1 - sign(\lambda_l)]U_{i+1/2,R}\right\}. \tag{2.12.7}
$$

It should be noted that the interpolation outlined in Eqs. 2.12.4, 2.12.5 and 2.12.6 do not strictly give schemes which are first-, second-, and third-order accurate, respectively, but do assure this accuracy in the term $(U_R - U_L)$ in Eq. 2.10.1.

2.12.2 MUSCL method and limiters for variable interpolation

The MUSCL acronym stands for Monotone Upstream-centred Schemes for Conservation Laws, after the name of the first code applying this method as developed by van Leer [186]. To represent the numerical approximation of the solution as a piecewise constant is equivalent to a first-order spatial discretisation. Hence, a linear approximation of the solution on each cell would produce a second-order space discretisation, while a quadratic representation on each cell leads to a third-order spatial discretisation.

The standard MUSCL interpolation can be represented as;

$$
U^L_{i+1/2} = U_i + \frac{1}{4}[(1-k)(U_i - U_{i-1}) + (1+k)(U_{i+1} - U_i)]. \tag{2.12.8}
$$

$$
U^R_{i+1/2} = U_{i+1} - \frac{1}{4}[(1-k)(U_{i+2} - U_{i+1}) + (1+k)(U_{i+1} - U_i)]. \tag{2.12.9}
$$

This form of the extrapolation is symmetric about the interface $i + 1/2$, and k is a free parameter between -1 and 1. The interface values can be considered as resulting from a combination of backward and forward extrapolations. In particular $k = -1$ corresponds to a linear one-sided extrapolation at the interface between the averaged values at the two upstream cells i and $(i - 1)$ (see Fig. 2.7):

$$
\begin{aligned}
U^L_{i+1/2} &= U_i + \frac{1}{2}(U_i - U_{i-1}) \qquad & k = -1 \\
U^R_{i+1/2} &= U_{i+1} - \frac{1}{2}(U_{i+2} - U_{i+1}) \qquad & k = -1
\end{aligned}
\tag{2.12.10}
$$

leading to a second order fully one-sided scheme.

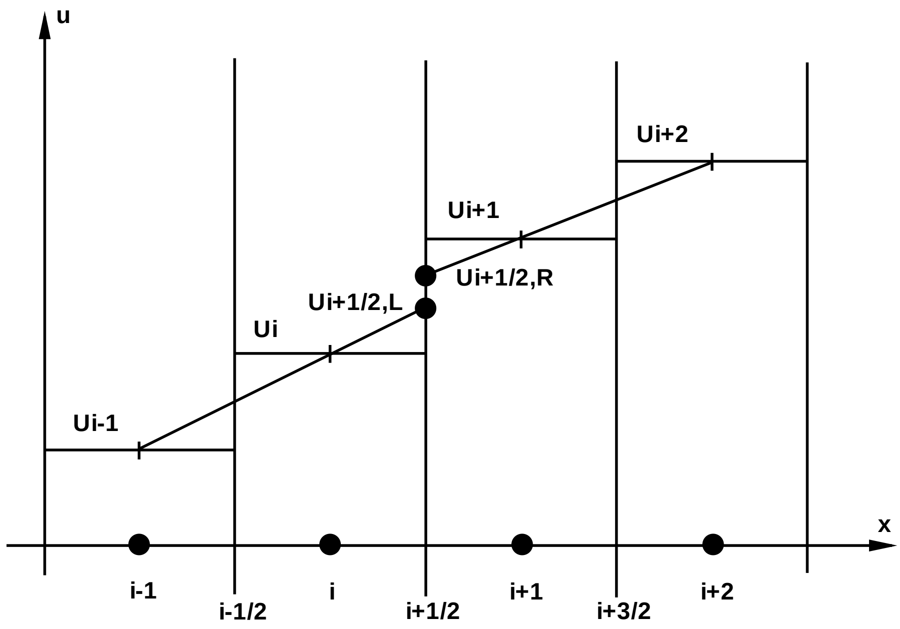

Figure 2.7: Linear one-sided extrapolation of interface values for $k = -1$. Figure taken from Hirsch [78]

For $k = 0$ the interface value is approximated by a linear interpolation between one upstream and one downstream cell:

$$\begin{aligned} U^L_{i+1/2} &= U_i + \frac{1}{4}(U_{i+1} - U_{i-1}) \qquad k = 0 \\ U^R_{i+1/2} &= U_{i+1} - \frac{1}{4}(U_{i+2} - U_i) \qquad k = 0 \end{aligned} \tag{2.12.11}$$

It should be noted that when $k = 1$ the interface values are the arithmetic mean of the adjacent cell values and the upwind character is totally lost. This corresponds to a central scheme since there is no discontinuity at the cell interfaces. When $k = 1/3$ the MUSCL reconstruction is third-order accurate, however, this does not translate to third-order accuracy in space when the extrapolated variables are used to calculate the fluxes, instead the fluxes reduce to second order accuracy.

Second-order upwind schemes are naturally oscillatory around discontinuities and on there own are not stable enough to avoid over- and undershoots in the numerical solutions. The physical solution to the Euler and Navier-Stokes equations, however, do not seem to allow the appearance of new extrema in the evolution of the flow variables. This can be proven for one-dimensional flows. Therefore, the numerical generation of oscillations is due to the treatment of the second-order approximation, since first-order schemes are free of these over- and undershoots. The extension of Godunov's method from a piecewise constant representation of the state variables to a piecewise linear representation obtains second-order spatial accuracy. This can create problems in that the slope of the linear variation can cause oscillations due to large differences of the slope in one cell compared to the difference of adjacent mean values. As seen in Fig. 2.8 if the slope in cell i is too large, the solution to the linear convection equation at time step $n+1$, obtained after a translation $a\delta t$ of the distribution at time $n\delta t$, will lead to cell averaged values $u_i^{n+1} < u_{i-1}^{n+1}$, while at level n one had $u_i^n > u_{i-1}^n$ and hence an undershoot in the solution at time $n+1$ will appear.

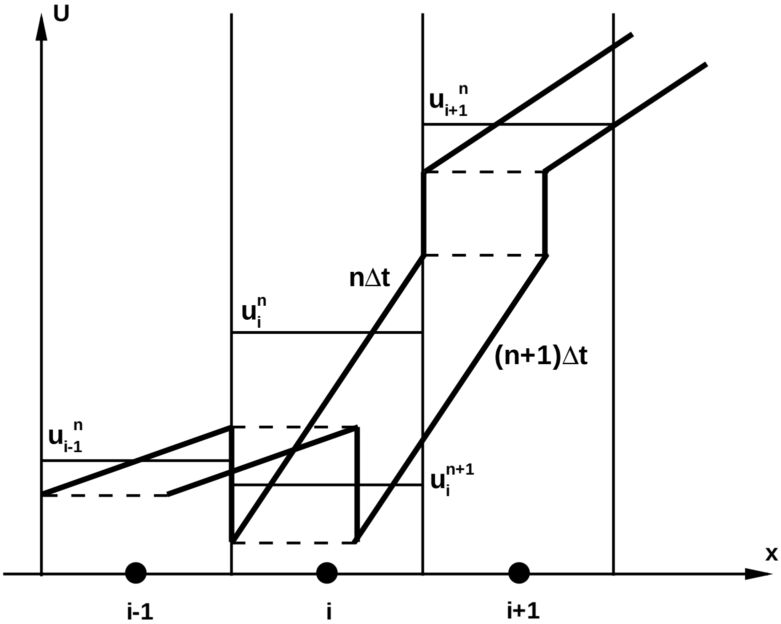

Figure 2.8: Generation of oscillations in numerical solutions. Figure taken from Hirsch [78]

In order to define a scheme which is non-oscillatory excessive large gradients should be avoided. One way to obtain a numerical scheme which is non-oscillatory is to use limiters. Limiters provide a non-linear correction factor and were initially introduced by van Leer [182] and separately by Boris and Book [17]. The idea behind limiters is to ensure that the interpolation procedure itself cannot produce any new extrema in the data at the cell interface, i.e. that the cell interface value must lie between the values of the neighbouring cell.

The MUSCL scheme as presented in Eqs. 2.12.8 and 2.12.9 is not stable on it's own and hence a limiting method must be incorporated. Limiters are generally defined using the parameter r where;

$$r^L = \frac{U_{i+1} - U_i}{U_i - U_{i-1}}, \qquad r^R = \frac{U_{i+1} - U_i}{U_{i+2} - U_i}. \tag{2.12.12}$$

A limiting function $\phi(r)$ is defined giving a symmetric limited MUSCL scheme in the form;

$$U^L_{i+1/2} = U_i + \frac{1}{4}[(1-k)\phi(r^L)(U_i - U_{i-1}) + (1+k)\phi\left(\frac{1}{r^L}\right)(U_{i+1} - U_i)]. \quad (2.12.13)$$

$$U^R_{i+1/2} = U_{i+1} - \frac{1}{4}[(1-k)\phi(r^R)(U_{i+2} - U_{i+1}) + (1+k)\phi\left(\frac{1}{r^R}\right)(U_{i+1} - U_i)]. \quad (2.12.14)$$

It is important to point out that for a limiting scheme to be high-resolution it must satisfy the TVD (*total-variation-diminishing*) concept. This will not be discussed here in detail and the reader is referred to the texts of Toro [174] and Drikakis and Rider [50]. A simple way to describe the TVD concept is to consider the equation below in conservation form

$$\frac{\partial u}{\partial t} + \frac{\partial f}{\partial x} = 0 \quad (2.12.15)$$

where $f = f(u)$. At any given point along the x axis, both u and its derivative, $\partial u/\partial x$, are known at time level n. An important property of physical solutions governing by Eq. 2.12.15 is that $|\partial u/\partial x|$ integrated over the entire domain on the x axis does not increase with time. This integrated quantity is called the total variation, TV, given by

$$\mathrm{TV} = \int \left|\frac{\partial u}{\partial x}\right| dx \quad (2.12.16)$$

Hence, for a physically proper solution, TV does not increase with time. In terms of a numerical solution of Eq. 2.12.15, where $\partial u/\partial x$ can be discretised by $(u_{i+1} - u_i)/\delta x$, the Eq. 2.12.16 can be written as;

$$\mathrm{TV}(u) \equiv \sum_i |u_{i+1} - u_i| \quad (2.12.17)$$

Equation 2.12.17 defines the total-variation in x of a discrete numerical solution. If $\mathrm{TV}(u^{n+1})$ and $\mathrm{TV}(u^n)$ represent Eq. 2.12.17 evaluated at time level $n+1$ and n, respectively, and if

$$\mathrm{TV}(u^{n+1}) \leq \mathrm{TV}(u^n) \quad (2.12.18)$$

the numerical algorithm is said to be *total-variation-diminishing* (TVD). From the above discussion, if a numerical solution is to properly follow the physical behaviour of a given flow field, then the scheme should be a TVD scheme.

Baines and Sweby [11] outlined a TVD region shown in Fig. 2.9 for the design of slope limiters. They showed that for a negative r the TVD region is a single line $\phi = 0$ and for a positive r the TVD region lies between 0 and $\min\{\phi_L(r), \phi_R(r)\}$.

Various limiters have been described in the literature of Toro [174] and several have been used during the course of this thesis, namely: van Albada (VA) (van Albada et al. [181]); van Leer (VL) (van Leer [184]); Minbee (MB) (Harten [75]); Superbee (SB) (Roe [143]); the limiter developed by Drikakis (DD) (Zóltak and Drikakis [196]); and a 5th order limiter (KK5) by Kim and Kim [84]. They can be each be described as;

$$\phi_{VA} = \frac{r(1+r)}{1+r^2} \quad (2.12.19)$$

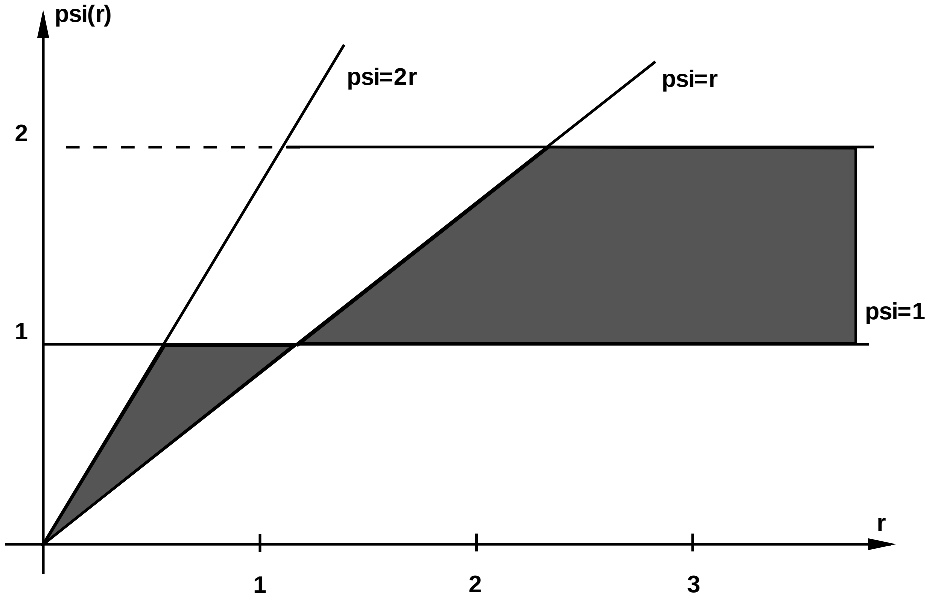

Figure 2.9: Limiter region for second-order TVD schemes. Figure taken from Hirsch [78]

$$\phi_{VL} = \frac{2r}{1+r} \tag{2.12.20}$$

$$\phi_{MB} = \min(1, r) \tag{2.12.21}$$

$$\phi_{SB} = \max(0, \min(1, 2r), \min(r, 2)) \tag{2.12.22}$$

$$\phi_{DD} = 1 - \left(1 + \frac{2Nr}{1+r^2}\right)\left(1 - \frac{2r}{1+r^2}\right)^N \tag{2.12.23}$$

$$\phi_{KK5,L} = \frac{-2/r^L_{i-1} + 11 + 24r^L_i - 3r^L_i r^L_{i+1}}{30}, \tag{2.12.24}$$

$$\phi_{KK5,R} = \frac{-2/r^R_{i+2} + 11 + 24r^R_{i+1} - 3r^R_{i+1} r^R_i}{30}, \tag{2.12.25}$$

where monotonicity is maintained by limiting Eqs. 2.12.24 and 2.12.25 using

$$\phi_{KK5,L} = \max(0, \min(2, 2r^L_i, \phi_{M5,L})), \tag{2.12.26}$$

$$\phi_{KK5,R} = \max(0, \min(2, 2r^R_i, \phi_{M5,R})). \tag{2.12.27}$$

The limiter applied by van Albada et al. [181] tends to have a smoother behaviour than the limiter of van Leer [184]. It has the property of tending to 1 for large values of r. The Minbee limiter takes the lowest value of the considered TVD domain and is a commonly applied limiter. It's resolution at contact discontinuities is not so good but is very simple to implement. The Superbee limiter proposed by Roe [143] considers the upper limit of the second-order TVD domain and has been shown to have excellent resolution properties for contact discontinuities. This limiter actually amplifies certain contribution, when $\phi > 1$, while remaining within the TVD bounds. This explains the property of the limiter in counteracting the excessive spreading of contact discontinuities.

The above limiters share the symmetry property

$$\frac{\phi(r)}{r} = \phi\left(\frac{1}{r}\right) \tag{2.12.28}$$

indicating that forward and backward gradients are treated in the same way. Alternatively, this property ensures that the limited gradients remain associated with a linear variation of the u variable within each cell.

Thornber et al. [172, 173] have carried out a theoretical analysis of the dissipation of kinetic energy within Godunov-type schemes for the simulation of low Mach number flows. In relation to shock flows, Thornber et al. [172] report that the leading order dissipation rate of a Godunov method is proportional to the velocity jump squared multiplied by the speed of sound, and is caused by the reaveraging process in the finite volume method. At low Mach numbers the dissipation due to velocity jumps dominates the flow. Thornber et al. [173] have proposed a low Mach 'correction' to the finite volume Godunov method and have shown that a significantly improved solution of low Mach perturbations for use in mixed compressible/incompressible flow can be obtained. The simple modification of the limiting method is applied only to velocity jumps across the cell interface and ensures that the leading order dissipation rate is constant as Mach tends to zero. Thornber et al. [173] originally developed this low Mach correction for the limiting method of Kim and Kim [84] but has since extended it for various other limiters. The modification scales the limited velocities by Mach number, hence removing the dependency of the leading order kinetic energy dissipation rate on the speed of sound. The modification can be shown for the KK5 limiter as:

$$\begin{aligned} \mathbf{u}_{L,KK} &= \frac{\mathbf{u}_L + \mathbf{u}_R}{2} + z\frac{\mathbf{u}_L - \mathbf{u}_R}{2}, \\ \mathbf{u}_{R,KK} &= \frac{\mathbf{u}_L + \mathbf{u}_R}{2} + z\frac{\mathbf{u}_R - \mathbf{u}_L}{2}, \end{aligned} \tag{2.12.29}$$

where $z = \min(M_{local}, 1)$ and $M_{local} = \max(M_L, M_R)$. The parameter $\mathbf{u}$ is the velocity.

2.13 Time Integration

One of the most popular temporal discretisation methods are explicit Runge-Kutta time-stepping schemes. An explicit scheme starts from some known solution and employs the corresponding residual in order to obtain a new solution at time $(t + \Delta t)$.

Thus, the new solution depends solely on values already known. This fact makes explicit schemes very simple and easy to implement. A fourth-order Runge-Kutta time-stepping method is used for the time integration of the incompressible Navier-Stokes equations, whereas the compressible solver uses a third-order Runge-Kutta strongly stability preserving (SSP) method (Gottleib et al. [68]). This method is also known as Heun's method and has been documented in the books of Ascher and Petzold [9] and Oran and Boris [124]. The two methods are described below, starting with the fourth-order Runge-Kutta method used in the incompressible solver.

The three-dimensional Navier-Stokes equations can be written in the context of the artificial compressibility formulation in curvilinear coordinates as:

$$(JU)_\tau + (J\tilde{I}U)_t + (E_I)_\xi + (F_I)_\eta + (G_I)_\zeta = (E_V)_\xi + (F_V)_\eta + (G_V)_\zeta \tag{2.13.1}$$

U is the unknown solution vector, $\tilde{I}$ is a matrix and J is the jacobian of transformation from cartesian (x, y, z) to curvilinear (ξ, η, ζ) coordinates. Eq. 2.13.1 can be re-written as,

$$(Q)_\tau + (NQ) = 0 \tag{2.13.2}$$

where $Q = JU$ and the operator $N(Q)$ contains the discretised inviscid and viscous fluxes as well as the term $(\tilde{I}Q)_t$. The time intergration of Eq. 2.13.2 requires iterations to be performed at the pseudo time level τ. Let ν and n denote the pseudo-iterations and real time steps, respectively. In order to forward the solution from n to $n+1$ we consider the $(m+1)$th TVD Runge-Kutta discretisation of Eq. 2.13.2 as proposed by Shu and Osher [158]. The general discretisation form is:

$$Q^{(i)} = \sum_{k=0}^{i-1} \left(\tilde{a}_{ik} Q^{(k)} + b_{ik}\Delta t N(Q^k)\right), \qquad i = 1, 2, ..., m \tag{2.13.3}$$

with

$$Q^{(0)} = Q^{(\nu)}, \qquad Q^{(m)} = Q^{(\nu+1)} \tag{2.13.4}$$
$$\lim_{Q_\tau \to 0} Q^{(\nu+1)} \to Q^{(n+1)}$$

The fourth-order Runge-Kutta time-stepping method can be written in consolidated form as:

$$Q^{(0)} = Q^\nu \tag{2.13.5}$$
$$Q^{(1)} = Q^\nu - \frac{\Delta\tau}{2} N(Q^{(0)}) \tag{2.13.6}$$
$$Q^{(2)} = Q^\nu - \frac{\Delta\tau}{2} N(Q^{(1)}) \tag{2.13.7}$$
$$Q^{(3)} = Q^\nu - \Delta\tau(Q^{(2)}) \tag{2.13.8}$$
$$Q^{(\nu+1)} = Q^\nu - \frac{\Delta\tau}{6}[N(U^{(0)}) + 2N(U^{(1)}) + 2N(U^{(2)}) + N(U^{(3)})] \tag{2.13.9}$$

By implementing the above with a non-linear multigrid method high numerical efficiency can be achieved. The artificial compressibility and dual time stepping formulation allows us to implement the multigrid approach directly to the Navier-Stokes equations (see section 2.7).

Local time stepping Δt is used to accelerate the convergence to the steady state solution.

$$\Delta t = \frac{\text{CFL}}{\max(\lambda_j)} \qquad j = 0, 1, 2 \tag{2.13.10}$$

where CFL is the Courant-Friedrichs-Lewy number.

The third-order Runge-Kutta strongly stability preserving (SSP) method used in the compressible code can be described by firstly showing Heun's third-order method (Ascher and Petzold [9]; Oran and Boris [124]) as:

$$\left.\begin{aligned} \frac{U^1 - U^n}{\Delta t} &= \tfrac{1}{3} f(U^n, t^n) \\ \frac{U^2 - U^n}{\Delta t} &= \tfrac{2}{3} f(U^n, t^n) \\ \frac{U^{n+1} - U^n}{\Delta t} &= \tfrac{1}{4}\left[f(U^n, t^n) + 3f(U^2, t^{n+2/3})\right] \end{aligned}\right\} \tag{2.13.11}$$

The third-order TVD method can be represented as:

$$\left.\begin{aligned} \frac{U^1 - U^n}{\Delta t} &= f(U^n, t^n) \\ \frac{U^2 - U^n}{\Delta t} &= \tfrac{1}{4}\left[f(U^n, t^n + f(U^1, t^{n+1}))\right] \\ \frac{U^{n+1} - U^n}{\Delta t} &= \tfrac{1}{6}\left[f(U^n, t^n) + 4f(U^2, t^{n+1/2}) + f(U^1, t^{n+1})\right] \end{aligned}\right\} \tag{2.13.12}$$

The recent work of Spiteri and Ruuth [167] has shown that SSP methods can produce larger CFL limits at the cost of more function evaluations. A four-stage method is given as:

$$\left.\begin{aligned} \frac{U^1 - U^n}{\Delta t} &= \tfrac{1}{2} f(U^n, t^n) \\ \frac{U^2 - U^n}{\Delta t} &= \tfrac{1}{2} f(U^1, t^{n+1}) \\ \frac{U^{n+1} - \frac{2}{3}U^2 - \frac{1}{3}U^2}{\Delta t} &= \tfrac{1}{3}\left[f(U^2, t^{n+1/2}) + f(U^1, t^{n+1/2})\right] \end{aligned}\right\} \tag{2.13.13}$$

This method extends the CFL limit to 2 rather than 1.

CHAPTER 3

Preconditioning of Incompressible Flows

This chapter describes the investigation into a form of preconditioning approach for the incompressible Navier-Stokes equations. Computations have been carried out for flows through suddenly expanded-contracted and suddenly expanded geometries, for a broad range of Reynolds numbers, featuring flow separation as well as instabilities. The instabilities are manifested in a symmetry-breaking bifurcation of the flow. A comparison of the preconditioned and non-preconditioned solution against experimental and previous computational results are presented. The effect of preconditioning on the accuracy of the computed solution and rate of convergence to the steady state has been investigated.

3.1 Introduction

The aim of preconditioning techniques is to alleviate the stiffness of the Euler and Navier-Stokes equations for incompressible and low speed compressible flows. Some would argue that the equations for solving incompressible flow do not experience the same type of stiffness as with the low speed compressible flow equations. This however is unfounded. When solving the hyperbolic incompressible flow equations using the artificial compressibility formulation (2.6), at Reynolds numbers of $Re = 0.1$ and below, the advective fluxes behave in much the same manner as solving the low speed compressible flow equations and require a lengthy time to converge to a steady state. The artificial compressibility parameter scales inversely to Reynolds number to obtain the best convergence rate. Hence as Reynolds number becomes very low the artificial compressibility parameter becomes large. This results in the equations becoming more "incompressible" which in turn results in the advective equations becoming more stiff.

There are two main streams of research regarding preconditioning. Firstly, the development of preconditioning for low Mach number and incompressible flows (Choi and Merkle [34]; Turkel [178, 179]; Hirsch and Hakimi [79]; van Leer et al. [187]). The artificial compressibility method of Chorin [35] can also be viewed as a preconditioning technique. Secondly, methods that aim to alleviate discrete stiffness in the Euler and

Navier-Stokes equations, including clustering high frequency eigenvalues away from the origin, thus providing rapid damping by a multi-stage scheme (Pierce and Giles [130]), directional coarsening multigrid (Mulder [119]) and alternating direction implicit preconditioners (Allmaras [2]; Buelow et al. [24]). Preconditioning methods for the compressible equations have been investigated by several researchers; see Turkel [179] for a review on this topic. They present generalisations of the incompressible artificial compressibility formulation to compressible equations. Turkel's approach modifies the transient behaviour of the Navier-Stokes equation in such a way that the stiffness is removed from the eigenvalues. Lee and van Leer [95] preconditioner uses a minimum range in the characteristic speeds and a minimum variation from the associated eigenvectors. Lynn [101] further developed the idea of Lee and van Leer [95] and found that at stagnation points the preconditioner produced instabilities which could not be fixed. The details of the various types of preconditioning techniques for compressible low speed flows will not be presented here and the reader is referred to the papers by Turkel [179] and Choi and Merkle [34] and the book by Drikakis and Rider [50] for further details.

As stated above, the artificial compressibility formulation can be considered as a type of preconditioning technique in which the incompressible equations are marched to a steady state solution. In 2.9 an overview of the equations for solving the preconditioned incompressible Navier-Stokes equations in the context of the artificial compressibility formulations were presented. The method introduced by Turkel [177] considered a generalisation to the artificial compressibility approach by allowing artificial time derivatives in all the equations and not only the continuity equation as is the case in the standard artificial compressibility approach. Turkel [177] reports that this technique allows for faster convergence and also facilitates a uniform treatment for both primitive and conservative variables. The equations which results from this technique form a symmetric hyperbolic system and is hence well posed for both primitive and conservative formulations. The system of equations have already been presented in 2.9.

The effect of preconditioning on the accuracy and efficiency of separated internal incompressible flows featuring instabilities manifested as symmetry-breaking bifurcations was investigated. In general, the aim was to investigate the circumstances in which preconditioning should be used. The preconditioner of Turkel [177] in conjunction with the artificial compressibility formulation of the Navier-Stokes equations was implemented within the characteristics-based scheme used for the discretisation of the advective terms (Drikakis et al. [51]). An explicit, TVD fourth-order order Runge-Kutta scheme developed by Shu and Osher [158] and the multigrid algorithm of Drikakis et al. [52] were used for the time stepping and acceleration to the steady state.

3.2 Problem Description

A sudden expansion-contraction geometry was setup following the previous study of Mizushima and Shiotani [115]. Figure 3.1 shows the considered geometry with the flow direction left to right. The parameter h is the inlet width and $3h$ is the width of the expanded channel. The contracted channel is of the same width (h) as the inlet width. The expansion ratio is defined as $E = 3h/h$, and was fixed during the coarse of this study. The aspect ratio A is defined as $A = L_0/3h$, where L_0 is the length of the expanded channel. The lengths L_1 and L_2 are set equal to $3h$. All the sudden expansion-contraction cases considered in this thesis have an aspect ratio of $A = 7/3$.

The second geometry investigated was the plane two-dimensional sudden expansion. A geometry with a 1:2 expansion ratio defined by the ratio of inlet channel height to expanded channel height was created in accordance with the study by Drikakis [46]. The length of the outlet channel was 300 step heights in order to ensure that the outflow gradients of the flow variables in the streamwise direction could be considered equal to zero.

In both cases the Reynolds number is defined as:

$$Re = \frac{U_{max}h}{\nu} \tag{3.2.1}$$

where, U_{max} is the maximum inlet velocity. A fully-developed plane Poiseuille velocity profile was specified at the inlet and the outlet condition was consistently checked after each case in order to make sure a fully developed parabolic profile was obtained. The boundary conditions on all the walls were the non-slip condition.

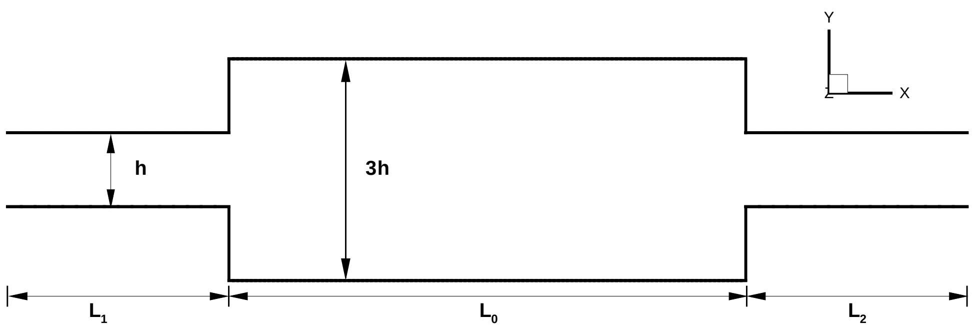

Figure 3.1: Sudden expansion-contraction geometry

Different computational grid sizes were employed and was found that approximately 30,000 and 14,000 grid points were sufficient to obtain grid independent solution for the expanded-contracted and suddenly-expanded channels, respectively.

3.3 Results

The importance of understanding non-linear bifurcation phenomena in fluid mechanics is motivated by the quest to obtain a deeper understanding of hydrodynamic stability and laminar-to-turbulent transition. It is also equally important to understand the behaviour of numerical methods that are used to simulate such phenomena. Therefore, several numerical experiments for unstable, separated channel flows with and without the use of preconditioning have been performed.

Various numerical experiments for flows through suddenly expanded-contracted (SEC) and suddenly-expanded (SE) geometries at low Reynolds numbers have been carried out. At certain Reynolds numbers these flows feature instabilities manifested in the form of a symmetry-breaking bifurcation. Visualisations from experiments performed by Mizushima and Shiotani [115] for the suddenly expanded-contracted geometry are available (see Fig. 3.3(a)) for comparing the computational results with and without preconditioning. The suddenly expanded channel is a classic case and both computational and numerical results are well documented in the literature (Drikakis [46]; Chedron et al. [29]; Patel and Drikakis [127]). The suddenly expanded-contracted and the suddenly expanded geometries have been fully investigated in chapters 4 and 5 respectively.

Computations have been carried out for a broad range of low Reynolds numbers spanning from 1 to 250, based on the maximum inlet velocity and upstream channel height. Both flow geometries lead to symmetric flow separation at lower Reynolds numbers and present a symmetry-breaking bifurcation as the Reynolds number increases. The expanded-contracted channel returns to a symmetric flow as the Reynolds number further increases.

The variable α was varied to investigate the effect it has on the speed of convergence to the steady state for both flow geometries. The best convergence results were obtained for α values between 0 and 1 and was independent of the flow geometry. When $\alpha = -1$ the original artificial compressibility formulation is obtained, while for $\alpha = 1$ the eigenvalues λ_1 and λ_2 are only functions of β. In some cases, this has dissipative effects on the solution. It was found that preconditioning does not have any significant effect on the convergence at Reynolds numbers $Re < 10$, but it does have a positive effect at higher Reynolds numbers. In this case the total number of multigrid cycles can be reduced by 30%. The calculation of β as proposed by Turkel (Eq. 2.9.9) was found not to work effectively when the Reynolds number was reduced below 20. A fixed β value was found to provide better convergence results (both for preconditioned and non-preconditioned solutions) and its precise values can significantly affect the convergence. For example, for a Reynolds number of 10 and $\beta = 1$ the number of multigrid cycles needed to obtain a converged solution was approximately 1780. For $\beta = 0.8$ a converged solution was reached after 800 multigrid cycles.

The most important, however, effects of preconditioning were found to be on the accuracy of the flow solution, especially in the range of Reynolds numbers where symmetry-breaking bifurcation occurs. For lower Reynolds numbers, where the flow is symmetrically separated the accuracy of the solution was found not to be altered by the use of preconditioning for the entire range of α and β values investigated here. Figure 3.2 shows streamwise velocity contours and streamlines for a non-preconditioned and a preconditioned solution at $Re = 10$. The degree of separation in both cases is the same with the symmetric separation bubbles equal in size. The flow reattachment on the upper and lower walls is also the same for both flow cases.

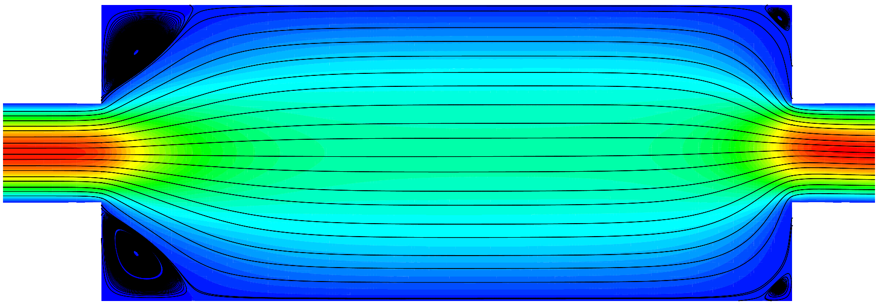

(a) Non-preconditioned solution

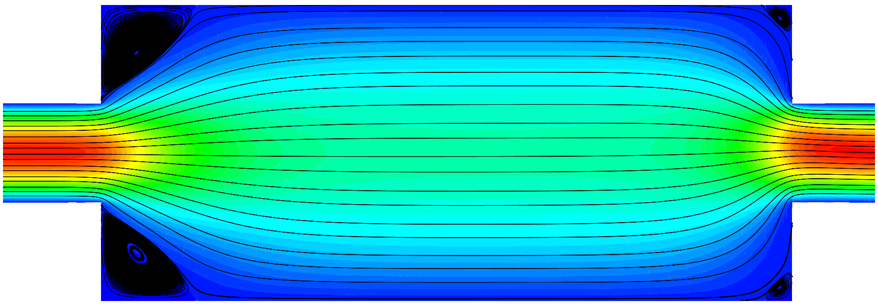

(b) Preconditioned solution

Figure 3.2: Comparison between non-preconditioned and preconditioned solutions at $Re = 10$.

Figures 3.3(b) to 3.4(b) as well as Tables 3.1 and 3.2 summarise the results of the preconditioned and non-preconditioned solutions. Table 3.2 provides comparisons between the present results and previous experimental and computational studies. All the results refer to grid independent solutions. For the expanded-contracted channel the experimental flow visualisation clearly shows the occurrence of instability in the form of an asymmetric separation of the fluid flow (Fig. 3.3(a)). This asymmetry is captured by both the non-preconditioned solution (Fig. 3.3(b)) and preconditioned solution (Fig. 3.3(c)). A second separation bubble exists at the far end of the expanded part on the upper surface of the non-preconditioned solution. This second separation bubble does not seem to be present in the experimental visualisation. Mullin et al. [122] described these small recirculation zones as "moffatt" eddies (Moffatt [118]). Further, for the same geometry at $Re = 200$ the flow becomes again symmetric but the preconditioned solution still remains asymmetric (Table 3.1) with different sized bubbles on the lower and upper walls. At Re = 116 the computed distance Δx between the re-attachment points of the upper and lower bubbles without using preconditioning agrees well (Table 3.2) with the experimental results of Mizushima and Shiotani [115], whereas in the preconditioned solution the bubble does not re-attach before reaching the wall of the contracted part of the channel (i.e., Δx = 0 in Table 3.2).

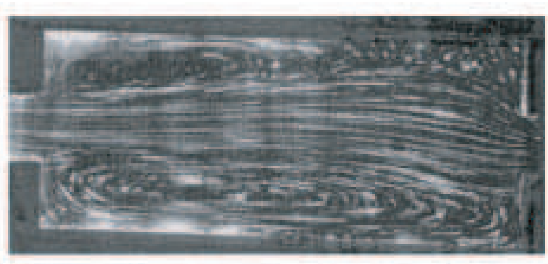

(a) Experimental results from Mizushima and Shiotani [115] at Re=116 for the suddenly contracted-expanded geometry. Reproduced with permission from Cambridge University Press.

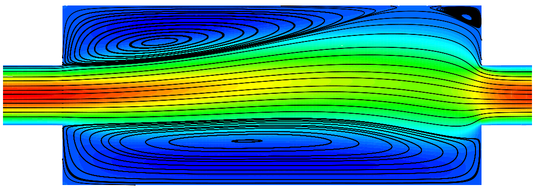

(b) Non-preconditioned solution

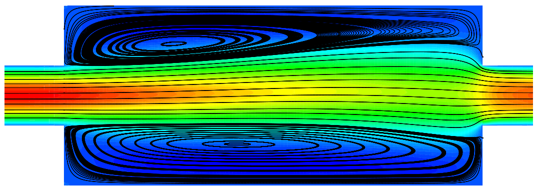

(c) Preconditioned solution

Figure 3.3: Comparison between non-preconditioned and preconditioned solution to experimental flow visualisation

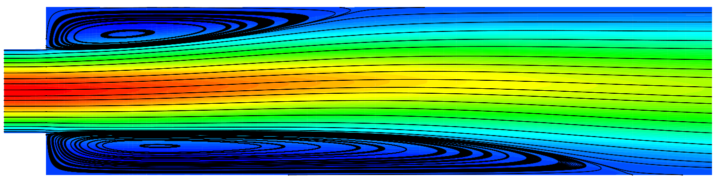

(a) Non-preconditioned solution

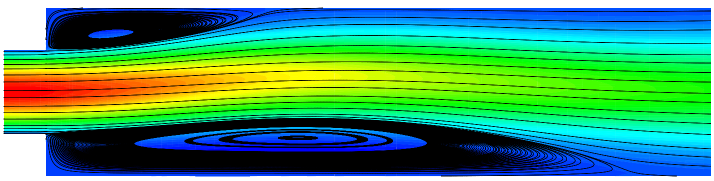

(b) Preconditioned solution

Figure 3.4: Comparison between non-preconditioned and preconditioned solution Preconditioned solution at Re = 250.

Table 3.1: Results for preconditioned and non-preconditioned solutions for the two channel geometries (see text for details).

Case	Reynolds number	Preconditioned solution	Non-preconditioned solution
SEC	1-20	Symmetric	Symmetric
SEC	60	Symmetric (diffusive)	Symmetric
SEC	116	Asymmetric (diffusive)	Asymmetric
SEC	200	Asymmetric	Symmetric
SE	0.1-1	Symmetric	Symmetric
SE	100	Symmetric (diffusive)	Symmetric
SE	250	Asymmetric (diffusive)	Asymmetric

Table 3.2: Comparison of solutions with previously published results of Drikakis [46]; Mizushima and Shiotani [115]; Chedron et al. [29] for the two geometries, for symmetric (S) and asymmetric (A) cases.

Case	Re	Published results	Preconditioned solution	Non-preconditioned solution
SEC	Re=116	Δx = 0.019 m (A)	Δx = 0 (A)	Δx = 0.018 m (A)
SEC	Re=200	Symmetric	Asymmetric	Symmetric
SE	Re=100	Bubble size = 0.016 m (S)	Bubble size = 0.019 m (S)	Bubble size = 0.0159 m (S)
SE	Re=250	Δx = 0.02 m (A)	Δx = 0.027 m (A)	Δx = 0.02 m (A)

Similarly, the preconditioner has adverse effects on the accuracy of the suddenly-expanded channel flow. For example, at $Re = 250$ where the flow exhibits an instability (Figs. 3.4(a) and 3.4(b)) the preconditioned solution is qualitatively correct, but not with respect to the size of the separation bubble. Table 3.2 compares the present preconditioned and non-preconditioned solutions with the results of Drikakis [46] and Chedron et al. [29] for symmetric (stable) flow at $Re = 100$ and asymmetric (unstable) flow at $Re = 250$.

Parallel to this investigation, several numerical experiments (Patel and Drikakis [127]) using different Godunov-type methods without the use of a preconditioning have been conducted (see chapter 4). These investigations showed that more dissipative advective schemes generally lead to a stable flow, especially when the solution is under-resolved. Even though a rigorous analysis of the dissipation effects of non-linear approximations such as high-resolution Godunov-type schemes in combination with preconditioning appears very difficult, the similarity in the behaviour of certain Godunov-type schemes with the preconditioned results obtained here seems to indicate that preconditioning has an added dissipation effect on the solution, when the flow exhibits symmetry-breaking bifurcation. Furthermore, this kind of "non-physical" behaviour exhibited by the preconditioned method at certain Reynolds numbers has also some similarities with the volatile numerical behaviour of some time integration methods, which perform differently depending on the solution problem (Miller [113]).

3.4 Summary

A numerical study showing the effects of preconditioning of flows through suddenly expanded-contracted and suddenly expanded channels was presented. Laminar flow calculations were performed with and without preconditioning in order to asses its effects on the accuracy and efficiency of computations. At higher Reynolds number flows the use of preconditioning reduced the number of multigrid cycles, but adversely affected the solution results. For Reynolds numbers in the range of symmetry-breaking bifurcation, the use of preconditioning led to an incorrect stable solution or to an improper estimation of the size of the separation bubble. At lower Reynolds number flows the present form of preconditioning neither altered the accuracy of the solution nor had a significant effect on the convergence.

CHAPTER 4

Prediction of Flow Instabilities in a Suddenly Expanded Suddenly Contracted Channel

A computational investigation to examine the numerical effects on the prediction of flow instabilities and bifurcation phenomena for flow through a suddenly expanded-contracted channel have been carried out. High-resolution Godunov-type methods in conjunction with first-, second- and third-order accurate interpolation schemes for the calculation of the intercell flux have been employed and the effect grid resolution has on these schemes in predicting the flow instabilities has been studied.

4.1 Introduction

THE phenomenon of asymmetric separation in a suddenly expanded and contracted channel has been discussed by Mizushima et al. [117]; Mizushima and Shiotani [115] both experimentally and numerically. Mizushima et al. [117] carried out numerical simulations for the flow and analysed the data using bifurcation theory. At very low Reynolds numbers the flow remains symmetric with separation regions of equal length on both channel walls directly after the sudden expansion and before the sudden contraction. As Reynolds number is increased the separation length is also increased. A critical value of Reynolds number (Re_{c1}) upon which the flow separates asymmetrically is reached when one recirculation region grows at the expense of the other. This symmetry-breaking is due to a pitchfork bifurcation. A further increase in the Reynolds number makes the asymmetry between the two recirculation regions becoming more prominent to the extent that both bubbles can reach the size of the entire length of the expanded part. A second critical value of the Reynolds number (Re_{c2}) is reached as the Reynolds number is further increased and the asymmetric separation returns to a stable symmetric solution due to a second pitchfork bifurcation. Mizushima et al. [117] also found that the symmetric flow became oscillatory at a third critical Reynolds number (Re_{c3}) due to a Hopf bifurcation. These critical Reynolds numbers were used to obtain a transition diagram of the flow. The bifurcation diagram obtained was incomplete due to unexpected discontinuous lines in place of the smooth continuous lines presumed.

Mizushima and Shiotani [115] built on the previous work discussed above and carried out an investigation of transition and instabilities of the flow in the same suddenly expanded and contracted channel, experimentally, numerically and theoretically. Velocity measurements were obtained using Laser Doppler Velocimetry (LDV) experimental techniques. Flow visualisations were used to examine the flow behaviour. Mizushima and Shiotani [115] used three different numerical methods in the numerical calculations, namely; time marching method for dynamical equations; SOR iterative method and the finite element method for steady state equations. The work of Mizushima et al. [117] has been extended by applying weakly nonlinear stability theory to the flow to elucidate the bifurcation structure near the critical Reynolds numbers for the pitchfork bifurcations. Mizushima and Shiotani [115] also investigated the impinging free shear layer instability, which was found to make the flow oscillatory. The characterisation of the impinging free shear layer is described as a stepwise change of the Strouhal number with a continuous change of parameter and observed when a jet like stream impinges on an object featuring sharp edges (Rockwell and Naudascher [142]).

More recently Mullin et al. [122] studied the effect of varying the ratio of the inlet and outlet channel widths in a symmetric two-dimensional channel with an expanded and contracted section. Mullin et al. [122] carried out both experimental and numerical studies and found that there is a type of rivalry between the instability associated with the expansion from the inlet to the expanded section, and the instability associated with the expansion from the inlet to the outlet. As with the study by Mizushima and Shiotani [115], Mullin et al. [122] found that the length of the expanded sections plays a significant role in determining the outcome of the previously discussed rivalry. Mullin et al. [122] introduced geometric imperfections into the computational domain to approximate the physical imperfections that must be present in the experimental geometry. These simulations found that there is a greater sensitivity to imperfections for the case which the symmetry-breaking bifurcation is associated with the outlet.

4.2 Problem Description

A sudden expansion-contraction geometry was setup following the previous study of Mizushima and Shiotani [115], which has been described in detail in Chapter 3. The artificial compressibility formulation of the steady incompressible Navier-Stokes equations was implemented together with three different high-resolution methods for the calculation of the advective fluxes, namely; the characteristics-based method of Drikakis et al. [51]; the Rusanov scheme (Rusanov [148]) and the HLLE scheme (Einfeldt [56]). An investigation into the effect of the spatial accuracy used in the reconstruction step of the advective fluxes was undertaken for each of the three high-resolution methods. The reader is referred to section 2.12 of Chapter 2 for a mathematical description of the high-order spatial reconstruction. An explicit fourth-order TVD Runge-Kutta scheme developed by Shu and Osher [158] and the nonlinear multigrid method of Drikakis et al. [52] are used to drive the numerical solution to a steady state.

Different grid resolutions were employed and it was found that 30,000 grid points were sufficient to obtain grid independent solutions. A coarser grid with 7,000 grid points was also used to investigate the effect of the different numerical schemes at under-resolved grid conditions. A comparison among the various numerical schemes was obtained for several flow cases on two different grids in order to test if the asymmetric separation is affected by the numerical scheme employed.

4.3 Under-resolved simulations

Under-resolved simulations were carried out using three high-resolution schemes in conjunction with various orders of spatial reconstruction. An extensive range of Reynolds numbers from 10-200 were investigated in order to cover both critical Reynolds numbers as predicted by Mizushima and Shiotani [115]. It should be noted here that the objective of this study is not to investigate the actual critical Reynolds number for symmetry breaking bifurcation or the critical Reynolds number for where the flow regains symmetry. Mizushima and Shiotani [115] published a critical Reynolds number for symmetry breaking bifurcation as $Re_{c1} = 47.7$ and another for where the flow regains symmetry as $Re_{c2} = 65.2$. These Reynolds numbers were based on the maximum inlet velocity and half the upstream channel height. Hence, the equivalent Reynolds numbers based on the definition in Eq. 5.2.1 are $Re_{c1} = 95.4$ and $Re_{c1} = 130.4$.

Figure 4.1(a) shows streamwise velocity contours and streamlines showing a symmetric separation of the fluid entering the expanded channel at a Reynolds number $Re = 10$. All three numerical methods predicted a symmetric separation of the fluid flow and the effect of changing the order of accuracy used in the reconstruction was negligible. As the Reynolds number is increased the size of the recirculation zones on the upper and lower walls increase in size. Figure 4.1(b) shows streamlines and velocity contours for a Reynolds number $Re = 80$. According to Mizushima and Shiotani [115] the separation associated with this Reynolds number should be symmetric as it is lower than the first critical Reynolds number for symmetry-breaking bifurcation. All three numerical methods correctly predict this symmetric separation of the fluid flow. The size of the recirculation regions on the upper and lower walls are very similar for each of the three different numerical methods.

A closer look at Fig. 4.1 shows two small recirculation zones at the upper and lower corners at the far end of the expanded section. The investigations by Mizushima and Shiotani [115] and Mizushima et al. [117] do not mention anything regarding these small recirculation zones and the experimental flow visualisations they present are not clear enough to see whether these recirculation zones exist or if they are simply numerical artifacts. However, the more recent paper of Mullin et al. [122] does comment on these small recirculation zones and refer to them as 'Moffat' eddies (Moffatt [118]).

According to Mizushima and Shiotani [115] the flow should become asymmetric due to a pitchfork symmetry breaking bifurcation on exceeding a Reynolds number of $Re = 95.4$ (using the definition of Reynolds number based on the maximum velocity

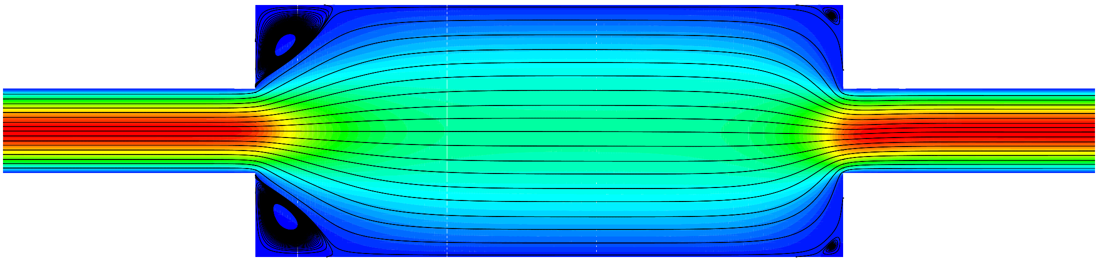

(a) $Re = 10$

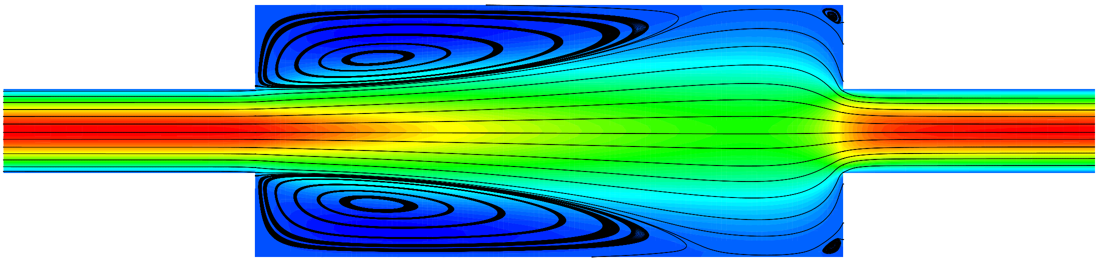

(b) $Re = 80$

Figure 4.1: Streamwise velocity contours and streamlines showing a symmetric separation of the fluid flow at two different Reynolds numbers.

and inlet channel height). Figure 4.2 shows streamwise velocity contours and streamlines for the flow at a Reynolds number of $Re = 96$. Each different numerical method correctly predicts the asymmetric separation of the fluid flow. It should be noted here that the reconstruction used is 3rd order accurate. The differences between the three numerical methods is significant in that the HLLE scheme (Fig. 4.2(b)) and the Rusanov scheme (Fig. 4.2(c)) predict a much larger degree of asymmetry in comparison to the characteristics-based scheme (Fig. 4.2(a)). The HLLE scheme predicts the larger recirculation bubble on the lower wall in comparison to the Rusanov scheme which shows the larger recirculation bubble on the upper wall. It is believed that the tendency for the fluid to be drawn to the upper or lower wall is purely random especially in an experimental setup, but in a symmetric computational setup this phenomena can be attributed to the details of the truncation error. The asymmetry predicted by the characteristics-based scheme is very slight with the corner recirculation zone at the lower wall enclosed by the larger recirculation region. As the Reynolds number is only slightly above the first critical Reynolds number for symmetry-breaking bifurcation, the expected asymmetry would be small.

Some experimental flow visualisations have been printed in Mizushima and Shiotani [115] showing the asymmetric separation of the fluid. Figure 4.3 shows a direct comparison of the numerical solution obtained using the characteristics-based scheme with

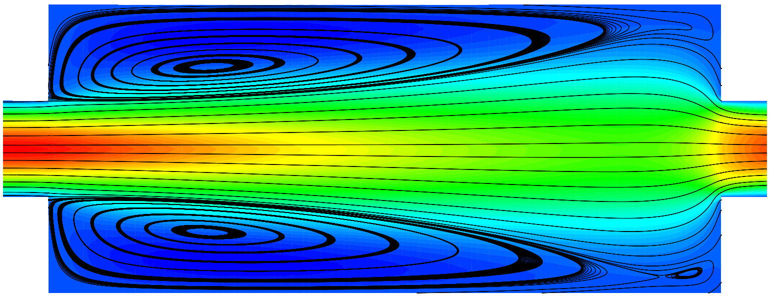

(a) CB scheme

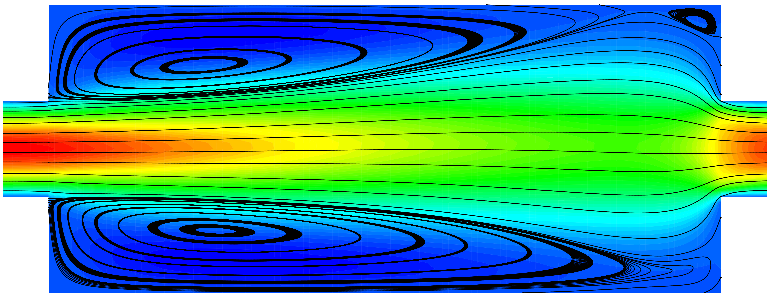

(b) HLLE scheme

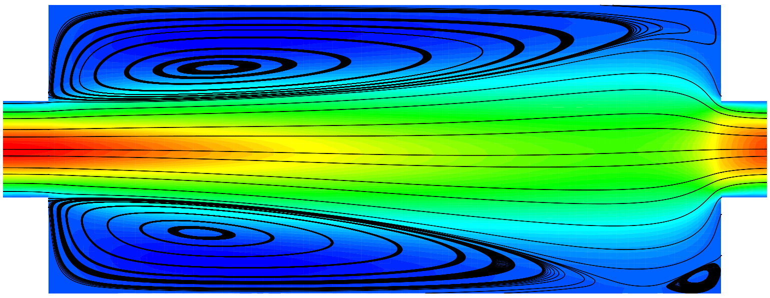

(c) Rusanov scheme

Figure 4.2: Streamwise velocity contours for three numerical schemes at $Re = 96$.

third-order spatial accuracy and the experimental flow visualisation, at a Reynolds number of $Re = 116$. The numerical solution obtained shows the larger recirculation zone at the upper wall whereas the experimental visualisation shows the larger recirculation zone at the lower wall. As discussed above this is due to the particular properties of the numerical scheme and in an experimental setup the flow can break either way. The numerical solution shows the presence of a small corner recirculation zone at the lower wall which does not appear in the experimental flow visualisation. The lack of appearance of the small corner recirculation zone in the experimental visualisations could be due to poor seeding of the flow.

Once symmetry-breaking bifurcation has occurred i.e. on increasing Reynolds number above the first critical value, one of the recirculation zones increases in size at the expense of the second recirculation zone. Figure 4.4 shows how the effect of increasing

Reynolds number changes the degree of asymmetry. The recirculation zone on the upper wall increases in size until it spans the entire length of the expanded channel. This leads to the growth of the lower recirculation zone until it itself spans the entire length of the expanded channel. This is shown clearly in Fig. 4.4(c). At a Reynolds number of $Re = 140$, the flow has returned to a stable symmetric separation with both recirculation zones equally sized, spanning the entire length of the expanded channel (Fig. 4.4(d)). The re-stabilisation of the flow from asymmetric to symmetric is due to a second pitchfork bifurcation as reported by Mizushima and Shiotani [115]. The results shown in Fig. 4.4 have been obtained using the characteristics-based scheme in conjunction with third-order reconstruction.

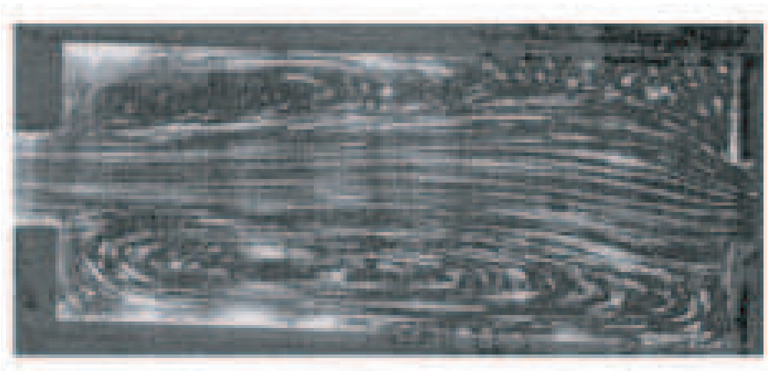

(a) Experimental visualisation

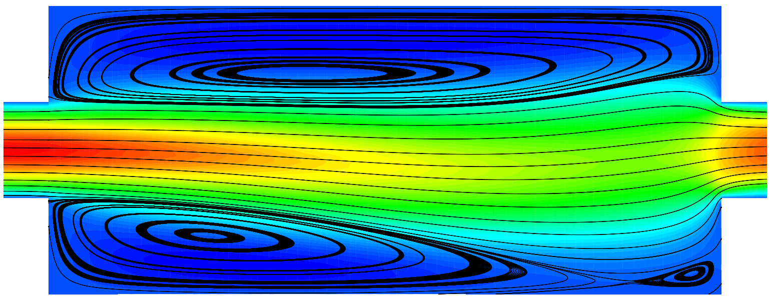

(b) CB scheme

Figure 4.3: Comparison between the experimental flow visualisation of Mizushima and Shiotani [115] and the numerical solution using the characteristics-based scheme, at $Re = 116$.

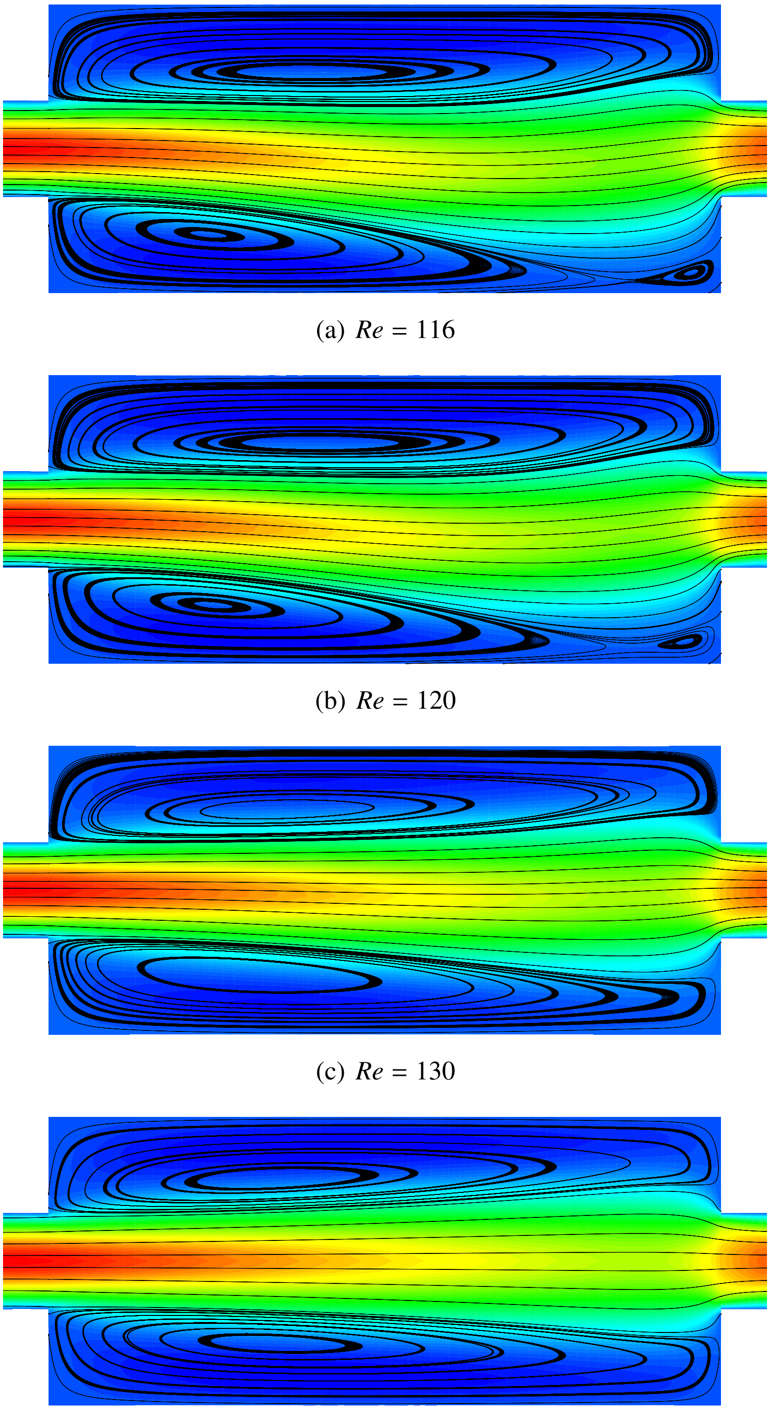

(a) $Re = 116$

(b) $Re = 120$

(c) $Re = 130$

(d) $Re = 140$

Figure 4.4: Streamwise velocity contours and streamlines at various Reynolds numbers using the characteristics-based scheme.

4.4 Grid-independent simulations

In order to asses the characteristics of the three numerical schemes more accurately, grid-independent simulations were required. Two grid resolutions were investigated; an intermediate grid consisting of approximately 30,000 grid points and a finer grid consisting of approximately 60,000 grid points. The fine grid resolution provided results which were in agreement to within 0.1% of the intermediate grid resolution (30,000 grid points). It was hence decided that the grid resolution of approximately 30,000 was sufficient enough to provide grid independent solutions. The reconstruction accuracy was investigated further to see how the numerical schemes behave under grid-independent conditions. The grid-independency was carried out using first-order reconstruction hence it was assumed that the same grid-resolution would be grid-independent for higher-orders of accuracy. The characteristics-based scheme with first-order interpolation in the calculation of the left and right states led to an asymmetric flow at a Reynolds number of 120 for grid independent conditions. Whereas, the HLLE and Rusanov schemes led to symmetric solutions for the same Reynolds number when using first-order reconstruction. Higher order interpolations (second- and third order) at the same Reynolds number led to asymmetric separation for all numerical schemes investigated. Figure 4.5 show grid independent results for the characteristics-based scheme (CB) and the Rusanov scheme for first-, second-, and third-order interpolation in the calculation of the left and right states for a Reynolds number of 120.

A comparison between the characteristics-based scheme and the Rusanov scheme with 3rd-order reconstruction (Figs. 4.5(e) and 4.5(f)), shows very little difference with regards to the degree of asymmetry predicted. However, using a 2nd-order reconstruction the degree of asymmetry predicted by the Rusanov scheme (Fig. 4.5(d)) is larger than that predicted by the characteristics-based scheme using the same order of reconstruction (Fig. 4.5(c)). There is very little difference between characteristics-based scheme when using the 2nd-order or 3rd-order reconstruction. The difference between the three schemes lies mainly in the calculation of the second term on the right-hand-side of the Godunov flux (see Eq. 2.10.1). This term is a nonlinear wave-speed dependent term which encompasses information about the eigenstructure of the system of equations and is also responsible to adapt the discretisation according to the local solution data. The Rusanov scheme is based on the calculation of the maximum wave speed (Eq. 2.11.9) and hence cannot recognise the slowest moving acoustic waves thus causing a larger amount of dissipation. This diffusive nature of the Rusanov scheme will tend to have a “smoothing” effect on the solution and hence may be the reason as to why the solutions obtained, especially when using 1st-order reconstruction, do not accurately represent the physics of the flow.

Mizushima and Shiotani [115] have reported that the first critical Reynolds number for symmetry-breaking bifurcation occurs at a Reynolds number of $Re = 95.4$. Under-resolved simulations showed that at a Reynolds number of $Re = 96$ the flow is indeed asymmetric. Grid independent studies have found that the first critical Reynolds number is somewhat lower than $Re = 95.4$ and in fact at a Reynolds number of $Re = 70$ the

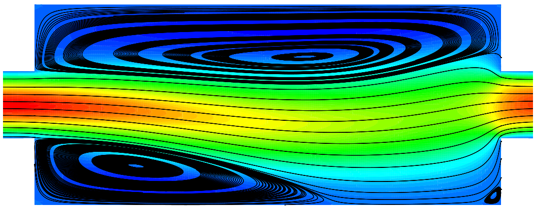

(a) CB scheme with 1st-order interpolation.

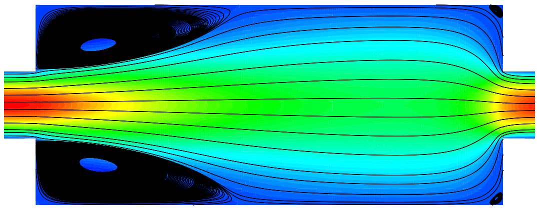

(b) Rusanov scheme with 1st-order interpolation.

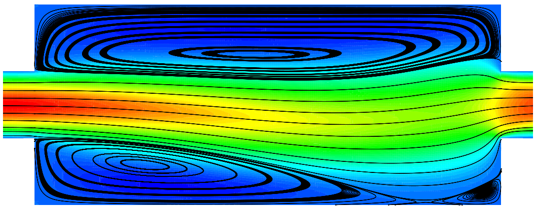

(c) CB scheme with 2nd-order interpolation.

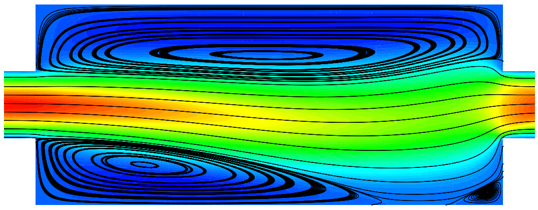

(d) Rusanov scheme with 2nd-order interpolation.

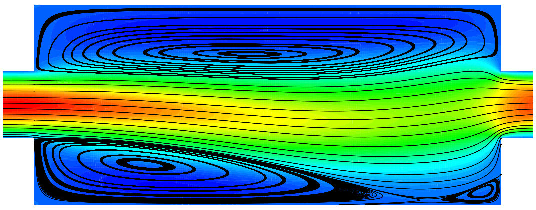

(e) CB scheme with 3rd-order interpolation.

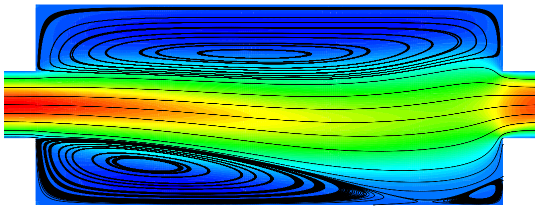

(f) Rusanov scheme with 3rd-order interpolation.

Figure 4.5: Streamwise velocity contours and streamlines showing the effect of various interpolation at $Re = 120$.

fluid flow was already asymmetric. Figure 4.6 shows the streamwise velocity contours and streamlines for the asymmetric flow at $Re = 70$ using the characteristics-based method and third-order reconstruction. The asymmetry in the flow is noticeable if one considers the reattachment points of the recirculation zone streamlines, to the upper and lower walls. Even though a full investigation into the critical Reynolds number for symmetry-breaking bifurcation was not undertaken, it is speculated that this critical Reynolds number is close to $Re = 70$ due to the small degree of asymmetry predicted at this Reynolds number.

Grid independent studies at a Reynolds number $Re = 140$ which, is higher than the second critical Reynolds number predicted by Mizushima and Shiotani [115] ($Re_{c2} = 130.4$), showed that the flow remained asymmetric. Figure 4.7 shows velocity contours and streamlines of the asymmetric flow at $Re = 140$. Mizushima and Shiotani [115] do not present any experimental flow visualisations at this particular Reynolds number and their predictions for the critical Reynolds numbers are based on the various numerical methods they employed. Flow visualisations have however been shown by Mizushima and Shiotani [115] at a Reynolds number of $Re = 200$, and are presented here in Fig. 4.8 together with the grid independent solution obtained using the characteristics-based scheme in conjunction with third-order reconstruction. The experimental visualisation shows a secondary recirculation zone inside of the main recirculation zones (both upper and lower) located at the far end of the expanded channel. The computational result does not capture this physical phenomena. However, on increasing the Reynolds number to Re = 230 (Fig. 4.9) the presence of the secondary recirculation zones become more apparent.

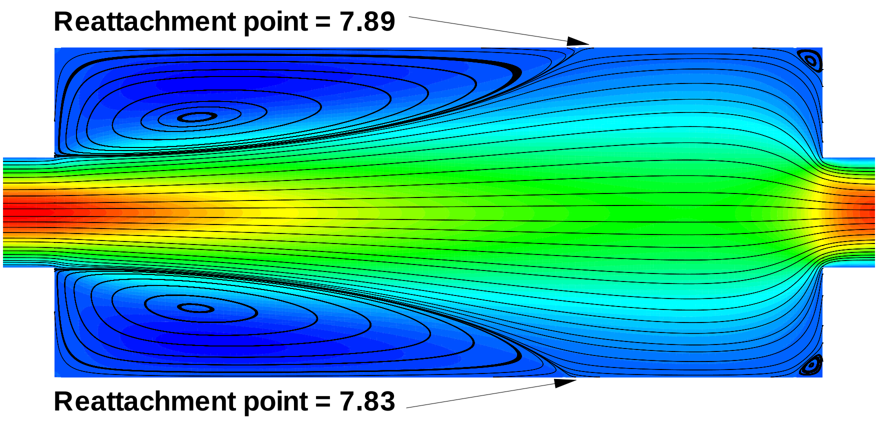

Figure 4.6: Streamwise velcoity contours and streamlines showing an asymmetric flow at Re = 70.

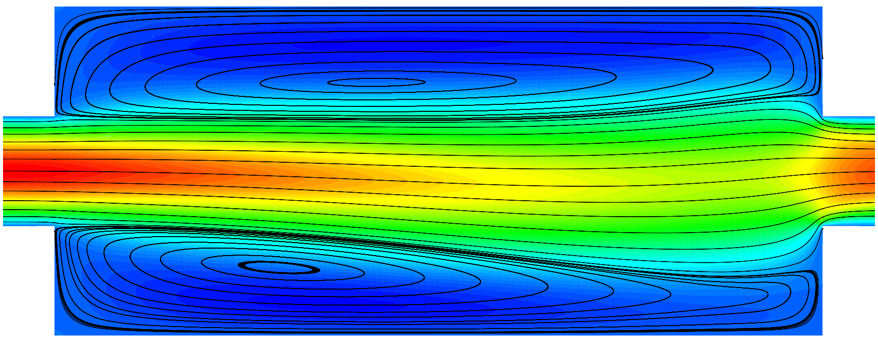

Figure 4.7: Streamwise velcoity contours and streamlines showing an asymmetric flow at Re = 140.

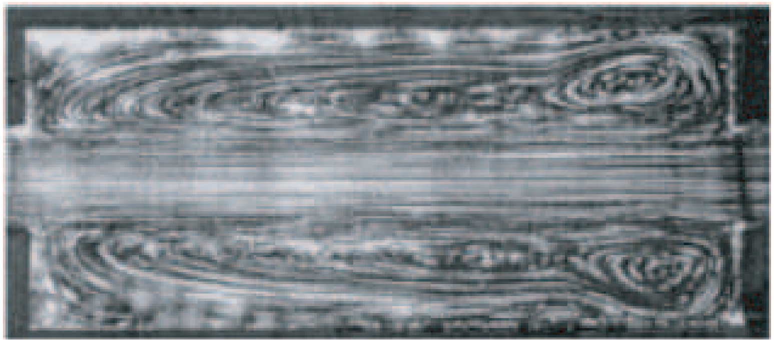

(a) Experimental visualisation

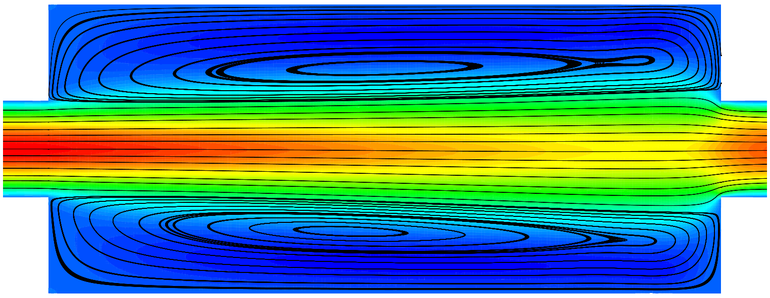

(b) CB scheme

Figure 4.8: Comparison between the experimental flow visualisation of Mizushima and Shiotani [115] and the numerical grid independent solution using the characteristics-based scheme, at $Re = 200$.

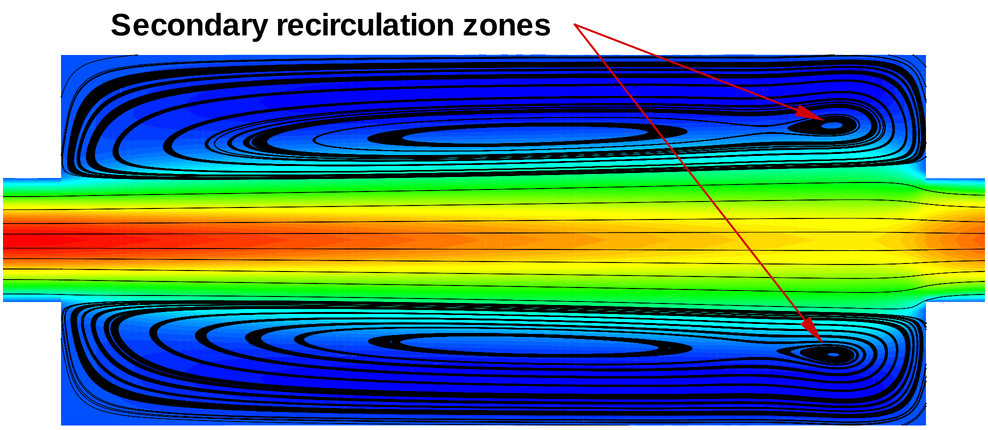

Figure 4.9: Streamwise velcoity contours and streamlines showing the presence of secondary recirculation zones at $Re = 230$.

4.5 Summary

A numerical study for bifurcation phenomena in a symmetric plane suddenly expanded and contracted channel was presented. Laminar flow calculations were performed using three Godunov-type schemes for various Reynolds numbers on two different sized grid resolutions in conjunction with first-, second- and third-order interpolation in the calculation of the intercell flux. The calculations on both grids showed that for low Reynolds numbers the flow separated symmetrically. As Reynolds number was increased symmetry-breaking bifurcation occurs at a critical Reynolds number and separation bubbles of different sizes form on the lower and upper walls. The asymmetries become stronger with increasing Reynolds number till a second critical Reynolds number is reached and the flow regains symmetry.

Under-resolved grid simulations showed that the choice of numerical scheme effects the solution obtained especially in the range of Reynolds number where symmetry breaking bifurcation occurs. The prediction of the degree of asymmetry in the HLLE and Rusanov schemes was less than that obtained by the characteristics-based scheme. This may be due to the increased dissipation of the HLLE and Rusanov schemes compared to the characteristics-based scheme. Grid independent cases showed that the choice of interpolation used in the calculation of the intercell flux has a significant effect on the solution obtained. First-order interpolation using the characteristics-based scheme correctly predicted the asymmetric solution at a Reynolds number of $Re = 120$. Whereas the HLLE and Rusanov schemes incorrectly predicted a stable symmetric solution. Higher-orders of interpolation at the same Reynolds number led to asymmetric separation for all numerical schemes investigated with little noticeable difference between the three schemes when using third-order interpolation.

Two critical Reynolds numbers exist for this particular case of a suddenly expanded and contracted channel with an aspect ratio (length of expanded part to height of expanded part) of 7/3. The first critical Reynolds number, Re_{c1}, is for the symmetry breaking bifurcation and the second critical Reynolds number, Re_{c2}, is for the return from asymmetric flow to stable symmetric flow. Mizushima et al. [117] carried out a numerical study and have published values of $Re_{c1} = 95.4$ and $Re_{c2} = 130.4$, for the two critical Reynolds numbers, based upon the same definition of Reynolds number used in this investigation. A full investigation into the critical Reynolds number for symmetry breaking bifurcation was not carried out as this was not the aim of this study. However, simulations were carried out at Reynolds numbers close to the published critical Reynolds numbers using both under-resolved grid and grid independent conditions. Under-resolved simulations at Reynolds numbers slightly above the published critical Reynolds numbers showed a similar representation of the flow physics as was documented by Mizushima et al. [117]. Grid-independent simulations showed that the first critical Reynolds numbers for symmetry-breaking bifurcation is somewhat lower than that which was published by Mizushima et al. [117]. Also, the second critical Reynolds number upon where the flow returns to a stable symmetric solution is much higher than the Reynolds number published by Mizushima et al. [117]. Possible reasons for the discrepancies between the published data and the results produced using the grid independent model are that the results obtained by Mizushima et al. [117] were produced from different numerical methods on grid resolutions coarser than the ones used in the present study.

CHAPTER 5

Flow Through Plane Symmetric Suddenly Expanded Channels

The phenomenon of non-linear bifurcation is studied via computations using high-resolution numerical methods performed on a suddenly expanded channel in both two- and three-dimensions. The study includes the effect of expansion ratio on the prediction of the critical Reynolds number for symmetry-breaking bifurcation in a two-dimensional setup. Extending this to three-dimensions, the stabilising effect of the vertical side walls on the flow is examined for two different aspect ratio channels. Finally, the investigation into higher Reynolds number flows where the flow becomes time-dependent is presented. All simulations have been validated with experimental and or computational data where available.

5.1 Introduction

Incompressible flow in sudden expansions is one of the classical examples in fluid mechanics which exhibit non-linear bifurcation phenomena. Experimental studies by Durst et al. [53]; Chedron et al. [29]; Fearn et al. [59] have shown that flows through suddenly-expanded geometries feature symmetric separation at low Reynolds numbers and beyond a certain Reynolds number exhibit bifurcation phenomena (instabilities) that are manifested as an asymmetric separation of the fluid flow. It should be noted that similar asymmetric flow patterns have also been observed in axisymmetric suddenly-expanded channels by Sheen et al. [156]; Macagno and Hung [102]; Revuelta [136]. The critical Reynolds number for symmetry-breaking depends on the expansion ratio and upstream flow conditions. As the Reynolds number further increases the flow may encompass unsteadiness, three-dimensionality and chaos (Mullin and Cliffe [121]).

The early experimental studies by Durst et al. [53] were carried out for two different expansion ratios 1:2 and 1:3. Both flow geometries revealed similar flow phenomena with instabilities appearing over a certain critical Reynolds number. Chedron et al. [29] demonstrated experimentally that a stable symmetric solution could only exist under a certain critical Reynolds number, beyond which the flow becomes unstable and asymmetric. An experimental and numerical study for a 1:3 sudden expansion was published by Fearn et al. [59] showing that the change from symmetric stable separation to an unstable asymmetric separation maybe due to a pitchfork symmetry-breaking bifurcation point. The experimental results of Fearn et al. [59] showed that the bifurcation diagram is disconnected due to small imperfections that are always present in an experimental setup. They observed no critical Reynolds number for symmetry-breaking and hence a symmetric state was never observed. Fearn et al. [59] attempted to numerically model the small imperfections observed in the experimental setup in order to try and account for the disconnection in the experimental bifurcation diagram. They repeated the numerical simulations with the downstream section of the grid shifted up by 0.05mm with respect to the axis of symmetry. This perturbation caused a disconnection of the bifurcation diagram as observed in the experiments. The size of the disconnection found experimentally was of the same order as the decoupling produced by perturbing the numerical problem. Linear stability analysis carried out by Shapira et al. [155] verified the experimental findings and obtained a good agreement with respect to the critical Reynolds number when compared to the work of Drikakis [46]. Fearn et al. [59] postulated that the transition to asymmetric flow was abrupt, which disagreed with the finding of Shapira et al. [155], who claimed that the transition is actually smooth. Numerical simulations carried out by Durst et al. [54] to validate previous experimental findings (Durst et al. [53]) found that the transition from symmetric to asymmetric separation caused by a pitchfork bifurcation is in fact smooth.

Computational studies based on high-order methods, (Drikakis [46]) were performed to numerically investigate the asymmetric flow structure at different Reynolds numbers, while continuation and Arnoldi-based iterative methods have been used by Alleborn et al. [1] to calculate the most unstable eigenmodes for steady flow in a symmetric channel and the bifurcation structure of the steady state solution of the flow. Drikakis [46] and Alleborn et al. [1] demonstrated that as the expansion ratio increases the critical Reynolds number decreases. Battaglia et al. [15] conducted a linear stability analysis and also performed numerical computations of steady flow through a suddenly expanded channel with various expansion ratios. They made use of bifurcation theory in order to determine numerically the bifurcation point and the results agreed with those of Drikakis [46] and Alleborn et al. [1]. Luo [100] numerically investigated symmetry-breaking of flow in 2-dimensional channels using Lattice-Boltzmann methods. Their predictions of the critical Reynolds numbers for a suddenly expanded channel with an expansion ratio of 1:3 compared well with the studies of Fearn et al. [59] and Drikakis [46].

Goldstein et al. [67] carried out an experimental investigation of the laminar flow of air over a downstream-facing step. They observed that the laminar reattachment length cannot be expressed as a fixed number of step height as is the case for turbulent flow and provided an equation to predict the reattachment length. Goldstein et al. [67] also observed the presence of a secondary flow pattern in the separated zone. They found that when fluid from the boundary layer in the corner of the test section enters the separated zone at the step it recirculates in a spiral fashion to the geometry centerline and leaves the separated region near the reattachment point on the centerline plane.

Furthermore, Neofytou and Drikakis [123] have investigated flow instabilities in suddenly expanded channels for non-Newtonian fluids showing similar solutions to the Newtonian case, which, however, differ with respect to the critical values of Reynolds number where the symmetry-breaking bifurcation occurs. Simulations of suddenly expanded flows for power-law fluids were carried out by Manica and De Bartoli [106]. They found that power-law fluids (shear-thinning and shear thickening) behaved in a similar manner as Newtonian fluids. Critical Reynolds numbers, in which the solution becomes asymmetric, were found to be in close agreement for all cases. The effect of shear thinning and shear thickening was to increase and decrease, respectively, the Reynolds number upon where the third downstream separation bubble appears in comparison to the Newtonian case. Mizushima and Shiotani [116] used weakly nonlinear stability analysis to investigate the structural instability of the bifurcation for flow through a sudden expansion showing that the parameter range for weakly nonlinear stability analysis is limited to the vicinity of the critical point. Hawa and Rusak [77] and Rusak and Hawa [147] have also performed bifurcation analysis, linear stability and numerical simulations to study the dynamics of the flow through a sudden expansion. They showed that the flow instability is a result of the interaction of viscous dissipation, upstream convection induced by the asymmetric disturbances and downstream convection of perturbations by the symmetric base flow. Other studies which have been concerned with instabilities and bifurcation phenomena in similar geometries include the works of Sobey [165]; Sobey and Drazin [164]; Tsui and Wang [176] for two-dimensional diffuser-like channel flows; Mizushima and Shiotani [115]; Mizushima et al. [117] for suddenly expanded and contracted channel; Revuelta et al. [137] for axisymmetric laminar jets with large expansion ratios and Mallinger and Drikakis [104] for three-dimensional flows in pipes with stenosis.

The majority of the numerical studies involving investigations into instabilities in suddenly expanded flows have been simulated in 2-dimensions with an infinite aspect ratio. However, the experimental studies listed in Table 5.1 are 3-dimensional with a finite aspect ratio. The studies of Durst et al. [53]; Chedron et al. [29]; Fearn et al. [59]; Ouwa et al. [125] discussed above investigated various aspect ratio channels and found that the critical Reynolds number is dependent on the size of the aspect ratio. Chedron et al. [29] found that as aspect ratio was increased the critical Reynolds number decreased. This suggest that the side walls of the channel act to stabilise the flow and delay the onset of symmetry-breaking bifurcation.

A three-dimensional numerical study of bifurcation in sudden channel expansions was undertaken by Schreck and Schäfer [153]. Their investigation focused on the three-dimensional effects of a suddenly expanded channel for two different aspect ratios. They found that the critical Reynolds number at which symmetry breaking bifurcation occurs, increases as the aspect ratio decreases, hence confirming the trend observed by Chedron et al. [29]. Thiruvengadam et al. [171] simulated bifurcated 3-dimensional laminar forced convection in a plane symmetric suddenly expanded channel in order to illustrate how flow bifurcation effects temperature and heat transfer distributions at moderately low Reynolds numbers ($Re < 800$). They found that for a channel with an expansion ratio of 1:2 and an aspect ratio of 2 defined by the ratio of the spanwise length to the downstream channel height, the flow was steady and asymmetric in the transverse direction, but symmetric relative to the centre width of the channel in the spanwise direction. Several papers by Chiang et al.[31; 32; 33] have been published on three-dimensional flow through suddenly expanded or suddenly contracted channels. An in-depth study (Chiang et al. [31]) on the affect aspect-ratio has on the fluid flow characteristics showed that as the aspect ratio decreased the Reynolds number at which symmetry-breaking bifurcation occurs increases. This confirmed experimental observations made by Chedron et al. [29] that a decrease in the aspect ratio has a stabilising effect on the subsequent fluid flow. Chiang et al. [32] found that there exists a critical aspect ratio for which the symmetry-breaking pitchfork bifurcation evolves with different symmetry-breaking orientations on the left and right sides of the channel in the spanwise direction. This second mode of bifurcation which occurs in the spanwise direction was found to be difficult to obtain due to the unstable flow symmetry at the spanwise symmetry plane.

More recently Battaglia and Papadopoulos [14] investigated the effects of three-dimensionality on low Reynolds number flows past a sudden expansion in a channel. The geometry of the channel investigated had an expansion ratio of 1:2 and an aspect ratio of 6 defined by the ratio of the spanwise length to the step height. An experimental investigation using two-dimensional particle image velocimetry to visualise the fluid flow was carried out in tandem with two- and three-dimensional numerical simulations for Reynolds numbers in the range of 150-600. Battaglia and Papadopoulos [14] found that the two-dimensional simulations failed to capture the total expansion effect of the flow in comparison to the experimental results. The expansion effect of the flow is influenced by both geometric and hydrodynamic effects. They found that in order to correctly capture these expansion effects an effective expansion ratio, defined by the ratio of the downstream and upstream hydraulic diameters, hence taking into account both expansion and aspect ratios, needs to be defined.

$$\Delta_h = \mathrm{ER}\frac{2 + \mathrm{AR}(\mathrm{ER} - 1)}{2 \cdot \mathrm{ER} + \mathrm{AR}(\mathrm{ER} - 1)} \tag{5.1.1}$$

where, $\mathrm{ER} = D_2/D_1$ the expansion ratio defined by the ratio between the height of the downstream to upstream channel; $\mathrm{AR} = S/h$ where $h = (D_2 - D_1)/2$ and S the spanwise length of the channel. Two-dimensional simulations using this effective expansion ratio were performed and compared very well with three-dimensional simulations and the experimental results. They also reported that the critical Reynolds number for symmetry-breaking bifurcation when using this effective expansion ratio for two-dimensional simulations is much closer to three-dimensional simulated results with a fixed aspect ratio and also to experimental results (see Tables 5.1 and 5.2). As reported by various other authors, Battaglia and Papadopoulos [14] also comment on the stabilising effect of the side wall proximity, in that the lower the aspect ratio the greater the influence the side walls have in stabilising the flow and hence increasing the critical Reynolds number for symmetry-breaking bifurcation.

Mizushima and Inui [114] have used numerical simulations to study transition of three-dimensional flow through a rectangular duct with a suddenly expanded and contracted part. Bifurcation analysis was carried out of the numerical simulation data. Similar physical description of the transition from a steady symmetric flow to a steady asymmetric flow is reported. The side walls provided a stabilising effect on the critical Reynolds number for the first pitchfork bifurcation and that the critical Reynolds number is proportional to the inverse of the width of the duct. Comparisons between a three-dimensional geometry with a width aspect ratio $A_W = W/h$ of 4 (where, W is the width, and h is the height of the inlet channel), and an essentially two dimensional configuration with $A_W = \infty$, were reported. They found that the side walls significantly extending the stability of the flow by increasing the critical Reynolds number for symmetry-breaking bifurcation. Also, the symmetry plane in the streamwise direction showed streamlines with a smaller deviation from the centerline when compared to the two-dimensional flow case at the same Reynolds number. This in turn reduced the degree of asymmetry in the flow field and hence confirmed the stabilising effect of the side walls. Sau [152, 151] studied three dimensional vortex dynamics and mass entrainment in both a three dimensional rectangular sudden expansion and also for a suddenly expanded and contracted channel. They focused on vortex generation by the use of rectangular-shaped protrusions into the flow. They found that the placement of these tabs could either stop or augment the axis switching mechanism.

Latornell and Pollard [92] and Back and Roshke [10] have carried out experimental investigations into higher Reynolds number flows in the range $400 < Re < 1000$ based on the upstream channel height for axisymmetric sudden expansions. Latornell and Pollard [92] show that the onset of shear layer instabilities is dependent on the inlet velocity profile. They also show that there is a linear relationship between the reattachment length of the shear layer and the inlet Reynolds number. This linear relationship is however dependent on the nature of the expansion inlet velocity profile. Latornell and Pollard [92] identified three different modes of laminar flow which can exist downstream of the expansion, depending on the inlet Reynolds number. At low Reynolds number there exists an unconditionally stable mode characterised by a steady reattachment length and recirculation zone shape. The evolution of shear layer instability begins with the generation of sinusoidal waves in the shear layer, at higher Reynolds numbers. Small oscillations in the reattachment length occur due to the interaction of the waves in the shear layer and the wall. A further increase in Reynolds number causes a grossly unstable mode of flow to develop. Discrete vortices replace the shear layer waves in the vicinity of the reattachment point. This in turn causes large oscillations in the reattachment length.

Tables 5.1 and 5.2 summarise the literature to show values of critical Reynolds number for symmetry-breaking bifurcation with various expansion ratios determined by experiments and numerical methods respectively. These table were partly reproduced from the recent paper by Battaglia and Papadopoulos [14].

Table 5.1: Critical Reynolds numbers for symmetry-breaking bifurcation determined using experimental methods. (Table reproduced from Battaglia and Papadopoulos [14]).

Reference	ER	AR	Re_{cr}
Chedron et al. [29]	2	4	368
	2	8	267
	2	16	194
	2	32	153
	3	4	112
	3	8	65
	3	16	40.5
	3	32	35
Durst et al. [53]	3	27.6	56-114
Durst et al. [54]	2	32	120-200
Fearn et al. [59]	3	24	70
Ouwa et al. [125]	5	12.5	45
Battaglia and Papadopoulos [14]	2	6	320-380

Table 5.2: Critical Reynolds numbers for symmetry-breaking bifurcation determined using numerical methods. (Table reproduced from Battaglia and Papadopoulos [14]).

Reference	ER	AR	Re_{cr}
Alleborn et al. [1]	2	∞	218
	3		80
	5		42.5
	1000		8.5
Battaglia et al. [15]	2	∞	225-233
	3		85-87
	4		52-60
	5		40-45
Battaglia et al. [15]	1.5	∞	446
	2		215
	3		81
	4		54
	5		43
	7		16
Drikakis [46]	2	∞	216
	3		80
	4		53
	5		41
	6		33
	8		28
	10		26
Durst et al. [54]	2	∞	125-200
Fearn et al. [59]	3	∞	80.9
Hawa and Rusak [77]	3	∞	80.7
Kadja and Touzopoulos [83]	2	∞	200
Kudela [89]	3	∞	84-187
Luo [100]	3	∞	92.4
Manica and De Bartoli [106]	3	∞	80-100
Shapira et al. [155]	2	∞	215
	3		82.6
Schreck and Schäfer [153]	3	∞	81
	3	2	113
	3	5	91
Battaglia and Papadopoulos [14]	1.61	∞	340-345
	2	∞	217
	2	6	340-345

5.2 2-Dimensional Flow Through Suddenly Expanded Channels

As described in the introduction above, two-dimensional flow through a plane symmetric suddenly expanded channel has been investigated in the past both experimentally and computationally. This study aims to show that the phenomenon of symmetry-breaking bifurcation can be accurately captured with the use of high-resolution methods.

The suddenly expanded channel geometry was setup following the previous study of Drikakis [46]. Two different expansion ratios were investigated, namely a 1:2 and 1:3 expansion ratio. The expansion ratio is defined by the ratio of the inlet channel to outlet channel height. The Reynolds number is defined as:

$$Re = \frac{U_{max}h}{\nu} \tag{5.2.1}$$

where, U_{max} is the maximum inlet velocity and h is the inlet channel height. A fully-developed plane Poiseuille velocity profile was specified at the inlet and the outlet condition satisfies the condition of a divergence free flow field. The length of the outlet channel was 300 step heights in order to ensure that the outflow gradients of the flow variables in the streamwise direction could be considered equal to zero. In addition to this the outlet velocity conditions were checked after each case in order to make sure a fully developed parabolic profile was obtained. The boundary conditions on all the walls were the non-slip condition. The artificial compressibility formulation of the steady incompressible Navier-Stokes equations was implemented together with characteristics-based method of Drikakis et al. [51] (high-resolution method) for the calculation of the advective fluxes. As was shown in Chapter 4 the characteristics-based methods proved to be the most accurate in computing flows featuring symmetry-breaking bifurcation. Third-order spatial accuracy was used in the reconstruction step of the advective fluxes. The reader is referred to section 2.12 of Chapter 2 for a mathematical description of the high-order spatial reconstruction. An explicit fourth-order TVD Runge-Kutta scheme developed by Shu and Osher [158] and the nonlinear multigrid method of Drikakis et al. [52] are used to drive the numerical solution to a steady state. A steady-state solution is said to be achieved when the size of the separation bubbles stop changing.

In order to determine the effect of grid resolution a grid sensitivity study was performed at a Reynolds number where the flow separates asymmetrically ($Re > 215$ for the 1:2 expansion ratio and $Re > 80$ for the 1:3 expansion ratio). Several grid resolutions ranging from approximately 3,400 grid points to 208,000 grid points were examined. It was found that approximately 14,000 grid points were sufficient to obtain grid independent solutions (within a threshold of 0.5% differences) for both expansion ratios investigated.

Reynolds numbers in the range of $10 \leq Re \leq 600$ were investigated in order to assess the physical mechanism of symmetry-breaking bifurcation. It was found that at low

Reynolds numbers (below the critical value for symmetry-breaking bifurcation) the flow separated symmetrically. As Reynolds number within this range was increased the separation bubbles increased in size along the upper and lower walls. Figure 5.1 shows velocity streamlines at different Reynolds numbers for the 1:2 expansion ratio channel. Symmetry-breaking bifurcation was observed at a Reynolds number of $Re = 216$, which agrees with previously computed results of Drikakis [46]; Battaglia et al. [15]; Alleborn et al. [1]; Shapira et al. [155]. The experimental results of Chedron et al. [29] with an aspect ratio of 16 predicted a critical Reynolds number of $Re = 194$. This ambiguity can be associated with the fact that an experimental setup can never be fully symmetric and hence these imperfections in the flow setup can trigger symmetry-breaking earlier than in a symmetric numerical setup (Shapira et al. [155]). Durst et al. [54] numerically predicted a range for the critical Reynolds number between 125 and 200. This result is much lower than that found in this investigation and in the above cited literature. Drikakis [46] documented that the reason for this large discrepancy could be due to the fact that the work by Durst et al. [54] was initialised using an artificially perturbed flow field in order to accelerate convergence. This then leads to two possibilities: (1) the results obtained by Durst et al. [54] had not actually reached the steady-state solution, or (2) the initial artificial perturbation of the flow field led the stability of the system of equations to predict a much lower critical Reynolds. Drikakis [46] also pointed out that the standard convergence criteria used in most CFD computations are poor indicators of convergence when the size of the perturbed velocities is very small. Drikakis [46] suggested that a more accurate convergence criteria would be to compare skin friction distribution and the size of the separation bubbles during iterations. When the two variables do not change a steady-state solution is achieved.

On increasing the Reynolds number further one of the separation bubbles grew at the expense of the other separation bubble. This growth in one separation bubble causes a larger deviation of the flow until a point is reached that a third separation bubble is formed downstream of the smaller separation bubble (Fig. 5.1 $Re = 600$). The existing literature, both numerical and experimental, shows that on increasing the expansion ratio the critical Reynolds number for symmetry-breaking bifurcation decreases. Figure 5.2 shows velocity streamlines for a range of Reynolds numbers for the 1:3 expansion ratio channel. Symmetry-breaking bifurcation was found to occur at Reynolds numbers greater than 80. This result agrees with the values predicted by Drikakis [46]; Battaglia et al. [15]; Alleborn et al. [1]; Fearn et al. [59]; Hawa and Rusak [77]; Manica and De Bartoli [106]; Schreck and Schäfer [153].

In Fig. 5.3 the bifurcation diagram is based on the distance of the re-attachment points of the separation bubbles on the upper and lower walls of the channel. When the flow is symmetric the distance is zero and increases its values as the asymmetry develops. The bifurcation diagrams encompasses two branches that correspond to two kind of solutions depending on which wall, upper or lower, the larger bubble may appear. The present results are in agreement with previous investigations of Drikakis [46]; Battaglia et al. [15]; Alleborn et al. [1].

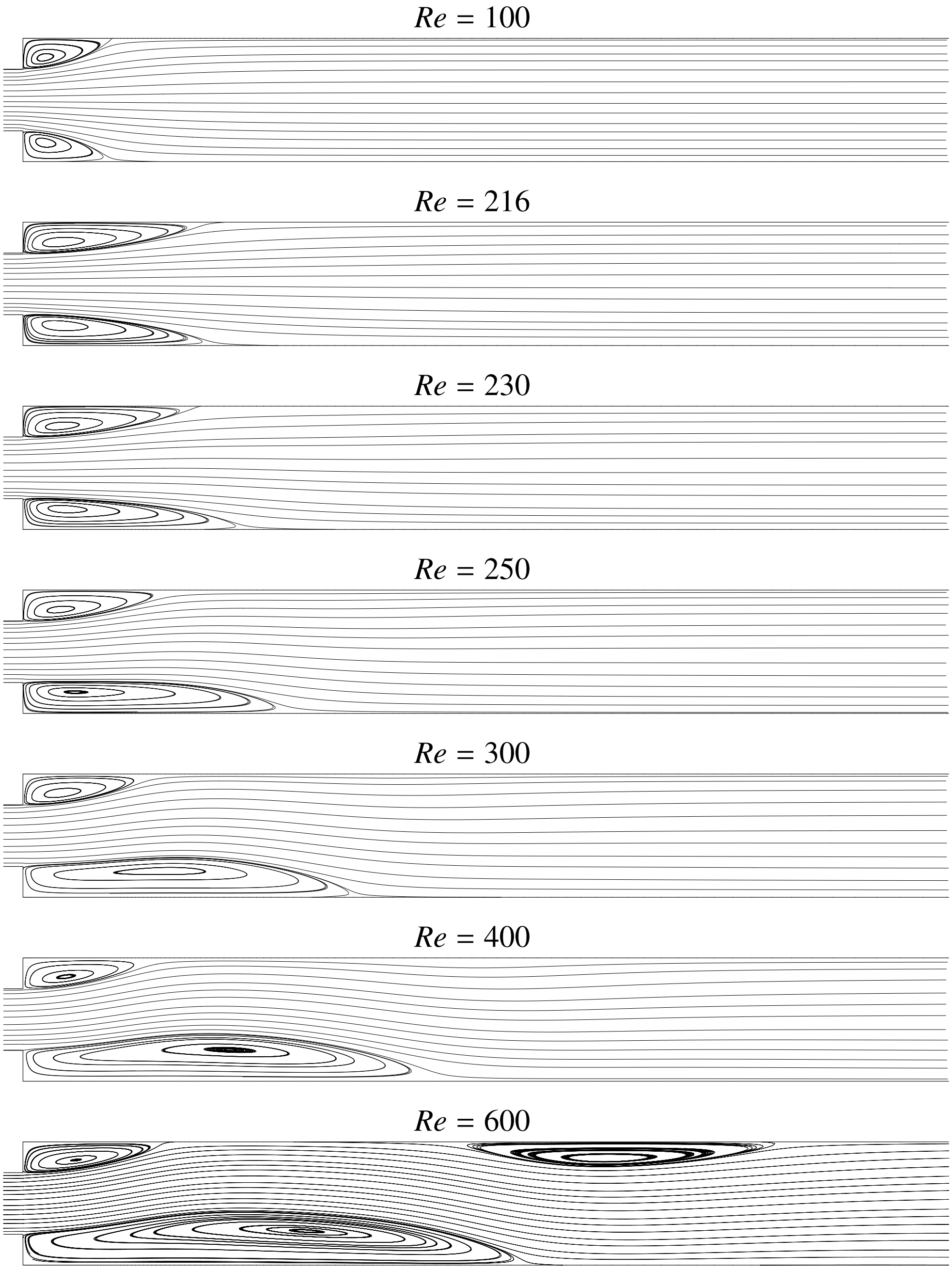

Figure 5.1: Streamlines at different Reynolds numbers for a suddenly expanded channel with a 1:2 expansion ratio.

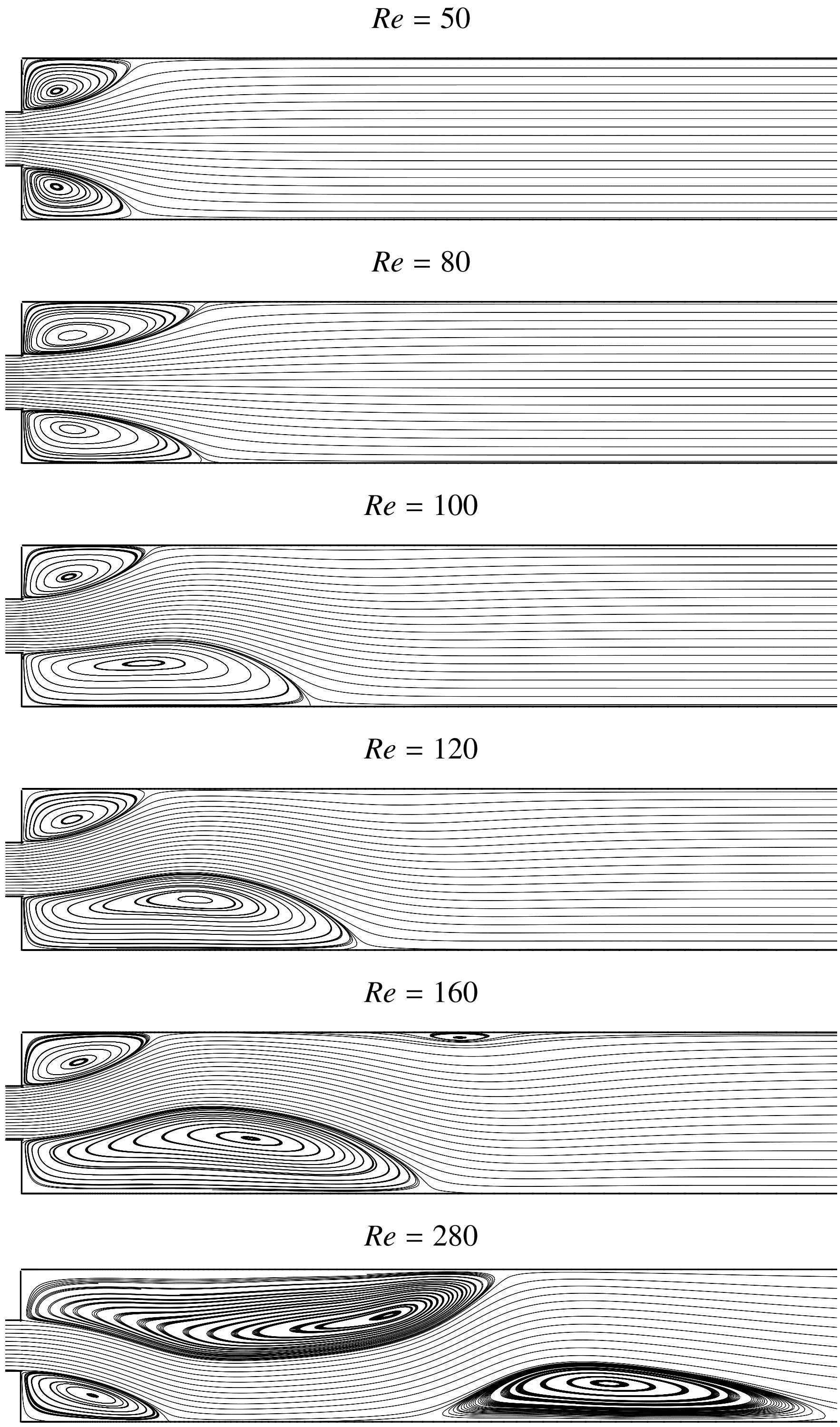

Figure 5.2: Streamlines at different Reynolds numbers for a suddenly expanded channel with a 1:3 expansion ratio.

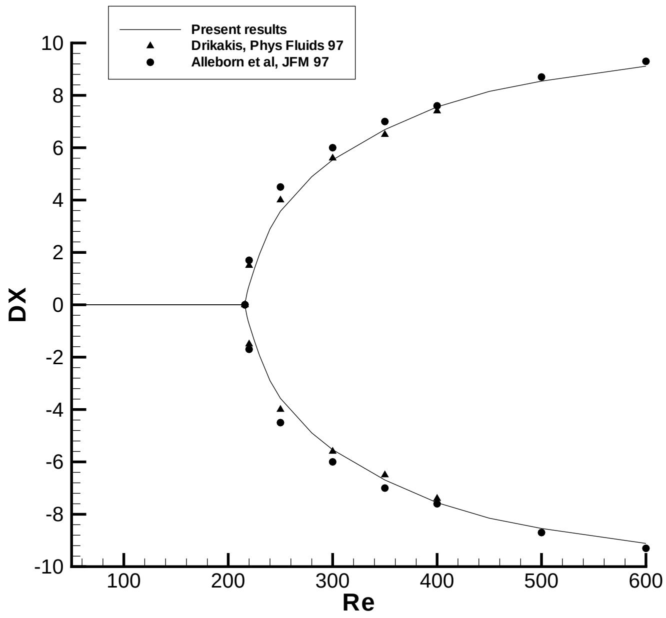

(a) 1:2 expansion ratio

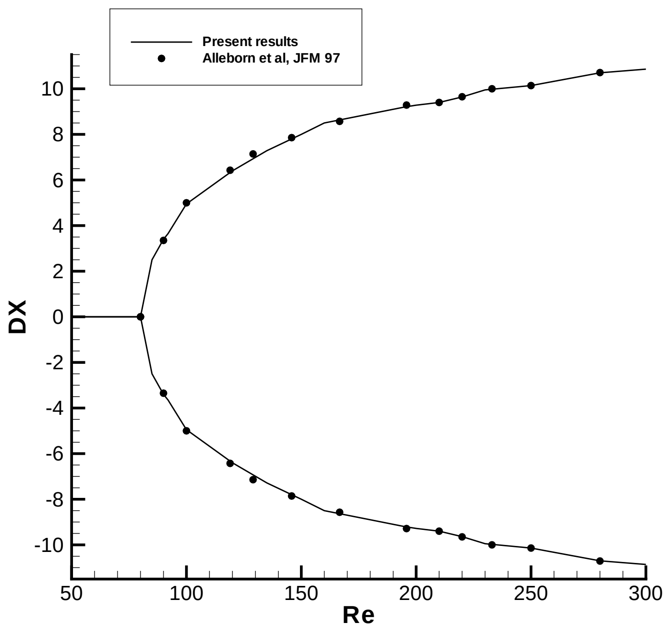

(b) 1:3 expansion ratio

Figure 5.3: Bifurcation diagram for two different expansion ratios.

5.3 3-Dimensional Flow Through a Suddenly-Expanded Channel

After the work regarding two-dimensional suddenly expanded flows it was a natural step to investigate the flow in a three-dimensional setup. The introduction to this chapter already discussed the importance of side wall effects in a three-dimensional suddenly expanded channel. This section aims to reconfirm the current literature using high-resolution methods and also to investigate the effects of higher Reynolds numbers where the flow becomes time-dependent.

5.3.1 Side Wall Effects

Following the work by Schreck and Schäfer [153] a three-dimensional 1:3 sudden expansion channel was setup. Two different aspect ratios (width to expansion height ratio), $w/H = 2$ and $w/H = 5$ were investigated in order to see how the side wall proximity effected the flow. In order to fully investigate the effect of the side walls on the flow, Reynolds numbers in the range 75-115 were investigated. This range covers the regime in which symmetry-breaking bifurcation should occur and has already been reported in the literature by Schreck and Schäfer [153]. The Reynolds number is defined as in the previous section investigating a two-dimensional suddenly expanded channel. Figure 5.4 shows the 3-dimensional setup used in the current investigation, where w is the spanwise length, h is the step height, L is the length of the expanded channel and H is the height of the expanded channel. As with the two-dimensional case, a fully-developed plane Poiseuille velocity profile was specified at the inlet and the outlet condition satisfies the condition of a divergence free flow field. The length of the outlet channel was 300 step heights in order to ensure that the outflow gradients of the flow variables in the streamwise direction could be considered equal to zero. All walls including those in the spanwise direction were prescribed with a no-slip boundary condition. The high-resolution numerical scheme used to solve the advective fluxes is the characteristics-based scheme using third-order spatial accuracy in the reconstruction step.

A grid sensitivity study was carried out in order to rule out any grid dependencies in the solution obtained. The two-dimensional grids used in the previous investigation were extended in the spanwise direction. By performing computations at a Reynolds number where the flow separates asymmetrically for various spanwise grid resolutions it was found that for the aspect ratio of $w/H = 2$ a grid resolution of 38 cells in the spanwise direction was sufficient to provide the necessary numerical accuracy. As the aspect ratio increased to $w/H = 5$ the spanwise grid resolution was increased and it was found that 52 cells were adequate in providing relatively grid independent solutions.

It was found that the flow in the centre plane of the channel is purely two-dimensional. Figure 5.5 shows velocity streamlines of the fluid flow in the centre plane for various Reynolds numbers with a width to expansion height aspect ratio w/H of 2. It should

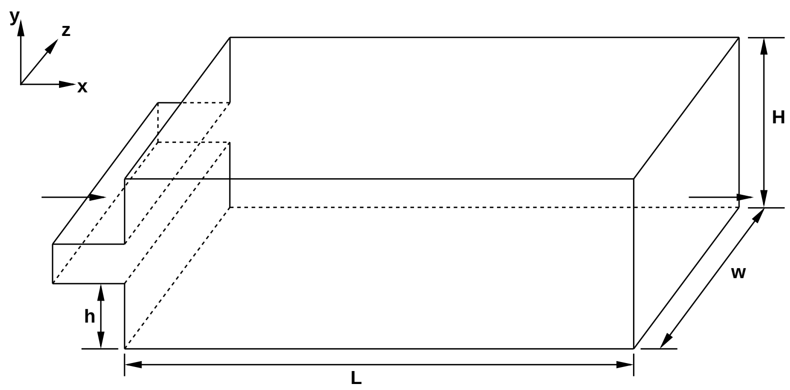

Figure 5.4: Geometry of the three-dimensional channel.

be noted that the critical Reynolds number found in the previous section for a two-dimensional case was $Re = 80$ based on maximum inlet velocity and upstream channel height. It can clearly be seen that even for a Reynolds number $Re = 100$ (which is above the critical Reynolds number) the flow separates symmetrically. On increasing the Reynolds number further i.e. $Re = 115$ the flow separates asymmetrically. This confirms the results obtained by Schreck and Schäfer [153] who found that the critical Reynolds number for a three-dimensional suddenly expanded channel with an aspect ratio of $w/H = 2$ is $Re_{cr} = 113.2$.

If the width to expansion height aspect ratio (w/H) is increased the symmetry breaking occurs at a lower Reynolds number. Figure 5.6 shows velocity streamlines at various Reynolds numbers for a w/H ratio of 5. It can be seen that for a Reynolds number of $Re = 100$ the flow is already significantly asymmetric. This confirms that as the aspect ratio is decreased the critical Reynolds number for symmetry-breaking bifurcation increases due to the stabilising effect on the fluid flow by the side walls. Schreck and Schäfer [153] reported a critical Reynolds number for symmetry breaking bifurcation in a three-dimensional suddenly expanded channel with an aspect ratio of $w/H = 5$ as $Re_{cr} = 91.0$. Computed results from the current investigation show that at a Reynolds number of $Re = 92$ symmetry-breaking bifurcation has already occurred. Velocity streamlines of the flow shown in Fig. 5.6 at the Reynolds number of $Re = 92$ do not clearly show the asymmetry of the flow due to fact that the Reynolds number is so close to the critical value. However, detailed examination of the size of the recirculation zones shows that the lower zone is very slightly larger than the upper recirculation zone. This lower recirculation zone grows at the expense of the upper recirculation zone as Reynolds number is increased.

Figure 5.7 shows three dimensional plots of streamwise velocity contours at various spanwise planes of the channel for the two different aspect ratios investigated at a Reynolds number of $Re = 100$. It can clearly be seen that for both aspect ratios the flow is nominally two-dimensional with little variation in the size of the separation bubbles in the spanwise direction. This remains partly true even when the flow separates asymmetrically at Reynolds numbers close to the critical value for symmetry-breaking bifurcation (see Fig. 5.7(b)). To shed more light on this velocity vectors on the lower and upper planes closest to the lower and upper walls of the expanded channel for the channel with aspect ratio of $w/H = 5$ have been plotted in Fig. 5.8. Figure 5.8(a) shows the scenario where the flow separates symmetrically ($Re = 70$) and Fig. 5.8(b) the asymmetric scenario ($Re = 100$). The symmetric case shows that the three-dimensionality of the flow is the same at both the lower and upper walls whereas for the case where the flow separates asymmetrically it can be seen that the three-dimensional effects are more pronounced on the bottom wall where the recirculation zone is larger. This was also observed in the experimental investigation by Durst et al. [53]. It can also be seen that the smaller recirculation zone shows hardly any variation in the transversal channel direction. The larger recirculation zone shows significant variation in the transversal channel direction in the region close to the side walls. This is due to the stabilising effect of the side walls which reduce the size of the recirculation zone close to the wall.

Another aspect of the three-dimensionality of the the flow can be shown by a stream trace starting at the side wall of the inlet channel for the case $w/H = 5$. Figure 5.9(a) shows the stream trace for a symmetric case $Re = 75$ and Fig. 5.9(b) the asymmetric case $Re = 100$. This figure corresponds to the experiments of Goldstein et al. [67], who incorporated smoke in a laminar flow over a backward facing step. If one were to regard the stream trace as a the trace of a particle it can be seen that the after the particle enters the recirculation area the particle moves in a screwed trace with increasing radius towards the centre plane and then leaves the recirculation zone. This flow behaviour agrees completely with one observed in Goldstein et al. [67] and Schreck and Schäfer [153]. The reasoning behind this screwed particle motion lies in the physics of the side wall boundary layer. The side wall boundary layer imposes shear drag on the primary motion of the fluid particles behind the expansion. This in-turn results in pressure gradients along the spanwise direction giving rise to an increasingly large spanwise velocity component. It is this increasing velocity component that gives rise to the spiral motion focused around a vortical core line towards the symmetry plane of the channel.

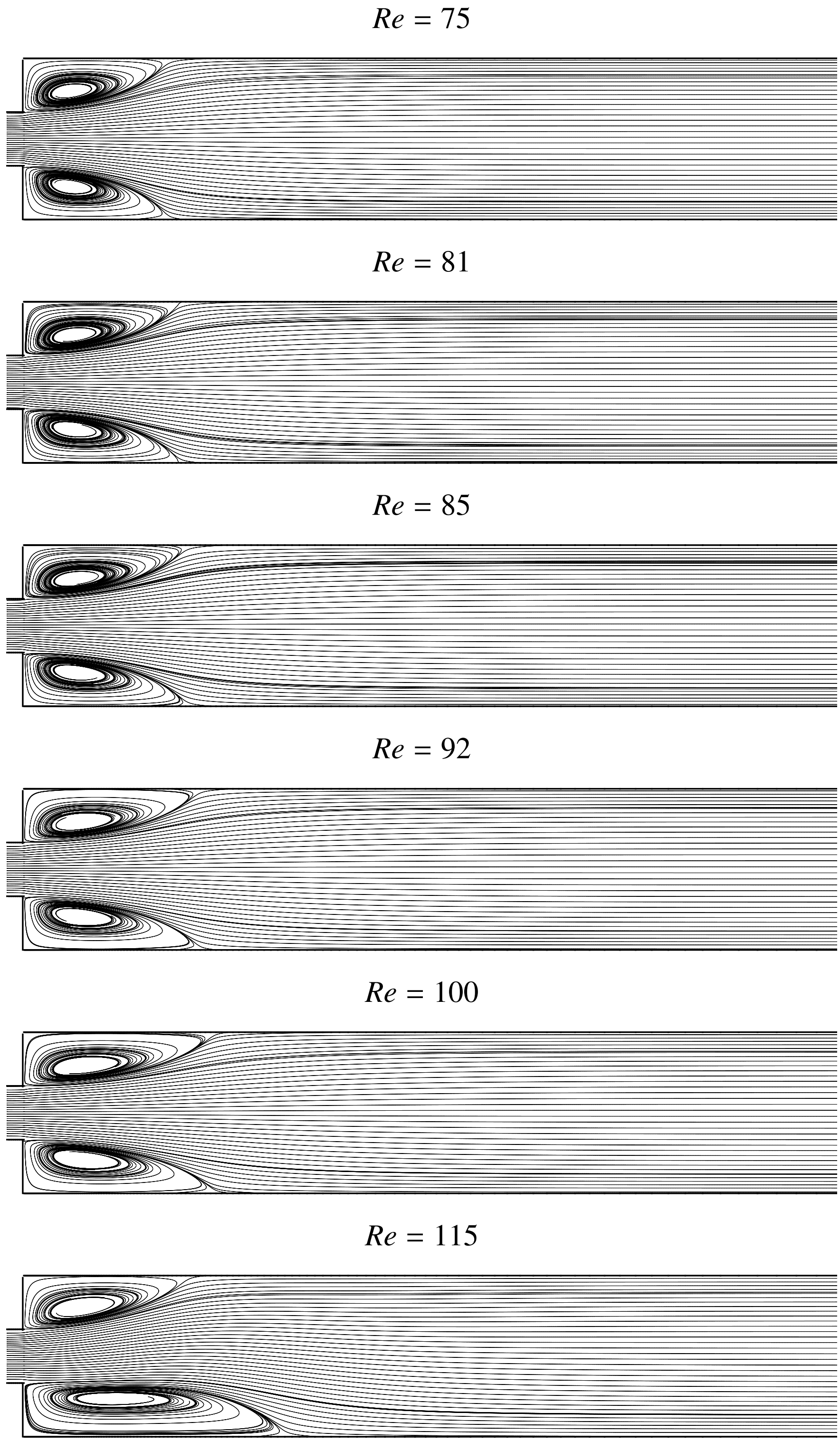

Figure 5.5: U-velocity streamlines in the $x - y$ middle cross section of the channel, where the flow is two-dimensional for various Reynolds numbers, $w/H = 2$.

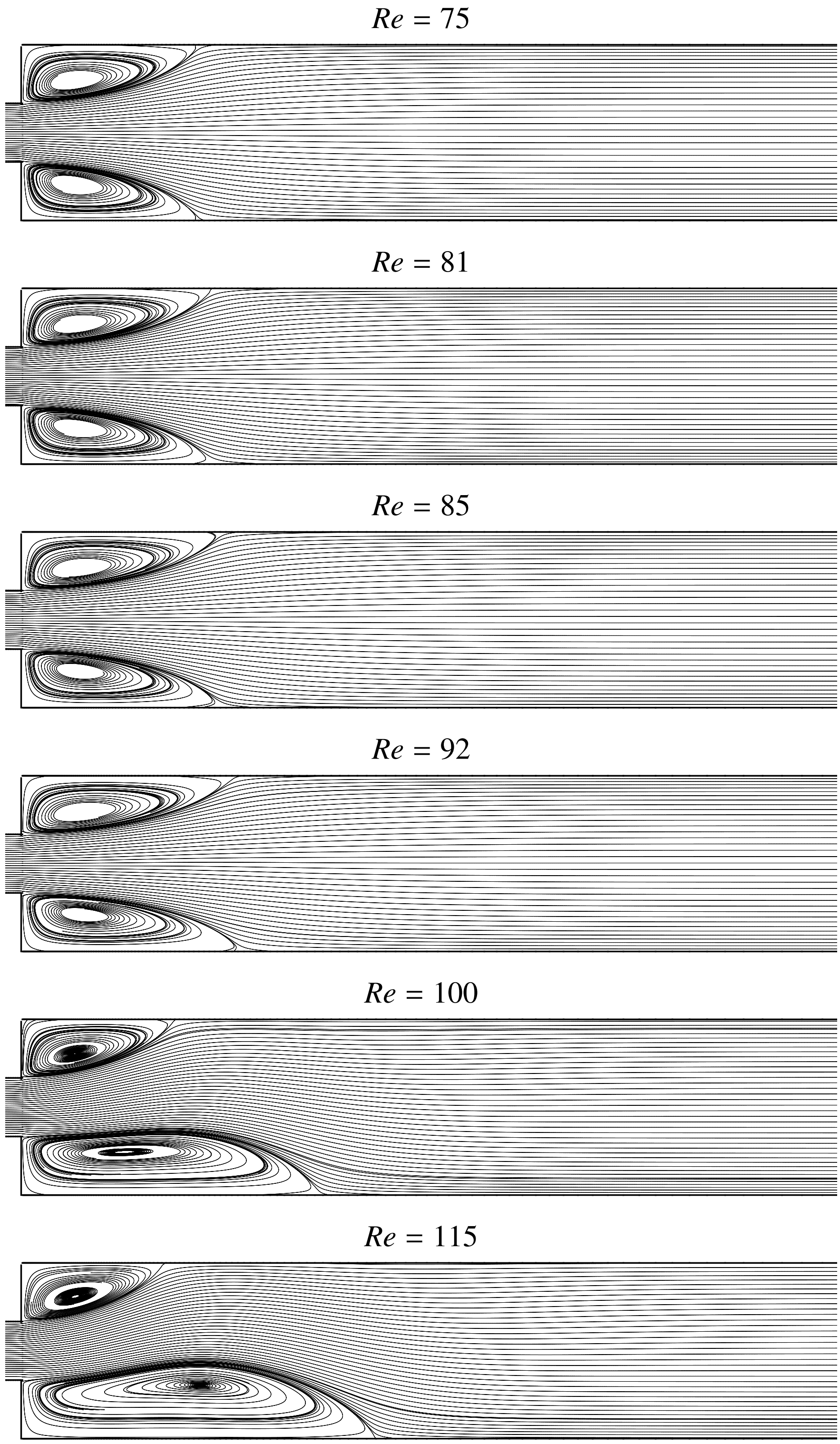

Figure 5.6: U-velocity streamlines in the $x - y$ middle cross section of the channel, where the flow is two-dimensional for various Reynolds numbers, $w/H = 5$.

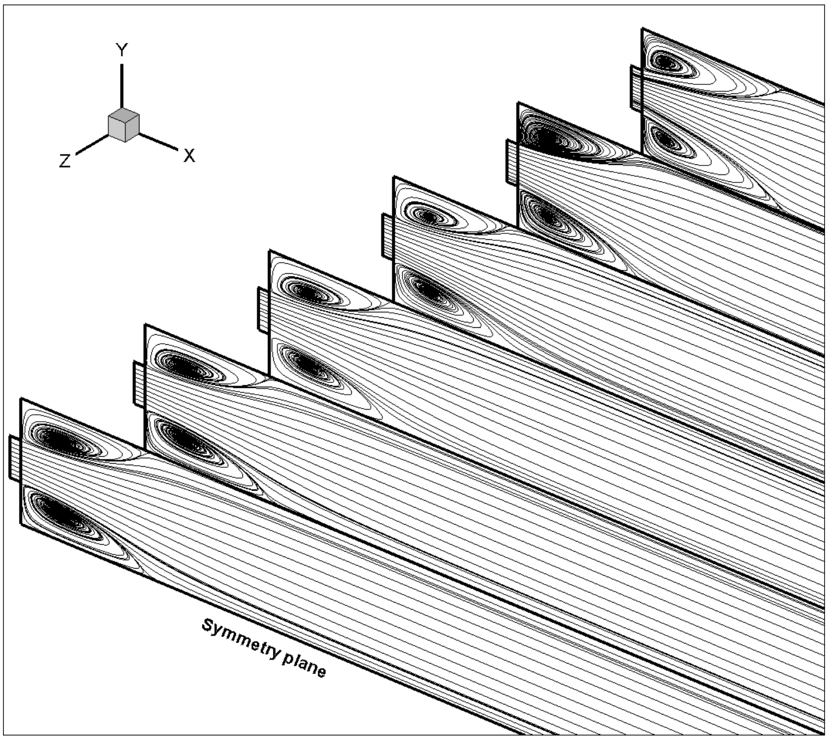

(a) $w/H = 2$

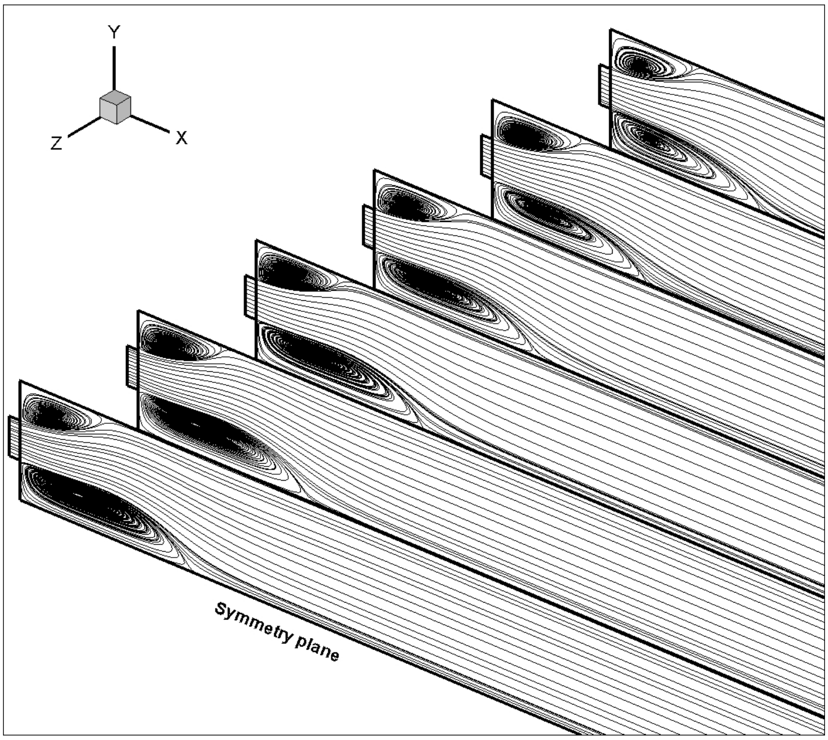

(b) $w/H = 5$

Figure 5.7: U-velocity streamlines at various spanwise planes at $Re = 100$.

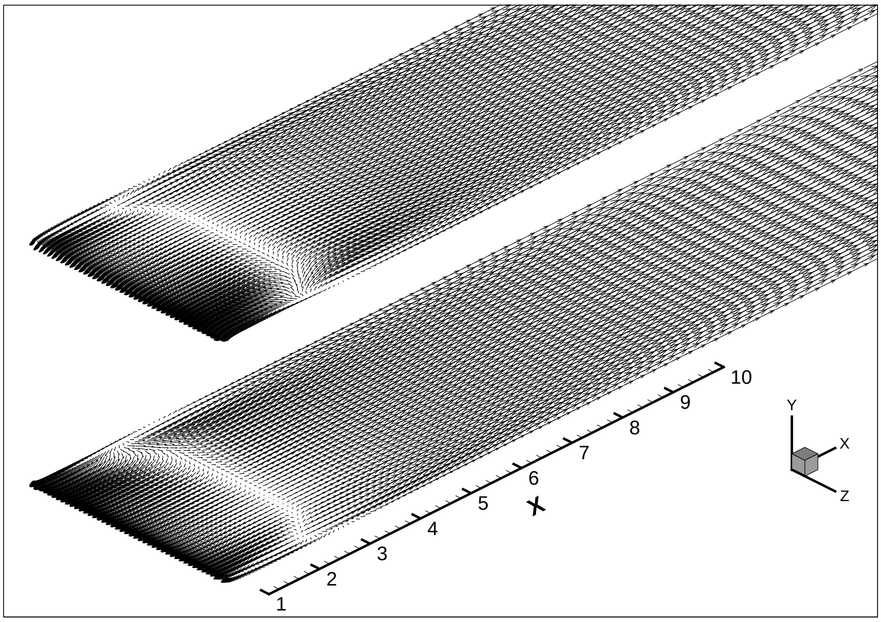

(a) $Re = 70$

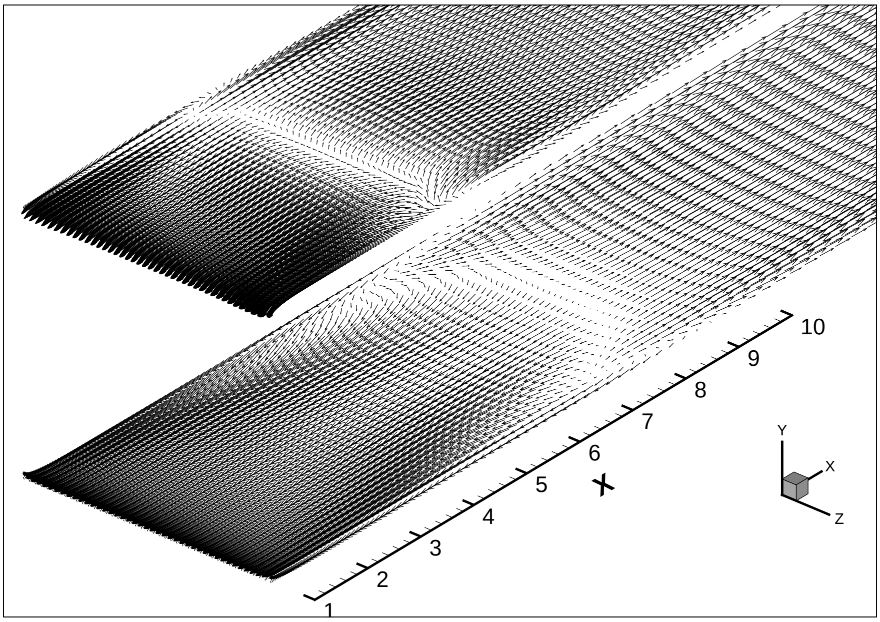

(b) $Re = 100$

Figure 5.8: Velocity vectors near the top and bottom walls of the channel after the expansion, $w/H = 5$.

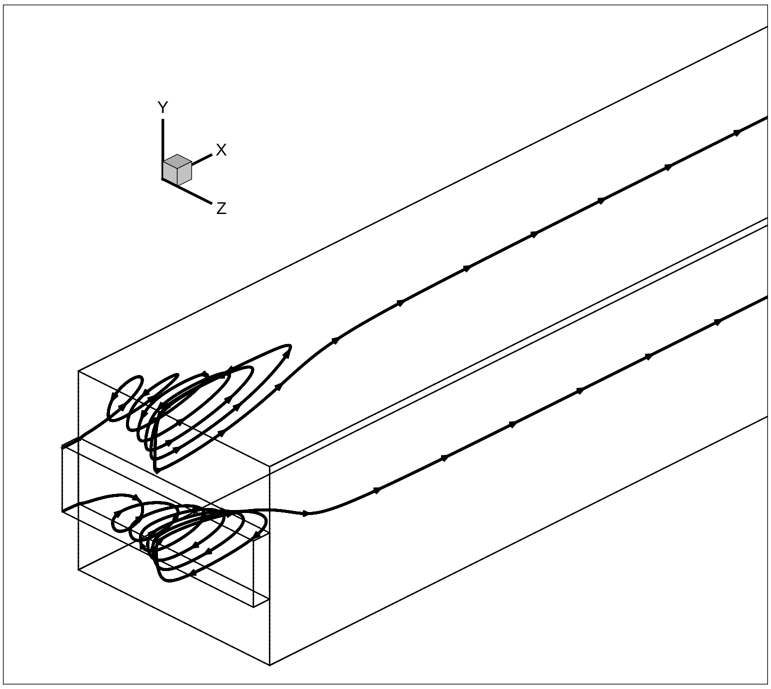

(a) $Re = 75$

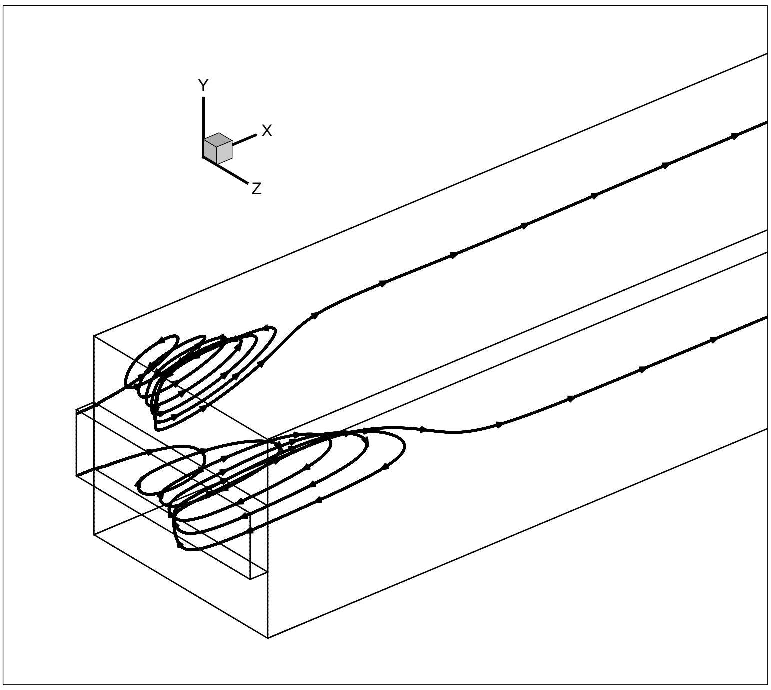

(b) $Re = 100$

Figure 5.9: Streamtrace starting at the side wall of the inlet channel for the case, $w/H = 5$.

5.3.2 Higher Reynolds Number Effects

Unsteady flow through a three-dimensional suddenly expanded channel at moderately high Reynolds numbers have been experimentally investigated by Fearn et al. [59]. The present study aims to shed light on the physics of unsteady flow through a suddenly expanded channel with an expansion ratio of 1:3 and an aspect ratio of 8. The aspect ratio is defined to be the width to the height ratio of the downstream channel as in the previous section. A range of moderately high Reynolds numbers have been investigated beyond the point of symmetry-breaking bifurcation and into the regime where the flow becomes time-dependent. The aim is to show, using high resolution numerical methods, that the time-dependency of the flow is characterised by the shedding of vortices from the shear layer of the upstream recirculation bubbles. Furthermore, it has been found that three-dimensional effects become more pronounced with increasing Reynolds number and that the flow becomes three-dimensional before becoming time-dependent.

Following the previous study of Fearn et al. [59], a sudden expansion geometry with an 1:3 expansion ratio and aspect ratio of 8 was used in the simulations. Fully developed channel flow conditions were used at the inlet to the upstream channel. The Reynolds number was defined by the maximum inlet velocity and the upstream channel height. The outflow conditions were checked after each computational case in order to make sure a fully parabolic profile was obtained. No-slip boundary conditions were used for the walls in both the cross-streamwise and spanwise directions. Low Reynolds number flows were initially computed and compared to the experimental data from Fearn et al. [59] in order to partially validate the setup before moving onto higher Reynolds number flows where quantitative experimental validation could not be found.

At low Reynolds numbers the fluid flow was found to separate symmetrically with equal sized bubbles attached to the upper and lower walls as expected. As Reynolds number was increased the separation regions increased in size and upon exceeding the critical Reynolds number for symmetry-breaking bifurcation the flow became unstable with an instability manifested as an asymmetric separation of the flow. Although the solution is regarded to be unstable the flow remained steady. The aim of this investigation was not to investigate the critical Reynolds number since this is dependent on the aspect ratio and has been investigated in the past by various authors. It was found that at low Reynolds numbers the flow in the centre plane of the channel was purely two-dimensional. Figure 5.10 shows velocity streamlines of the fluid flow in the centre plane for various Reynolds numbers. The figure shows the progression of the flow from a stable symmetric separation to unstable asymmetric separation with increasing Reynolds number. At a Reynolds number of $Re = 280$ a third separation bubble appears on the same side wall as the smaller upstream separation bubble. This has been confirmed experimentally and numerically by Fearn et al. [59].

Fearn et al. [59] provide experimental velocity profiles for various low Reynolds number flows. This data has been compared to the present results and are presented in Fig. 5.11. For $Re = 50$ the flow is shown to separate symmetrically and agrees well

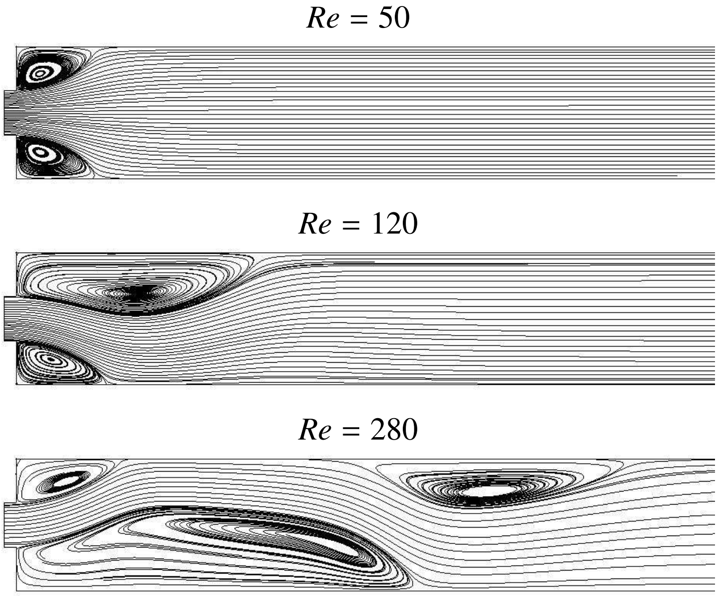

Figure 5.10: Streamlines at different Reynolds numbers.

with the experimental data from Fearn et al. [59]. The size of the recirculation zones is also captured well by the numerical simulation and can be seen from the region of flow reversal represented by the negative flow velocity. The flow has regained the fully developed parabolic profile at a downstream position of 10 step heights which corresponds well with the experimental data. As the flow separates asymmetrically at $Re = 120$ the profile shows that at downstream positions of 1.25 and 2.5 the velocity is negative close to both the lower and upper wall since both positions lie in the region of the recirculation zones. As we move further down the channel at a position of 5 step heights the velocity profile is positive at the lower wall but negative at the upper wall. This shows that the flow has separated asymmetrically with a larger recirculation bubble situated at the upper wall (see Fig. 5.10). Due to the asymmetric separation, the flow takes longer to regain the fully developed symmetric profile which is achieved at a downstream position of 20 step heights. The percentage difference between the computed results and the experimental data is within 5%. Figure 5.11(c) shows the velocity profile corresponding to $Re = 280$. The main feature of the flow at this Reynolds number is the third recirculation region situated at the top wall downstream from the small upstream recirculation region. The third recirculation bubble is shown at a downstream position of 20 step heights by a positive velocity at the lower wall and negative velocity at the upper wall. The velocity profiles at downstream positions of 5 and 10 step heights show an inconsistency when compared to the experimental data. This is primarily due to the difference in size and shape of the separation bubble at the lower wall obtained with the computations compared to the experiments. A fully developed profile is attained at a downstream position of 40 step heights.

In order to be sure that the solutions obtained are relatively grid independent veloc-

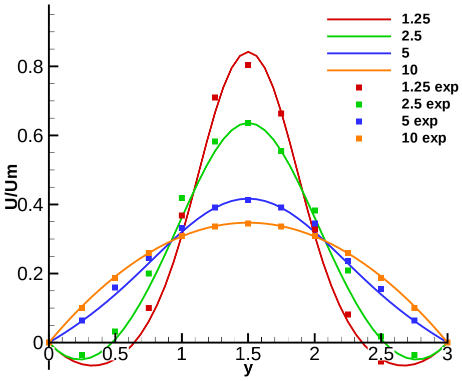

(a) Re = 50

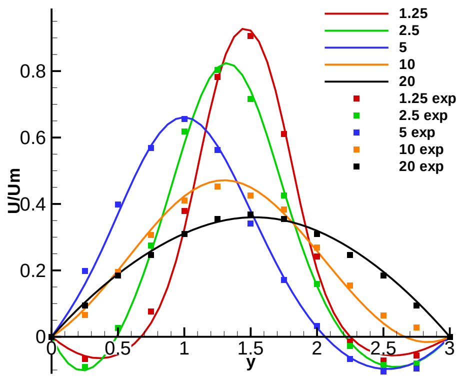

(b) Re = 120

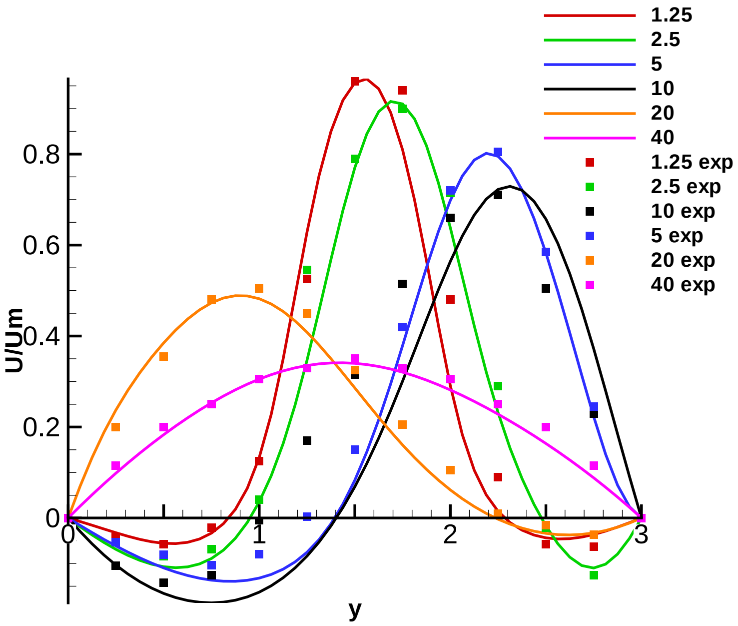

(c) Re = 280

Figure 5.11: Velocity profiles at various streamwise positions comparison to experimental data of Fearn et al. [59].

ity profiles at Reynolds numbers of $Re = 120$ and $Re = 280$ at various streamwise positions on the centre plane have been plotted in Fig. 5.12. The line legend in the figures correspond to two different grid resolutions. Grid 1 refers to a grid resolution of approximately 420,000 grid points and Grid 2 refers to a grid resolution of approximately 805,000 grid points. It can clearly been seen that there is very little difference between the two solutions obtained from the two different grid resolutions. A small difference can be seen in the prediction of the third recirculation bubble at a position of 20 step heights. It should be noted that the solution obtained on the finer grid resolution predicted the larger recirculation bubble formed immediately after the sudden expansion to be situated on the upper wall, whereas the coarser grid predicted this bubble to be formed on the lower wall. For ease of comparison the coarser grid solution has been inverted to coincide with the finer grid solution. It has already been discussed in this thesis that the formation of the asymmetry can have two orientations depending on which wall the larger recirculation bubble attaches itself to. In the experiments this switching of the large recirculation zone can occur due to small imperfections in the upstream channel or at the sudden expansion entrance. Durst et al. [53] revealed that this switching can be manipulated even once a steady state had been achieved. The inversion was achieved by blowing into one of the recirculation regions through a small tube. They reported that strong blowing was needed in order to disturb the flow position from the steady state solution.

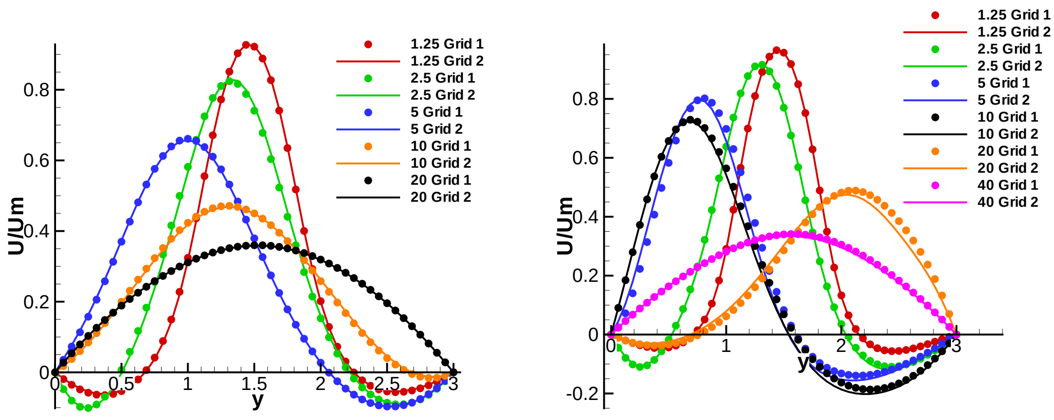

(a) Re = 120 (b) Re = 280

Figure 5.12: Velocity profiles at various streamwise positions comparing two different grid resolutions.

To shed light on the surface topology streamlines were plotted on the upper and lower surfaces of the channel (see, Fig. 5.13). The streamlines show clearly lines of reattachment for two different Reynolds numbers. At Re = 160 the flow separates asymmetrically and the two lines of reattachment can be clearly seen on the upper and lower surfaces. The streamlines show that the flow is very nearly invariant in the spanwise direction except in the regions close to the side walls. For the case of Re = 280 there are two lines of reattachment on the upper surface corresponding to the two recirculation zones. The tendency of the streamlines within the recirculation zones to move from the side walls towards the centre plane is a characteristic of the three-dimensionality of the flow.

In order to best depict the three-dimensionality of the flow, velocity streamlines at various spanwise planes parallel to the side wall plane have been plotted in Figs. 5.14 and 5.15. Both figures show that the flow is nominally two-dimensional, except in

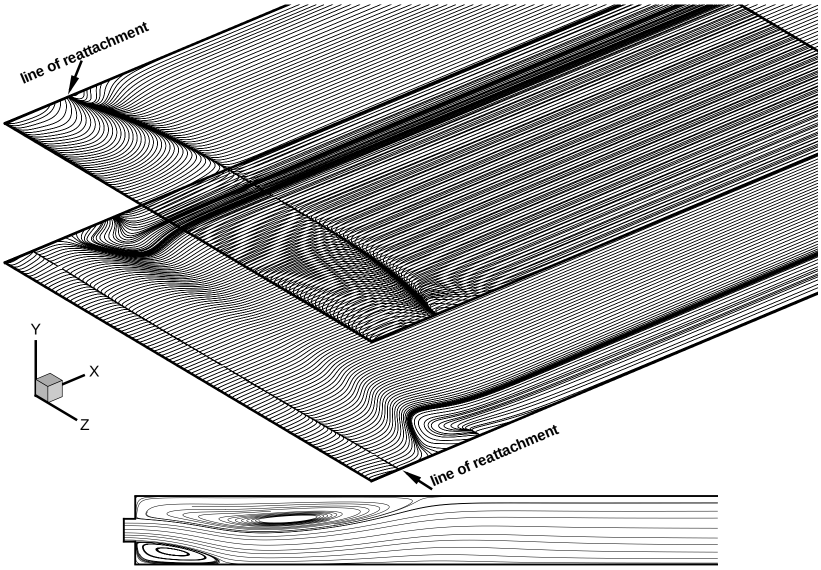

(a) Re = 160

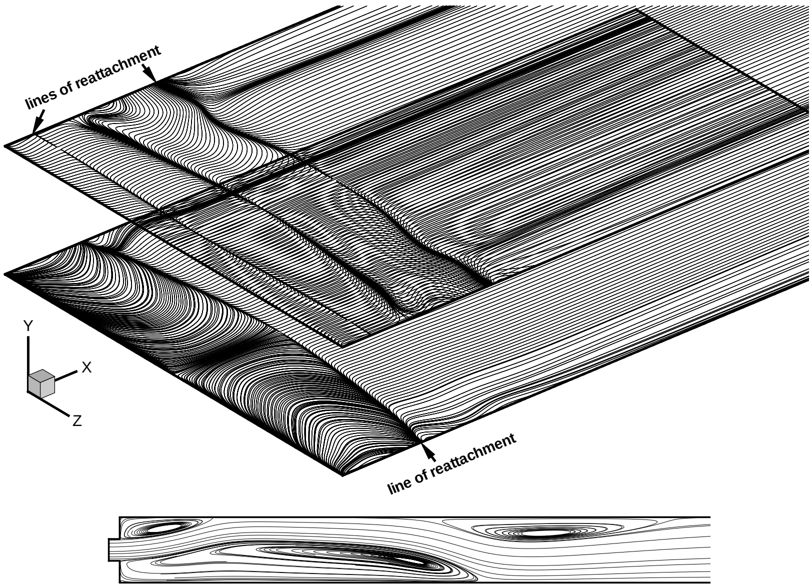

(b) Re = 280

Figure 5.13: Velocity streamlines of the upper and lower surface flow topology for two different Reynolds numbers.

the planes closest to the side wall where boundary layer phenomenon prevails. Shear forces due to the side wall boundary layer resist fluid particles to proceed to the side wall. Chiang et al. [31] reported that a secondary flow results due to the complex interaction between the curved flow, manifested by the presence of the primary recirculation regions directly behind the step, and the boundary layer which develops over the vertical side wall. It should be noted that in Fig. 5.14 there exists a floor eddy in the vicinity of the vertical side wall. This secondary eddy is not found in two-dimensional analysis and is too weak to extend it's influence into the whole span of the expanded channel. As Reynolds number is increased (Fig. 5.15) to Re = 280 the three-dimensional effects become more pronounced especially in the region close of the vertical side wall. The effect of the secondary eddy is strong enough to extend the whole spanwise direction towards the symmetry plane. This secondary eddy varies significantly in the region close to the vertical side wall where the boundary layer exists until settling to a stable separation region at planes closer to the symmetry plane.

As Reynolds number was increased the third separation bubble grew in length and eventually the flow became unsteady. It has been suggested by Fearn et al. [59] that the flow becomes fully three-dimensional before becoming time-dependent. This has been proven to be correct from the above analysis of the flow topology via the use of streamlines at various spanwise planes as well as analysing the flow topology on the upper and lower planes of the expanded channel. In order to study the physics of the flow at higher Reynolds number where the flow is fully three-dimensional and time-dependent a range of Reynolds numbers was investigated up to Re = 800. At higher Reynolds numbers the unsteady flow was characterised by the shedding of vortices which alternate from one side to the other with consequent asymmetry of the mean flow. This shedding pattern is due to small disturbances at the edge of the sudden expansion being amplified in the shear layer formed between the main flow and the recirculation flow in the corners of the channel. Fearn et al. [59] and Chedron et al. [29] both observed the same physical behaviour with regards to the shedding of vortices from the upstream recirculation regions. The shedding of the vortices was observed to increase in frequency as Reynolds number was further increased.

Betchov and Criminale [16] referred to the amplification of disturbances in shear layers, and the existence of oscillations maintained by appropriate feedback mechanisms was postulated by Martin [110]; Martin et al. [111] with regards to single regions of flow. The same mechanisms can be applied to the current flow but are further complicated by the interaction between the two shear layers. Velocity fluctuations normal to the main flow in one half of the channel generated from the vortex patterns influence the flow in the opposite half of the channel. These velocity fluctuations extend from each shear layer to the duct centre. Chedron et al. [29] reports that the flow generated at these higher Reynolds numbers can only exist if the fluctuating normal velocities originating from one shear are out of phase with those from the other shear layer. As a result of this the shedding of the vortex structures are antisymmetric. The existence of velocity oscillations perpendicular to the mean separation line causes the flow in the separated regions to be continuously entrained into the shear layers and replaced by fluid from the main flow. Martin [110] postulated a requirement for stable recirculation regions to exist. This 'locking-on' condition stated that only an uneven number of complete oscillation cycles will feed back the correct in-phase disturbance to the edge of the expansion from which the separation occurs.

Figures (5.16-5.19) show instantaneous streamlines parallel to the side wall plane at various time instances for two different Reynolds numbers. At a Reynolds number of Re = 400 the flow takes longer to develop to a fully three-dimensional flow with streamline patterns changing significantly in the spanwise direction. Although, it can clearly be seen that due to the side wall shear layer the flow possess three-dimensional characteristics. Vortices are shed periodically from both the upper and lower main recirculation regions formed directly after the sudden expansion. The shed vortices on the lower wall interact with the third recirculation zone downstream from the main recirculation regions. At later times (see Fig. 5.17) the structure of the third recirculation zone has been destroyed by the shedding of vortices from the lower main recirculation region. As Reynolds number was increased to Re = 800, the shedding of vortices from the main recirculation regions increased in frequency. Figures 5.18-5.19 show velocity streamlines at various spanwise planes at three different time instances for Re = 800. The shedding of vortices is initiated earlier in comparison to that of Re = 400. Again the streamline pattern constantly changes in time and also as the flow traverses from the side wall to the centre plane. The shed vortices move faster downstream as expected in comparison to the lower Reynolds number of Re = 400. An interesting point to note is how the structure of the large main recirculation region, directly behind the expansion, changes with time. As fluid is periodically entrained and replaced in the recirculation zone multiple recirculation zones appear to be formed within the large recirculation zone. This then forces the large recirculation zone to shed vortices in order to remain relatively stable.

Figure 5.20 shows iso-surfaces of vorticity for Re = 280. From this figure one can see that there is an increase in vorticity at the upper surface in the region of the third recirculation zone. The vorticity increases towards the centre plane with a regular pattern. There are no small scale irregular areas of vorticity which could disrupt the solution and cause unsteadiness. Figure 5.21 shows iso-surfaces of vorticity for two different Reynolds numbers in the unsteady regime. It can clearly be seen that as Reynolds number increases the vorticity becomes more complex with small scale structures become more prominent. High values of vorticity are shown to appear at the upper wall downstream from the expansion in the region where there is periodic shedding of vortices. The vorticity contours at the top wall show an irregular distribution, whereas for lower Reynolds numbers this distribution has a regular pattern. This is due to the vortical shedding taking place in this region.

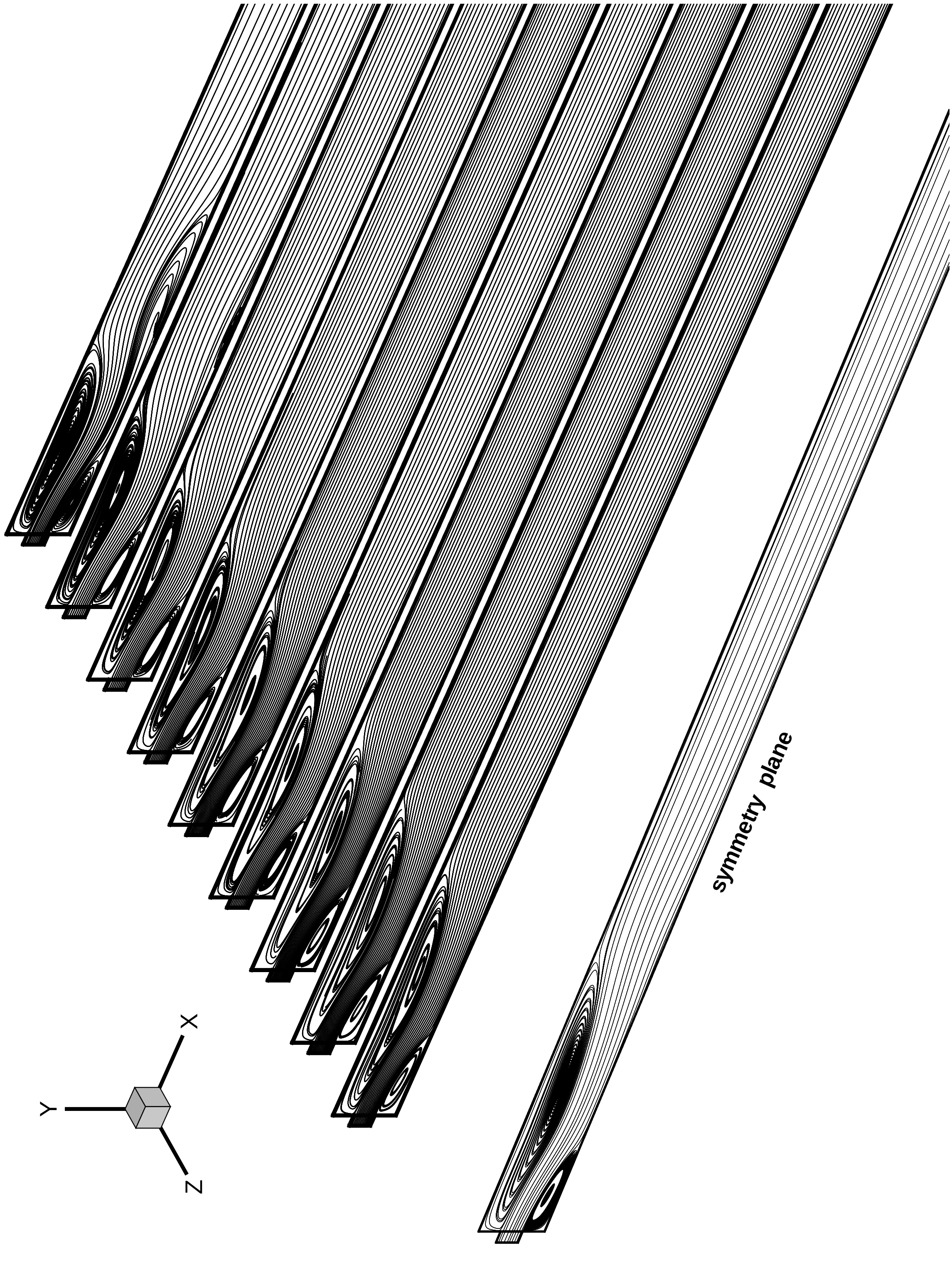

Figure 5.14: Velocity streamlines at various spanwise planes for Re = 160.

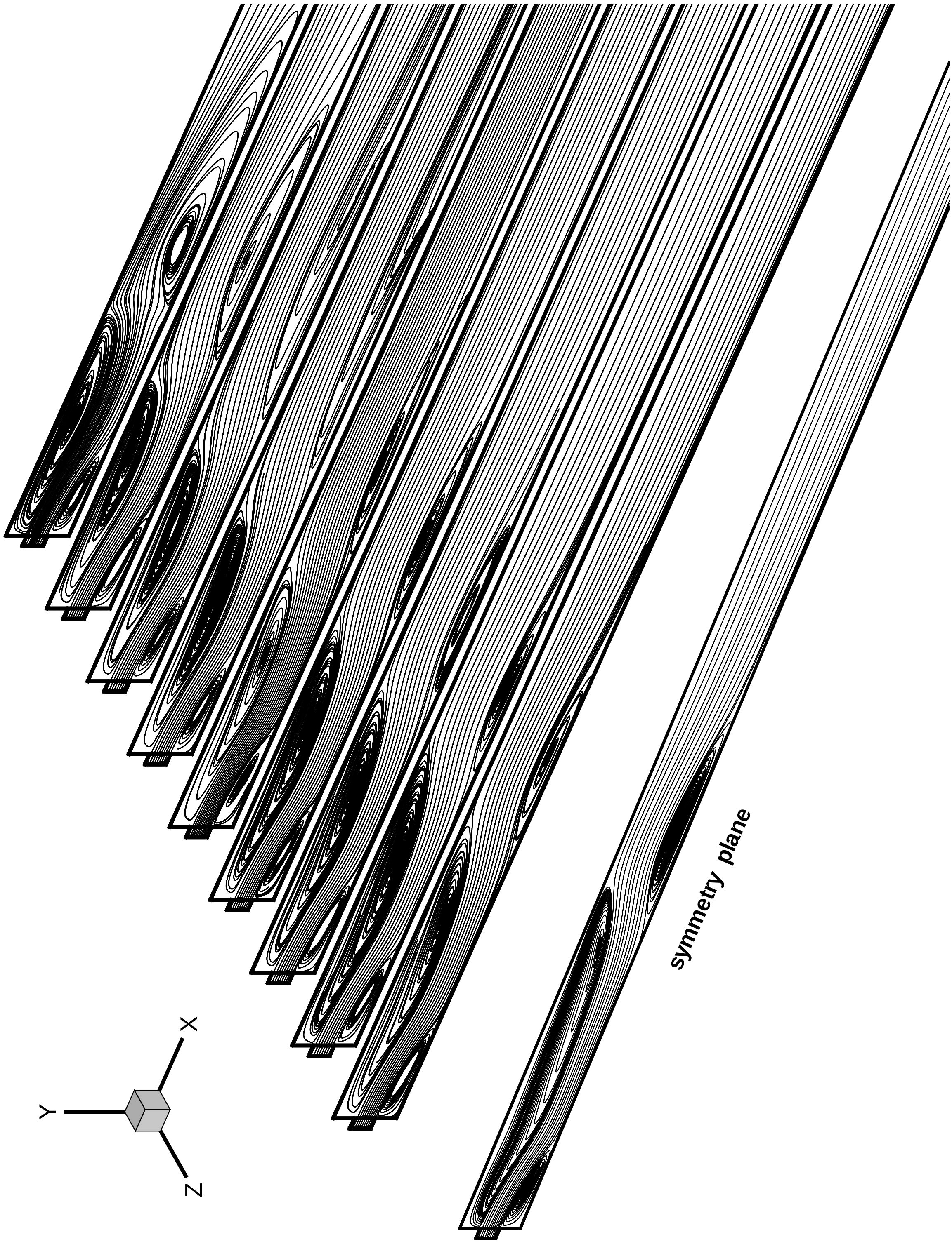

Figure 5.15: Velocity streamlines at various spanwise planes for Re = 280.

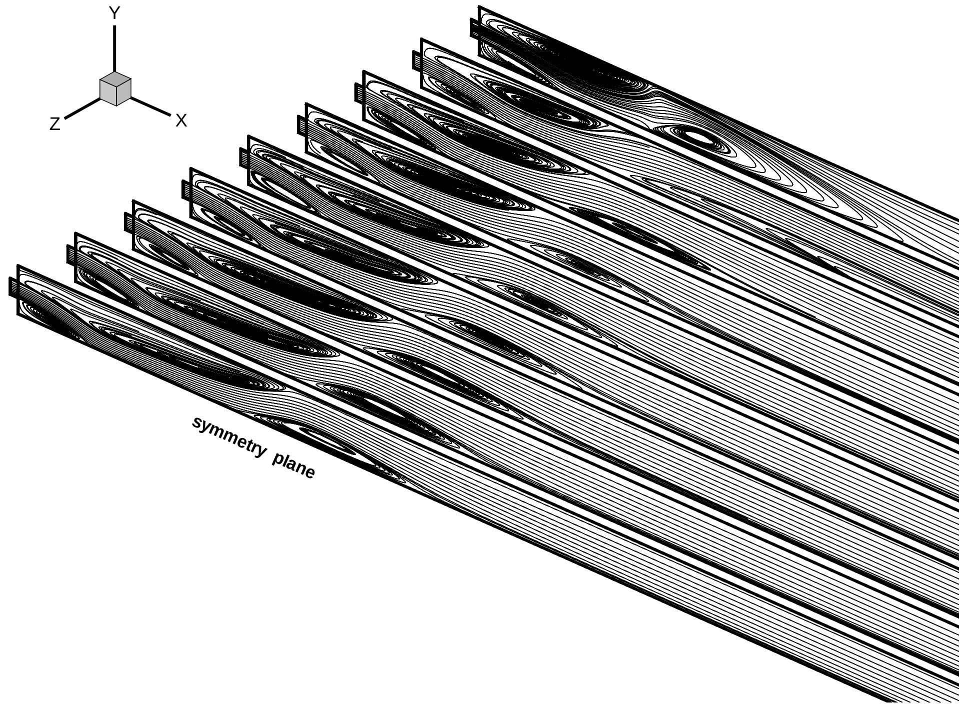

(a) t = 8.038 (non-dimensional time).

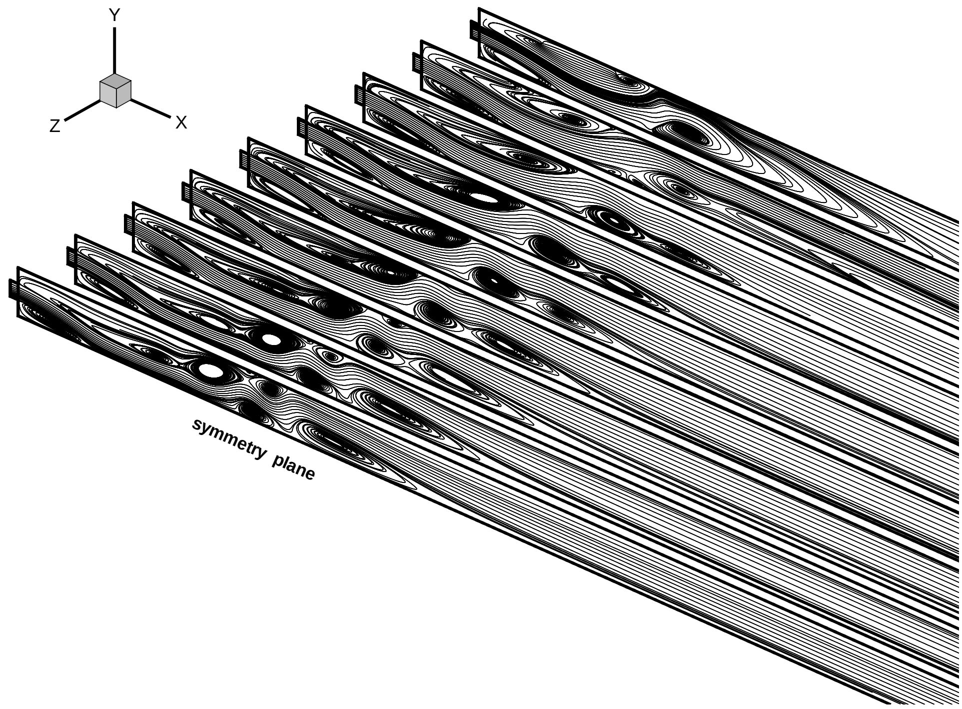

(b) t = 16.077 (non-dimensional time).

Figure 5.16: Three-dimensional flow patterns plotted at different spanwise positions for Re = 400.

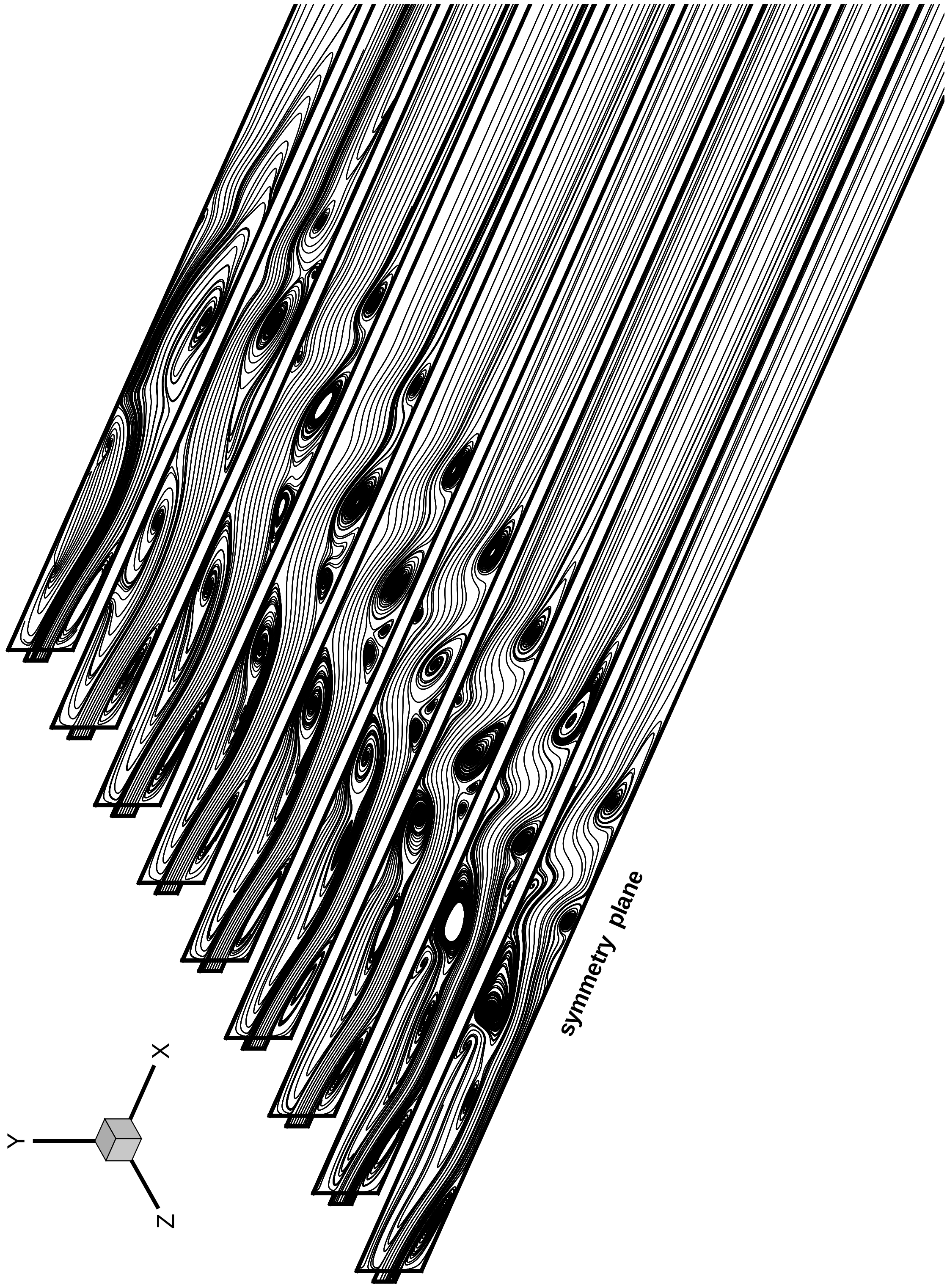

Figure 5.17: Three-dimensional flow patterns plotted at different spanwise positions for Re = 400 at t = 32.154 (non-dimensional time).

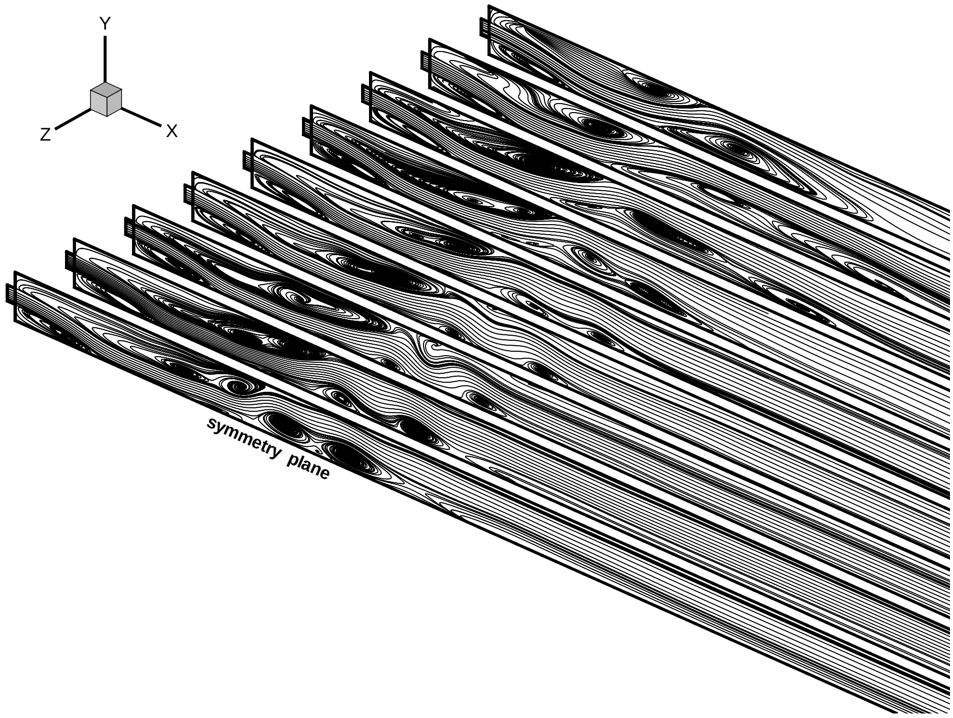

(a) t = 8.038 (non-dimensional time).

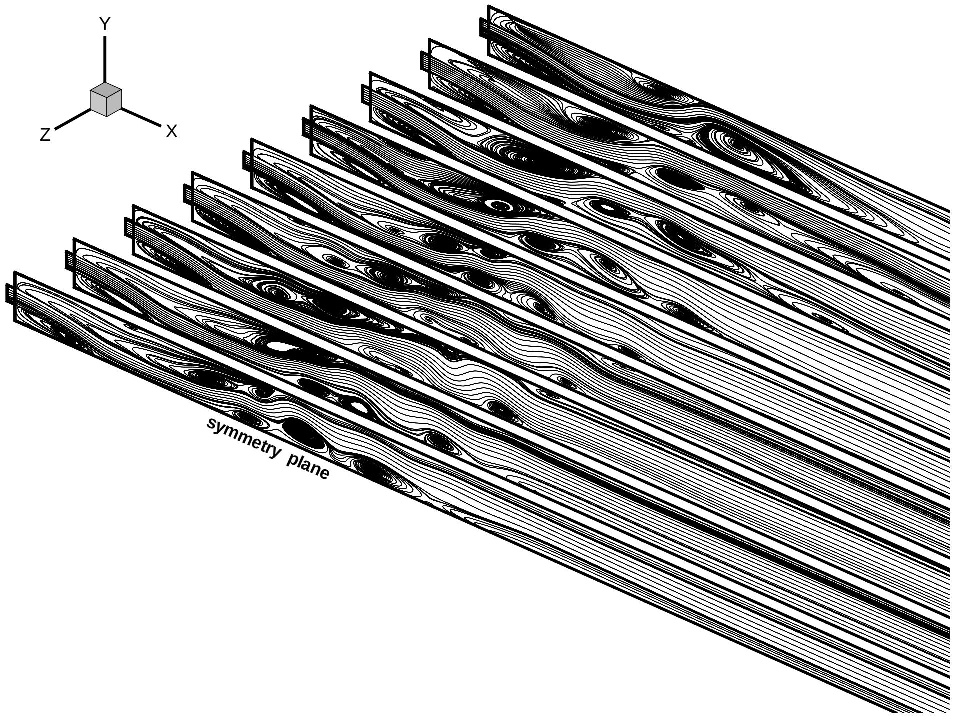

(b) t = 16.077 (non-dimensional time).

Figure 5.18: Three-dimensional flow patterns plotted at different spanwise positions for Re = 800.

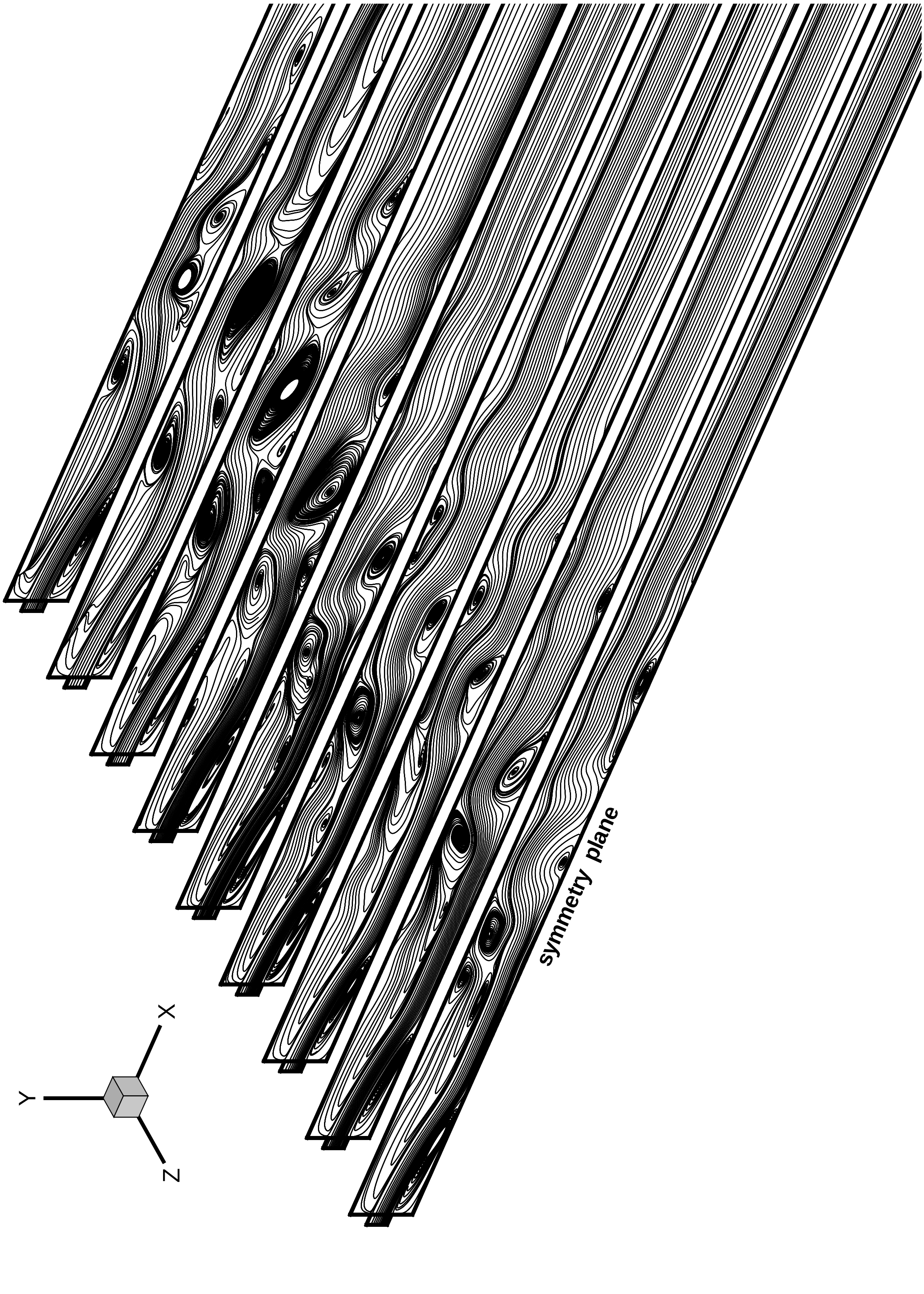

Figure 5.19: Three-dimensional flow patterns plotted at different spanwise positions for Re = 800 at t = 32.154 (non-dimensional time).

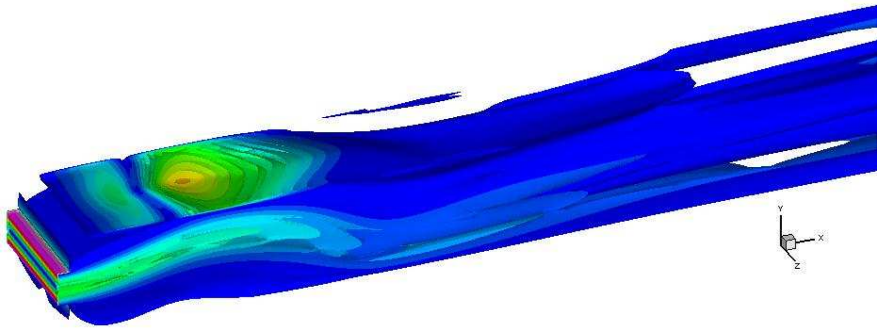

Figure 5.20: Iso-surfaces of vorticity for a Re = 280.

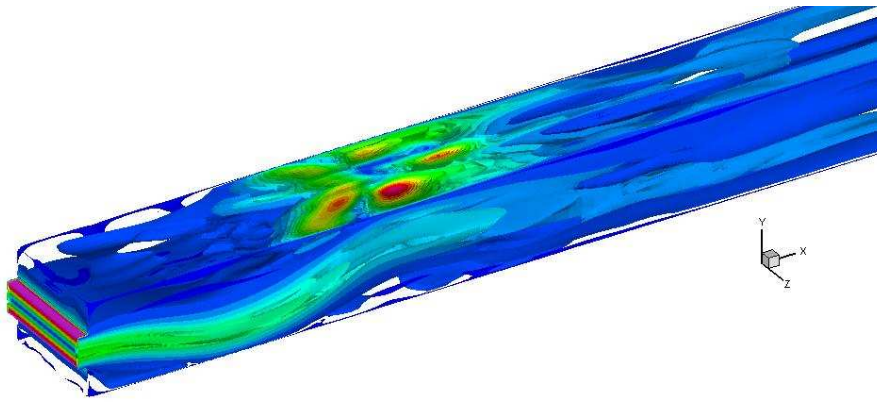

(a) Re = 400

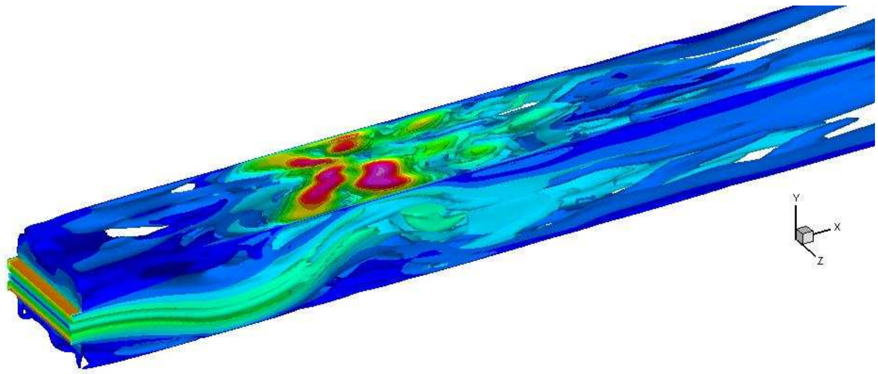

(b) Re = 800

Figure 5.21: Iso-surfaces of vorticity for two different Reynolds numbers at t = 16.077 (non-dimensional time).

5.4 Summary

A numerical study of flow through suddenly expanded channels has been presented for both two-, and three-dimensional geometries. The study included the investigation of two different expansion ratios and the transition from a stable symmetric separated flow to stable asymmetric separated flow. The calculations showed that for low Reynolds numbers the flow separated symmetrically. As Reynolds number was increased symmetry-breaking bifurcation occurs at a critical Reynolds number and recirculation region of different sizes form on the lower and upper walls. The asymmetries become stronger with increasing Reynolds as the size of one recirculation region grows at the expense of the other. The effect of increasing the expansion ratio lead to an earlier onset, with respect to Reynolds number, of symmetry-breaking bifurcation. Computed results were compared to previous works by Drikakis [46] and Alleborn et al. [1] via velocity streamline plots and bifurcation diagrams. A three-dimensional investigation concerning an expansion ratio of 1:3 was presented in order to investigate side wall effects, three-dimensionality and transition to time-dependent flow at higher Reynolds numbers. Two different aspect ratios were considered following the work by Schreck and Schäfer [153] and it was confirmed that as aspect ratio decreases the critical Reynolds number for symmetry-breaking bifurcation increases. This is due to a stabilising effect from the vertical side walls on the subsequent fluid flow. At lower Reynolds numbers in the regime of asymmetric separation of the fluid flow, the flow in the expanded channel is nominally two-dimensional except at planes closest to the vertical side walls. This irregularity at the side walls is due to the effects of the side wall boundary layer acting to stabilise the flow. On increasing Reynolds number the flow take on more of a three-dimensional character with side wall effects extending the whole spanwise domain. Further increases in Reynolds number lead to the flow to become time-dependent characterised by the time-periodic shedding of vortices from the two main recirculation regions formed directly behind the sudden expansion. The loss of stability of the steady asymmetric flow to a time-dependent one is a consequence of the three-dimensional effects in the channel. Therefore one can conclude that the flow in this particular configuration becomes three-dimensional before becoming unsteady and that the unsteadiness is caused by a three-dimensional disturbance in the flow. It has been shown that high-resolution numerical methods can correctly predict non-linear bifurcation phenomena in both two- and three-dimensions. The present computational results have been compared to available experimental data over a range of Reynolds numbers and have shown to agree to within a percentage difference of approximately 5% of the available data. At Reynolds numbers where quantitative data was unavailable the computed results have shown to qualitatively capture the flow physics which so importantly characterises the flow through such geometries during both steady and unsteady computations.

CHAPTER 6

Symmetry-Breaking Mechanism for a Suddenly Expanded Channel

It has been shown in chapter 5 that above some critical Reynolds number symmetry-breaking bifurcation occurs in flow through a suddenly expanded channel. This instability has been well documented in both experimental and computational studies. The reader is referred to chapter 5 for a more complete discussion of the existing literature. This chapter aims to shed light on the mechanism of symmetry-breaking bifurcation in the context of a numerical simulation. The common question often raised is why in a fully symmetric numerical setup does this symmetry-breaking bifurcation occur. A closer look into the numerical methods used throughout this thesis shows us that the non-linearity of high-resolution methods is the "trigger" mechanism for the onset of symmetry-breaking bifurcation.

6.1 Introduction

Both experimental and computational studies agree that there is a critical point above which the flow through suddenly expanded channels features symmetry-breaking bifurcations. In the experiments the instabilities may be triggered by geometrical imperfections and asymmetries in the inflow conditions upstream of the expansion. With regard to the triggering mechanism for asymmetric flow, the main difference between laboratory and numerical experiments is that a perfectly symmetric laboratory experiment cannot be performed while a symmetric set-up can be created in the numerical simulation framework (with only exception being the round-off error of the computer). The computational set-up should preserve symmetry in terms of initial and boundary conditions; discretisation of the equations in space and time, including discretisation at the boundaries; symmetry in the inversion of the system of equations including acceleration techniques (e.g., multigrid); coding issues and computational mesh. If one has taken care of the above then the numerical solution (converged to the machine zero in 64-bit mode) has to be symmetric. However, this is not the case. Foumeny et al. [61] argued that symmetry-breaking bifurcation was due to truncation and rounding errors in the numerical calculations, but De Zilwa et al. [44]

found that steady simulations always returned symmetric results for the flow separation. De Zilwa et al. [44] state that the asymmetry in the solution results from an unsteady phenomenon and that the symmetric solutions of the time-dependent equations become unstable beyond some critical Reynolds number.

The flow separation in a sudden expansion using a fully symmetric set-up as described above, as well as in the framework of different methods, has been investigated. It was found that although these precautions have been taken, asymmetric flow is still predicted by high-resolution schemes. This numerical behaviour is also found in agreement with several other papers published in the literature. If one argues that the asymmetric computational solution is not correct but instead it is an artifact, then this would be paradoxical because the asymmetric solution happens to agree both with the experiment and stability analysis (Drikakis [46])! Therefore, the asymmetric solution is correctly captured and is due to a mechanism embedded in high-resolution numerical methods which is yet unknown. The quest is to understand this mechanism.

The aim of the present study is twofold: (i) to shed light on the onset of symmetry-breaking bifurcation in two-dimensional direct numerical simulations of suddenly-expanded flows; (ii) to show the extent to which the numerical (non-linear) dissipation of modern computational methods models the imperfections of an experimental set-up responsible for triggering symmetry-breaking in fluid flows. It is shown that the symmetry-breaking of the flow is associated with the dissipation mechanism encompassed by high-resolution methods used in the discretisation of the convective terms. This mechanism responds automatically to the Reynolds number change and triggers the onset of the flow asymmetry.

6.2 Problem Description

A two-dimensional plane symmetric suddenly expanded channel with an expansion ratio of 1:2 was setup as described in chapter 5. No-slip boundary conditions for the velocities are implemented on the channel walls and zero pressure gradient normal to the wall. Similar to previous studies (Drikakis [46]; Battaglia et al. [15]; Alleborn et al. [1]; Fearn et al. [59]), a fully parabolic velocity profile (Poiseuille flow) is considered at the inlet of the upstream channel. In contrast to previous computational studies where the upstream inlet condition was implemented at the entrance of the expansion, in the present study the condition was implemented farther upstream in order to allow downstream disturbances to be convected upstream. A fully developed flow is assumed at the outlet of the downstream channel, thus the outflow gradients of the flow variables in the streamwise direction could be considered equal to zero, assuming and computationally verifying that the downstream channel is long enough. Moreover, the numerical methods used in this study take into account the characteristic information of the travelling waves at the inflow and outflow boundaries thus ensuring no artificial reflections of the pressure waves at the boundaries. In order to ensure independence of the numerical solution from the outflow boundary condition, another condition was also employed, this one considering a travelling wave to describe the open boundary. The latter was used in previous sudden-expansion flow studies (Durst et al. [53]; Drikakis [46]). The two boundary conditions yielded identical results.

A brief description of the numerical methods used in this study is presented below for completeness. For more details the reader is referred to chapter 2. The numerical discretisation of the convective fluxes is obtained by high-resolution schemes. To examine the behaviour of the dissipation mechanism let us focus attention on the x-direction convective flux in all three equations of the system of equations: $\mathbf{E} \equiv (u, u^2+p, uv)^T$. In all methods employed in this study, the convective flux derivative $\partial \mathbf{E}/\partial x$ is discretised at the centre of the control volume (i, j) using the values of the intercell fluxes, i.e., $\partial \mathbf{E}/\partial x = (\mathbf{E}_{i+1/2,j} - \mathbf{E}_{i-1/2,j})/h$, where h is the grid spacing; to simplify the notation, the subscript j will be omitted below. The general form for a Godunov (first-order) flux is given by

$$\mathbf{E}_{i+1/2} = \frac{1}{2}(\mathbf{E}_i + \mathbf{E}_{i+1}) - \frac{1}{2}|\mathbf{A}|(\mathbf{U}_{i+1} - \mathbf{U}_i) \ , \tag{6.2.1}$$

where $\mathbf{A}$ approximates $\partial \mathbf{E}/\partial \mathbf{U}$ (the entries of the Jacobian matrix). Higher-order versions of the fluxes can be obtained by writing the flux as

$$\mathbf{E}_{i+1/2} = \frac{1}{2}[\mathbf{E}(\mathbf{U}_L) + \mathbf{E}(\mathbf{U}_R)] - \frac{1}{2}|\mathbf{A}|(\mathbf{U}_R - \mathbf{U}_L) \ , \tag{6.2.2}$$

where $\mathbf{E}_L$ and $\mathbf{E}_R$ denote the left and right states of the flux respectively, at the cell face of the computational volume. Similarly, $\mathbf{U}_L$ and $\mathbf{U}_R$ are the left and right states of the vector of the primitive variables $\mathbf{U} = (p, u, v)^T$ at the cell face of the computational volume. The left and right states can be computed by second- or higher-order interpolation schemes (2.12.1).

The second term on the rhs of (6.2.1) is the wave-speed dependent term (WST), which effectively contains the non-linear numerical dissipation that is embedded in the high-resolution method. The averaged part of the flux, $[\mathbf{E}(\mathbf{U}_L) + \mathbf{E}(\mathbf{U}_R)]/2$, is calculated according to the left and right states of the primitive variables. Note, however, that in some methods (e.g., Drikakis et al. [51]) the calculation of the flux $\mathbf{E}_{i+1/2}$ is reconstructed by solving locally a one-dimensional Riemann problem (see Drikakis and Rider [50] for more details). Thus, the flux cannot explicitly be written in the form (6.2.1) or (6.2.2). In this case the dissipation of the flux can be extracted by writing the flux as: $\mathbf{E}^{cb}_{i+1/2} \equiv \mathbf{E}^{a}_{i+1/2} - (\mathbf{E}^{a}_{i+1/2} - \mathbf{E}^{cb}_{i+1/2})$, where $\mathbf{E}^{a}_{i+1/2} = [\mathbf{E}(\mathbf{U}_L) + \mathbf{E}(\mathbf{U}_R)]/2$ and $\mathbf{E}^{cb}_{i+1/2}$ is the reconstructed flux, for example, the characteristics-based (cb) scheme of Drikakis et al. [51], or another method based on numerical reconstruction. The term $(\mathbf{E}^{a}_{i+1/2} - \mathbf{E}^{cb}_{i+1/2})$ is the equivalent of the WST term in the rhs of (6.2.1) and (6.2.2). Non-linear numerical dissipation terms emerge from the convective fluxes associated with each of the system's equation. In this investigation we have employed a variety of numerical methods such as characteristics-based scheme (Drikakis et al. [51]); Einfendt's HLLE (Einfeldt [56]); Rusanov's scheme (Rusanov [148]); Lax-Friedrichs scheme (Lax [93]), as well as variants of these schemes in conjunction with first, second and higher-order reconstructions. Details of these methods can be found in chapter 2 section 2.11.

The built-in dissipation and numerical reconstruction of the above family of methods, principally aiming at increasing numerical accuracy, result in non-linear (high-resolution) schemes. This numerical framework provides monotonic and non-oscillatory properties to the numerical solution, which are essential elements for achieving accuracy in the computation of complex flows spanning from laminar to transitional and turbulent flows (Grinstein and DeVore [70]; Fureby and Grinstein [62]; Drikakis [48]). Examination of the modified equations associated with high-resolution methods has yielded the enticing hint that characteristics implicit in these methods describe certain aspects of turbulence flow modelling (Margolin and Rider [107]). The central objective of the study is to understand if there is a physical mechanism embedded in modern numerical methods that returns the correct physical behaviour with respect to symmetry-breaking in a class of flows prone to develop instabilities.

Computations were performed using several variants of numerical methods to examine symmetry-breaking scenarios for the flow through a sudden-expansion. In all simulations the computational mesh was sufficiently fine (200×68) to provide mesh independent solutions with respect to symmetry-breaking bifurcation. The length of the downstream and upstream channels were 300 and 1 step heights, respectively. Numerical experiments using different downstream channel lengths confirmed that 300 step heights are sufficient to allow the independence of the solutions from the downstream boundary conditions, i.e., a zero outflow gradient of the flow variables in the streamwise direction.

6.3 Results

Previous experiments and computations have revealed that for the 1:2 sudden-expansion geometry the flow remains symmetric for Reynolds numbers up to 215 (the critical Reynolds number based on the maximum inlet velocity and upstream channel diameter). On exceeding this critical Reynolds number the flow develops as an asymmetric separation of the fluid flow (see chapter 5 for further details). Symmetry-breaking realisations can be numerically predicted using the high-resolution methods mentioned in the preceding section. We have performed hundreds of numerical simulations and found that the symmetry-breaking mechanism is similar for all these methods. The objective of this study is not to compare in a quantitative manner the results obtained by different methods but to discuss the mechanism leading to symmetry-breaking in the framework of computations, as well as to show the physical relevance (and its numerical behaviour) of the non-linear dissipation encompassed by high-resolution methods. Clearly, these two issues are interwoven. Although the objective of this work is not to compare different methods, in the course of this and other studies, central finite-difference schemes (linear schemes, fourth-order accurate) in conjunction with symmetric time-integration have been investigated and have found that symmetric solutions can indeed be obtained. Moreover, we have also investigated classical central schemes in conjunction with explicitly added dissipation, thus still linear schemes, and have found that the solution remains symmetric due to excessive numerical diffusion. On the other hand, in the case of high-resolution schemes the numerical reconstruction of the convective terms results in non-linear dissipation (implicitly embedded onto the numerics) and this leads, as will be shown below, to asymmetric flow solutions. Most importantly, it should be noted that in both the 'simpler' and high-resolution based scheme computations, the same discretisation scheme for the viscous terms and time integration have been used in order to eliminate doubts about the contribution of these terms to the symmetry-breaking. The above behaviour clearly proved that the non-linear dissipation of the (non-linear) convective terms *triggers* the asymmetry and not the (linear) viscous terms. Euler computations (i.e., very high Reynolds number limit) have also been carried out and shown that the flow separates asymmetrically for a fully inviscid case. This further proves that the asymmetry is due to the non-linear advective flux term and not the viscous terms.

An examination of the non-linear dissipation for Reynolds numbers at which the flow is stably symmetric shows that the dissipation remains symmetric throughout the channel, both upstream and downstream. This is shown in Figure 6.1 by means of contour lines of dissipation associated with the momentum flux in the x (streamwise) and y (cross-streamwise) direction, for the flow at $Re = 100$. The dissipation values range from -10^{-7} to 10^{-5} (dimensionless) in double precision computations. Simulations using several different methods have confirmed that the dissipation patterns are unfolded in a similar fashion preserving a symmetry throughout the channel. This behaviour persists throughout the Reynolds numbers where experiments also show that the flow retains its symmetry.

Increasing the Reynolds number beyond its critical value unravels an interesting behaviour. The non-linear dissipation begins to develop asymmetric patterns, which mostly appear downstream of the separation region (Figure 6.2). Note that both the flow and the non-linear dissipation retain symmetry farther downstream as well as near the entrance of the expansion. It can clearly be seen from Figs. 6.2-6.6 that the distribution of the dissipation associated with the flux in the streamwise direction is more asymmetric than the distribution of the flux in the cross-streamwise direction. It should be noted that the dissipation contour values are of the same order of magnitude in both directions.

At higher Reynolds numbers we observe that the symmetry-breaking of the dissipation patterns spreads in both upstream and downstream direction (Figure 6.3). Even though the flow may have developed a significant asymmetry at higher Reynolds numbers (for example, see the streamlines for $Re = 230$ Fig. 5.1 in Chapter 5) the dissipation still retains its symmetry around the orifice of the upstream channel in both the streamwise and cross-streamwise directions. The simulations showed that the symmetry-breaking of the dissipation starts to spread in the upstream channel for Reynolds numbers larger than $Re = 230$. For $Re = 250$ and $Re = 300$ the dissipation patterns of both the x

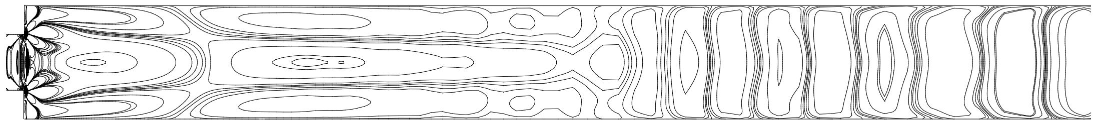

(a) momentum flux in the x direction

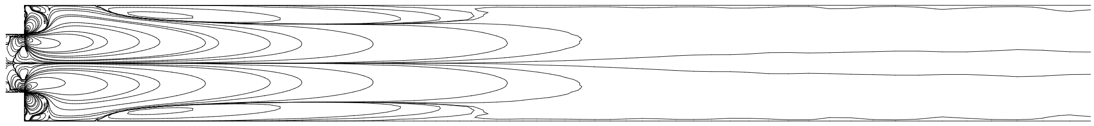

(b) momentum flux in the y direction

Figure 6.1: Contours showing the symmetric patterns of the non-linear dissipation at $Re = 100$.

and y momentum flux show that the asymmetries have occupied large regions of the upstream and downstream channels (Figs. 6.5 and 6.6). Interestingly, for all Reynolds numbers where symmetry-breaking is observed, the extent of the asymmetric dissipation patterns goes beyond the separation regions. Analysis of the averaged part of the flux ($[\mathbf{E}(\mathbf{U}_L) + \mathbf{E}(\mathbf{U}_R)]/2$) found no signs of contribution to the "triggering" effect of symmetry-breaking bifurcation. Hence, the symmetry breaking mechanism in flows computed using high-resolution methods is due to the non-linear dissipation contribution of the wave-speed dependent term in computing the convective fluxes.

The physical mechanism of the symmetry-breaking as captured by the simulations is not a surprise. As pointed out in Margolin and Rider [107] the success of non-oscillatory methods is a reflection of their more accurate approximation of the governing equations for the motion of a finite volume of fluid and the associated entropy production. The physically correct behaviour of the schemes dissipation is strongly related to the inherent properties of non-oscillatory finite volume methods, often referred to as high-resolution methods. Note that these properties have also led to the increasing interest in the implicit large eddy simulations of complex flows using high-resolution methods (Grinstein and DeVore [70]; Fureby and Grinstein [62]; Margolin and Rider [107]; Youngs [192]; Drikakis [48]). To understand the physical relevance of the non-linear dissipation that correctly leads to symmetry-breaking in the simulations, we need to bear in mind that all the numerical methods encompass dissipation which acts to regularise the flow, thereby allowing flow features to be captured physically realistically even if the flow is not fully resolved on the computational mesh. The development of numerical schemes is carried out with two competing criteria in mind: a desire for high accuracy coupled with protections against catastrophic failure due to nonlinear wave steepening or unresolved features. Nonlinear mechanisms in high-resolution methods guard the methods from such catastrophic failures by triggering entropy producing mechanisms that safeguard the calculation when the need arises. The key question is to what extent numerical dissipation accounts for transitional (and turbulent) flow effects.

6.4 Summary

The above simulations show the physical relevance of the non-linear dissipation provided by high-resolution methods with respect to the symmetry-breaking in suddenly-expanded flows. In particular, the asymmetric dissipation arising downstream of the separation regions is responsible for triggering the symmetry-breaking in the flow. This effect is convected both upstream and downstream as the Reynolds number increases. It also seems that the non-linear dissipation has a significant effect on flow separation. In a laboratory experimental set-up the flow asymmetries may be triggered by geometrical imperfections, asymmetries in the upstream flow profile and small perturbations that exist throughout system. The present results suggest that this mechanism is also provided in the simulations as a result of a delicate balance of truncation 'errors' due to wave-speed-dependent terms (chiefly responsible for numerical dissipation) of non-oscillatory finite volume methods. Therefore, these terms are not numerical error, but legitimately describe the physics.

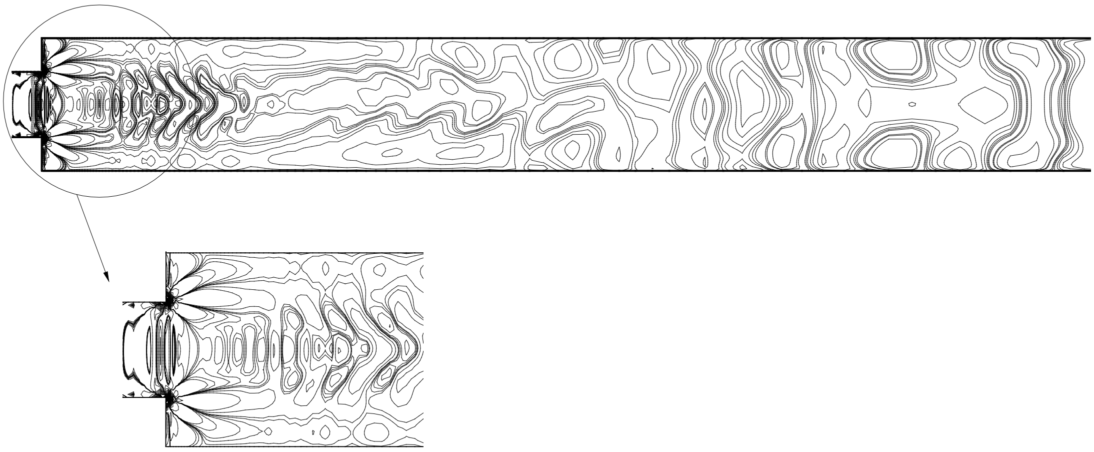

(a) momentum flux in the x direction

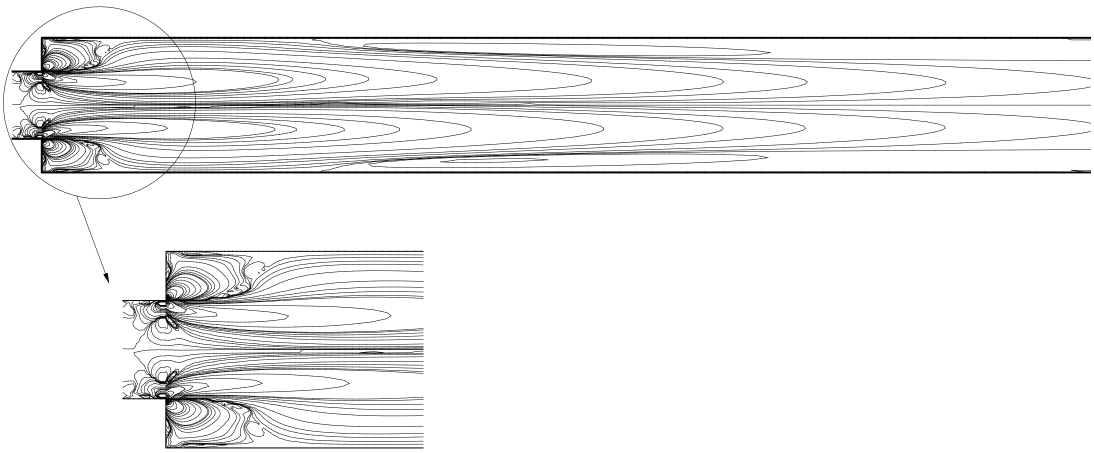

(b) momentum flux in the y direction

Figure 6.2: Contours showing the convection of the non-linear dissipation at the critical Reynolds number, $Re = 216$.

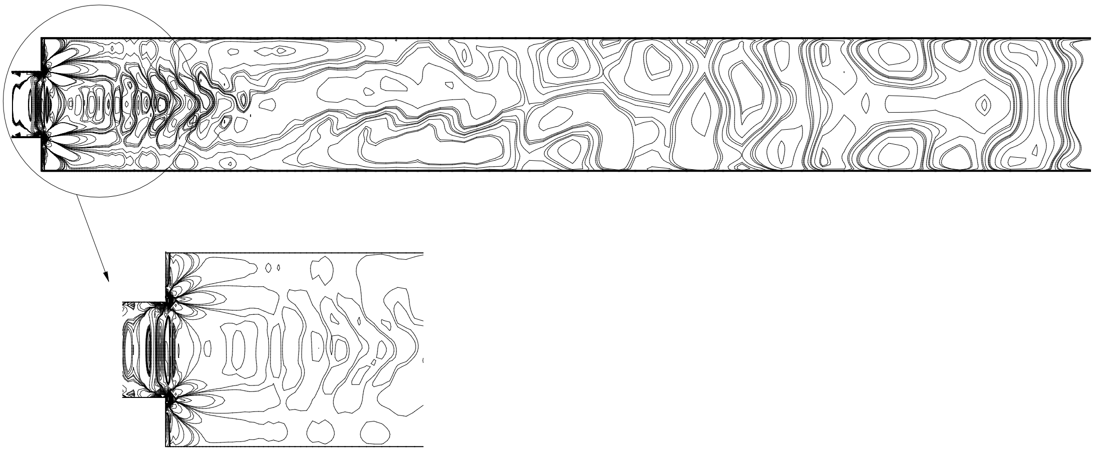

(a) momentum flux in the x direction

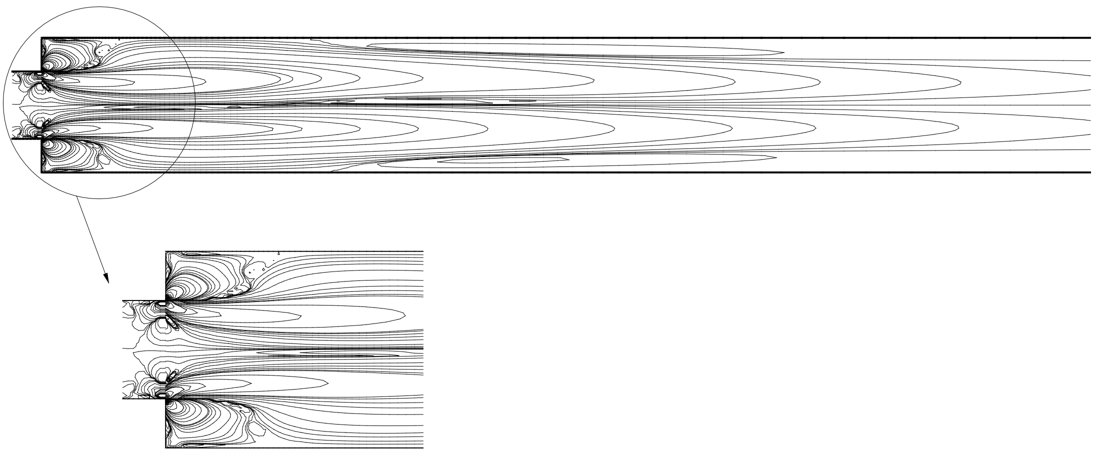

(b) momentum flux in the y direction

Figure 6.3: Contours showing the convection of the non-linear dissipation at a Reynolds number of, Re = 220.

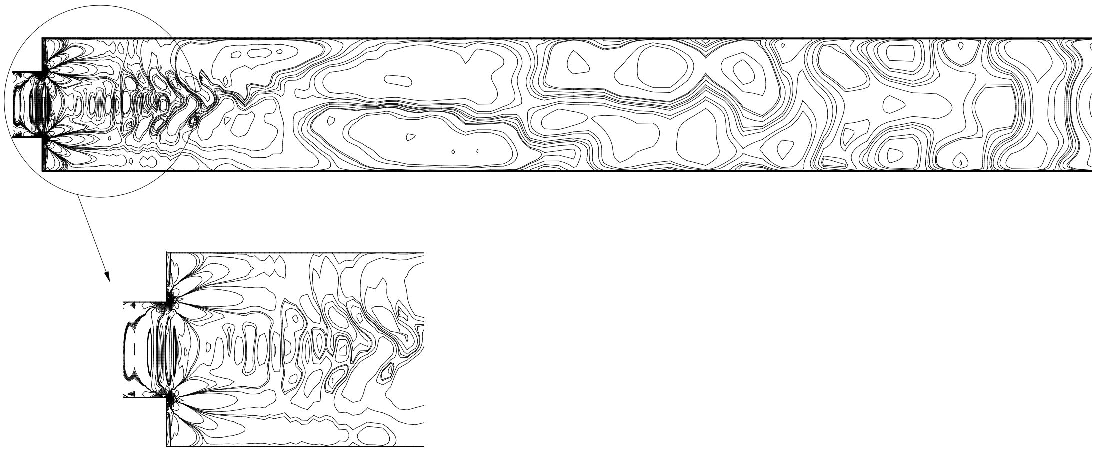

(a) momentum flux in the x direction

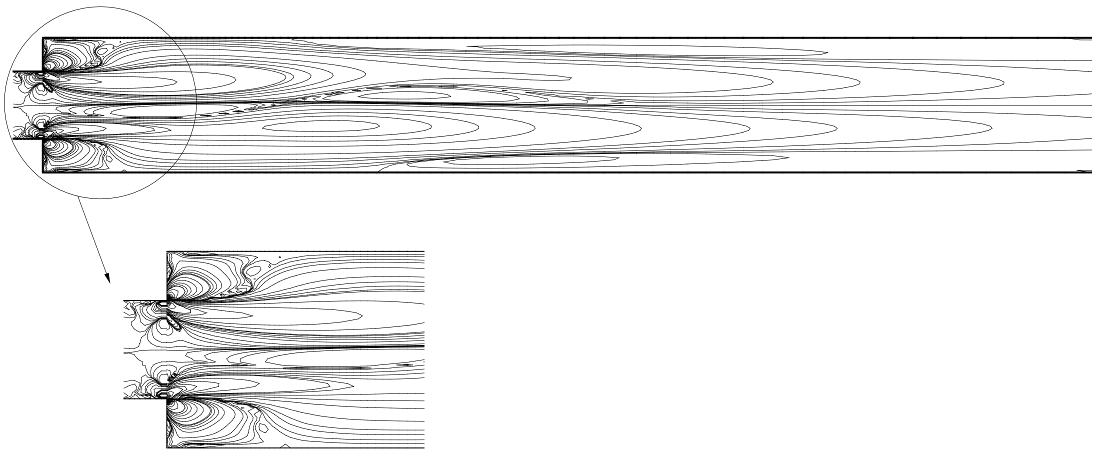

(b) momentum flux in the y direction

Figure 6.4: Contours showing the convection of the non-linear dissipation at a Reynolds number of, Re = 230.

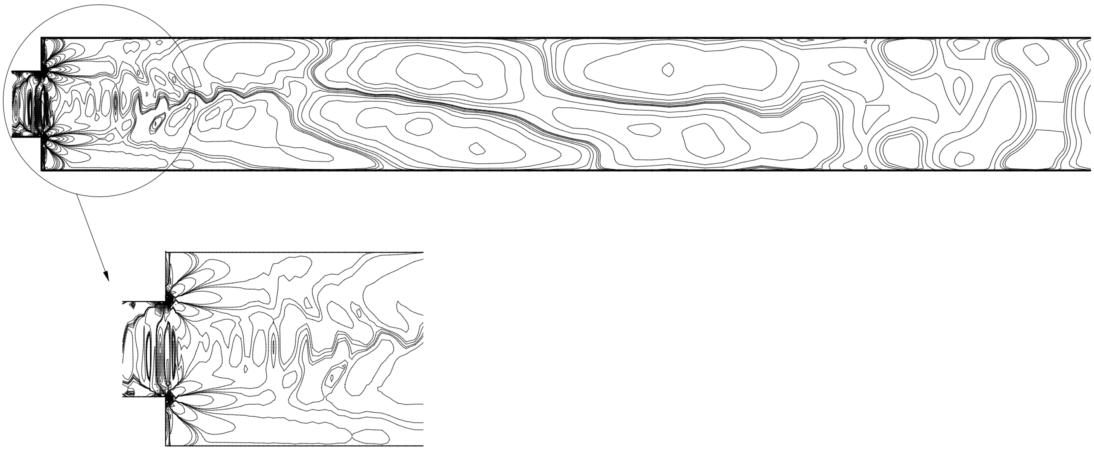

(a) momentum flux in the x direction

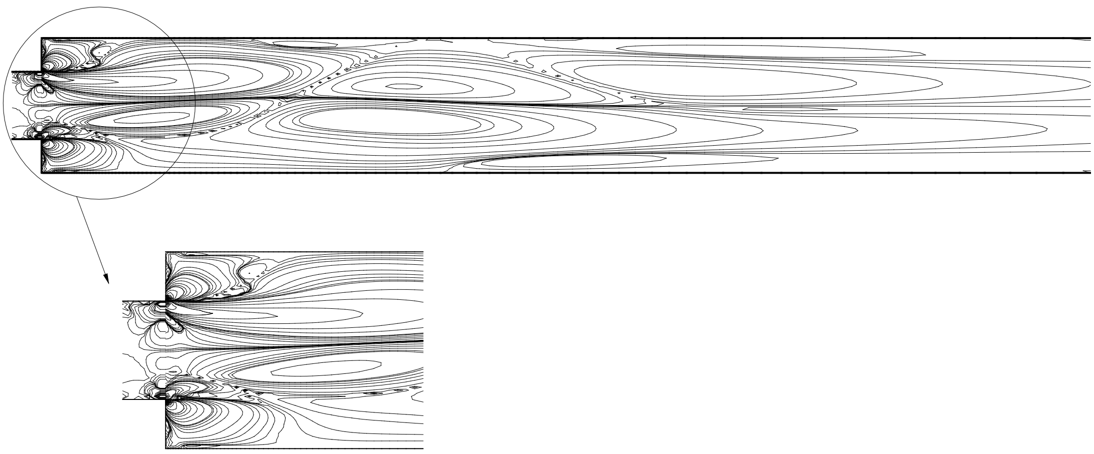

(b) momentum flux in the y direction

Figure 6.5: Contours showing the convection of the non-linear dissipation at a Reynolds numbers of $Re = 250$ exhibiting symmetry-breaking bifurcation of the dissipation both upstream and downstream of the expansion.

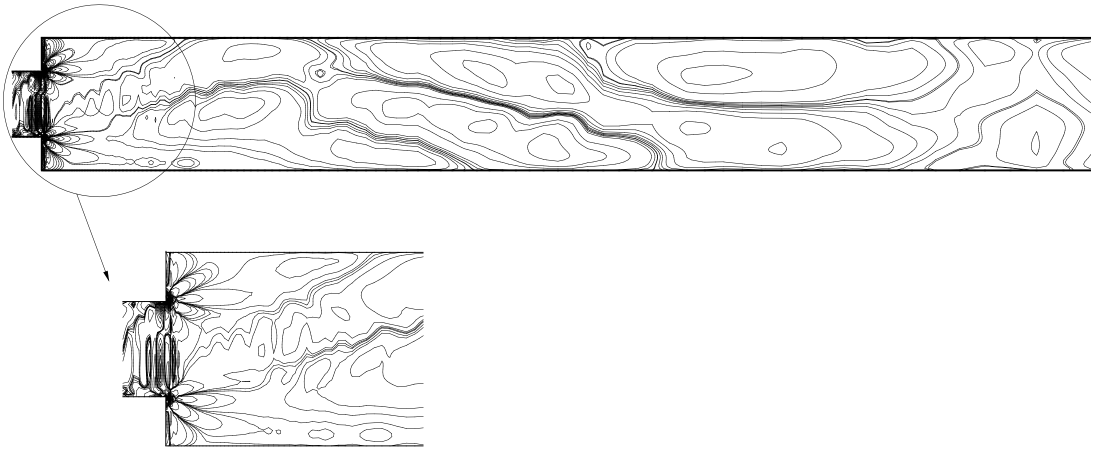

(a) momentum flux in the x direction

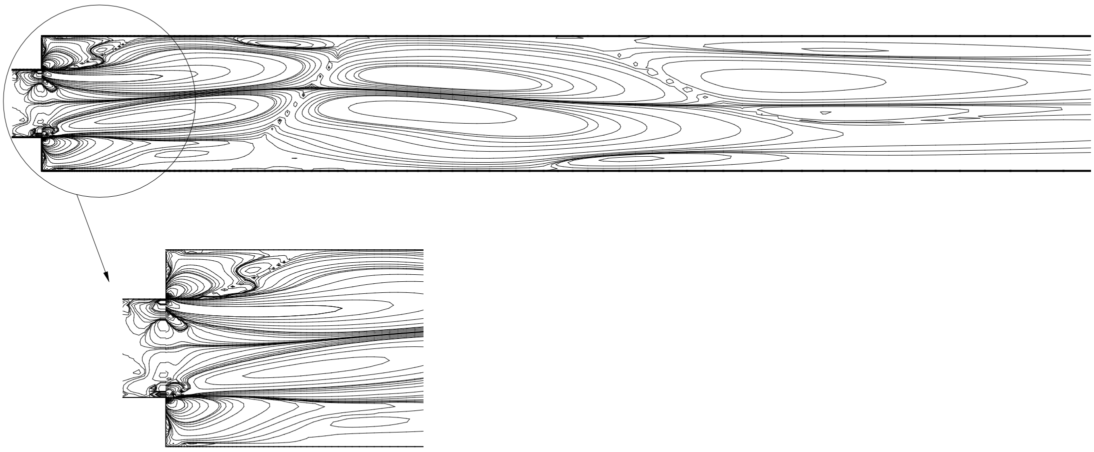

(b) momentum flux in the y direction

Figure 6.6: Contours showing the convection of the non-linear dissipation at a Reynolds numbers of $Re = 300$ exhibiting symmetry-breaking bifurcation of the dissipation both upstream and downstream of the expansion.

CHAPTER 7

Slope Limiting Schemes for the Simulation of Synthetic Jets

A computational investigation concerning the study of various slope limiters in the context of a synthetic jet issuing into quiescent air has been carried out. The results obtained from this study have been compared to experimental data from NASA Langley, who had previously organised a workshop on CFD validation of synthetic jet and turbulent separation control.

7.1 Introduction

The term “Synthetic Jet” refers to a flow created with no net mass flux and are hence sometimes referred to as “zero-net-mass-flux” jets. They are generally generated using a device where flow is alternately pushed in and out of an orifice. The distinction between this and a classical streaming flow is that the mean motions are of the same order as the oscillation amplitude, while for streaming flows, the mean motion is 2nd order. The exiting fluid separates and rolls into a vortex ring (or vortex pair for 2-D geometries) and propagates away from the exit plane due to its self induced velocity. Figure 7.1 shows a schematic of a synthetic jet generated from an oscillating diaphragm. A slug of fluid is discharged through the orifice which separates at the orifice edges forming a vortex sheet. This sheet rolls up into an isolated vortex which is advected downstream under its own self-induced velocity. The flow produced from the synthetic jet can significantly vary depending on the geometry and design of the actuator device driving the jet.

Synthetic jet flows can be similar to pulsed jets in that they are both produced by the advection and interaction of trains of vortices. However, synthetic jets have a unique property in that they are zero-mass-flux in nature; i.e., they are synthesised from the working fluid of the flow system in which they are deployed. Thus, in contrast to conventional continuous or pulsed jets, synthetic jets transfer linear momentum to the flow without net mass injection across the flow boundary. The zero-net-mass nature of a synthetic jet makes them attractive for flow-control applications. They are able to provide momentum flux, alter pressure distribution, and to introduce arbitrary scales

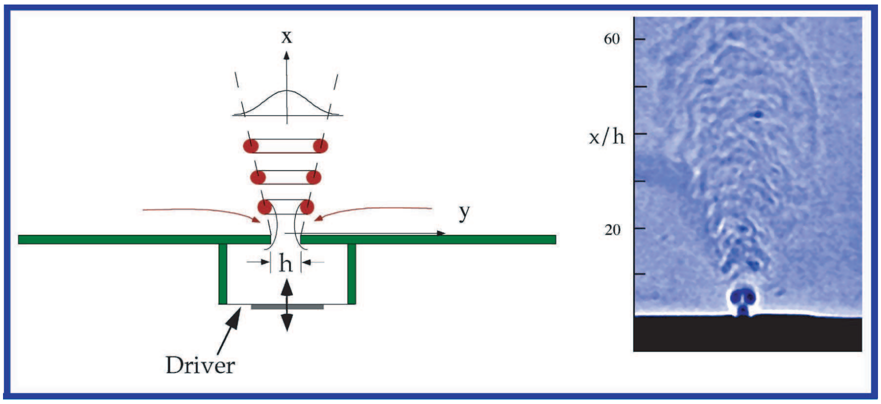

Figure 7.1: Schematic of a synthetic jet, reproduced from Smith and Glezer [160].

to another flow. For the 2-D case in the far field, the synthetic jet is similar to conventional jets in that cross-stream distributions of the time-averaged velocity and the corresponding rms fluctuations appear to collapse when plotted in the usual similarity coordinates (Smith and Glezer [160]). However compared to conventional 2-D jets, the streamwise decrease of the mean centerline velocity of the synthetic jet is a somewhat higher, and the streamwise increase of its width and volume flow rate is lower. This departure from conventional self similarity is associated with the streamwise decrease in the jet's momentum flux as a result of an adverse streamwise pressure gradient near its orifice. The self induced velocity which drives the vortex rings in the streamwise direction comes from the fact that a counter rotating pair of vortices exist within the vortex ring itself. The left vortex pushes the right one forward and the right one returns the favour, hence inducing a self imparted velocity.

Applications of synthetic jets can range from thrust vectoring of jet engines to active control of separation and turbulence in boundary layers. The interaction of synthetic jets with an external cross flow over the surface in which they are mounted can displace the local streamlines and induce an apparent or virtual change in the shape of the surface and thereby effecting flow changes on scales that are one to two orders of magnitude larger than the characteristic scale of the jets (Smith and Glezer [160]).

A vast interest in the use of synthetic jets as a device for flow control has been established in both the experimental and computational fluid dynamics community. An exhaustive description of the current literature concerning synthetic jets will not be presented in this thesis as the subject is so vast. However, several key experimental and computational papers will be discussed. A comprehensive review of synthetic jets was written by Glezer and Amitay [65] in which both synthetic jets in quiescent conditions and the interaction with a cross-flow are discussed. Plane and round synthetic jets formed by time-periodic changes of the working fluid flowing through an orifice have been investigated both experimentally (Smith and Glezer [161, 160]; Smith et al. [163]; Mallinson et al. [105]; Crook and Wood [39]; Rediniotis et al. [135]; Chen et al. [30]; Cater and Soria [27]; Cannelle and Amitay [25]; Amitay and Cannelle [3]) and numerically (Kral et al. [88]; Rizzetta et al. [140]; Guo and Kral [71]; Muller et al.

[120]; Cui and Argarwal [41]; Utturkar et al. [180]; Kotapati and Mittal [87]).

Investigations by Smith and Glezer [161, 160] have shown that close to the jet exit plane the synthetic jet flow is dominated by time-periodic formation, advection and interactions of discrete vortical structures, which will ultimately become turbulent, slow down and lose their coherence. The suction phase causes the time-averaged static pressure close to the exit plane to be lower than the ambient pressure hence both the streamwise and cross-stream velocity components reverse their direction during the suction cycle.

The majority of the investigations concerning the physics of synthetic jets have focused on two-dimensional flow and have neglected to address the formation of three-dimensional structures that may exist in the flow field. These three-dimensional structures are important to the flow and may have a direct influence on entrainment, mixing, turbulence production and noise generation. It is therefore essential that these flows are studied in a three-dimensional context in order to further the understanding of synthetic jet flow. Amitay and Cannelle [3] carried out an experimental investigation into the effect of the orifice aspect ratio on the development of the synthetic jet, and the spatial evolution of secondary three-dimensional vortical structures in the flow field. They found that the flow close to the orifice exit is two-dimensional, however at positions further downstream the vortex pair lines develop secondary counter-rotating structures. Amitay and Cannelle [3] also found that the effect of aspect ratio increases as aspect ratio decreases. Hence the secondary structures in the flow are more pronounced for low aspect ratio geometry orifices.

The flow within the actuator cavity has been numerically investigated by Rizzetta et al. [140]. They solved the compressible Navier-Stokes equations for both the flow within the cavity and for the jet formation above the orifice. The motion of the actuator was modelled via a moving wall boundary condition applied to the boundary opposite the orifice exit. Rizzetta et al. [140] conducted two-dimensional simulations for either a fixed Reynolds number or a fixed cavity height. They found that on the suction stroke, a pair of counter rotating vortices were formed from the inner edges of the orifice. These vortex pairs impinge onto the opposite wall and dissipate towards the centre of the cavity before the consequent ejection cycle begins. As cavity height is decreased, the strength of the vortex pairs produced on both sides of the orifice increases at a given Reynolds number. This has been confirmed by Lee and Goldstein [94].

The interaction of synthetic jets with an external cross flow has attracted a wide range of interest. This interaction can displace the local streamlines and induce an apparent change in the shape of the surface and is hence considered an interesting concept for flow control applications. The idea of flow control by changing the the apparent shape to the aerosurfaces in order to prescribe the streamwise pressure distribution, is not new and investigations have been carried out since the 1940s and 1950s, Perkins and Hazen [128]. The main attraction of synthetic jets are that they can be coupled with actuators which can easily be integrated into the flow surface without the need of complex piping and fluidic packaging. This feature makes them very attractive as fluidic actuators for flow control for both internal and external flows. The apparent surface modification is achieved by operating the synthetic jet actuator on timescales which are smaller than the characteristic timescale of the base flow. Significant global changes on scales that are one or two orders of magnitude greater than the characteristic length scale of the jets themselves can be obtained by using the unsteady effects of the actuation and coupling these to the inherent instabilities of the base flow. Flow control using synthetic jets using vectoring of conventional jets in the absence of extended control surfaces was demonstrated by Smith and Glezer [162, 161] and in more detail by Smith et al. [163]. Since then this approach has been adopted in a number of other applications, including the modification of the aerodynamic characteristics of bluff bodies (Amitay et al. [4]), control of lift and drag on airfoils, (Kral et al. [88]; Smith and Glezer [160]; Amitay et al. [5, 7]; Seifert and Pack [154]), reduction of skin friction of a flat-plate boundary layer, (Lorkowski et al. [99]), mixing in circular jets, (Davis and Glezer [42]), and control of internal flow separation (Amitay et al. [6]).

7.2 Problem Description

Gatski and Rumsey [64] organised a workshop concerning CFD validation of synthetic jets and turbulent separation control. This workshop was held in order to assess the current CFD capabilities in predicting unsteady flows for flow control. Three cases were proposed for the workshop: (1) a synthetic jet issuing into quiescent air, (2) a synthetic jet in a cross-flow and (3) the control of separated flow over a wall-mounted hump model by means of both steady suction and synthetic jets. A summary of the validation workshop was written by Rumsey et al. [146] containing brief descriptions and results obtained for the three different cases. This Chapter of the thesis concerns the investigation of high-resolution methods for the problem of a synthetic jet issuing into quiescent air (case 1). A brief description of the experimental setup as well as a summary of the workshop results is presented in Appendix A.

7.3 Results

The investigation proceeded in two stages; Firstly the synthetic jet was modelled in 3-dimensions without the cavity section followed by modelling the cavity section in quasi 3-dimensional simulations prescribing periodic boundary conditions in the long-axis of the slot, in correspondence with the study by Kotapati and Mittal [87]. A compressible solver was chosen due to the fact that the Mach number at the slot exit is approximately 0.1. The numerical methods associated with the compressible flow equations are described in Chapter 2. Various limiting approaches have been considered in the context of high-resolution methods. Limiters are the general nonlinear mechanism that distinguishes modern methods from classical linear schemes. Their role is to act as a nonlinear switch between more than one underlying linear method thus adapting the choice of numerical method based upon the behaviour of the local solution. Limiters result in nonlinear methods even for linear equations in order to achieve second-order accuracy simultaneously with monotonicity. Limiters can act like dynamic, self-adjusting models, modifying the numerical viscosity to produce a nonlinear eddy viscosity (Drikakis [48]; Margolin and Rider [107]). The high-resolution scheme employed here is the Godunov-type, characteristics-based scheme by Eberle [55]. The scheme has been presented in detail in Chapter 2 section 2.11.5. The cell centred data is interpolated to the cell faces using a MUSCL-type high-order interpolation which incorporates the various slope limiters studied in this Chapter. The limiters investigated in this study are the van Albada (VA), Minbee (MB), Superbee (SB), van Leer (VL) (see Toro [174] for more details) a limiter developed by Drikakis (DD) Zóltak and Drikakis [196] and a 5th order limiter developed by Kim and Kim [84](KK5). Further details of the limiters were outlined in section 2.12.

7.3.1 Simulations Without Cavity Section

A fully three-dimensional domain was created with dimensions conforming to the experimental setup. The slot was located at the centre of the domain and a sinusoidal blowing/suction velocity boundary condition ($U sin(2\pi f t)$) was prescribed to the slot exit due to the absence of the cavity section. The Reynolds number based on the slot width and average velocity over the discharge phase of a cycle was 1150. The forcing frequency (f) that the diaphragm oscillates at was 444.7 Hz taken from the experimental data. No-slip boundary conditions were applied to the sides of the enclosed domain and an outflow boundary condition applied to the upper surface opposite to the slot exit. The flow was allowed to develop over several cycles in order to obtain a fully developed flow. Once this was achieved the results were post-processed to calculate both phase- and time-averaged velocity profiles in order to compare with the experimental data. Figure 7.2 shows the grid used for the simulations. It should be noted that the coordinates x, y and z are in the streamwise, cross-streamwise and spanwise directions respectively. In order to capture the vortices that form at the slot exit, sufficient clustering of the grid cells in both the streamwise and cross-streamwise directions was provided. The grid resolution was approximately 3.2 millon grid points. The domain was split into 9 or 27 blocks to enable the code to be used in parallel on the high performance computer (hpc). Approximately 15800 time-steps were needed for one complete ejection/suction cycle and typically each case was run for 5-7 cycles in order to obtain phase-averaged results over a sufficient number of cycles.

Figures 7.3-7.5 show a comparison between computed streamwise velocity contours and experimental PIV contours of the flow at various phase angles in the blowing/suction cycle. Comparing the computational and experimental results it can be seen that the flow structures are captured well by the computations. The vortices are shown to travel under there own self induced velocity in the streamwise direction during the expulsion phase (phase angles 0° to 180°, Figs. 7.3(a)-7.4(c)) . The experimental data shows that the vortices formed either side of the slot exit travel faster downstream than in the computational results during the expulsion phase. This behaviour is also present in the

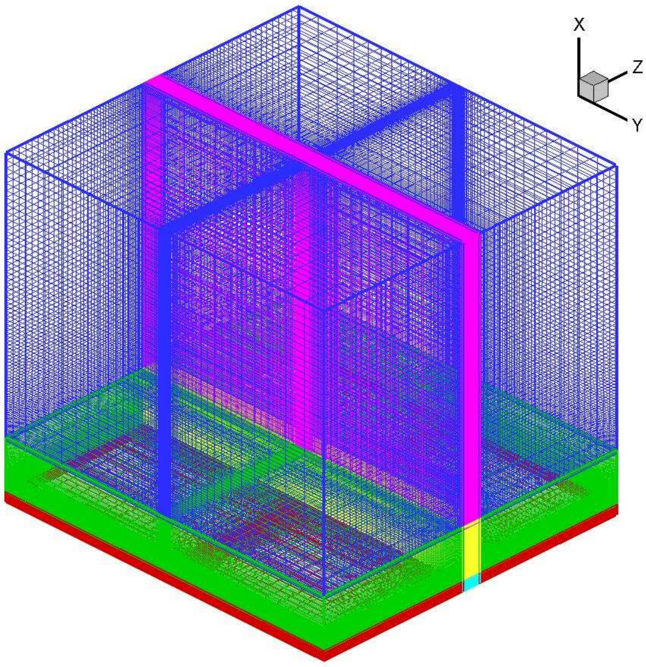

Figure 7.2: Computational mesh used in the simulation.

suction phase with the fluid being drawn back in faster during the experiments than in the computations (phase angles 225° to 315°, Figs. 7.4(e)-7.5(c)).

Comparing the workshop results of phase-averaged contours at 90°, (Figs. A.7-A.8) to those obtained in this study, it can be seen that none of the results actually manage to capture the vortex core in the same position as the experimental PIV data. Furthermore the results obtained from Washington University shown in Figs. A.7(e) and A.7(f) show an asymmetry in the flow with respect to the slot centre line. This asymmetry is not present in the current study or in the PIV data plots. A much stronger asymmetry in the flow is also predicted by the results submitted by NC A&T State U. shown in Fig. A.8(b). A reasoning as to why this asymmetry occurred could be due to effects from the domain boundaries interfering with the computed flow or due to specifics of the numerical setup. Cui and Agarwal [40] and Yamaleev and Carpenter [189] do not discuss why this asymmetry occurs in the flow and hence one can only guess as to why it occurs. Suction phase contour comparisons at a phase angle of 225° show a good likeness to the experimental PIV data. Results from the workshop at the same phase angle show some unusual behaviour (Figs. A.9 and A.10). Contour plots from George Washington University (Figs. A.9(c) and A.9(d)) show an incorrect flow pattern in comparison to that obtained by the PIV data. This discrepancy can be attributed to a Reynolds number which doesn't correspond to the experimental Reynolds number. As mentioned before Kotapati and Mittal [87] based their flow Reynolds number on the lower bound of the averaged expulsion velocity, hence the vortices generated move through the domain much slower than in the experimental data. The asymmetry in the flow is again predicted by the results of Washington University and NC A&T State U.

Some discrepancies between the present results and the experimental data can be partly explained by considering the phase averaged streamwise velocity profile at a position of 0.1mm above the slot exit, shown in Fig. 7.6. The figure shows velocity profiles of the experimental data from the three different measurement techniques as well as results obtained with the various slope limiters discussed at the beginning of this section. It can obviously be seen that the data obtained by three experimental measurement techniques disagree with each other, both with regards to velocity profile and relative velocity magnitude. Also, the profile obtained from the experiments are far from a perfect sine wave, whereas the computed profile is almost a perfect sine wave. This irregular velocity profile is obtained in the experiments due to the fluid having to travel through the complex cavity section which was not modelled in these computations. The computed results compare well with the PIV data with regards to both profile shape and velocity magnitude during the expulsion phase. All three experimental techniques show that the maximum velocity is obtained earlier in the ejection cycle in comparison to the computational results. This results in a type of ‘phase-lag’ between the experimental data and the computed results. This phase-lag accounts for the fact that the experimental vortices appear to move faster downstream than the computed vortices. The absolute value of maximum velocity obtained during the suction phase is much higher than that obtained in the ejection phase as shown by the experimental PIV and LDV profiles. The Hot-wire data does however show a much higher maximum velocity in comparison to the two other experimental techniques. As the inlet boundary condition in the computational setup was a perfect sine wave prescribed to the slot exit, the profile would not be expected to change much at a position of 0.1mm downstream. This is proven to be true as the suction phase shows a absolute maximum velocity comparable to that predicted by the ejection phase. Clearly one would need to adapt the inlet boundary condition if the flow close to the slot exit is to be modelled correctly. The various limiters, as expected, showed very little deviation from one another at a position so close to the slot exit. Velocity profiles from the workshop at the same position above the slot exit (Fig. A.2) show that it was difficult to match the maximum and minimum velocity magnitudes as well as phase angles to the experimental data. Large discrepancies can be seen with regards to the suction phase mainly due to whether or not the cavity section was modelled.

Further comparisons at various distances above the slot exit can be seen in Figs. 7.7 and 7.8. At 1mm above the orifice exit the various limiters show little difference and compare well with the PIV data on the expulsion phase capturing the peak velocity. The presence of the phase-lag between the computed results and the experimental data is still present, with the experimental data showing a peak velocity earlier in the expulsion cycle than in the simulations. The suction phase over predicts the minimum velocity in comparison to the PIV data but compares well with the hot wire data. As distance increases away from the slot exit the discrepancies between the various limiters used in the calculations become more apparent. The main differences between the various limiters lie in there predictions of the maximum and minimum velocities. Figures 7.8(c) and 7.8(d) also show a phase difference between the various limiters in their prediction of the peak velocity. The computed results also show a large difference in the prediction of the magnitude of peak velocity in comparison to the experimental PIV data but compare much better with the hot-wire data. The various limiters compare well with the experimental PIV data during the suction phase, with the DD limiter and the van Albada giving the best results.

Phase averaged results of the cross-stream distributions of u- and v-velocity profiles along the horizontal line 2mm, 4mm and 6mm above the orifice exit at phase angles of 90° and 270° are shown in Figs. 7.9 and 7.10 respectively. At a position of 2mm above the slot exit the various limiters slightly over predict the peak u-velocity at phase of 90°. It should be noted that the slot width is between -0.5mm and 0.5mm. In contrast the cross stream velocity (v-velocity) is under predicted by all limiters except the superbee limiter which provides a good comparison with the PIV data with regards to profile and velocity magnitude. Workshop results at the same streamwise position above the slot exit can be seen in Fig. A.4. These results show that the peak velocity at the centre of the slot is not captured accurately by most of the numerical methods used. Also, many of the methods used do not manage to predict the velocity profile at the edges of the slot, predicting a much lower velocity in comparison to the PIV data. At a position of 4mm above the slot exit the PIV data shows a much higher peak velocity compared to the present results (Fig. 7.9(c)). This discrepancy is due to the positioning of the counter rotating vortices. It has already been shown by the means of velocity contours that the vortices formed at the edges of the slot travel faster downstream in the PIV data compared to the computed results. At a phase angle of 90° the centre of the vortices is approximately at a position of 3.5mm above the slot exit obtained from the PIV data, whereas the computed results show the centre of the vortices to be approximately 2.8mm above the slot exit. It is this reason that the computed velocity profile at 4mm shows a much lower peak velocity in comparison to the PIV data. The cross-stream velocity profile however show a good comparison across the slot using the DD and Superbee limiters. Away from the slot edge all limiters tend to give a poor representation of the flow, especially the van Albada and Minbee limiters. Workshop results shown in figure A.5 show a similar trend with respect to the streamwise velocity profile. Further away from the slot exit at a position of 6mm the DD and Superbee limiters give a good prediction of the u-velocity magnitude and flow profile. The Minbee and van Albada limiters tend to over-predict the maximum velocity at the centre of the slot. However, the cross-stream velocity is predicted better by the Minbee, Superbee and van Albada limiters with the DD limiter tending to under-predict the velocity magnitude.

At maximum suction (270°) all four limiters give different results (Fig. 7.10) in comparison with the PIV u-velocity data. At a position of 2mm above the slot exit all limiters over predict the minimum u-velocity with van Albada and the DD limiter showing the best results with respect to the velocity profile distribution. The computed v-velocity profile shows a steep gradient across the slot exit whereas the PIV data shows a more smoother transition across the slot. At distances further downstream from the slot exit 4mm and 6mm, the u-velocity is best predicted by the van Albada limiter and DD limiter, respectively. The magnitude of the computed v-velocity out-side the core region of the jet is consistently higher than the experimental measurements which implies that there is greater entrainment in the computed flow field than that of the experiments.

A comparison of phase averaged centerline streamwise velocity at maximum expulsion and suction are shown in Fig. 7.11. Both plots show that the velocity at the slot exit is over predicted by all the different limiters. No limiter manages to capture the position and magnitude of the maximum expulsion velocity. The computed results show that the maximum velocity is reached at a position closer to the slot exit in comparison to the PIV data. This is the reason as to why the counter rotating vortices formed at the slot edges move slower in the downstream direction compared to the PIV data. The maximum velocity is found at a position of approximately 3mm above the slot exit. This position is related to the vortex core of the counter rotating vortices. The van Albada and DD limiters are shown to best predict the velocity at positions further downstream at both phase angles. Workshop results shown in Fig. A.6 show that an accurate prediction of the peak velocity was extremely difficult to obtain with the majority of results showing a peak velocity at a streamwise position much closer to the slot exit than that given by the PIV data.

In order to study the structure of the vortices formed at the slot edges, iso-surfaces of vorticity coloured by streamwise velocity were plotted at various phase angles (Fig. 7.12). It can clearly be seen that a ring type vortex forms as the flow separates at the edges of the slot. This vortex ring then starts to moves away from the slot under it's own self induced velocity. The suction phase allows the ring vortex to fully detach itself from the slot edges to move further away in the downstream direction.

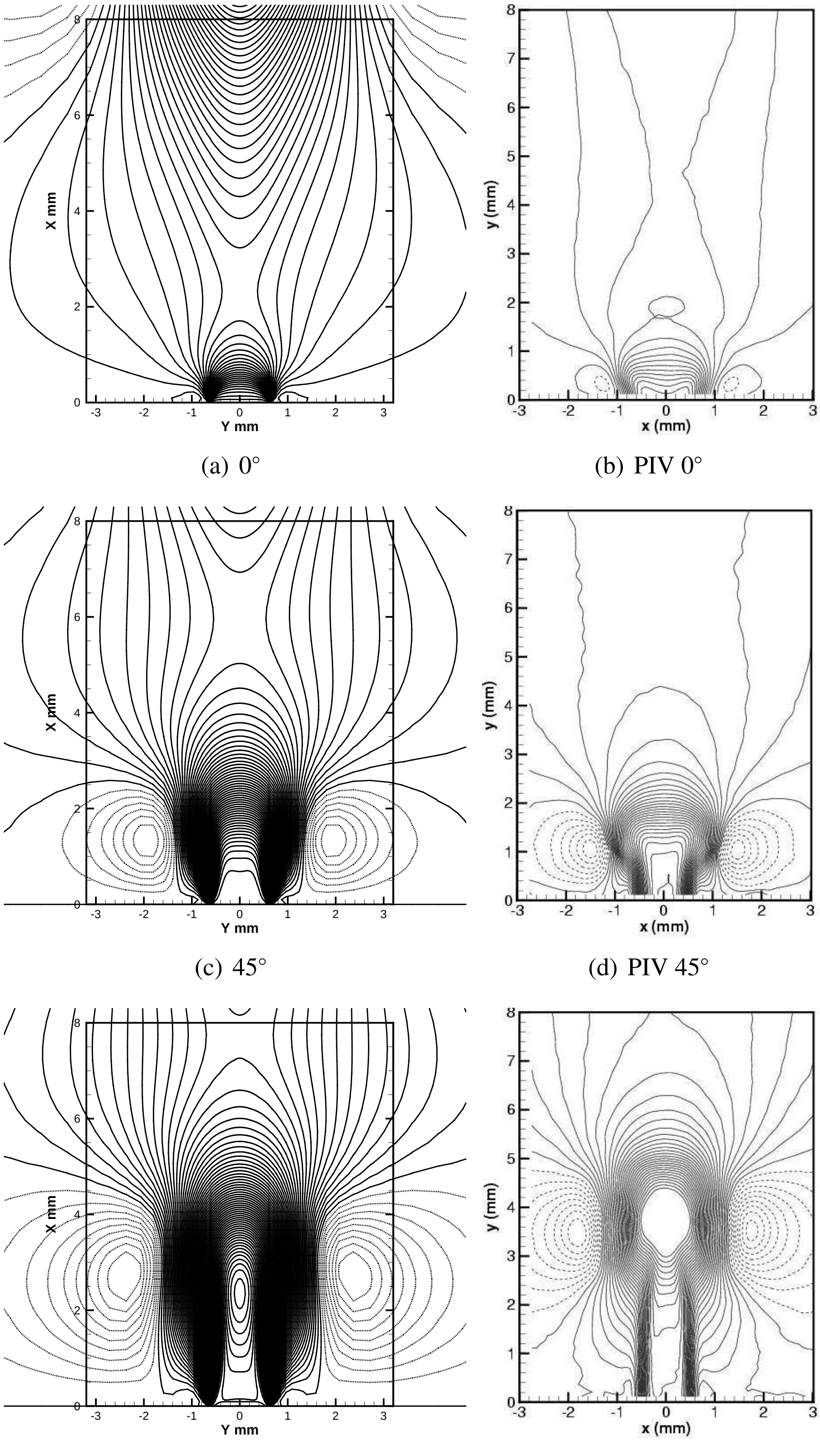

(a) 0° (b) PIV 0°

(c) 45° (d) PIV 45°

(e) 90° (f) PIV 90°

Figure 7.3: Comparison of computed streamwise velocity contours and experimental PIV data at various phase angles.

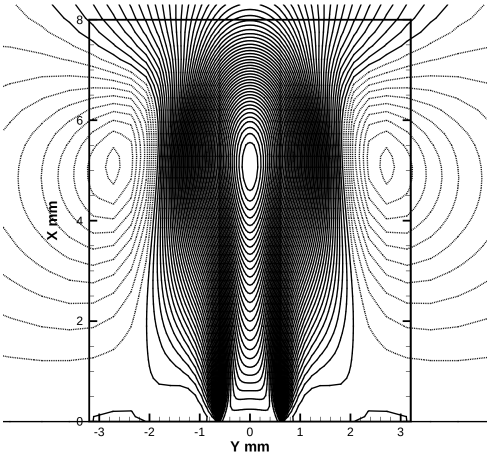

(a) 135°

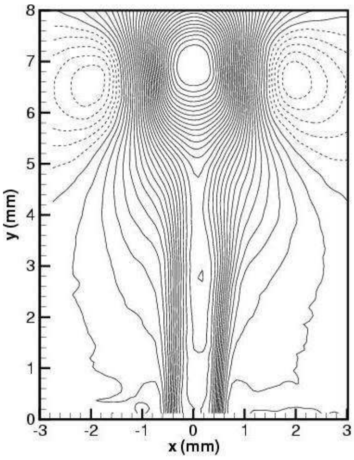

(b) PIV 135°

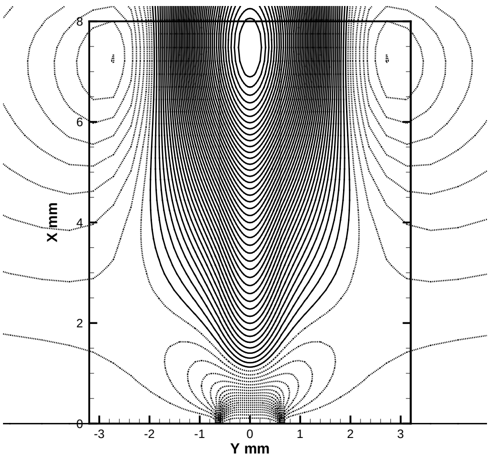

(c) 180°

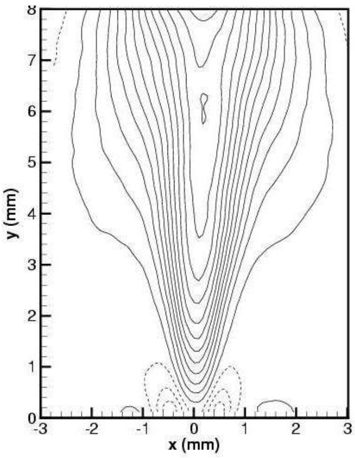

(d) PIV 180°

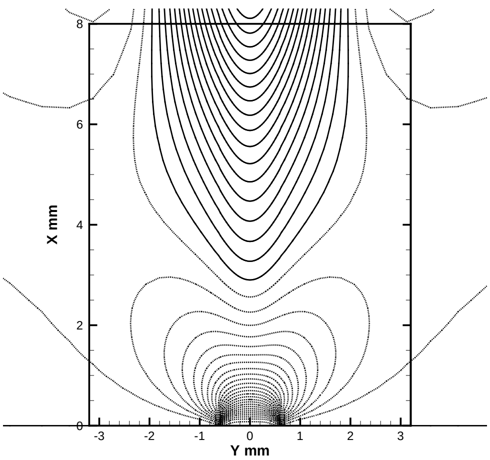

(e) 225°

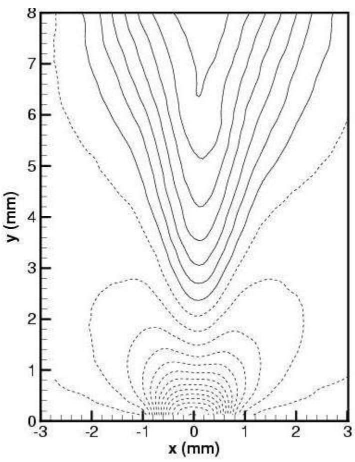

(f) PIV 225°

Figure 7.4: Comparison of computed streamwise velocity contours and experimental PIV data at various phase angles.

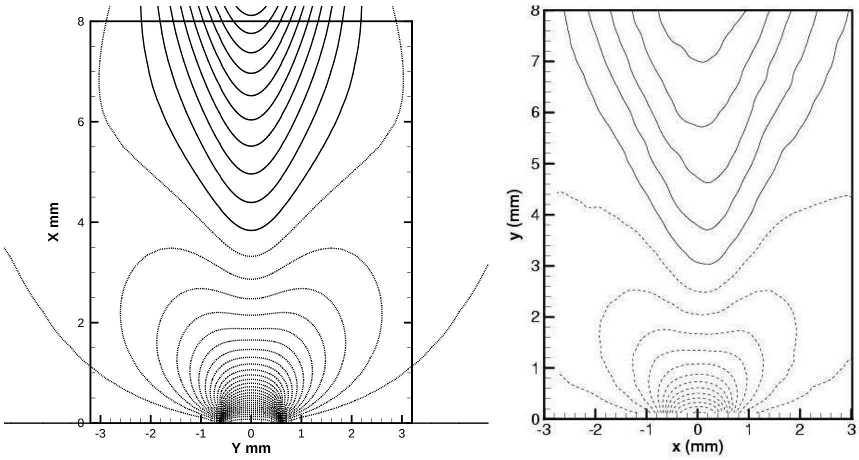

(a) 270° (b) PIV 270°

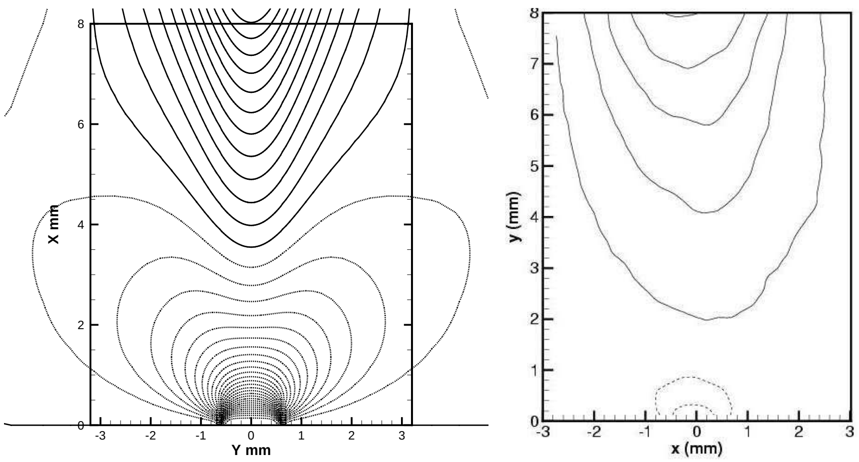

(c) 315° (d) PIV 315°

Figure 7.5: Comparison of computed streamwise velocity contours and experimental PIV data at various phase angles.

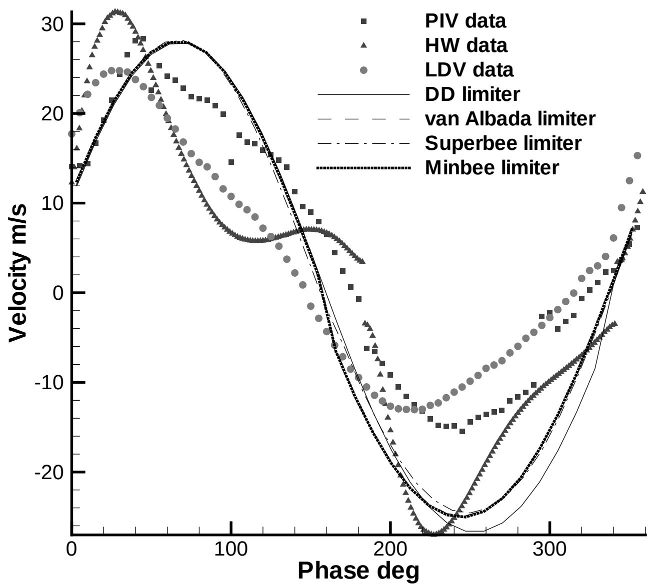

Figure 7.6: Phase-averaged u-velocity at 0.1mm above the centre of the slot exit.

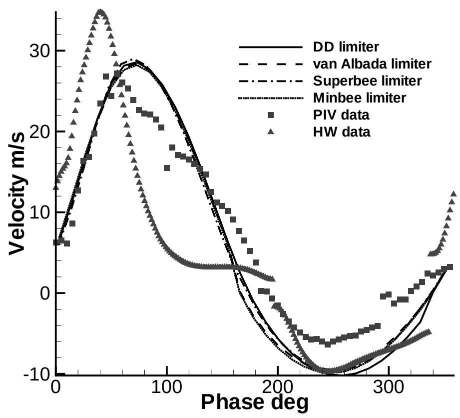

(a) 1 mm

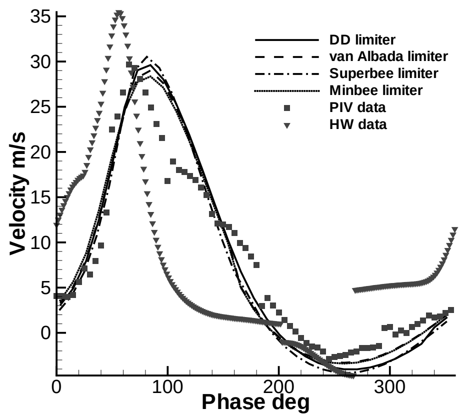

(b) 2 mm

Figure 7.7: Phase-averaged u-velocity at 1mm (a) and 2mm (b) above the centre of the slot exit.

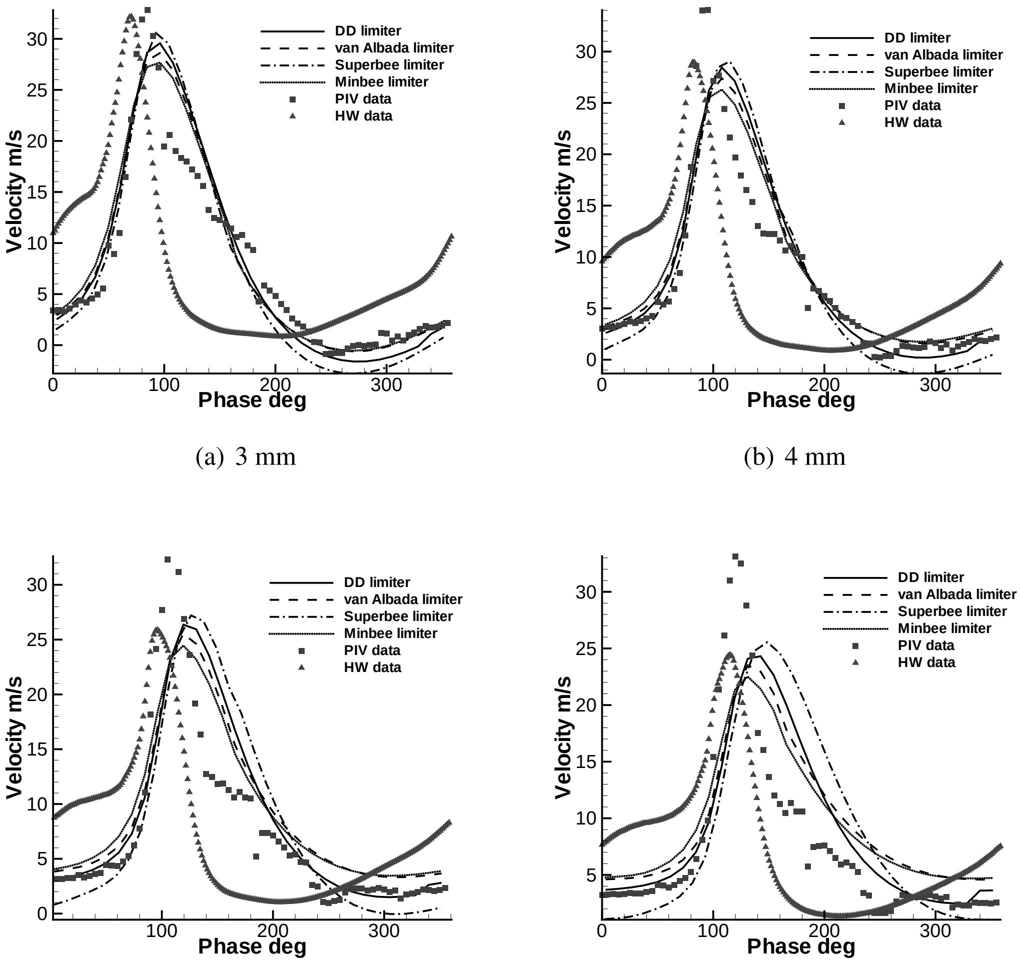

(a) 3 mm

(b) 4 mm

(c) 5 mm

(d) 6 mm

Figure 7.8: Phase-averaged u-velocity at various downstream positions above the centre of the slot exit.

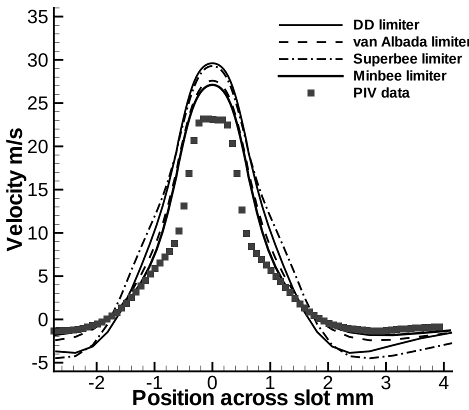

(a) U-velocity 2mm

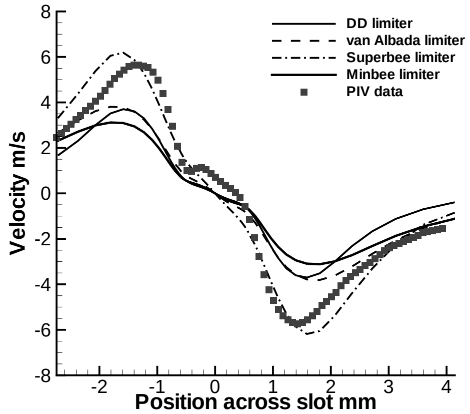

(b) V-velocity 2mm

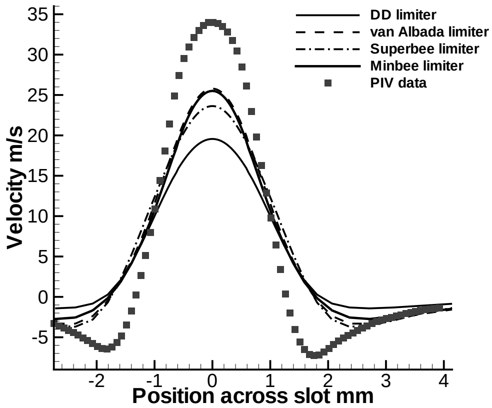

(c) U-velocity 4mm

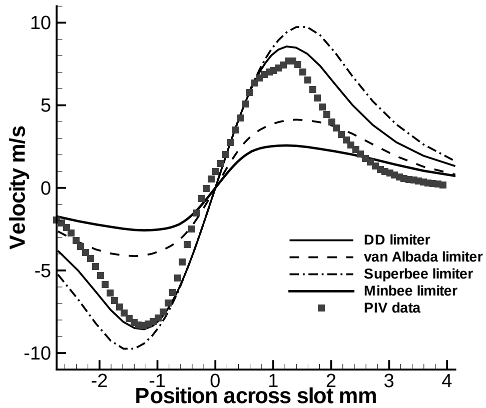

(d) V-velocity 4mm

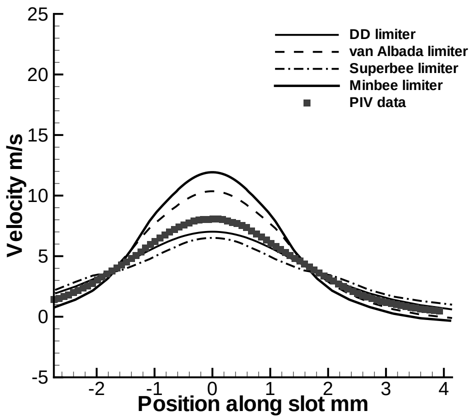

(e) U-velocity 6mm

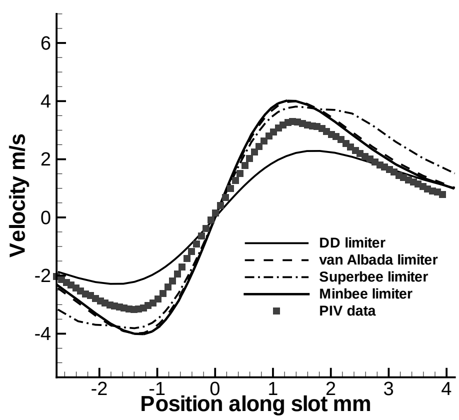

(f) V-velocity 6mm

Figure 7.9: Phase-averaged velocity profiles along various downstream horizontal lines above the jet exit plane at 90°.

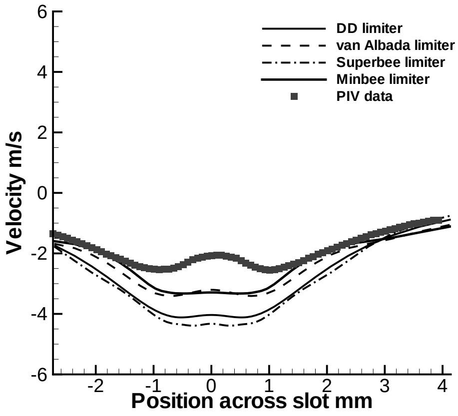

(a) U-velocity 2mm

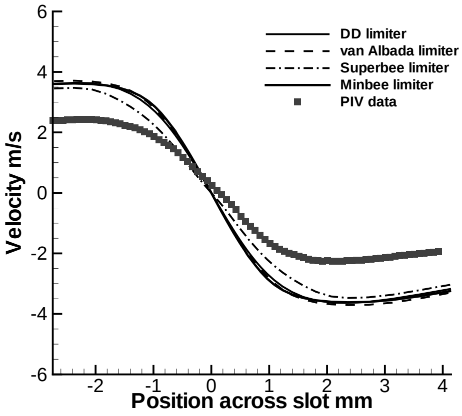

(b) V-velocity 2mm

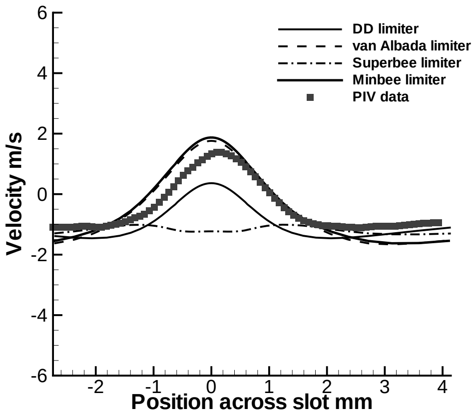

(c) U-velocity 4mm

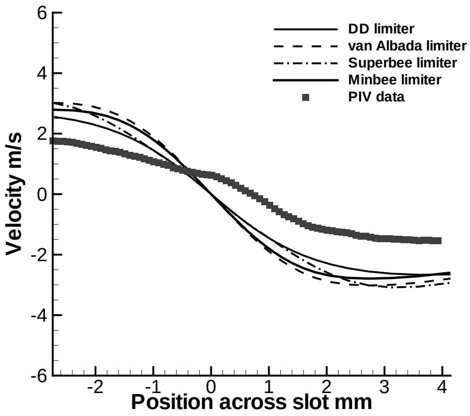

(d) V-velocity 4mm

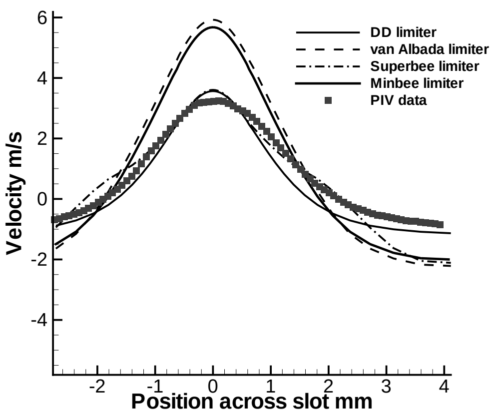

(e) U-velocity 6mm

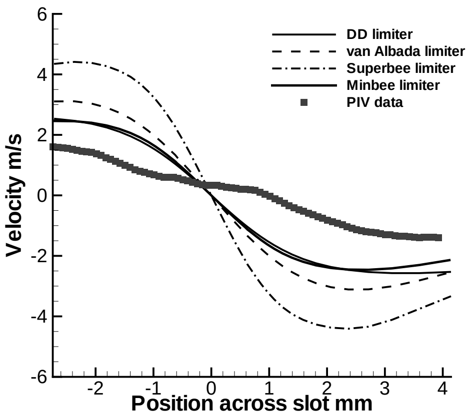

(f) V-velocity 6mm

Figure 7.10: Phase-averaged velocity profiles along various downstream horizontal lines above the jet exit plane at 270°.

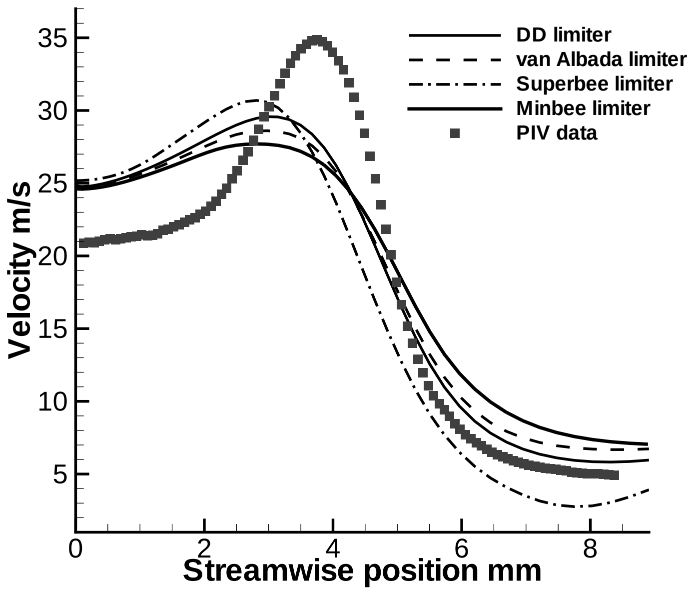

(a) Phase 90°

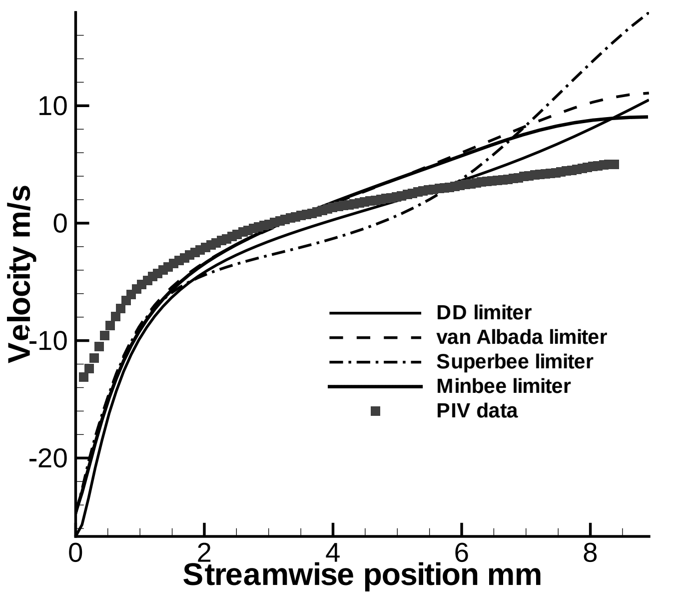

(b) Phase 270°

Figure 7.11: Phase-averaged centerline u-velocity at 90° (a) and 270° (b).

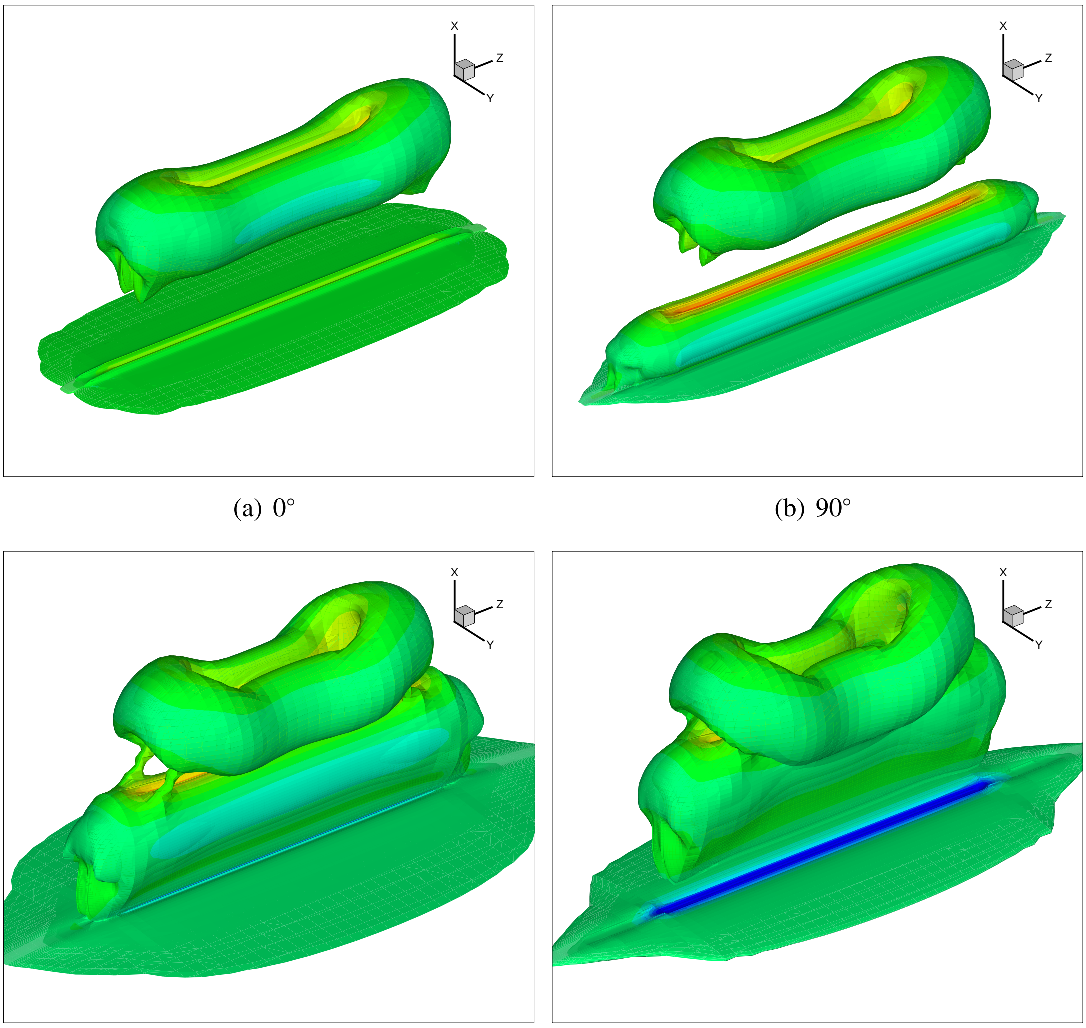

(a) 0°

(b) 90°

(c) 180°

(d) 270°

Figure 7.12: Iso-surfaces of vorticity magnitude coloured by streamwise velocity at various phase angles.

7.3.2 Simulations With Cavity Section

In order to obtain a good representation of the flow close to the slot exit one needs to take into account the cavity section. The following section will show results obtained by including the cavity section. The computational geometry was created in accordance with the investigation of Kotapati and Mittal [87] who simplified the cavity section by approximating the experimental cavity to a rectangular box. The details that make up the interior of the experimental cavity were neglected and the oscillating diaphragm was positioned at the base of the rectangular box. Figure 7.13 shows a schematic of the computational domain used in the simulations. Utturkar et al. [180] showed that large differences in the internal cavity flow, with symmetric forcing, do not translate into similar differences in the external flow. The coordinates x, y and z are in the streamwise, cross-streamwise and spanwise directions respectively. As in the study by Kotapati and Mittal [87] the cavity is defined by the width (W) and the height (H). Kotapati and Mittal [87] tried to match the dimensions of the experimental geometry as closely as possible, however the cavity height and the slot height (h) could not be properly defined as in the experiments due to the variable width of the channel between the cavity and the slot exit defined in the experimental setup. The experiments were carried out using a finite aspect ratio but as found in the previous investigation and from the workshop results, this did not significantly affect the flow in the centre plane of the jet. The experimental aspect ratio of the slot is large and hence one can assume that the flow is nominally two-dimensional except at the spanwise slot edges. Hence the following study made use of periodic boundary conditions in the spanwise direction. Outflow boundary conditions are applied to the upper surface as well as the two side surfaces to allow them to freely respond to the flow created by the jet. The dimensions L_x, L_y and L_z are $60d$, $60d$, $6d$ respectively, where d is the slot width.

The oscillating diaphragm is modelled using the same definition provided by Kotapati and Mittal [87]. They specified a sinusoidal velocity boundary condition $V_0 sin(2\pi f t)$ at the bottom of the cavity. The value of V_0 was determined by matching the Reynolds number in the experiments and the frequency (f) was determined by matching the Stokes number ($St = \sqrt{2\pi f d^2/\nu}$). The Reynolds number in the computations is defined by $Re = \bar{V}_j d/\nu$ where $\bar{V}_j$ is the average velocity over the discharge phase of the cycle, obtained from the experimental data. A Reynolds number of 1150 was used in the present simulations. Two different grid resolutions have been used in the present simulations. Both grids are non-uniform in the streamwise (x) and cross streamwise (y) directions and uniform in the spanwise (z) direction. Figure 7.14 shows the computational mesh for the case of the coarser grid. Sufficient clustering has been provided in the region closest to the slot exit in order to resolve the vortex structures formed at the edges of the slot and also to capture the shear layer in the slot. Coarse and fine grids corresponding to 750,000 grid points and 3 million grid points, respectively, needed approximately 16000 and 36000 time steps per oscillation cycle, respectively. The domain was split into a number of blocks in order to compute the flow on a number of processors. Typically between 4 and 29 processors were used in the parallel computations. The flow was allowed to evolve over a number of cycles in order to calculate phase-averaged and time-averaged data over a sufficient number of cycles. It should be noted that only two limiters were chosen to compute the flow on the fine grid (van Leer and KK5) due to the computational expense.

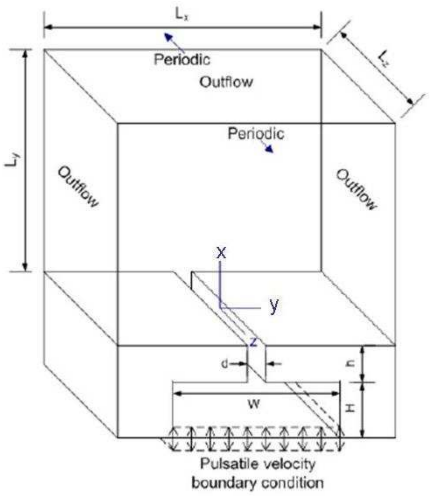

Figure 7.13: Computational domain reproduced from Kotapati and Mittal [87].

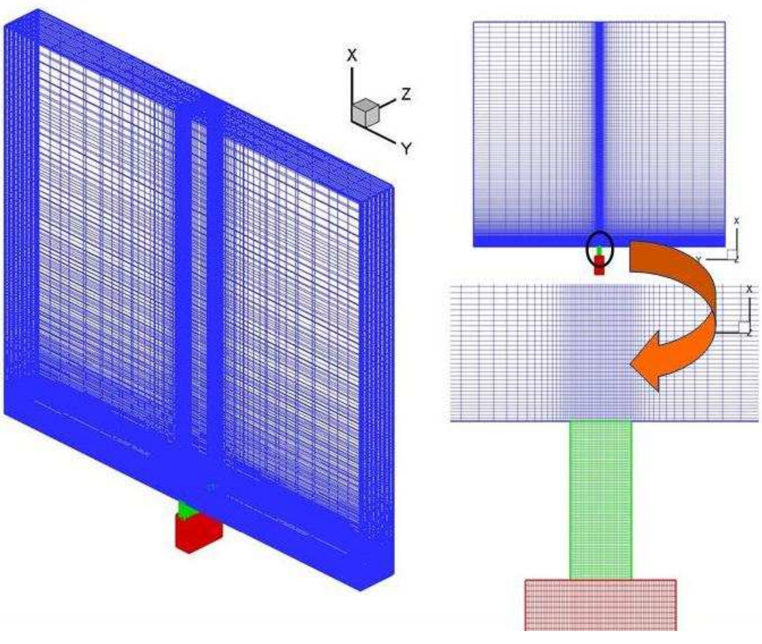

Figure 7.14: Computational mesh including cavity section.

Figure 7.15 shows phase-averaged u-velocity at the centre of the slot at a position of 0.1mm above the slot exit. The figure compares the various limiters used for the two grid resolutions as well as two of the experimental measuring techniques. One immediately sees that the velocity profile is no longer strictly sinusoidal as in the previous section. This is due to the presence of the cavity section. The expulsion peak velocity no longer compares with the suction peak velocity. However, the peak expulsion velocity predicted by all limiters except the van Albada and DD limiters show the velocity is higher than the PIV data and compares close to that predicted by the HW data. From Fig. 7.15 it can be seen that maximum suction is reached at a phase angle of 245°. At this phase angle the Low Mach Van Leer limiter provides the most accurate prediction of the velocity and agrees to within 5% of the PIV data. There appears to be little difference between the two different grid resolutions if one compares the same limiters used on both grids. The discrepancy which was shown in the previous section with regards to a phase 'lag' is already starting to show in the computed results. The PIV data as well as the HW data seem to reach a maximum velocity at an earlier position in the cycle compared to the computed results. The minimum velocity on the suction phase seems to coincide with that shown by the PIV data. It has already been discussed that the computational results presented at the workshop also encountered problems in matching phase with the experimental data. This could be due to processing results over insufficient positions in the cycle or due to the phase definition calculation provided by the workshop organisers.

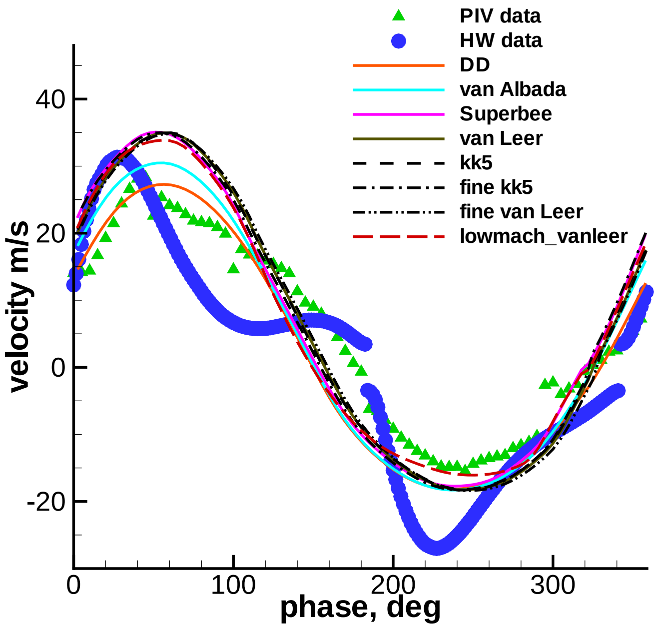

Figure 7.15: Phase-averaged u-velocity at 0.1mm above the centre of the slot exit.

Further comparisons of velocity distribution over a cycle at various position above the the slot exit are shown in Fig. 7.16. At all positions above the slot exit very little difference can be seen with regards to the choice of limiter used with the exception of the van Albada and DD limiters which consistently predict a lower maximum velocity in the expulsion phase. At a position of 1mm above the slot exit the computed results compare well with the HW data with regards to the maximum velocity in the expulsion phase. However, the PIV data shows a lower maximum velocity which compares to within a 3% difference with that predicted by the DD limiter. Moving further away from the slot exit, the trend observed is that the computed results tend to agree more with the PIV data with regards to the predicted value of the peak velocity. A noticeable feature is that the phase lag between the computational results in the previous section and the PIV data changes to a phase lead. The computed results reach a peak velocity at an earlier phase than the PIV data. This is true for all limiters with the exception of the DD limiter which remains roughly in phase with the PIV data at all streamwise positions above the slot. The computed results from the suction phase agree extremely well with the PIV data with all limiters predicting a similar trend at all positions above the slot exit.

Phase averaged results of the cross-stream distributions of u- and v-velocity profiles along various horizontal lines above the orifice exit at phase angles of 90° and 270° are shown in Figs. 7.17-7.18 and 7.19-7.20 respectively. At a position of 1mm above the slot exit at a phase angle of 90° the streamwise velocity over predicts the peak velocity for all limiters except the DD limiter. The jet width is defined by the width of the jet at the average velocity defined by $vavg = (vmax + vmin)/2$. Taking the maximum and minimum velocities predicted by the computations the jet width agrees to within a 6% difference to the PIV data. The various limiters predict the v-velocity at this position above the slot exit to within 5% of the PIV data except in the region towards the centre of the slot, where the PIV data shows a flatter profile in comparison to that predicted by the various limiters. Slightly further away from the slot exit at 2mm, the u-velocity profile tends to agree rather well with the PIV data. Although the computational results show that the peak velocity is slightly over-predicted the PIV data shows a rather flat profile over the slot width with no real peak at the centre line. The v-velocity, however, show large discrepancies between the computed results and the experimental PIV data. The relative peak magnitude either side of the slot edges is much larger than that predicted by the computational results. This anomaly can be attributed to the positioning of the counter rotating vortices formed either side of the slot edges and will be discussed later in this section with the use of contour plots. Further downstream at positions of 3mm and 4mm above the slot exit, the peak velocity is captured best by the van Leer limiter, predicting the peak velocity to within 4% and 7.5% of the PIV data at positions of 3mm and 4mm above the slot exit respectively. It should be noted that the effect of grid resolution did not change the peak velocity obtained, with the fine van Leer case predicting a peak velocity to within 0.2% of that predicted by the coarser van Leer case. The computed results do not however correspond well with the PIV data in the region beyond the slot edges. At both these streamwise positions the computed results show large discrepancies in the prediction of the v-velocity profile. As explained earlier, this is due to the positioning of the vortices either side of the slot.

Velocity profiles at maximum suction (Figs. 7.19-7.20) show very good comparisons with the PIV data especially at streamwise positions close to the slot exit. V-velocity profiles are captured to within 2% of the PIV data at positions close to the slot exit (Figs. 7.19(b) and 7.19(d)). As streamwise distance increases away from the slot the computed results show a small deviation away from the PIV data towards the centre of the slot. Away from the slot edges the comparison remains within 2% of the PIV data.

Comparing these results with those of the previous section (Fig. 7.10) one can see that the effect of the cavity allows a more realistic representation of the flow in the suction phase.

Centreline velocity at various positions above the slot exit at maximum expulsion and maximum suction have been plotted in Fig. 7.21. It can clearly be seen that none of the limiters used manage to capture the correct position and magnitude of the peak velocity at maximum expulsion. The DD limiter gives the best representation of the peak velocity position and compares well at positions further downstream, however fails to predict the peak velocity magnitude compared to the PIV data. All limiters over-predict the velocity at the slot exit and a maximum velocity is reached further downstream than the PIV data. Kotapati and Mittal [87] attribute the discrepancy in the magnitude of the peak velocity to end wall effects in the experiments that cause the fluid to accelerate between shear layers formed at the slot end walls. Comparing the present results with those presented at the workshop (Fig. A.6), one can see that all investigations found it difficult to match both the peak velocity magnitude and streamwise position. At maximum suction the computed results agree well with the PIV data at all streamwise positions except directly at the slot exit. The Superbee limiter predicts a type of plateau in velocity between approximately 2mm and 7mm upon which the flow rapidly increases. This trend is not observed by any of the other limiters.

Figures 7.22-7.24 show u-velocity contour comparisons at various phase angles. It should be noted that the contour plots correspond to simulations carried out using the KK5 limiter on the coarser grid. Velocity contours during the expulsion phase of the cycle show that the counter rotating vortices formed either side of the slot exit move faster downstream than those obtained by the PIV experiments. At a phase angle of 90° the computed vortex cores are approximately at a streamwise position of 5mm whereas the PIV data shows the vortex cores at a position of approximately 3.5mm. This is the reason as to why the v-velocity distribution plots across the slot exit at various streamwise positions shown in Fig. 7.18 do not coincide with the PIV data. This also accounts for the anomalies in the computed results for the centreline u-velocity at maximum expulsion. Velocity contours during the suction phase show a good comparison with the PIV data. It should be noted that all numerical limiters predict a symmetric separation of the fluid flow as opposed to some of the presented results from the workshop which were discussed in the previous section.

Computed time-averaged results of u-, and v-velocity profiles across the slot exit at various positions above the slot are presented in Figs. 7.25-7.27. At a position of 0.1mm above the slot exit all limiters with the exception of the DD and van Albada limiter give an accurate prediction of the u-velocity profile compared with the PIV data. Results presented at the workshop at the same streamwise position above the slot are shown in Fig. A.11. These results show a very poor comparison with the PIV data with some contributions failing to predict the actual shape of the velocity profile (UKY results). The reason as to why the results from UKY show a net suction velocity is possibly due to the input velocity profile specification at the diaphragm. The computed v-velocity at this position compares well with the PIV data in the region across the slot exit and close to the slot edges. Further away from the slot edge the velocity profile deviates away from the PIV data. Moving to a downstream position of 1mm above the slot exit the computed u-velocity profile compares well with the PIV data in the region directly over the slot exit. The computed results do not predict very well the spread of the jet in the region just beyond the slot edges. The workshop results of time-averaged streamwise velocity profiles at this position above the slot exit (Fig. A.12) show a relatively poor comparison with the PIV data. Most of the results tend to under-predict the peak velocity at the centre of the slot and the spread of the jet across the slot is poorly captured. The computed v-velocity shows an extremely good comparison with the PIV data with all limiters predicting the same result. Cross-stream velocity profiles presented at the workshop shown in Fig. A.14 reveal that most of the numerical methods used tended to over-predict the maximum and minimum velocity either side of the slot exit. Further away from the slot exit the computed velocity profiles continue to show a good comparison with the PIV data, with little variation between the various limiters used except for the DD and van Albada limiters. Workshop results at a position of 4mm above the slot exit tend to give a better agreement between streamwise velocity and PIV data than at positions closer to the slot exit (Fig. A.13). However, the cross-streamwise results shown in Fig. A.15 show that the agreement with the PIV data deteriorates with distance away from the slot exit.

The workshop results showed a greater disparity between laminar and turbulent simulations, with the turbulent simulations providing a much better representation of the velocity profile. High-resolution methods inherently decide whether the flow is turbulent or laminar and hence adapt themselves to the particular nature of the flow. This maybe the reason as to why such a good agreement of time-averaged velocity profiles were obtained.

Figure 7.28 shows contours of phase-averaged spanwise vorticity Ω_z at various phase angles, computed using the KK5 limiter on the coarser grid resolution. At 0°, the vorticity plot shows the previous vortex pair which have moved away in the downstream region over the period of the previous cycle. The plot also shows the initiation of the roll up process of the vortices either side of the slot exit. At phase angles of 45° and 90° the roll up process of the vortices is completed and it can clearly be seen that they have grown significantly in size. Upon the start of the suction phase i.e. at a phase angle of 180° the vortex pair detach themselves from the slot exit plane and begin to advect downstream. The suction phase generates vortex rollup in the interior of the cavity. This continues through the suction phase with the vortices growing in size until the whole of the cavity section is filled before the beginning of the next cycle. It is important to note that the suction phase does not harm the counter rotating vortex pair formed during the expulsion cycle. This is due to the frequency of the oscillating diaphragm. If the frequency is too high then the vortex pair do not have a chance to move sufficiently downstream in order to escape the suction phase and can in fact get destroyed by the suction phase and hence nullify any benefit in the use of the synthetic jet.

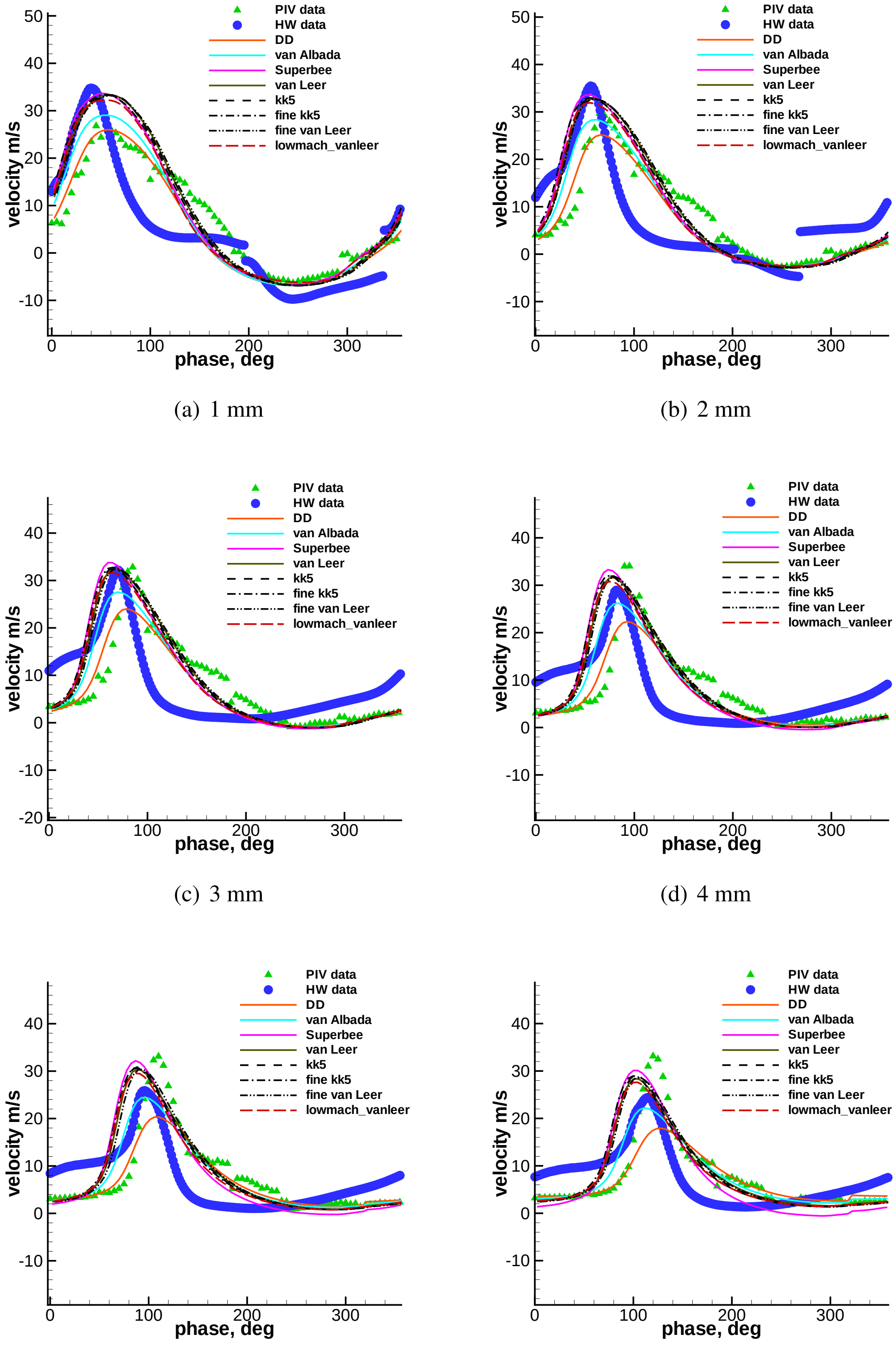

(a) 1 mm (b) 2 mm

(c) 3 mm (d) 4 mm

(e) 5 mm (f) 6 mm

Figure 7.16: Phase-averaged u-velocity at various downstream positions above the centre of the slot exit.

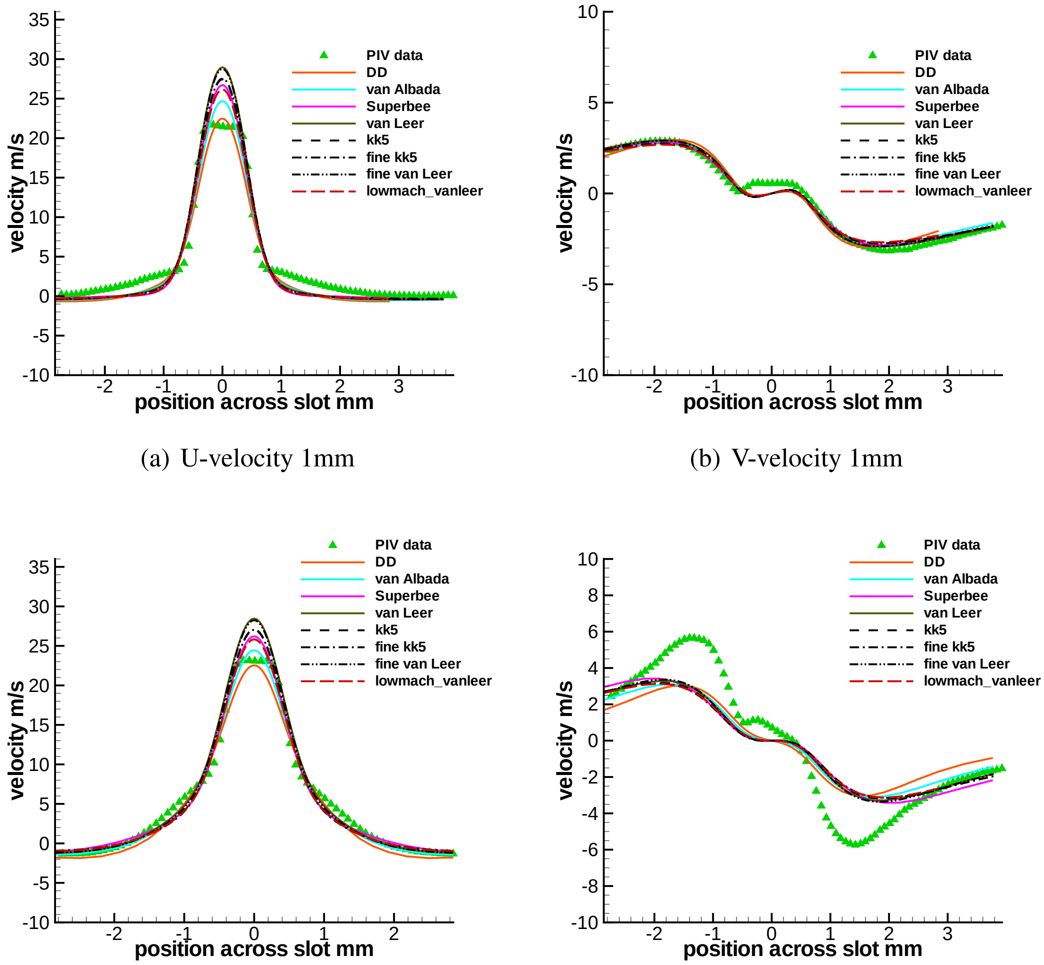

(a) U-velocity 1mm

(b) V-velocity 1mm

(c) U-velocity 2mm

(d) V-velocity 2mm

Figure 7.17: Phase-averaged velocity profiles along various downstream horizontal lines above the jet exit plane at 90°.

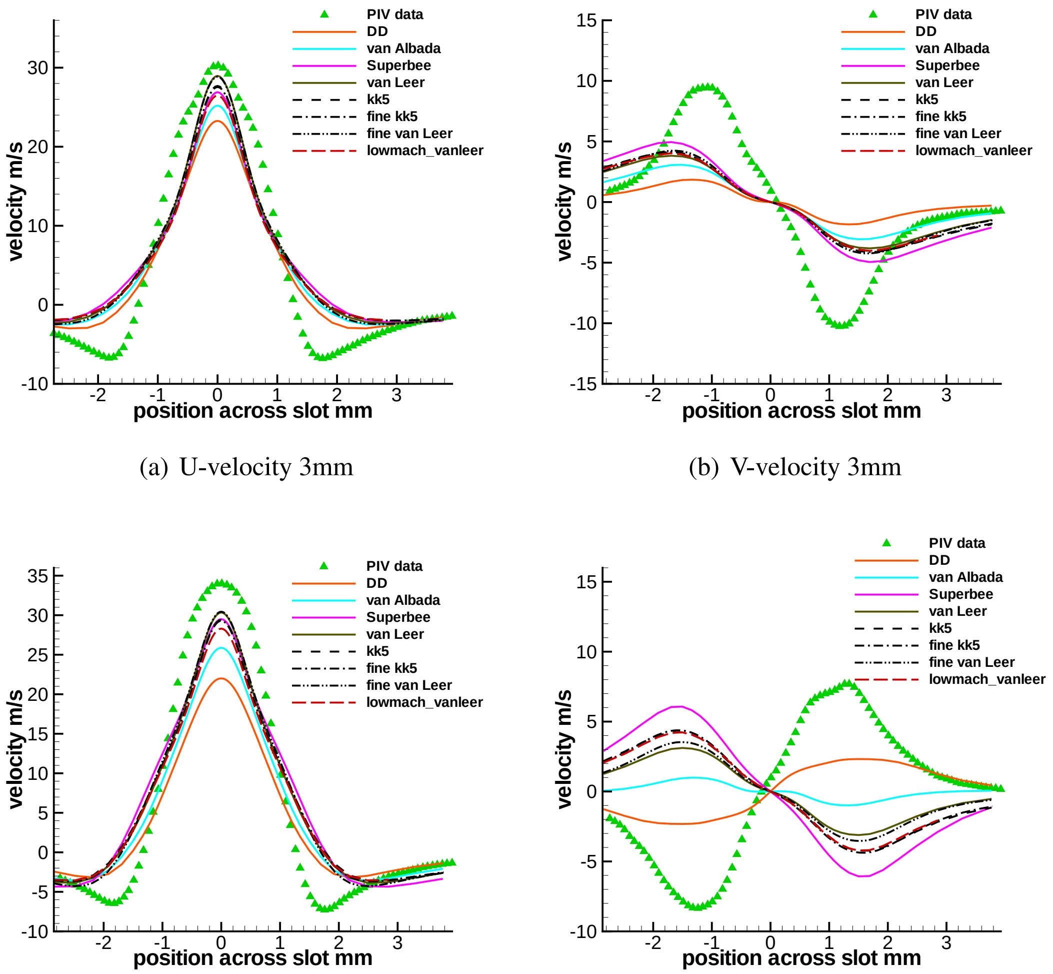

(a) U-velocity 3mm

(b) V-velocity 3mm

(c) U-velocity 4mm

(d) V-velocity 4mm

Figure 7.18: Phase-averaged velocity profiles along various downstream horizontal lines above the jet exit plane at 90°.

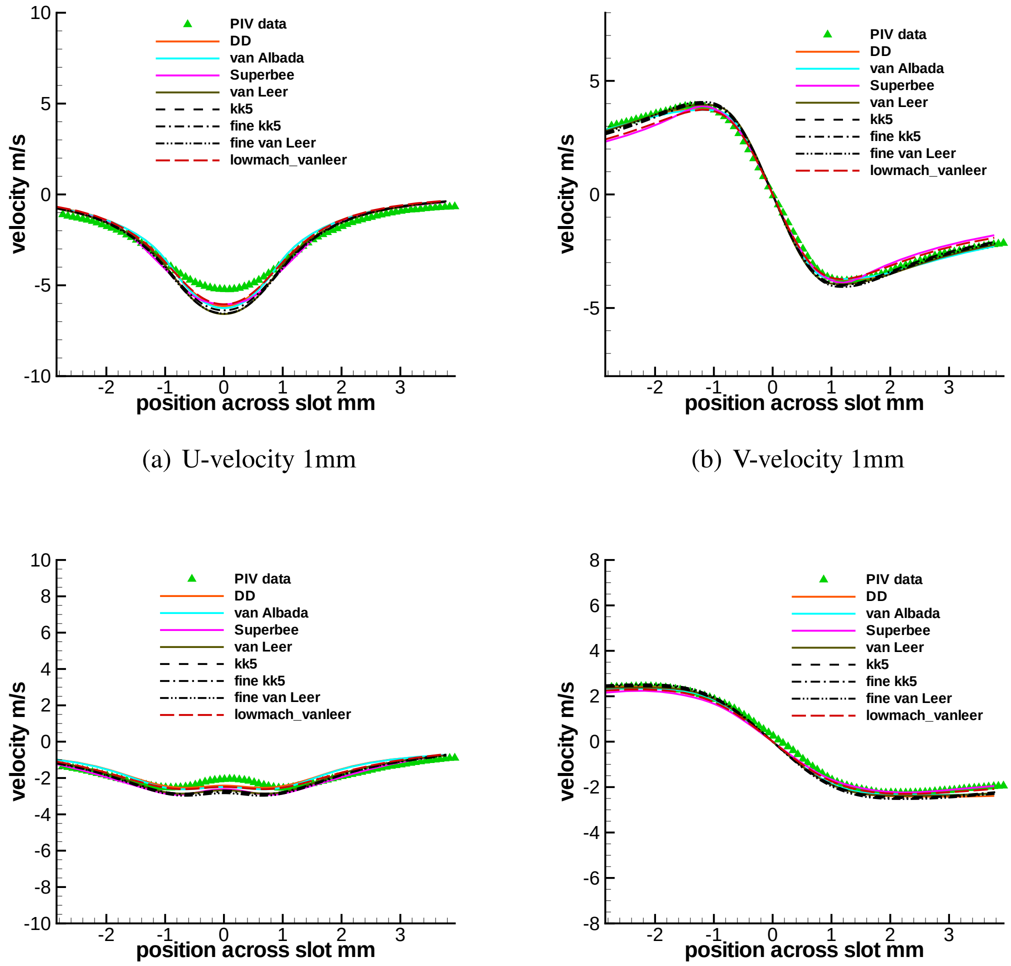

(a) U-velocity 1mm

(b) V-velocity 1mm

(c) U-velocity 2mm

(d) V-velocity 2mm

Figure 7.19: Phase-averaged velocity profiles along various downstream horizontal lines above the jet exit plane at 270°.

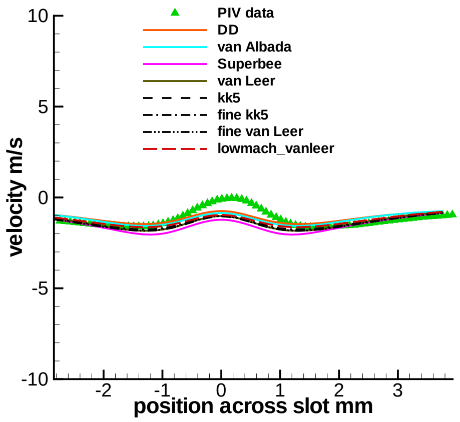

(a) U-velocity 3mm

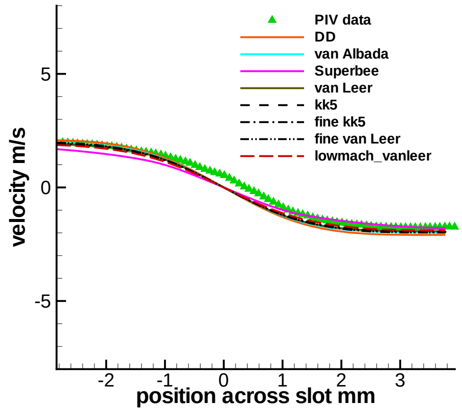

(b) V-velocity 3mm

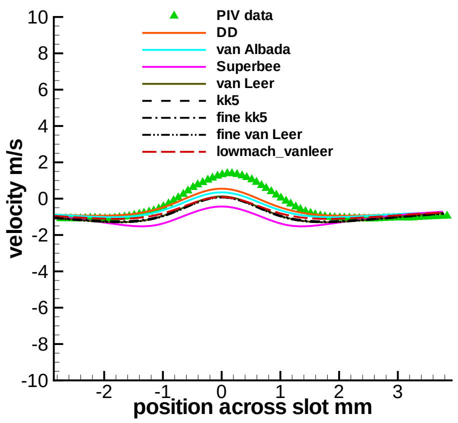

(c) U-velocity 4mm

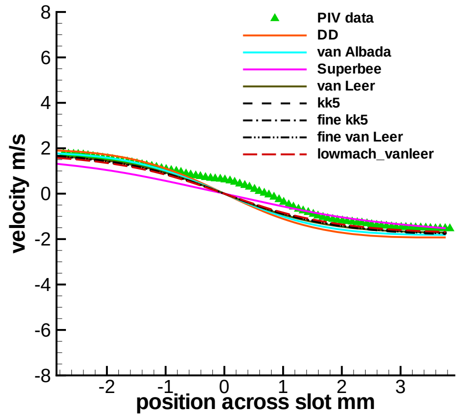

(d) V-velocity 4mm

Figure 7.20: Phase-averaged velocity profiles along various downstream horizontal lines above the jet exit plane at 270°.

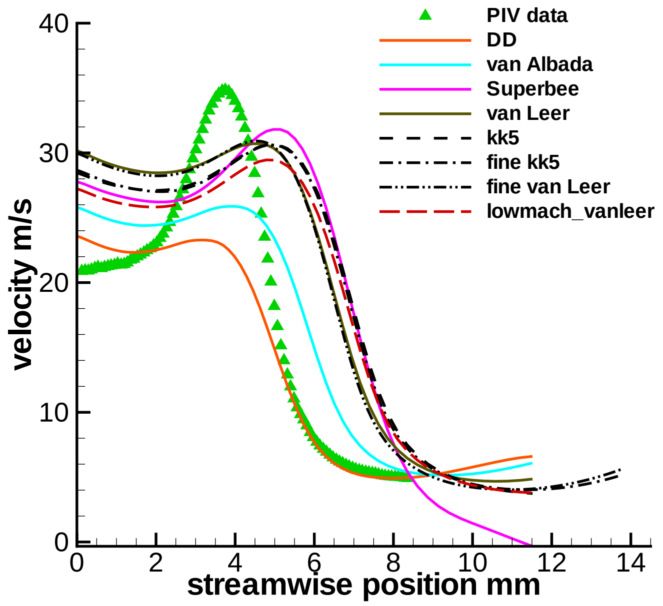

(a) Phase 90°

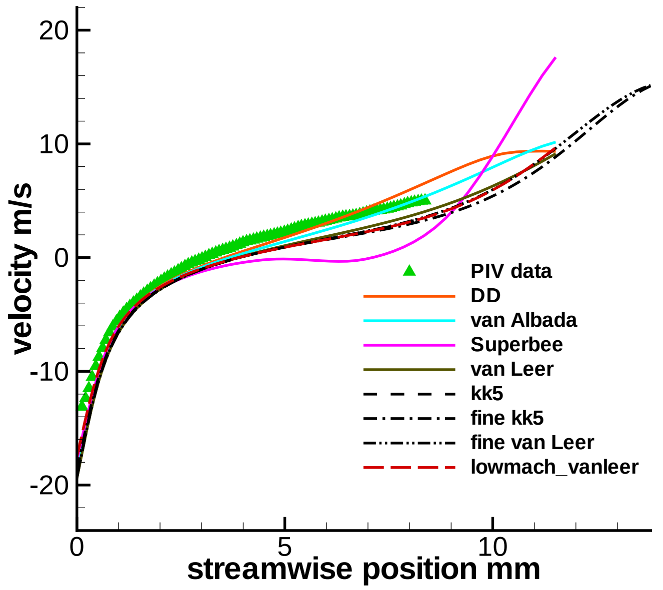

(b) Phase 270°

Figure 7.21: Phase-averaged centerline u-velocity.

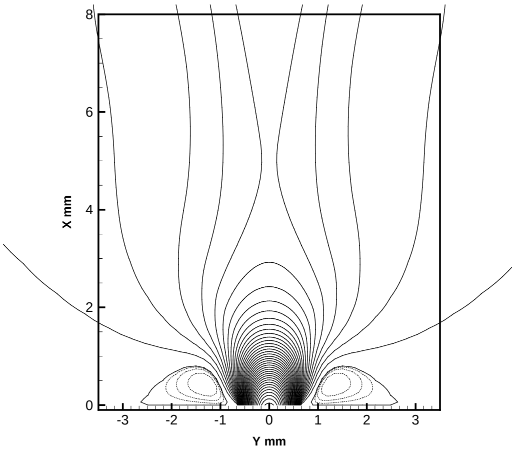

(a) 0°

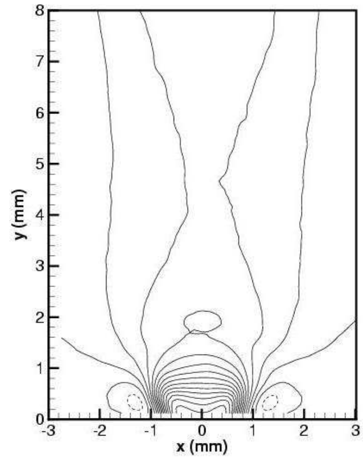

(b) PIV 0°

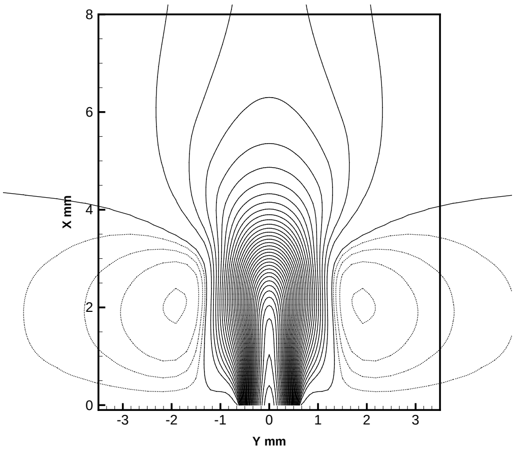

(c) 45°

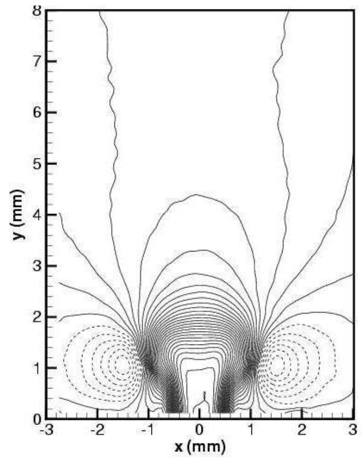

(d) PIV 45°

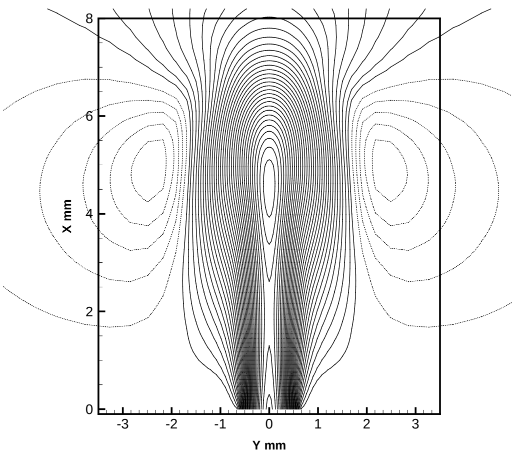

(e) 90°

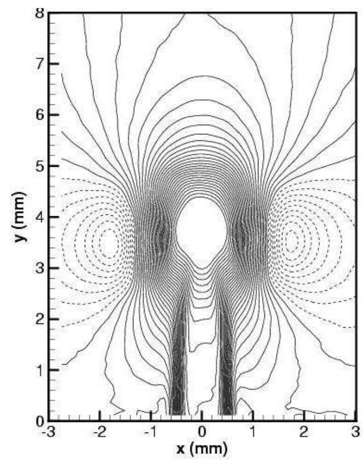

(f) PIV 90°

Figure 7.22: Comparison of computed streamwise velocity contours and experimental PIV data at various phase angles.

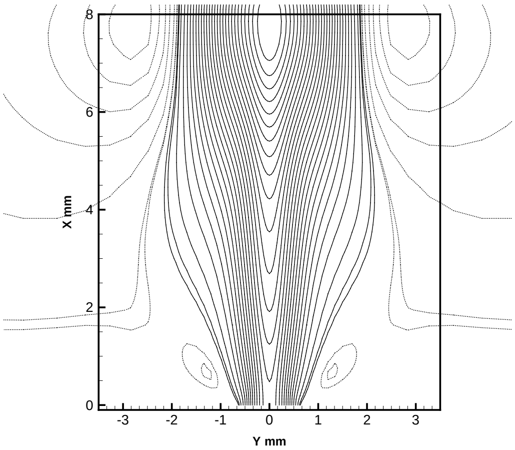

(a) 135°

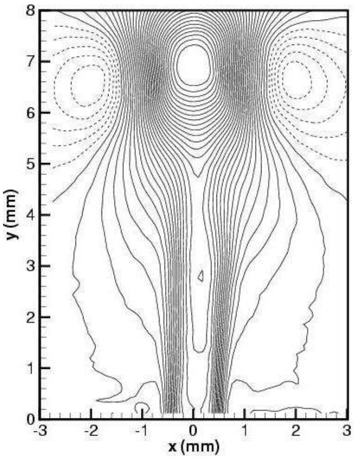

(b) PIV 135°

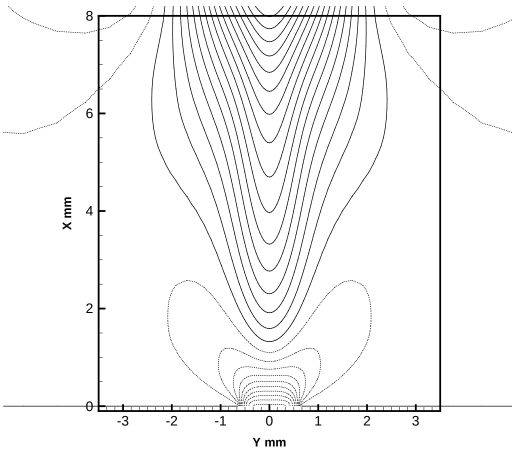

(c) 180°

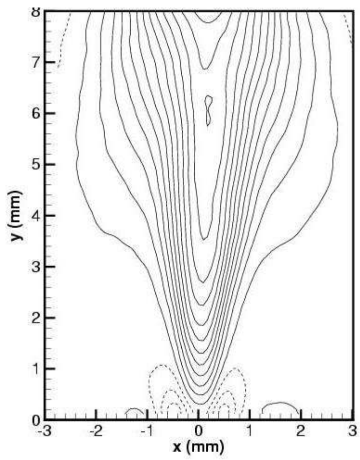

(d) PIV 180°

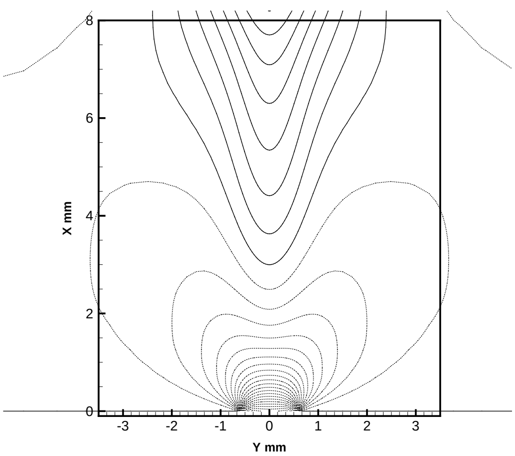

(e) 225°

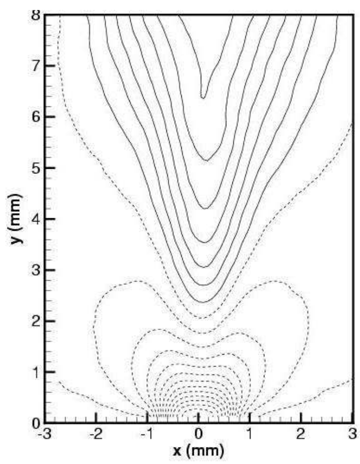

(f) PIV 225°

Figure 7.23: Comparison of computed streamwise velocity contours and experimental PIV data at various phase angles.

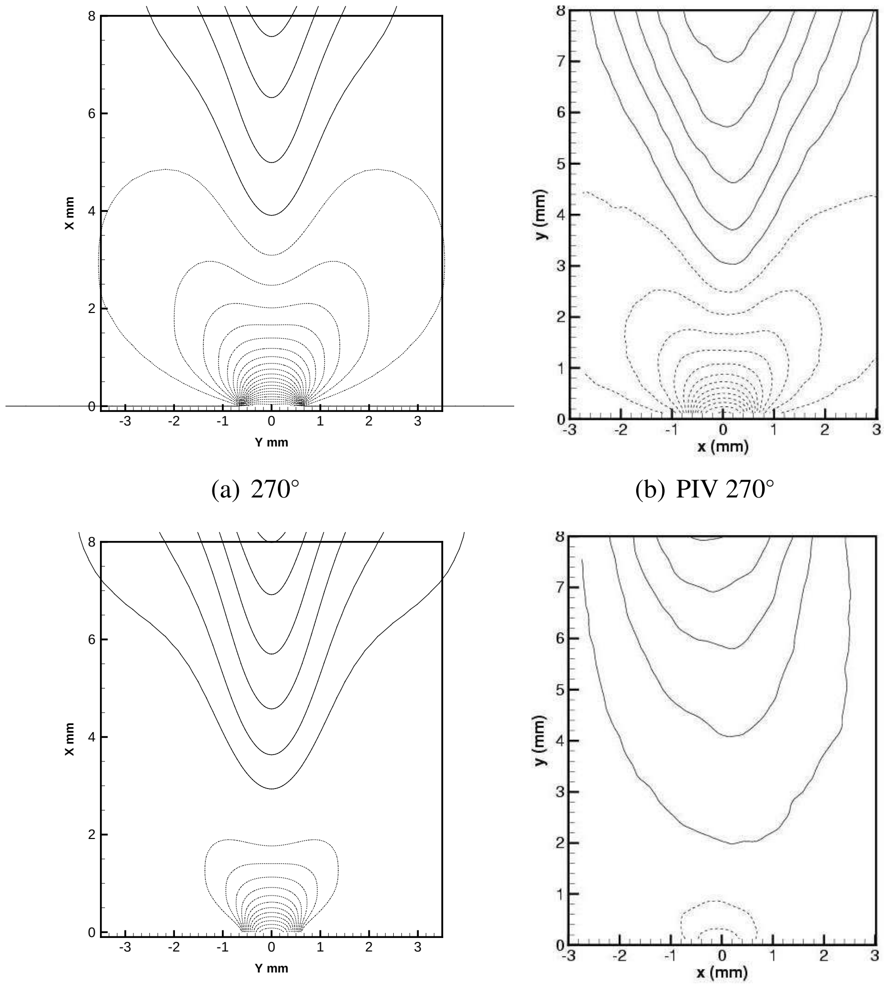

(a) 270°

(b) PIV 270°

(c) 315°

(d) PIV 315°

Figure 7.24: Comparison of computed streamwise velocity contours and experimental PIV data at various phase angles.

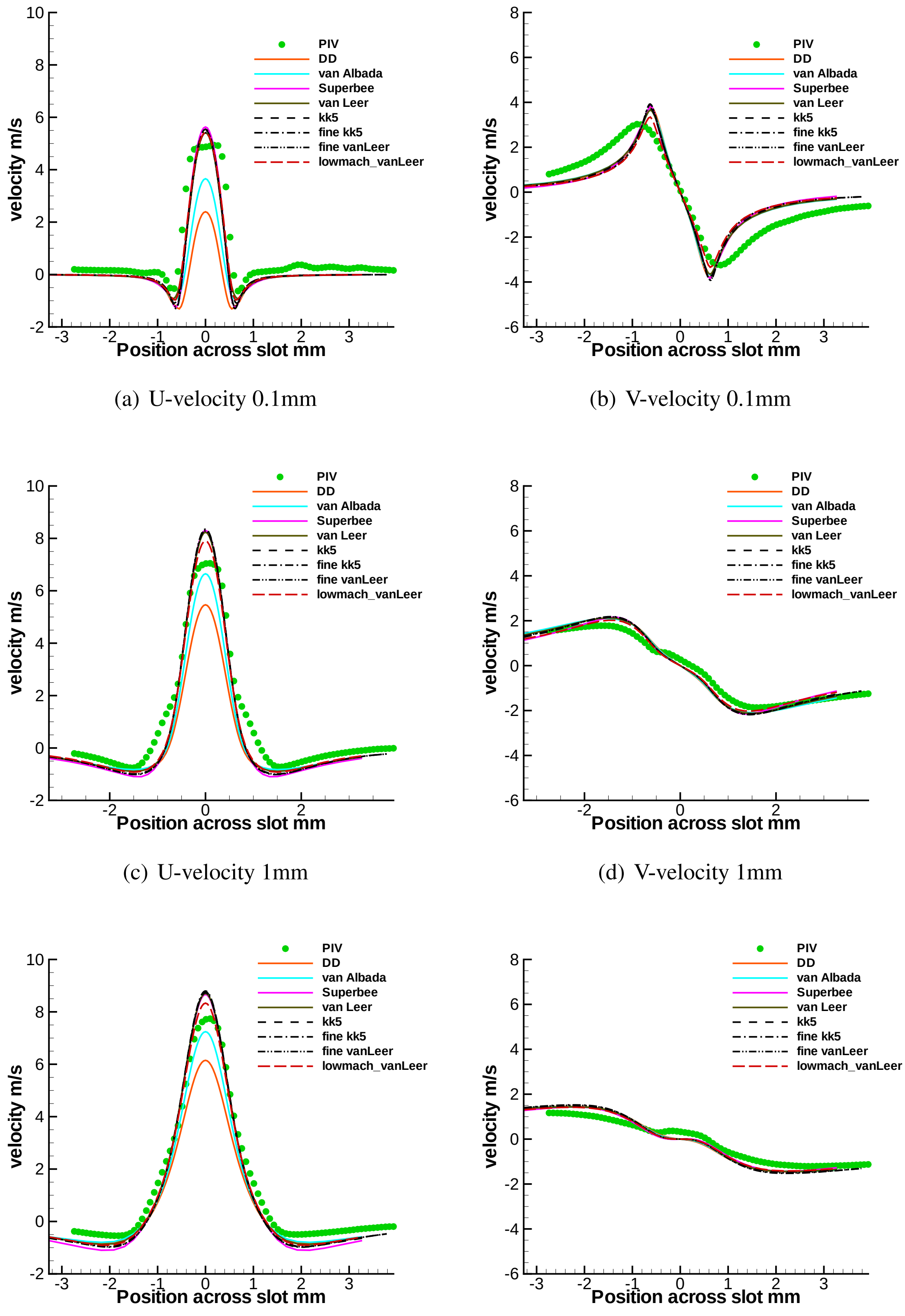

(a) U-velocity 0.1mm

(b) V-velocity 0.1mm

(c) U-velocity 1mm

(d) V-velocity 1mm

(e) U-velocity 2mm

(f) V-velocity 2mm

Figure 7.25: Time-averaged velocity profiles across the slot exit at various downstream positions above the slot exit.

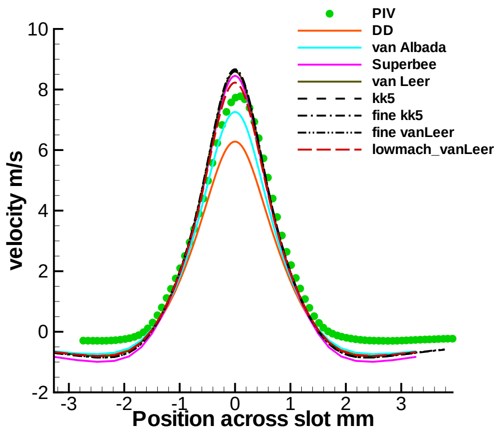

(a) U-velocity 3mm

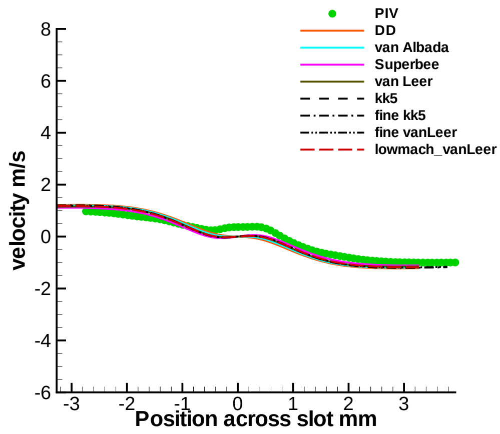

(b) V-velocity 3mm

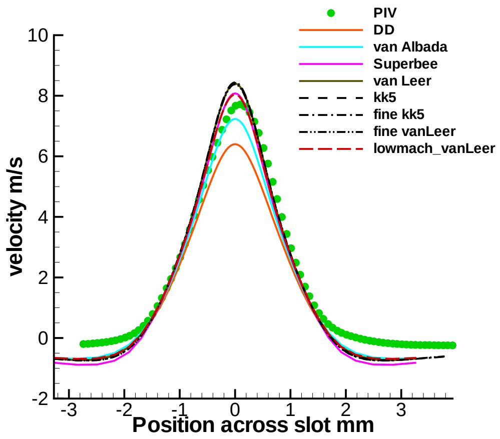

(c) U-velocity 4mm

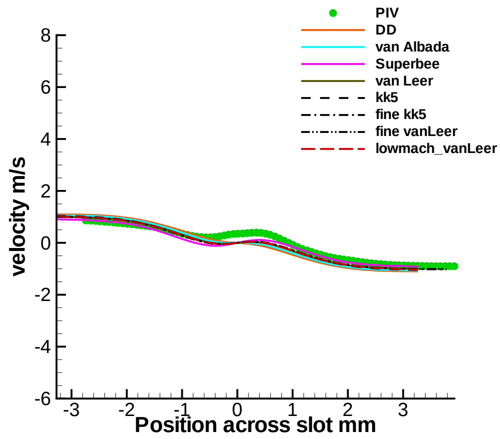

(d) V-velocity 4mm

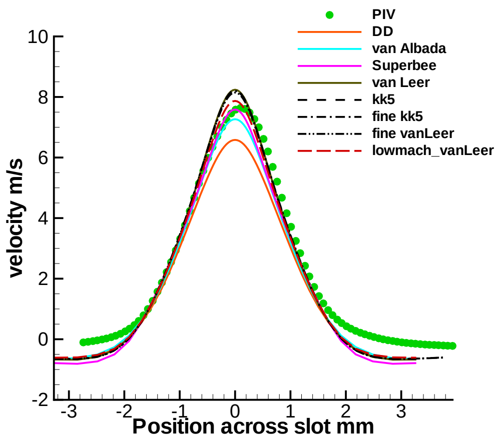

(e) U-velocity 5mm

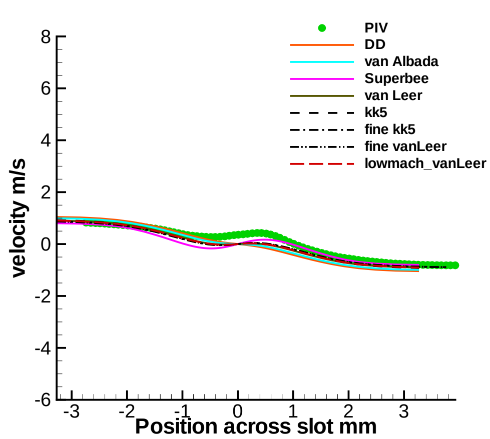

(f) V-velocity 5mm

Figure 7.26: Time-averaged velocity profiles across the slot exit at various downstream positions above the slot exit.

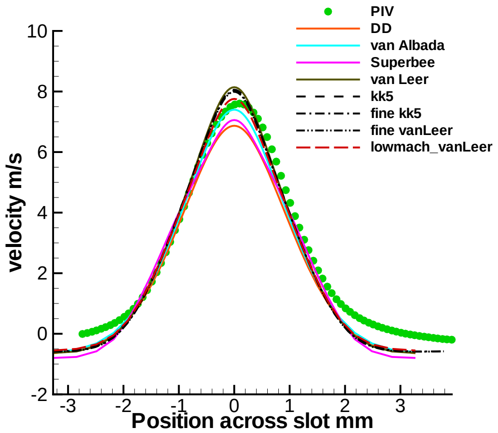

(a) U-velocity 6mm

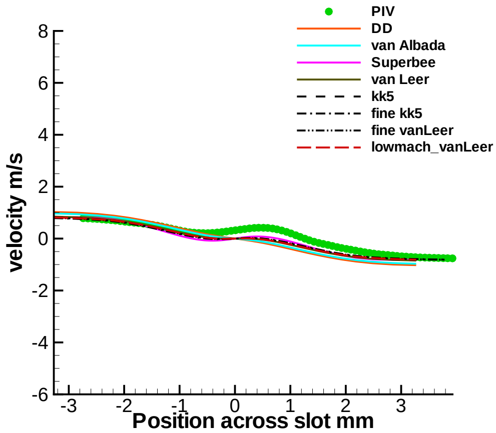

(b) V-velocity 6mm

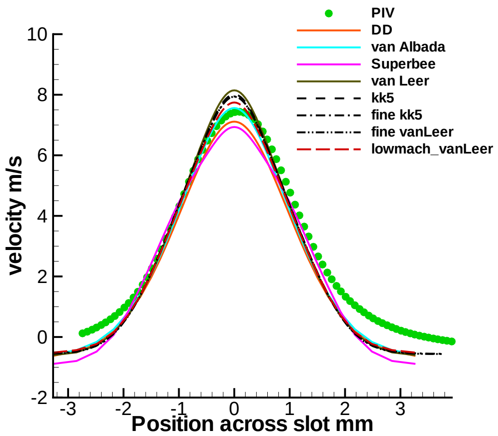

(c) U-velocity 7mm

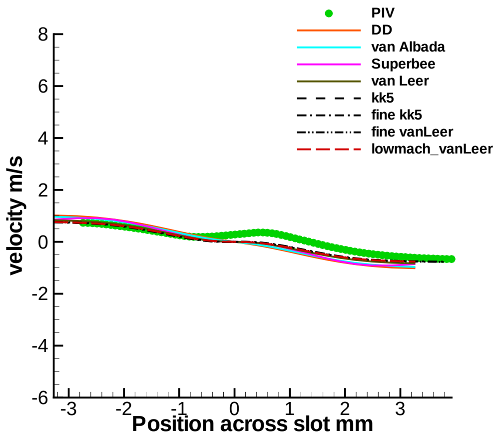

(d) V-velocity 7mm

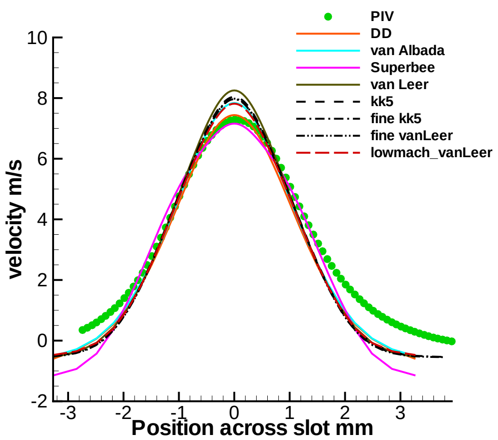

(e) U-velocity 8mm

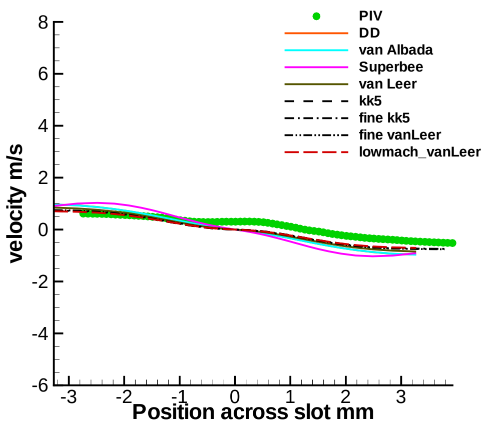

(f) V-velocity 8mm

Figure 7.27: Time-averaged velocity profiles across the slot exit at various downstream positions above the slot exit.

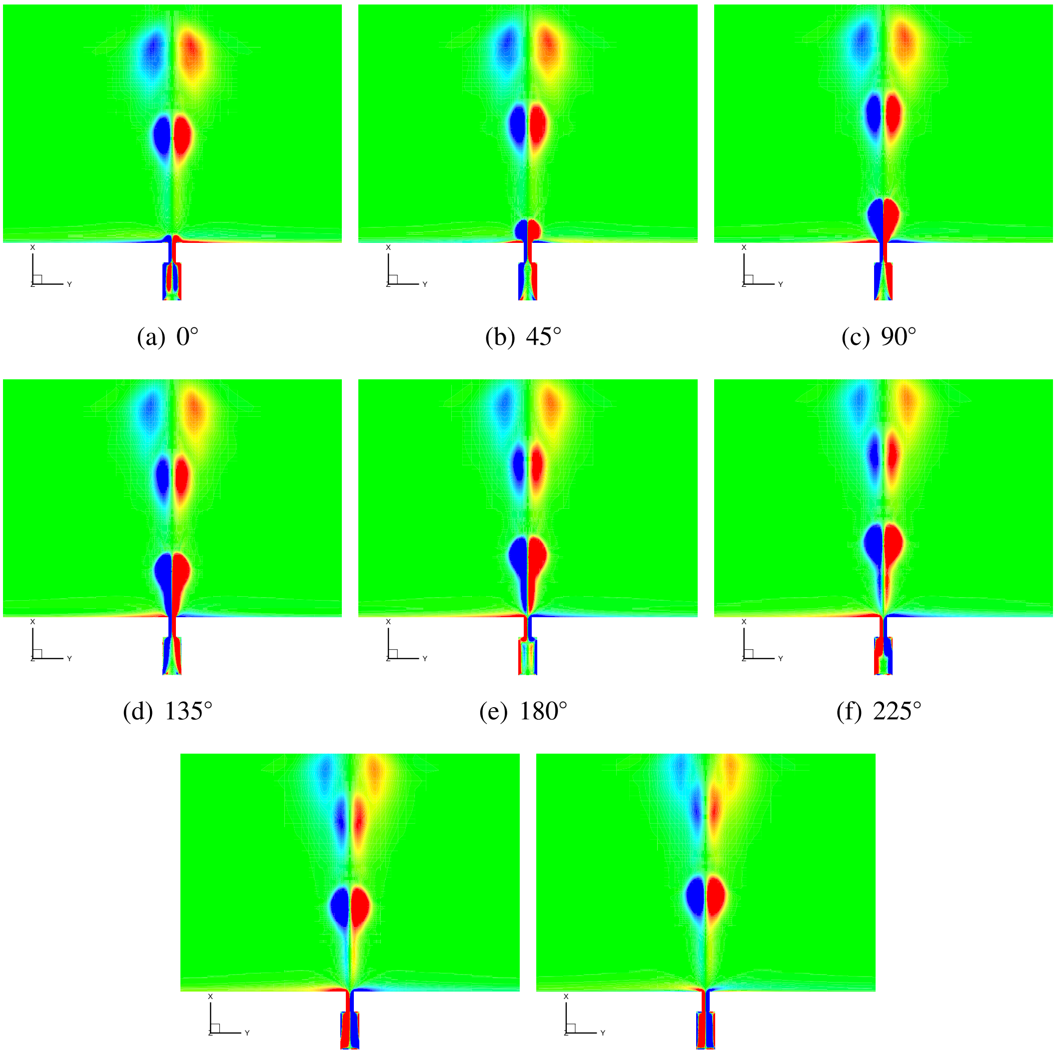

(a) 0° (b) 45° (c) 90°

(d) 135° (e) 180° (f) 225°

(g) 270° (h) 315°

Figure 7.28: Contours of phase-averaged spanwise vorticity (Ω_z) at various phase angles, computed using the KK5 limiter.

7.4 Summary

Simulations concerning the fluid flow of a synthetic jet issuing into quiescent air have been carried out. The simulations revealed that the flow is characterised by the generation of a counter rotating vortex pair at the edges of the slot exit. The vortices move away from the slot exit under their own self induced velocity during the expulsion/suction cycle. The simulations were carried out for two geometries. Firstly, a full three-dimensional setup was modelled with the exception of the cavity section. A sinusoidal velocity boundary condition was applied directly to the slot exit. The results of phase-averaged velocity profiles predicted that the flow at a position close to the slot exit remains sinusoidal. This was shown to be incorrect by the experimental data which revealed that the magnitude of the velocity is greater in the expulsion phase than in the suction phase. This was partly due to the design of the oscillating diaphragm but also due to the characteristics of the flow in the cavity. A good representation of the physics of the flow were captured and the difference between the various limiters employed only became significant at downstream positions further away from the slot exit.

The investigation was extended to include the cavity section and the computational domain was changed to a quasi-three-dimensional domain with the use of periodic boundary conditions in the spanwise direction. The aspect ratio of the slot is large enough to assume that the flow is nominally two-dimensional except close to the slot edges where side wall effects occur. Modelling the flow as periodic in the spanwise direction led to a significant saving in the computational cost. The results revealed that the effect of adding the cavity section corrected the suction phase velocity profile in accordance with the PIV data. The computations failed to predict the correct position and magnitude of the maximum streamwise velocity during the expulsion phase of the cycle. Increasing the grid resolution did not provide a substantial difference in the results obtained.

The data from the workshop firstly showed that there are significant differences between the three different experimental measuring techniques employed, especially in the region close to the slot exit. The computational contributions showed significant variations from the different groups. The effect of grid density and time-step refinement did not provide any substantial improvement to the results obtained. Laminar contributions resulted in the most inaccurate behaviour, however there was no particular turbulence model which proved to be superior to other models. Modelling the flow in three-dimensions did not appear to improve the correlation with the experimental data. Problems were found to occur in the comparison of phase at the slot exit with the experimental data leading to a mismatch of velocity profiles at the slot exit with regards to both phase and amplitude. This contributed to large errors in the results obtained.

Discrepancies between the various limiters investigated in the second study became more apparent at positions further away from the slot exit. However, the DD and van Albada limiters consistently predicted lower velocities during the expulsion phase of the cycle. The Superbee limiter tended to predict erroneous results at positions far away from the slot where the grid resolution was coarser. The Superbee limiter is well known for being inherently anti-diffusive and this may account for the unusual behaviour further from the slot exit. Overall the best results were obtained from the van Leer and KK5 limiters at all positions in the flow during both expulsion and suction. The low Mach correction limiting did not provide any significant benefit to the results obtained. The study of various limiters is complex with limiters behaving differently depending on the characteristics of the flow situation. Hence in deciding which limiter to use one needs to be fully aware of the flow characteristics being modelled and choose the limiter accordingly. It is hoped that this investigation helps to further the understanding of limiting flows featuring separation, vortical structures and the possible transition to turbulence.

CHAPTER 8

Conclusion

THE aim of this thesis was to investigate the ability of high-resolution methods to accurately capture flows featuring separation, instabilities, bifurcation and transition at relatively low Reynolds numbers. The above mentioned flow features are essentially non-linear in nature and the use of high-resolution methods, which are inherently non-linear, have shown, in the course of this thesis, to be able to accurately predict such flow phenomena. A secondary aim of this thesis was to further shed light on the non-linear mechanisms embedded in high-resolution numerical methods which enable these methods to accurately model the physics of complicated flows. The implementation and investigation of various Riemann solvers in the context of incompressible flows has been carried out and will be further discussed below.

It is well known that at low Reynolds numbers the Euler and Navier-Stokes equations exhibit stiffness making convergence difficult. In the context of the artificial compressibility approach to solving the hyperbolic incompressible equations, the advective fluxes behave in much the same manner as solving the low speed compressible flow equations and require a lengthy time to converge to a steady state at very low Reynolds numbers. Best convergence rates are obtained by inversely scaling the artificial compressibility parameter with Reynolds number. Hence as Reynolds number becomes very low the artificial compressibility parameter becomes large. This results in the equations becoming more "incompressible" which in turn results in the advective equations becoming more stiff. The effect of preconditioning is aimed at alleviating this stiffness.

The preconditioning technique of Turkel [177] was implemented and tested for a range of Reynolds numbers for flow through suddenly expanded and suddenly expanded-contracted geometries. Both these geometries are well know for exhibiting instabilities manifested as a symmetry breaking bifurcation of the flow, upon exceeding some critical Reynolds number. Laminar flow calculations were performed with and without preconditioning in order to assess its effects on the accuracy and efficiency of computations. At higher Reynolds number flows the use of preconditioning reduced the number of multigrid cycles, but adversely affected the solution results. For Reynolds numbers in the range of symmetry-breaking bifurcation, the use of preconditioning led to an incorrect stable solution or to an improper estimation of the size of the separation bubble. This leads to the belief that the effect of preconditioning on the solution is similar to that of adding a significant amount of extra dissipation to the flow. At lower Reynolds number flows, below the critical Reynolds number, the present form of preconditioning neither altered the accuracy of the solution nor had a significant effect on the rate of convergence. Overall, the ability to accurately predict flows featuring symmetry breaking bifurcation was diminished due to the effect of preconditioning and an increase in efficiency was obtained only for higher Reynolds number flows.

A detailed investigation into the prediction of flow instabilities in a suddenly expanded-contracted channel using various Riemann solvers in conjunction with first-, second- and third-order interpolation in the calculation of the intercell flux was carried out. Results were presented for three different Riemann solvers, namely; The HLLE scheme, Rusanov scheme and the Characteristics-based scheme. The calculations showed that for low Reynolds numbers the flow separated symmetrically. As Reynolds number was increased symmetry-breaking bifurcation occurs at a critical Reynolds number and separation bubbles of different sizes form on the lower and upper walls. The asymmetries become stronger with increasing Reynolds number until a second critical Reynolds number is reached and the flow regains symmetry.

Under-resolved grid simulations showed that the choice of numerical scheme effects the solution obtained especially in the range of Reynolds number where symmetry breaking bifurcation occurs. The prediction of the degree of asymmetry in the HLLE and Rusanov schemes was less than that obtained by the characteristics-based scheme. Grid independent cases showed that the choice of interpolation used in the calculation of the intercell flux can have a significant effect on the solution obtained for Reynolds numbers where symmetry breaking bifurcation occurs. First-order interpolation using the characteristics-based scheme correctly predicted the asymmetric solution, whereas the HLLE and Rusanov schemes incorrectly predicted a stable symmetric solution. Higher-orders of interpolation at the same Reynolds number led to asymmetric separation for all numerical schemes investigated with little noticeable difference between the three schemes when using third-order interpolation.

The three-different schemes differ in the calculation of the wave-speed dependent term which encompasses information about the eigenstructure of the system of equations and is also responsible to adapt the discretisation according to the local solution data. The Rusanov scheme is based on the calculation of the maximum wave speed and hence cannot recognise the slowest moving acoustic waves thus causing a larger amount of dissipation. This diffusive nature of the Rusanov scheme will tend to have a "smoothing" effect on the solution and hence may be the reason as to why the solutions obtained, especially when using 1st-order reconstruction, do not accurately represent the physics of the flow. Hence, it has been shown that the choice of numerical scheme together with the choice of reconstruction used in the calculation of the intercell flux can effect the solution obtained, even for grid-independent solutions.

A numerical study of flow through a plane suddenly expanded channel was conducted for both two-, and three-dimensional geometries. Suddenly expanded channel flow is well documented with a substantial amount of work, both experimental and computational, present in the current literature. The aim of this investigation was to show that non-linear bifurcation can be accurately captured using high-resolution numerical methods for both two-, and three-dimensional flows. The flow characteristics showed that at low Reynolds numbers the flow separates symmetrically and upon reaching a critical Reynolds number symmetry-breaking bifurcation is achieved. The asymmetry in the flow continues to grow with one recirculation zone growing at the expense of the other. The effect of varying the expansion ratio showed that the critical Reynolds number for symmetry-breaking bifurcation decreases as expansion ratio increases. This result is in accord with various experimental and computational data obtained from the literature. Values for the critical Reynolds number obtained compared extremely closely to the experimental values of Fearn et al. [59] and CFD results of Drikakis [46].

Three-dimensional simulations showed that the effect of the vertical side wall proximity (aspect ratio) provided a stabilising effect on the flow. This corresponded to an increase in critical Reynolds number as aspect ratio was decreased. Lower Reynolds numbers in the regime of asymmetric separation of the fluid flow, showed that the flow in the expanded channel is nominally two-dimensional except at planes closest to the vertical side walls. This irregularity at the side walls is due to the effects of the side wall boundary layer acting to stabilise the flow. On increasing Reynolds number the flow take on more of a three-dimensional character with side wall effects extending the whole spanwise domain. Streamlines at the side wall were found to move in a spiral motion towards the centre symmetry plane of the channel. This is due to the side wall boundary layer, which imposes shear drag on the primary motion of the fluid particles behind the expansion. This in-turn results in pressure gradients along the spanwise direction giving rise to an increasingly large spanwise velocity component. It is this increasing velocity component that gives rise to the spiral motion focused around a vortical core line towards the symmetry plane of the channel.

Furthermore, it was also confirmed that three-dimensional effects become more pronounced with increasing Reynolds number and that the flow becomes three-dimensional before becoming time-dependent. A secondary eddy is formed in the vicinity of the vertical side wall and as Reynolds number increases the effect of the secondary eddy becomes strong enough to extend the whole spanwise direction towards the symmetry plane. This secondary eddy varies significantly in the region close to the vertical side wall where the boundary layer exists until settling to a stable separation region at planes closer to the symmetry plane. Further increases in Reynolds number showed that the steady asymmetric flow becomes time-dependent, characterised by the shedding of vortices from the shear layer of the upstream recirculation bubbles. The shedding of the vortices was observed to increase in frequency as Reynolds number was further increased. It has been shown that high-resolution numerical methods can correctly predict non-linear bifurcation phenomena in both two- and three-dimensions. The computed results have been compared to available experimental data over a range of Reynolds numbers and have shown to agree to within 5% of the experimental data. At Reynolds numbers where quantitative comparison data was unavailable the computed results have shown to qualitatively capture the flow physics which so importantly characterise the flow through such geometries during both steady and unsteady computations.

To further shed light on the embedded 'artificial viscosity' of high-resolution methods, analysis of the non-linear wave speed dependent term (dissipation term) was carried out in the context of flow through a two-dimensional suddenly expanded channel. In a laboratory experimental set-up the flow asymmetries may be triggered by geometrical imperfections, asymmetries in the upstream flow profile and small perturbations that exist throughout system. The investigation showed that even in a fully symmetric computational set-up these asymmetries are still present, proving the ability of high-resolution methods to accurately model the physics of a particular flow. The contribution of the wave-speed dependent term to the flow solution was plotted via contours which showed that the the asymmetric dissipation arising downstream of the separation regions is responsible for triggering the symmetry-breaking in the flow. This effect is convected both upstream and downstream as the Reynolds number increases. It also seems that the non-linear dissipation has a significant effect on flow separation. Hence, the present investigation suggest that the mechanism of symmetry-breaking bifurcation is provided in the simulations as a result of a delicate balance of truncation 'errors' due to wave-speed-dependent terms (chiefly responsible for numerical dissipation) of non-oscillatory finite volume methods. Therefore, these terms are not numerical error, but legitimately describe the physics. This analysis of the symmetry-breaking bifurcation using high-resolution methods further proves that this family of numerical methods have embedded characteristics which enable them to correctly model the physics of flows featuring instabilities.

The final test case involved the simulation of a synthetic jet actuator issuing into quiescent air. The investigation focused on various slope limiters used in conjunction with the MUSCL scheme for high-order interpolation of the cell centred values. The computed results were compared to the experimental data generated by NASA Langley for a workshop on CFD validation of synthetic jets and turbulent separation control. Various CFD contributions to this workshop were also used as a comparison to the current results. The simulations were carried out for two geometries. Firstly a full three-dimensional geometry without a cavity section was modelled, using a sinusoidal velocity profile imposed directly to the slot exit. The results of phase-averaged velocity profiles predicted that the flow at a position close to the slot exit remains sinusoidal. This was shown to be incorrect by the experimental data which revealed that the magnitude of the velocity is greater in the expulsion phase than in the suction phase. A good representation of the physics of the flow were captured and the difference between the various limiters employed only became significant at downstream positions further away from the slot exit. The second phase of the simulations extended the geometry to simulate the cavity section and quasi-three-dimensional simulations were carried out with periodic boundary conditions in the spanwise direction of the slot. The results revealed that the effect of adding the cavity section corrected the suction phase velocity profile in accordance with the PIV data. The computations failed to predict the correct position and magnitude of the maximum peak streamwise velocity during the expulsion phase of the cycle.

The various computational contributions to the workshop showed significant variation between different groups. The effect of grid density and time-step refinement did not provide any substantial improvement to the results obtained. Also, laminar contributions resulted in the most inaccurate behaviour, however there was no particular turbulence model which proved to be superior to other models. Modelling the flow in three-dimensions did not appear to improve the correlation with the experimental data. Problems were found to occur in the comparison of phase at the slot exit with the experimental data leading to a mismatch of velocity profiles at the slot exit with regards to both phase and amplitude. This contributed to the large errors in the results obtained.

Discrepancies between the various limiters investigated in the second study became more apparent at positions further away from the slot exit. However, the DD and van Albada limiters consistently predicted lower velocities during the expulsion phase of the cycle. The Superbee limiter tended to predict erroneous results at positions far away from the slot where the grid resolution was coarser. The Superbee limiter is well known for being inherently anti-diffusive and this may account for the unusual behaviour further from the slot exit. Overall the best results were obtained from the van Leer and KK5 limiters at all positions in the flow during both expulsion and suction. The study of various limiters is complex with limiters behaving differently depending on the characteristics of the flow situation. Hence in deciding which limiter to use one needs to be fully aware of the flow characteristics being modelled and choose the limiter accordingly.

8.1 Summary of Contributions

This thesis has

- Shown that the preconditioning method of Turkel [177] fails to accurately predict instabilities manifested as an asymmetric separation of the fluid flow in suddenly expanded channels. Also the preconditioning method does not provide any substantial acceleration in convergence of low Reynolds number flows where the solution is a symmetric separation of the fluid flow.

- Investigated various Riemann solvers in the context of flow through a suddenly expanded-contracted channel. The choice in Riemann solver can substantially alter the result obtained especially at Reynolds number above the critical value where symmetry-breaking bifurcation occurs.

- Shown that the choice in the order of reconstruction used in obtaining the cell faced values from the cell centres can also significantly effect the flow solution obtained even for grid-independent simulations. Depending on the choice of Riemann solver, orders of reconstruction lower than second-order fail to correctly predict the symmetry breaking bifurcation.

- Investigated the flow physics of symmetry-breaking bifurcation in a plane symmetric suddenly expanded channel, both in two-, and three-dimensions.
- Corroborated previous experimental and computational investigations to show that the effect of the vertical side walls acts to stabilise the flow leading to higher critical Reynolds numbers for symmetry breaking bifurcation.
- Shown that the onset of time dependent flow in a three-dimensional suddenly expanded channel is due to three-dimensional spanwise instabilities initiated in the side wall boundary layer.
- Shown that time-dependency is characterised by the time-periodic shedding of vortices from the upstream recirculation zones.
- Provided an explanation as to the mechanism of symmetry breaking bifurcation using high-resolution numerical methods in the context of a fully symmetric computational set-up. The non-linear wave speed dependent term provides the 'trigger' mechanism via added asymmetric dissipation downstream of the separation region. As Reynolds number increases this asymmetric dissipation convects both upstream and downstream.
- Demonstrated that the choice of slope limiter can effect the solution obtained. Different limiters have various degrees of dissipative properties and should be chosen in conjunction to the flow being simulated.

8.2 Future Research

The work described in this thesis has concentrated on the key aspects of instabilities and transition in suddenly expanded channels using high-resolution numerical methods. It is expected that this work will be used as a guide in future simulations of flows featuring instabilities, separation and transition. Areas that can be addressed by future studies are outlined below.

The simulation of unsteady three-dimensional suddenly expanded flows using high-order methods such as Essentially Non-Oscillatory (ENO) and Weighted ENO (WENO) methods would compliment the current work carried out in this thesis. These schemes do not incorporate monotonicity limiting methods, instead ENO schemes, use uniform orders of accuracy by controlling any increase of the total variation of the numerical solution through an adaptive stencil in such a way that each grid point attempts to use the smoothest information available. Alternatively WENO schemes, use a convex combination of all the corresponding interpolating polynomials on the stencil in order to compute an approximate polynomial for each cell. The interpolating polynomials are combined by assigning weights to the convex combination. For further details regarding higher-order methods the reader is referred to the text of Drikakis and Rider [50].

A key addition to complete the work carried out for a plane sudden expansion geometry would be to carry out stability analysis and use bifurcation theory to numerically determine the bifurcation point. This may further shed light on the details of the bifurcation mechanism. The symmetry-breaking in a suddenly expanded channel could be further investigated by performing time-dependent simulations for steady flows, i.e. at Reynolds number slightly above and below the critical Reynolds number. This type of investigation would show the onset of the bifurcation in a time-dependent context such as that observed in an experimental set-up.

Finally, with regards to the work carried out on synthetic jet flows, an interesting parametric study would be to investigate various Reynolds numbers to see if this type of oscillatory suddenly expanded flow breaks symmetry at some critical Reynolds number similar to flow through a plane sudden expansion.

Bibliography

[1] N. Alleborn, K. Nandakumar, H. Raszillier, and F. Durst. Further contributions on the two-dimensional flow in a sudden expansion. *Journal of Fluid Mechanics*, 330:169–188, 1997.

[2] S. Allmaras. Analysis of semi-implicit preconditioners for multigrid solution of the 2-D compressible Navier-Stokes equations. *AIAA Paper 95-1651-CP*, 1995.

[3] M. Amitay and F. Cannelle. Evolution of finite span synthetic jets. *Physics of Fluids*, 18:054101, 2006.

[4] M. Amitay, A. M. Honohan, M. A. Trautman, and A. Glezer. Modification of the aerodynamic characteristics of bluff bodies using fluidic actuators. In *28th AIAA Fluid Dynamics Conference 97–2004*, 1997.

[5] M. Amitay, V. Kibens, D. E. Parekh, and A. Glezer. Flow reattachment dynamics over a thick airfoil controlled by synthetic jet actuators. In *37th AIAA Aerospace Science Meeting 99–1001*, 1999.

[6] M. Amitay, A. M. Honohan, and A. Glezer. Aerodynamic control using synthetic jets. In *AIAA Fluids 2000 Meeting 2000–2401*, 2000.

[7] M. Amitay, D. R. Smith, V. Kibens, D. E. Parekh, and A. Glezer. Aerodynamic flow control over an unconventional airfoil using synthetic jets actuators. *AIAA Journal*, 39:361–370, 2001.

[8] J. D. Anderson. *Computational Fluid Dynamics The Basics with Applications*. McGraw-Hill, 1995.

[9] U. M. Ascher and L. R. Petzold. *Computer Methods for Ordinary Differential Equations and Differential-Algebraic Equations*. SIAM, Philadelphia, PA, 1996.

[10] L. H. Back and E. J. Roshke. Shear-layer flow regimes and wave instabilities and reattachment lengths downtown of an abrupt circular channel expansion. *Journal of Applied Mechanics*, 39:677, 1972.

[11] M. J. Baines and P. K. Sweby. A flux limiter based on Fromm's scheme. Technical report, Department of Mathematics, University of Reading, UK., 1984.

[12] N. S. Bakhvalov. On the convergence of a relaxation method with natural constraints on the elliptic operator. *USSR Comput. Math. Phys.*, 6:101–104, 1966.

[13] J. Bardina, J. H. Ferziger, and W. C. Reynolds. Improved subgrid scale models for large eddy simulation. In *13th AIAA Fluid and Plasma Dynamics Conference,*, number AIAA-1980-1357, July 1980.

[14] F. Battaglia and G. Papadopoulos. Bifurcation characteristics of flows in rectangular sudden expansion channels. *Journal of Fluids Engineering*, 128:671–679, 2006.

[15] F. Battaglia, S. J. Tavener, A. K. Kulkarni, and C. L. Merkle. Bifurcation of low reynolds number flows in symmetric channels. *AIAA Journal*, 35:99–105, 1997.

[16] R. Betchov and W. O. Criminale. *Stability of Parallel Flows*. Academic Press, 1967.

[17] J. P. Boris and D. L. Book. Flux corrected transport: I. SHASTA, a fluid transport algorithm that works. *Journal of Computational Physics*, 11:38–69, 1973.

[18] J. P. Boris, F. F. Grinstein, E. S. Oran, and R. J. Kolbe. New insights into large eddy simulation. *Fluid Dynamics Research*, 10:199–228, 1992.

[19] A. Brandt. Multi-level adaptive solutions to boundary value problems. *Mathematics of Computation*, 31:333–390, 1977.

[20] A. Brandt. Multi-level adaptive techniques (MLAT) for fast numerical solution to boundary value problems. In *Proc. 3rd International Conference on Numerical Methods in Fluid Mechanics*, volume 18 of *Lecture Notes in Physics*. Springer-Verlag, Berlin and New York, 1973.

[21] A. Brandt. Multigrid Techniques: 1984 Guide with Applications to Fluid Dynamics. Technical report, The Weizmann Institute of Science, Rehovot, Israel, 1984.

[22] M. Breuer and D. Hänel. A dual time-stepping method for 3D viscous incompressible vortex flows. *Computers and Fluids*, 22(4-5):467–484, 1993.

[23] G. L. Brown and A. Roshko. On density effects and large structure in turbulent mixing layers. *Journal of Fluid Mechanics*, 64:775–816, 1974.

[24] P. E. O. Buelow, S. Venkateswaran, and C. L. Merkle. Effect of grid aspect ratio on convergence. *AIAA Journal*, 32(12):2401–2408, 1994.

[25] F. Cannelle and M. Amitay. Synthetic jets: Spatial evolution and transitory behaviour. In *AIAA Fluid Dynamics Conference, Reno, NV*, 2005.

[26] S. Carpy and R. Manceau. Turbulence modelling of statistically periodic flows: Synthetic jet into quiescent air. *International Journal of Heat and Fluid Flow*, 27:756–767, 2006.

[27] J. E. Cater and J. Soria. The evolution of round zero-net-mass-flux jets. *Journal of Fluid Mechanics*, 472:167, 2002.

[28] J. L. Chang and D. Kwak. On the method of pseudo compressibility for numerically solving incompressible flows. In *AIAA 22nd Aerospace Sciences Meeting*, number AIAA Paper 84-0252, 1984.

[29] W. Chedron, F. Durst, and J. H. Whitelaw. Asymmetric flows and instabilities in symmetric ducts with sudden expansions. *Journal of Fluid Mechanics*, 84: 13–31, 1978.

[30] F. J. Chen, C. Yao, G. B. Beeler, R. G. Bryany, and R. L. Fox. Development of synthetic jet actuators for active flow control at NASA langley. In *AIAA Meeting Fluids 2000, Denver CO*, June 2000.

[31] T. P. Chiang, T. W. H. Sheu, and S. K. Wang. Side wall effects on the structure of laminar flows over a plane-symmetric sudden expansion. *Computers and Fluids*, 29:467–492, 2000.

[32] T. P. Chiang, Tony. W. H. Sheu, Robert. R. Hwang, and A. Sau. Spanwise bifurcation in plane-symmetric sudden-expansion flows. *Physical Review E*, 65:016306–1–16, 2001.

[33] T. P. Chiang, T. W. H. Sheu, and R. R. Hwang. Numerical studies of a three-dimensional flow in suddenly contracted channels. *Physics of Fluids*, 14:1601–1616, 2002.

[34] D. Choi and C. L. Merkle. Application of time iterative schemes to incompressible flow. *AIAA Journal*, 23(10):1518–1524, October 1985.

[35] A. J. Chorin. A numerical method for solving incompressible viscous flow problems. *Journal of Computational Physics*, 2:12–26, 1967.

[36] A. J. Chorin and J. E. Marsden. *A Mathematical Introduction to Fluid Mechanics*. Springer-Verlag, 1993.

[37] P. Colella and P. R. Woodward. The Piecewise Parabolic Method (PPM) for gas-dynamical simulations. *Journal of Computational Physics*, 54:174–201, 1984.

[38] J. Cousteix. Turbulence et couche limite (in french). CEPADUES-Editions France, 1989.

[39] A. Crook and N. J. Wood. Measurements and visualisations of synthetic jets. *AIAA Paper 0145*, 2001.

[40] J. Cui and R. K. Agarwal. Three-dimensional computation of a synthetic jet in quiescent air. *AIAA Journal*, 44:2857–2865, 2006.

[41] J. Cui and R. K. Argarwal. 3D CFD validation of a synthetic jet in quiescent air (NASA Langley workshop validation Case 1). *AIAA Paper 2222*, 2004.

[42] S. A. Davis and A. Glezer. Mixing control of fuel jets using synthetic jet technology. In *AIAA 37th Aerospace Science Meeting 99–0447*, 1999.

[43] S. F. Davis. Simplified second order Godunov-type methods. *SIAM Journal on Scientific and Statistical Computing*, 9:445–473, 1988.

[44] S. R. N. De Zilwa, L. Khezzar, and J. H. Whitelaw. Flows through plane sudden-expansions. *International Journal for Numerical Methods in Fluids*, 32:313–329, 2000.

[45] D. Drikakis. Uniformly high order methods for unsteady incompressible flows. In E. F. Toro, editor, *Godunov Methods: Theory and Applications*, pages 263–283. Kluwer Academic Publishers, 2001.

[46] D. Drikakis. Bifurcation phenomena in incompressible sudden expansion flows. *Physics of Fluids*, 9(1):76–87, January 1997.

[47] D. Drikakis. *Godunov Methods: Theory and Applications.*, chapter Uniformaly high-order methods for unsteady incompressible flows., pages 263–283. Kluwer Academic Publishers, 2001.

[48] D. Drikakis. Advances in turbulent flow computations using high-resolution methods. *Progress in Aerospace Sciences*, 39:405–424, 2003.

[49] D. Drikakis and B. Geurts. *Turbulent Flow Computation*. Kluwer-Academic Publishers, 2002.

[50] D. Drikakis and W.J. Rider. *High-Resolution Methods for Incompressible and Low-Speed Flows*. Springer, 2004.

[51] D. Drikakis, P. A. Govatsos, and D. E. Papatonis. A characteristic-based method for incompressible flows. *International Journal for Numerical Methods in Fluids*, 19:667–685, 1994.

[52] D. Drikakis, O. P. Iliev, and D. P. Vassileva. A non-linear multigrid method for the three-dimensional incompressible navier-stokes equations. *Journal of Computational Physics*, 146:301–321, 1998.

[53] F. Durst, A. Melling, and J. H. Whitelaw. Low reynolds number flow over a plane symmetrical sudden expansion. *Journal of Fluid Mechanics*, 64:111–128, 1974.

[54] F. Durst, J. Pereira, and C. Tropea. The plane symmetric sudden-expansion flow at low reynolds numbers. *Journal of Fluid Mechanics*, 248:567–581, 1993.

[55] A. Eberle. 3-D Euler calculation using characteristic flux extrapolation. paper 85–0119, AIAA, 1985.

[56] B. Einfeldt. On Godunov-type methods for gas dynamics. *SIAM Journal on Numerical Analysis*, 25(2):294–318, 1988.

[57] J. Farmer, L. Martinelli, and A. Jameson. A fast multigrid method for solving incompressible hydrodynamic problems with free surfaces. *AIAA Paper*, 93-076, 1993.

[58] H. F. Fasel. *Numerical solution of the complete Navier-Stokes equations for the simulation of unsteady flows*. Number 771 in Lecture notes in mathematics. Springer-Verlag, Berlin, 1980.

[59] R. M. Fearn, T. Mullin, and K. A. Cliffe. Nonlinear flow phenomena in a symmetric sudden expansion. *Journal of Fluid Mechanics*, 211:595–608, 1990.

[60] R. P. Fedorenko. On the speed of convergence of an iteration process. *USSR Comput. Math. and Math. Phys*, 4:227–235, 1964.

[61] E. A. Foumeny, D. B. Ingham, and A. J. Walker. Bifurcations of incompressible flow through plane symmetric channel expansions. *Computers and Fluids*, 25: 335–351, 1996.

[62] C. Fureby and F. F. Grinstein. Large eddy simulation of high Reynolds number free and wall bounded flows. *Journal of Computational Physics*, 181:68–97, 2002.

[63] C. Fureby and F. F. Grinstein. Monotonically integrated large eddy simulation of free shear flows. *AIAA Journal*, 37:544–557, 1999.

[64] T. Gatski and C. Rumsey. CFD validation of synthetic jets and turbulent separation control. `http://cfdval2004.larc.nasa.gov`.

[65] A. Glezer and M. Amitay. Synthetic jets. *Annual Review of Fluid Mechanics*, 34:503–529, 2002.

[66] S. K. Godunov. Finite difference method for numerical computation of discontinuous of the equations of fluid dynamics. *Matematicheski Sbornik*, 47: 271–306, 1959.

[67] R. J. Goldstein, V. L. Eriksen, R. M. Olson, and E. R. G. Eckert. Laminar separation, reattachment, and transition of the flow over a downstream-facing step. *Journal of Basic Engineering, Transactions of the ASME*, 92:732–739, 1970.

[68] S. Gottleib, C.-W. Shu, and E. Tadmor. Strongly stability preserving high-order time discretization methods. *SIAM Review*, 43:89–112, 2001.

[69] D. F. Griffiths and J. M. Sanz-Serna. On the scope of the method of modified equations. *SIAM Journal on Scientific and Statistical Computing*, 7:994–1008, 1986.

[70] F. F. Grinstein and C. R. DeVore. Dynamics of coherent structures and transition to turbulence in free square jets. *Physics of Fluids*, 8:1237–1251, 1996.

[71] D. Guo and L. D. Kral. Numerical simulation of the interaction of adjacent synthetic jet actuators. In *AIAA Fluids 2000 Meeting, Denver, Colorado.*, 2000.

[72] W. Hackbusch. Ein iteratives verfahren zur schnellen auflösung elliptisccher randwert probleme. Technical report, Universitat Köln, 1976.

[73] W. Hackbush. *Multigrid Methods and Applications*. Springer Verlag, Berlin, Heidelberg, New York, Tokyo, 1985.

[74] F. H. Harlow and J. E. Welch. Numerical calculation of time dependent viscous incompressible flow with free surface. *Physics of Fluids*, 8:2182–2189, December 1965.

[75] A. Harten. High resolution schemes for hyperbolic conservation laws. *Journal of Computational Physics*, 49:357–393, 1983. Reprinted in Volume 135 Number 2, pp. 260–278, August 1997.

[76] A. Harten, P. D. Lax, and B. Van Leer. On upstream differencing and Godunov-type schemes for hyperbolic conservation laws. *SIAM Review*, 25(1):35–61, 1983.

[77] T. Hawa and Z. Rusak. The dynamics of a laminar flow in a symmetric channel with a sudden expansion. *Journal of Fluid Mechanics*, 436:283–320, 2001.

[78] C. Hirsch. *Numerical Computation of Internal and External Flows: Volume 2*. Wiley-Interscience, 1988.

[79] C. Hirsch and N. Hakimi. Preconditioning methods for time-marching Navier-Stokes solvers. In *Solution Techniques for Large-Scale CFD Problems, CMAS*, pages 333–353. Jown Wiley & Sons, 1995.

[80] A. Jameson. Solution of the Euler equations for two dimensional transonic flow by a multigrid method. *Applied Mathemathics and Computation*, 13:327–356, 1983.

[81] A. Jameson. A vertex based multigrid algorithm for three-dimensional flow calculations. *ASME Symposium on Numerical Methods for Compressible Flows*, December 1986.

[82] A. Jameson. Computational transonics. *Communication Pure Applied Mathematics*, 41:507–549, 1988.

[83] M. Kadja and D. Touzopoulos. Use of new convection scheme and multigrid acceleration for indepth study of bifurcation in channel expansions. In *Proceedings, Computational & Asymptotic Methods, BAIL, International Conference on Boundary and Interior Layers (BAIL)*, pages 1–8, 2004.

[84] K. H. Kim and C. Kim. Accurate, efficient and monotonic numerical methods for multi-dimensional compressible flows Part II: Multi-dimensional limiting process. *Journal of Computational Physics*, 208:570–615, 2005.

[85] W. W. Kim and S. Menon. An unsteady incompressible Navier-Stokes solver for large eddy simulation of turbulent flows. *International Journal for Numerical Methods in Fluids*, 31:983–1017, 1999.

[86] D. A. Knoll, L. Chacon, L. G. Margolin, and V. M. Mousseau. Nonlinearly consistent approximations for multiple time scale systems. *Journal of Computational Physics*, 2002. LA–UR–02–0927.

[87] R. B. Kotapati and R Mittal. Time-accurate three-dimensional simulations of synthetic jets in quiescent air. In *43rd AIAA Aerospace Sciences Meeting and Exhibit, Reno, NV*, 2005.

[88] L. D. Kral, J. F. Donovan, A. B. Cain, and A. W. Cary. Numerical simulation of synthetic jet actuators. In *28th AIAA Fluids Dynamics Conference 97–1824*, 1997.

[89] H. Kudela. Viscous flow simulations of a two-dimensional channel flow with complex geometry using grid-particle vortex method,. In *Proceedings, Third International Workshop of Vortex Flow and Related Numerical.*, volume 7 of *European Series in Applied and Industrial Mathematics (ESAIM), Methods, Société de Mathématiques Appliquées et Industrielles, Toulouse, France.*, pages 215–224, 1999.

[90] H. Kuerten and B. Geurts. Compressible turbulent flow simulation with a multigrid multiblock method. In Proceedings of Copper Mountain Multigrid Conference, pages 305–315, 1993.

[91] D. Kwak, J. L. C. Chang, S. P. Shanks, and S. R. Chakravarthy. A three-dimensional incompressible navier-stokes flow solver using primative variables. *AIAA Journal*, 24(3):390–396, March 1986.

[92] D. J. Latornell and A. Pollard. Some observations on the evolution of shear layer instabilities in laminar flow through axisymmetric sudden expansions. *Physics of Fluids*, 29:2828, 1986.

[93] P. D. Lax. Weak solutions of non-linear hyperbolic equations and their numerical computation. *Communications on Pure and Applied Mathematics*, 7: 159–193, 1954.

[94] C. Y. Lee and D. B. Goldstein. Two-dimensional synthetic jet simulation. In *AIAA Fluids Meeting, Denver, Colorado*, 2000.

[95] D. Lee and B. van Leer. Progress in local preconditioning of the euler and navier-stokes equations. Technical Report 3328, AIAA, 1993.

[96] F. B. Lin and F. Sotiropoulos. Strongly-coupled multigrid method for 3D incompressible flows using near-wall turbulence closures. *Journal of Fluids Engineering*, 119:314–324, 1997.

[97] P. F. Linden, J. M. Redondo, and D. L. Youngs. Molecular mixing in Rayleigh-Taylor instability. *Journal of Fluid Mechanics*, 265:97–124, 1994.

[98] F. Liu and A. Jameson. Multigrid Navier-Stokes calculations for three-dimensional cascades. *AIAA Journal*, 31(10):1785–1791, 1993.

[99] T. Lorkowski, R. Rathnasingham, and K. S. Breuer. Small-scale forcing of a turbulent boundary layer. In *AIAA 28th Fluid Dynamics Conference 97–1792*, 1997.

[100] Li-Shi Luo. Symmetry breaking of flow in 2d symmetric channels: simulations by lattice-boltzmann method. *International Journal of Modern Physics C*, 8: 859–867, 1997.

[101] J. F. Lynn. *Multigrid solution of the Euler equations with local preconditioning.* PhD thesis, University of Michigan, USA, 1995.

[102] E. O. Macagno and T. K. Hung. Laminar eddies in a two dimensional conduit expansion. *Journal of Fluid Mechanics*, 28:43–, 1967.

[103] A. Majda and S. Osher. Propogation of error into regions of smoothness for accuracte difference approximations to hyperbolic equations. *Communications on Pure and Applied Mathematics*, 30:671–705, 1977.

[104] F. Mallinger and D. Drikakis. Instability in three dimensional unsteady stenotic flows. *International Journal of Heat and Fluid Flow*, 23:657–663, 2002.

[105] S. G. Mallinson, G. Hong, and J. A. Reizes. Some characteristics of synthetic jets. In *AIAA 30th Fluid Dynamics Conference, Norfolk, VA*, 1999.

[106] R. Manica and A. De Bartoli. Simulation of sudden expansion flows for power-law fluids. *Journal of Non-Newtonian Fluid Mechanics*, 121:35–40, 2004.

[107] L. G. Margolin and W. J. Rider. A rationale for implicit turbulence modeling. *International Journal for Numerical Methods in Fluids*, 39:821–841, 2002.

[108] L. G. Margolin, P. K. Smolarkiewicz, and Z. Sorbjan. Large eddy simulations of convective boundary layers using nonoscillatory differencing. *Physica D*, 133: 390–397, 1998.

[109] L. G. Margolin, P. K. Smolarkiewicz, and A. A. Wyszogrodzki. Implicit turbulence modeling for high reynolds number flows. *Journal of Fluids Engineering*, 124:862–867, 2002.

[110] W. W. Martin. *Anwendung der hydrodynamischen Stabilitätstheorie auf die Schwingung von Schützen. Doktor-Ingenieur dissertation.* PhD thesis, Universität Karlsruhe, 1974.

[111] W. W. Martin, E. Naudascher, and M. Padmanabhan. Fluid-dynamic excitation involving flow instability. In *A.S.C.E.*, volume 101, page 681, 1975.

[112] C. L. Merkle and M. Athavale. Time accurate unsteady incompressible flow algorithms based on artificial compressibility. *AIAA Paper 87-1137*, 1987.

[113] R. H. Miller. A horror story about integration methods. *Journal of Computational Physics*, 93:469–476, 1991.

[114] J. Mizushima and T. Inui. Transitions of three-dimensional flow through a rectangular duct with a suddenly expanded and contracted part. *Journal of the Physical Society of Japan*, 70:1171–1174, 2001.

[115] J. Mizushima and Y. Shiotani. Transitions and instabilities of flow in a symmetric channel with a suddenly expanded and contracted part. *Journal of Fluid Mechanics*, 434:355–369, 2001.

[116] J. Mizushima and Y. Shiotani. Structural instability of the bifurcation diagram for two-dimensional flow in a channel with a sudden expansion. *Journal of Fluid Mechanics*, 420:131–145, 2000.

[117] J. Mizushima, H. Okamoto, and H. Yamaguchi. Stability of flow in a channel with a suddenly expanded part. *Physics of Fluids*, 8:2933–2942, 1996.

[118] H. K. Moffatt. Viscous and resistive eddies near a sharp corner. *Journal of Fluid Mechanics*, 18:1–18, 1964.

[119] W. A. Mulder. A new multigrid approach to convection problems. *Journal of Computational Physics*, pages 303–323, 1989.

[120] M. O. Muller, L. P. Bernal, P. K. Miska, P. D. Washabaugh, and T. K. A. Chou. Flow structure and performace of axisymmetric synthetic jets. In *AIAA 39th Aerospace Science Meeting, Reno, Nevada.*, 2001.

[121] T. Mullin and K. A. Cliffe. Symmetry-breaking and the onset of time dependence in fluid mechanical systems. In *In Nonlinear Phenomena and Chaos, (ed. S. Sarkar), Adam Hilger*, pages 96–112, 1986.

[122] T. Mullin, S. Shipton, and S. J. Tavener. Flow in a symmetric channel with an expanded section. *Fluid Dynamics Research*, 33:433–452, 2003.

[123] P. Neofytou and D. Drikakis. Non-newtonian flow instability in a channel with a sudden expansion. *Journal of Non-Newtonian Fluid Mechanics*, 111(2-3): 127–150, 2003.

[124] E. S. Oran and J. P. Boris. *Numerical Simulation of Reactive Flow*. Cambridge University Press, 2000.

[125] Y. Ouwa, M. Watanabe, and Y. Matsuoka. Behaviour of a confined plane jet in a rectangular channel at low reynolds number I. general flow characteristics. *Japanese Journal of Applied Physics, Part 1.*, 25:754–761, 1986.

[126] S. V. Patanker. *Numerical heat transfer and fluid flow.* Hemisphere Publishing, 1980.

[127] S. Patel and D. Drikakis. Numerical effects on the prediction of flow instabilities in channels with sudden-expansions. Technical Report 44616, Proceedings of ASME International Mechanical Engineering Congress and Exposition, Washington D. C., November 2003.

[128] C. D. Perkins and D. Hazen. Some recent advances in boundary layer and circulation control. In *4th Anglo-American Aeronautical Conference*, 1953.

[129] R. Peyret and T. D. Taylor. *Computational Methods for Fluid Flow*. Springer-Verlag: New York, 1983.

[130] N. A. Pierce and M. B. Giles. Preconditioned multigrid methods for compressible flow calculations on stretched meshes. *Journal of Computational Physics*, 136:425–445, 1997.

[131] D. H. Porter, A. Pouquet, and P. R. Woodward. Kolmogorov-like spectra in decaying three-dimensional supersonic flows. *Physics of Fluids*, 6:2133–2142, 1994.

[132] L. Prandtl. *Prandtl's Essential of Fluid Mechanics*, volume 158 of *Applied Mathematical Sciences*. Springer, second edition, 2004.

[133] M. M. Rai. A implicit, conservative, zonal-boundary scheme for euler equation calculations. *AIAA paper 85-0488*, 1985.

[134] G. D. Raithby and G. E. Scheider. Numerical solution of problems in incompressible fluid flow. treatment of the velocity-pressure coupling. *Numerical Heat Transfer*, 2:417–440, 1979.

[135] O. K. Rediniotis, J. Ko, X. Yue, and A. J. Kurdila. Synthetic jets, their reduced order modeling and applications to flow control. *AIAA Paper 99-1000*, 1999.

[136] A. Revuelta. On the two-dimensional flow in a sudden expansion with large expansion ratios. *Physics of Fluids*, 17:028102, 2005.

[137] A. Revuelta, A. L. Sánchez, and A. Linán. Confined axisymmetric laminar jets with large expansion ratios. *Journal of Fluid Mechanics*, 456:319–352, 2002.

[138] O. Reynolds. An experimental investigation of the circumstances which determine whether the motion of water shall be direct or sinuous, and of the law of resistance in parallel channels. *Philosophical Transactions of the Royal Society of London*, 174:935–982, 1883.

[139] O. Reynolds. On the dynamic theory of incompressible viscous fluids and the determination of the criterion. *Philosophical Transactions of the Royal Society of London*, 186:123–164, 1894.

[140] D. P. Rizzetta, M. R. Visbal, and M. J. Stanek. Numerical investigation of stnthetic jet flowfields. In *29th AIAA Fluid Dynamics Conference, Albuquerque, New Mexico*, 1998.

[141] A. Rizzi and L. E. Eriksson. Computation of inviscid incompressible flow with rotation. *Journal of Fluid Mechanics*, 153:275–312, 1985.

[142] D. Rockwell and E. Naudascher. Self-sustained oscillations of impinging free shear layers. *Annual Review of Fluid Mechanics*, 330:67–94, 1979.

[143] P. L. Roe. Some contributions to the modelling of discontinuous flows. In B. Engquist, editor, *Lectures in Applied Mathematics*, volume 22, pages 163–193, 1985.

[144] S. E. Rogers and D. Kwak. Upwind differencing scheme for the time-accurate incompressible Navier-Stokes equations. *AIAA Journal*, 28(2):253–262, 1990.

[145] S. E. Rogers, D. Kwak, and C. Kiris. Steady and unsteady solutions of the incompressible Navier-Stokes equations. *AIAA Journal*, 29(4):603–610, 1991.

[146] C. L. Rumsey, T. B. Gatski, W. L. Sellers, V. N. Vatsa, and S. A. Viken. Summary of the 2004 CFD validation workshop on synthetic jets and turbulent separation control. *AIAA Paper 2217*, 2204.

[147] Z. Rusak and T. Hawa. A weakly nonlinear analysis of the dynamics of a viscous flow in a symmetric channel with a sudden expansion. *Phys. Fluids*, 11:3629–3636, 1999.

[148] V. V. Rusanov. Calculation of interaction of non-steady shock waves with obstacles. *Journal of Computational Mathematics and Fluids*, 1:267–279, 1961.

[149] P. Sagaut. *Large Eddy Simulation for Incompressible Flows*. Springer, third edition, 2006.

[150] W. Saric. Görtler vortices. *Annual Review of Fluid Mechanics*, 26:379–409, 1994.

[151] A. Sau. Vortex dynamics and mass entrainment in a rectangular channel with a suddenly expanded and contracted part. *Physics of Fluids*, 14(9):3280–3308, 2002.

[152] A. Sau. Three-dimensional simulations of flow through a rectangular sudden expansion. *Physics of Fluids*, 11(10):3003–3016, 1999.

[153] E. Schreck and M. Schäfer. Numerical study of bifurcation in three-dimensional channel expansions. *Computers and Fluids*, 29:583–593, 2000.

[154] A. Seifert and L. G. Pack. Oscillatory control of separation at high reynolds numbers. *AIAA Journal*, 37(9):1062–1071, 1999.

[155] M. Shapira, D. Degani, and D. Weihs. Stability and existance of multiple solutions for viscous flow in suddenly enlarged chanels. *Computers and Fluids*, 18: 239–258, 1990.

[156] H. J. Sheen, W. J. Chen, and J. S. Wu. Flow patterns for an annular flow over an axisymmetric sudden expnasion. *Journal of Fluid Mechanics*, 350:177–188, 1997.

[157] C. Sheng, L. K. Taylor, and D. L. Whitfield. An efficient multigrid acceleration for solving the 3D incompressible Navier-Stokes equations in generalized curvilinear coordinates. *AIAA Paper 93-2335*, 1993.

[158] C. W. Shu and S. Osher. Efficient implementation of essentially non-oscillatory shock capturing schemes. *Journal of Computational Physics*, 77:439–471, 1988.

[159] J. Smagorinsky. General circulation experiments with the primitive equations. I. the basic experiment. *Monthly Weather Review*, 101:99–164, 1963.

[160] B. L. Smith and A. Glezer. The formation and evolution of synthetic jets. *Physics of Fluids*, 31:2281–2297, 1998.

[161] B. L. Smith and A. Glezer. Vectoring and small-scale motions effected in free shear flows using synthetic jet actuators. In *AIAA 35th Aerospace Science Meeting*, 1997.

[162] B. L. Smith and A. Glezer. Vectoring of a high aspect ratio air jet using zero-net-mass-flux control jet. *Bull. Am. Phys. Soc.*, 39:1894, 1994.

[163] B. L. Smith, M. A. Trautman, and A. Glezer. Controlled interactions of adjacent synthetic jets. In *AIAA 37th Aerospace Science Meeting 99–0069*, 1999.

[164] I. J. Sobey and P. G. Drazin. Bifurcations of two dimensional channel flows. *Journal of Fluid Mechanics*, 171:263–287, 1986.

[165] I.J. Sobey. Observation of waves during oscillatory channel flow. *Journal of Fluid Mechanics*, 151:395–426, 1985.

[166] W. Y. Soh and J. W. Goodrich. Unsteady solution of incompressible Navier-Stokes equations. *Journal of Computational Physics*, 79:113–134, 1988.

[167] R. J. Spiteri and S. J. Ruuth. A class of optimal high-order strong-stability-preserving time discretization methods. *SIAM Journal of Scientific Computing*, 40(2):469–491, 2002.

[168] J. L. Steger. Thoughts on the chimera method of simulation of three dimensional viscous flows. In *Computational Fluid Dynamics Symposium on Aeropropulsion*, 1991.

[169] J. L. Steger and P. Kutler. Implicit finite difference procedures for the computation of vortex wakes. *AIAA Journal*, 15:581–590, 1977.

[170] R. Temam. *Navier-Stokes Equations: Theory and Numerical Analysis*. North-Holland, 1984.

[171] M Thiruvengadam, J. H. Nie, and B. F Armaly. Bifurcated three-dimensional forced convection in plan symmetric sudden expansion. *International Journal of Heat and Mass Transfer*, 48:3128–3139, 2005.

[172] B. Thornber, D. Drikakis, and R. Williams. The dissipation of kinetic energy within Godunov schems 1: Theoretical analysis. *Submitted to Journal of Computational Physics*, 2007.

[173] B. Thornber, A. Mosedale, and D. Drikakis. The dissipation of kinetic energy within Godunov schems II: Numerical modification. *Submitted to Journal of Computational Physics*, 2007.

[174] E. Toro. *Riemann solvers and numerical methods for fluid dynamics*. Springer-Verlag, 1997.

[175] E. F. Toro, M. Spruce, and W. Speares. Restoration of the contact surface in the HLL-Riemann solver. *Shock Waves*, 4:25–34, 1994.

[176] Y. Y. Tsui and C. K. Wang. Calculation of laminar separated f low in symmetric two-dimensional diffusers. *Journal of Fluids Engineering*, 117:612–618, 1995.

[177] E. Turkel. Preconditioned methods for solving the incompressible and low speed compressible equations. *Journal of Computational Physics*, 72:277–298, 1987.

[178] E. Turkel. A review of preconditioning methods for fluid dynamics. *Applied Numerical Mathematics*, 12:257–284, 1993.

[179] E. Turkel. Preconditioning techniques in computational fluid dynamics. *Annual Review of Fluid Mechanics*, 31:385–416, 1999.

[180] Y. Utturkar, R. Holman, R. Mittal, B. Carroll, M. Sheplak, and L. Catafesta. A jet formation criterion for synthetic jet actuators. *AIAA Paper 0636*, 2003.

[181] G. D. van Albada, B. van Leer, and W. W. Roberts. A comparative study of computational methods in cosmic gas dynamics. *Astronomy and Astrophysics*, 108:76–84, 1982.

[182] B. van Leer. Towards the ultimate conservative differencing scheme I: The quest for monotonicity. In *Lecture Notes in Physics*, pages 163–168, Berkeley California, 1973.

[183] B. van Leer. Towards the ultimate conservative difference scheme. II. Monotonicity and conservation combined in a second-order scheme. *Journal of Computational Physics*, 14:361–370, 1974.

[184] B. van Leer. Towards the ultimate conservative difference scheme. IV. A new approach to numerical convection. *Journal of Computational Physics*, 23:276–299, 1977.

[185] B. van Leer. Towards the ultimate conservative difference scheme. III. Upstream-centered finite-difference schemes for ideal compressible flow. *Journal of Computational Physics*, 23:263–275, 1977.

[186] B. van Leer. Towards the ultimate conservative difference scheme V. A second order sequel to Godunov's method. *Journal of Computational Physics*, 32:101–136, 1979.

[187] B. van Leer, W. T. Lee, and P. L. Roe. Characteristic time-stepping or local preconditioning of the Euler equations. *AIAA Paper 91-1552*, 1991.

[188] R. F. Warming and B. J. Hyett. The modified equation approach to the stability and accurcay analysis of finite-difference methods. *Journal of Computational Physics*, 14:159–179, 1974.

[189] N. K. Yamaleev and M. H. Carpenter. A quasi-1-D model for arbitrary 3-D synthetic jet actuators. In *43rd AIAA Aerospace Sciences Meeting and Exhibit, Reno, NV*, 2005.

[190] H. Yan and D. Knight. Large eddy simulation of supersonic flat-plate boundary layers using the MILES technique. *Journal of Fluids Engineering*, 124:868–875, 2002.

[191] C. Yao, F. J. Chen, D. Neuhart, and J. Harris. Synthetic jet flow field database for cfd validation. In *2nd AIAA Flow Control Conference*, 2nd AIAA Flow Control Conference, 2004.

[192] D. L. Youngs. Application of miles to rayleigh-taylor and richtmyer-meshkov mixing. In *16th AIAA Computational Fluid Dynamics Conference*, June 2003.

[193] D. L. Youngs. Three-dimensional numerical simulation of turbulent mixing by Rayleigh-Taylor instability. *Physics of Fluids A*, 3:1312–1320, 1991.

[194] D. L. Youngs. Numerical simulation of mixing by Rayleigh-Taylor and Richtmyer-Meshkov instabilities. *Lasers and Particle Beams*, 12:725–750, 1994.

[195] O. C. Zienkiewicz and R. L. Taylor. *The Finite Element Method, Fourth Edition, Volume 1: Basic Formulation and Linear Problems*. McGraw-Hill, New York, 1980.

[196] J. Zóltak and D. Drikakis. Hybrid upwind methods for the simulation of unsteady shock-wave diffraction over a cylinder. *Computer Methods in Applied Mechanics and Engineering*, 162:165–185, 1998.

APPENDIX A

Overview of the NASA Langley Workshop on CFD Validation of Synthetic Jets and Turbulent Separation Control

A summary of the validation workshop was written by Rumsey et al. [146] containing brief descriptions and results obtained for the three different cases. This Appendix provides a brief description of the experimental setup as well as a summary of the workshop results.

A.1 Experimental Setup

The actuator used in the experiments was based on the earlier design by Chen et al. [30]. Figure A.1 shows the design of the actuator cavity. The synthetic jet emanates from a high aspect ratio rectangular slot of dimensions 1.25mm wide and 35.56mm long. The slot is covered by a glass enclosure, 2 ft $\times$ 2 ft $\times$ 2 ft in dimension. This glass enclosure isolates the synthetic jet from the ambient air and provides a means of containing the seeding particles used in the experimental measurements. The flow was driven by a side mounted piezoelectric diaphragm with an approximate diameter of 2 inches. The diaphragm was operated at a frequency of 444.7 Hz, which was slightly away from the cavity resonant frequency of 500 Hz. The flow medium was air at standard atmospheric conditions at sea level and the resulting maximum velocity obtained at a position slightly downstream of the slot exit by Particle Image Velocimetry (PIV) was 28 m/s. Three experimental measuring techniques, namely: PIV, Laser Doppler Velocimetry (LDV) and Hot-wire Anemometry (HW), were used to obtain velocity distributions and flow field visualisations. The details of these techniques will not be discussed here and the reader is referred to the text of Yao et al. [191] for further details. For each measurement technique a new diaphragm was installed in the actuator due to actuator failures or changes in the actuator performance. The experiments found that a close comparison was obtained between the LDV and PIV results with respect of the velocity profile, but found large discrepancies in the velocity magnitude predicted by these two techniques. The hot-wire data showed a faster decay of the synthetic jet and matched well with the LDV data in the far-fields.

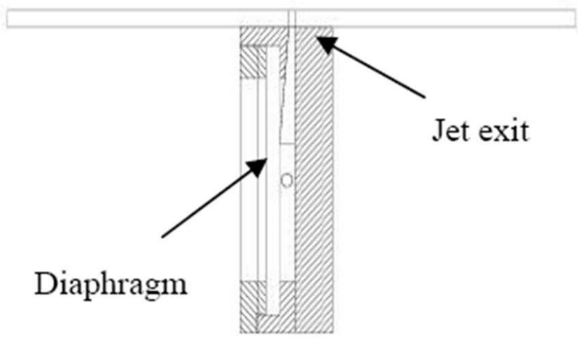

Figure A.1: Schematic diagram of cavity, reproduced from Yao et al. [191].

In order to be able to compare CFD results with each other and also with the experimental data a definition for the phase computation was outlined for the workshop. This definition has hence been implemented for the current investigation and is described below in a series of steps.

1. Output vertical phase-averaged velocity at the following point in space (above the slot) as a function of time step number: $(x, y, z) = (0, 0.1, 0)$mm. Find the maximum (umax)and minimum (umin) streamwise velocities over the course of one phase-averaged period.

2. Compute the mid-value uavg = (umax − umin)/2

3. Define Phase = 340° as the time when the velocity at this location approximately equals uavg (INCREASING). All other phases can be referenced from this, via the following relationship:

$$\text{Phase} = (\text{iter} - \text{it340}) \times 360/\text{nstep} + 360 \tag{A.1.1}$$

where:

iter	=	iteration (or time step) number
nstep	=	number of time steps per cycle
it340	=	iteration number when Phase = 340 according to the above.

A.2 Summary of Results

As this case was part of a workshop on CFD validation, it is important to discuss the various contributions and outcomes to the workshop. Overall, there were 8 contributors who ran in total 25 separate cases. Tables A.1 and A.2 summarise the methods and grids used respectively, by the various contributors. Most of the runs were computed in 2-dimensions with only a few people opting to compute the full 3-dimensional domain. It should be noted that at the time of the workshop none of the contributors who ran 3-dimensional computations modelled the actual shape of the cavity, including the circular diaphragm and instead opted to compute the flow using periodicity in the direction aligned with the slot's long axis. The paper by Cui and Argarwal [41] which followed shortly after the workshop shows results for both 2-dimensional and fully 3-dimensional simulations. The cavity and diaphragm were modelled as based on the actual experimental setup. Cui and Argarwal [41] found that the 3-dimensional simulations predicted most of the flow field quantities in better agreement than the 2-dimensional simulations in relation to the experimental data. The 3-dimensional results also predicted the spreading of the jet width more accurately than the 2-dimensional results. However, they conclude that the 3-dimensional simulations do not have a clear advantage in predicting the over all flow field features for this case. Many of the contributors to the workshop did not model the cavity choosing instead to apply a sinusoidal velocity profile boundary condition directly to the slot exit. Those who did model the cavity either applied a time varying velocity profile to the side of the cavity where the diaphragm was located, derived from diaphragm-centre-displacement (ONERA-flu3m and UKY-ghost) or applied a similar boundary condition but based on best matching of the data at the slot exit (WASHU-wind and NASA-tlns3d). The contributors from GWU altered the cavity shape and applied a time-varying velocity boundary condition to the bottom wall. Kotapati and Mittal [87] carried out direct numerical simulations for this particular workshop case. They built on their previous contribution (GWU) using the same geometry but adjusted the Reynolds number to the upper bound of the average velocity during the ejection phase from the experimental data. Their contribution at the workshop used the Reynolds number calculated from the lower bound of the average velocity during the ejection phase. Various other contributors have published their results from the workshop including; Yamaleev and Carpenter [189]; Carpy and Manceau [26]. Some of the above results from the workshop have been used as a comparison to the data obtained in this thesis and are discussed in detail in Chapter 7.

The results from the workshop can be grouped into three sections, i.e., phase-averaged velocity profiles, phase-averaged velocity contours and time-averaged velocity profiles. Figures A.2-A.15 show a selection of the results submitted to the workshop by various contributors. A full documentation of the workshop summary can be found at the workshop website [64] or in the report written by Rumsey et al. [146].

Table A.1: Summary of submissions. (Table reproduced from Rumsey et al. [146]).

Label	Organisation	Authors	Method
ONERA-flu3m-les-3d ONERA-flu3m-lam ONERA-flu3m-sa	ONERA	Mary	LES, 3-D Laminar N-S URANS, SA model
UKY-ghost-sst UKY-ghost-sst (fine)	U. Kentucky	Huang *et al*	URANS, SST model URANS, SST model(f)
GWU-vicar3d-3d (fine) GWU-vicar3d-3d GWU-vicar3d-3d	GWU	Rupesh *et al*	LaminarN-S, (f), 3-D Laminar N-S, 3-D Laminar N-S, larger domain, 3-D
NCAT-quas1d+rans	NC A&T State U. & NASA LaRC	Yamaleev *et al*	Reduced-order method in slot +4th order laminar N-S
POIT-saturne-ke0.5c POIT-saturne-ke0.25c POIT-saturne-ke0.25f POIT-saturne-rsm0.5c POIT-saturne-rsm0.125c	U. Poitiers	Carpy & Manceau	URANS, k-e model, *dt* = 0.5, coarse grid URANS, k-e model, *dt* = 0.25, coarse grid URANS, k-e model, *dt* = 0.25, fine grid URANS, RSM model, *dt* = 0.5, coarse grid URANS, RSM model, *dt* = 0.125, coarse grid
WARWICK-neat-ke WARWICK-neat-kenon WARWICK-neat-easm	U. Warwick & U. Wales	Preece *et al*	URANS, k-e model URANS, nonlinear k-e URANS, EASM model
WASHU-wind-sa WASHU-wind-sst WASHU-wind-sstles	Washington U.	Cui & Agarwal	URANS, SA model URANS, SST model SST-LES
NASA-tlns3d-sa NASA-tlns3d-sa(coar) NASA-tlns3d-sa(fine) NASA-tlns3d-sa(low-dt) NASA-tlns3d-sst	NASA LaRC	Vatsa & Turkel	URANS, SA model URANS, SA coarse URANS, SA fine URANS, SA model, with lower dt URANS, SST model

Table A.2: Summary of grids and time steps. (Table reproduced from Rumsey et al. [146]).

Label	Grid type	Grid size	Time steps/ cycles
ONERA-flu3m-les-3d	3D structured (P)	930,000 cells	5000
ONERA-flu3m-lam	2D structured	51,700 cells	5000
ONERA-flu3m-sa	2D structured	51,700 cells	5000
UKY-ghost-sst	2D structured	63,553 points	2880
UKY-ghost-sst (fine)	2D structured	198,545 points	2880
GWU-vicar3d-3d (fine)	3D structured (P)	696,960 points	14,000
GWU-vicar3d-3d	3D structured (P)	464,640 points	14,000
GWU-vicar3d-3d	3D structured (P)	696,960 points	14,000
NCAT-quas1d+rans	3D structured	98,379 points	118,567
POIT-saturne-ke0.5c	2D structured (no cav)	15,707 cells	720
POIT-saturne-ke0.25c	2D structured (no cav)	15,707 cells	1440
POIT-saturne-ke0.25f	2D structured (no cav)	62,828 cells	1440
POIT-saturne-rsm0.5c	2D structured (no cav)	15,707 cells	720
POIT-saturne-rsm0.125c	2D structured (no cav)	15,707 cells	2880
WARWICK-neat-ke	2D structured (no cav)	4851 points	3600
WARWICK-neat-kenon	2D structured (no cav)	4851 points	3600
WARWICK-neat-easm	2D structured (no cav)	4851 points	3600
WASHU-wind-sa	2D structured	35,986 points	10,000
WASHU-wind-sst	2D structured	35,986 points	10,000
WASHU-wind-sstles	2D structured	35,986 points	10,000
NASA-tlns3d-sa	2D structured	63,553 points	72
NASA-tlns3d-sa(coar)	2D structured	16,107 points	72
NASA-tlns3d-sa(fine)	2D structured	87,753 points	72
NASA-tlns3d-sa(low-dt)	2D structured	63,553 points	144
NASA-tlns3d-sst	2D structured	63,553 points	72

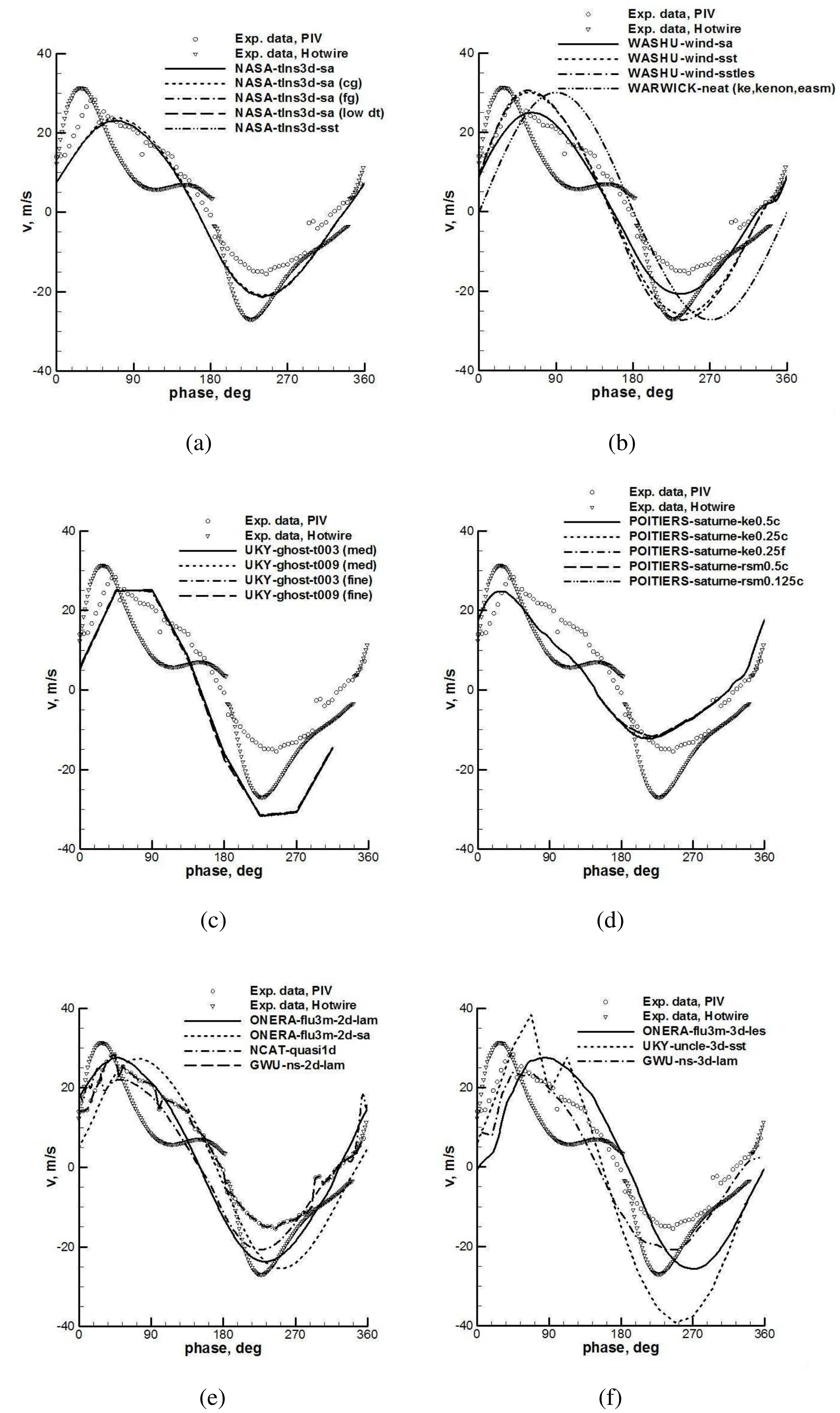

Figure A.2: Computed results from the CFD validation workshop of phase-averaged u-velocity at 0.1mm above the centre of the slot exit.

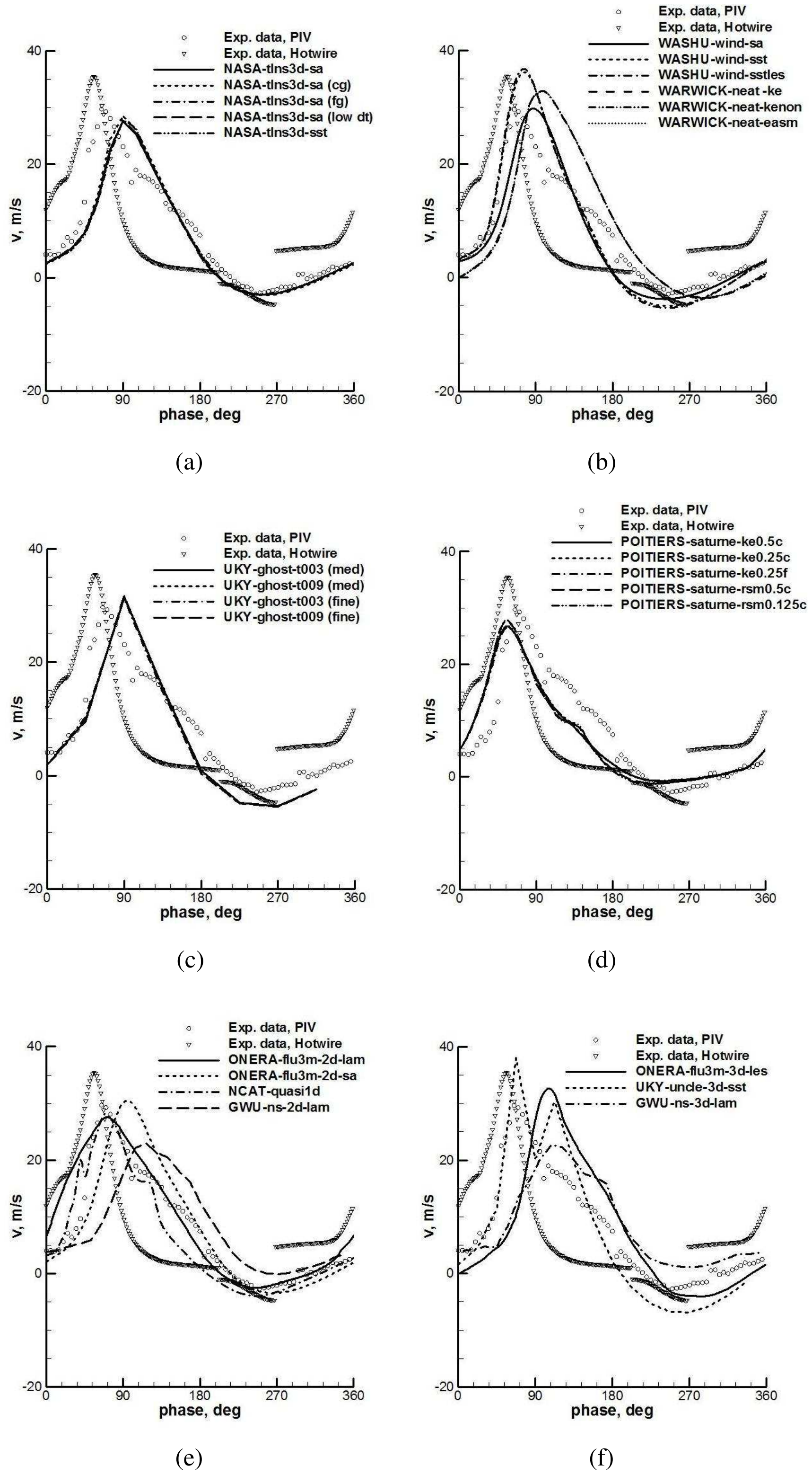

Figure A.3: Computed results from the CFD validation workshop of phase-averaged u-velocity at 2mm above the centre of the slot exit.

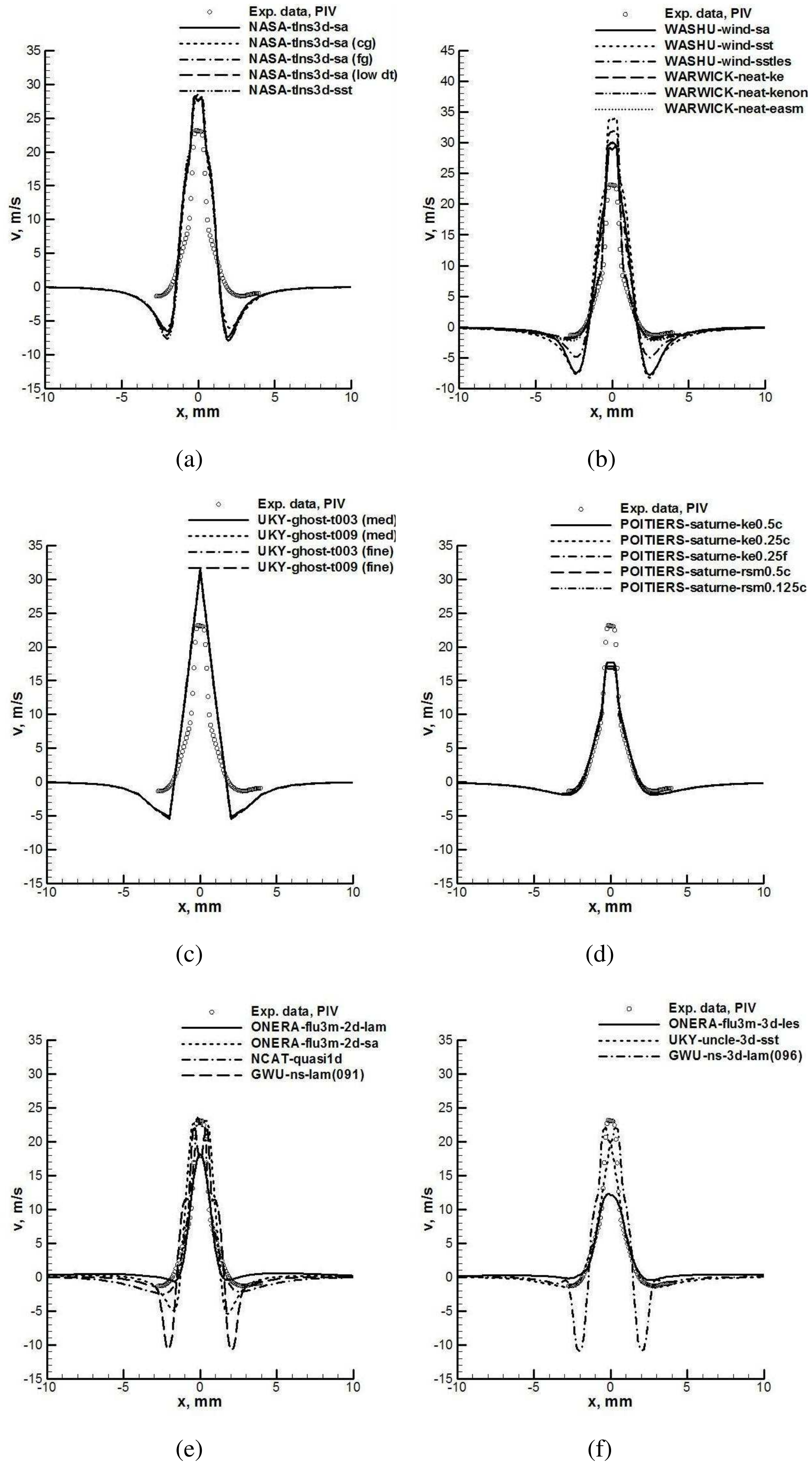

Figure A.4: Computed results from the CFD validation workshop of phase-averaged streamwise velocity across the slot exit at 2mm above the slot exit.

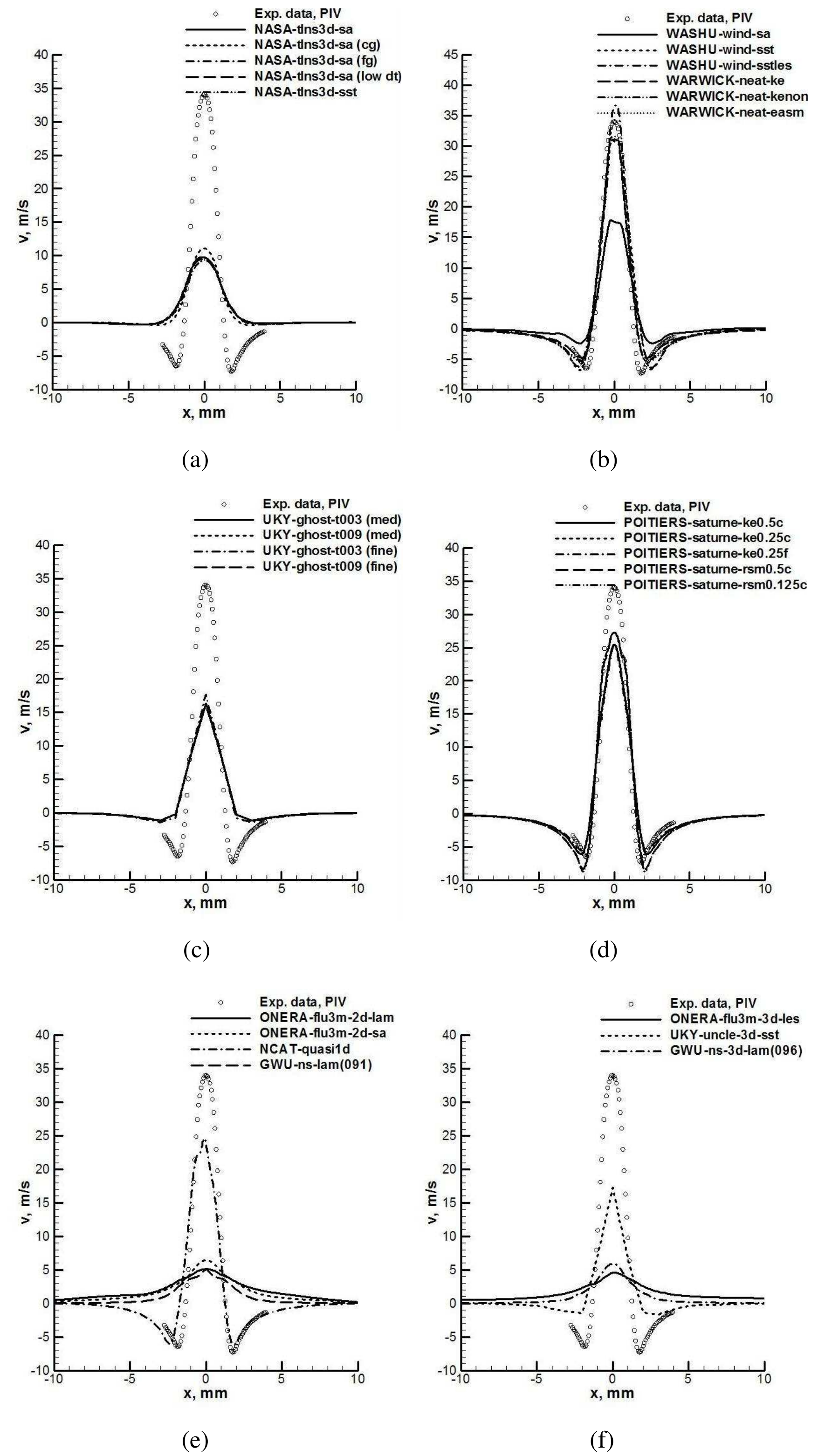

Figure A.5: Computed results from the CFD validation workshop of phase-averaged streamwise velocity across the slot exit at 4mm above the slot exit.

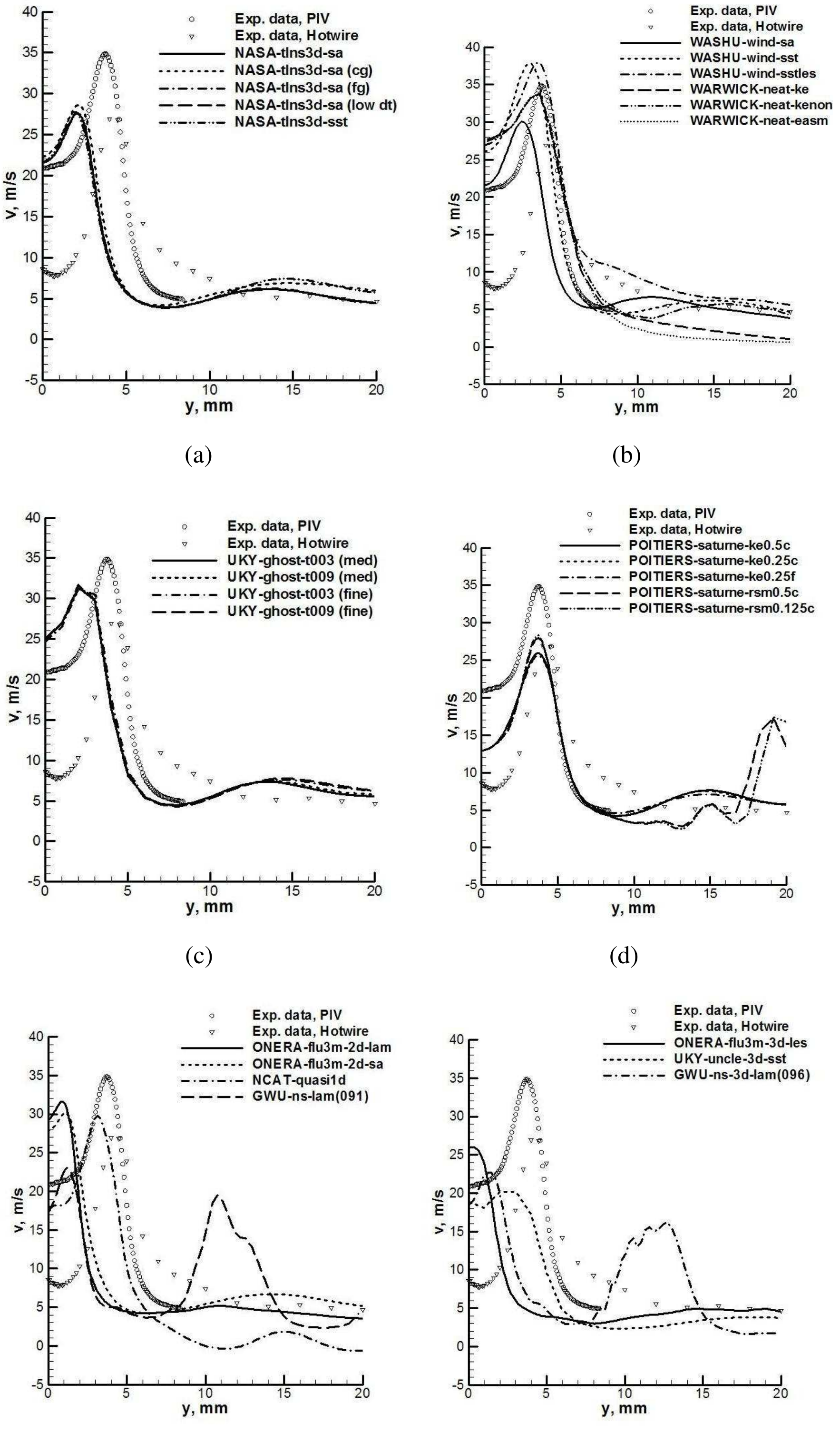

Figure A.6: Computed results from the CFD validation workshop of phase-averaged centreline streamwise velocity at 90°.

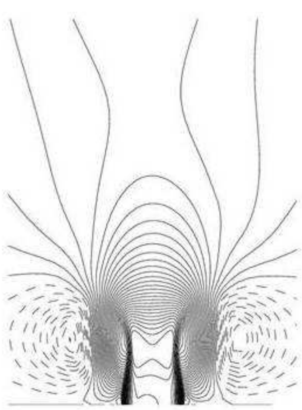

(a) ONERA-flu3m-2d-sa

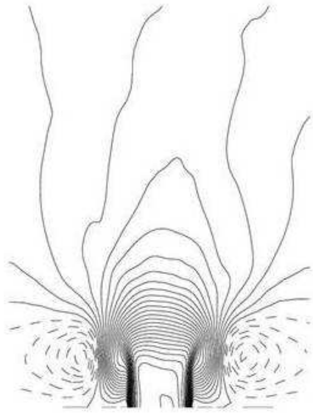

(b) ONERA-flu3m-les

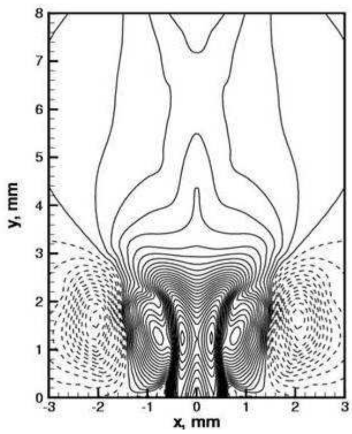

(c) GWU-ns-lam

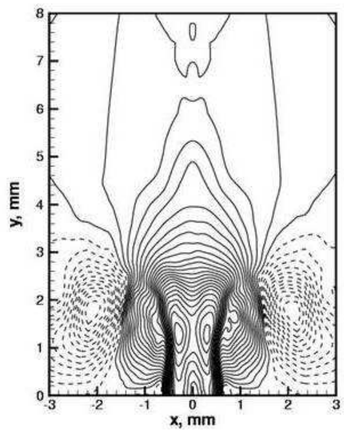

(d) GWU-ns-lam(3d)

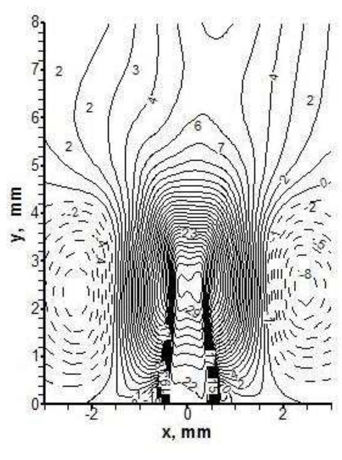

(e) WASHU-wind-sa

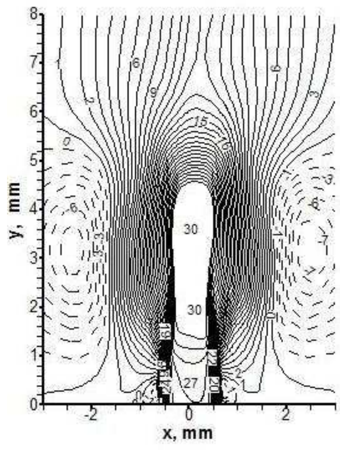

(f) WASHU-wind-sst/les

Figure A.7: Phase-averaged streamwise velocity contours at 90° taken from the CFD validation workshop.

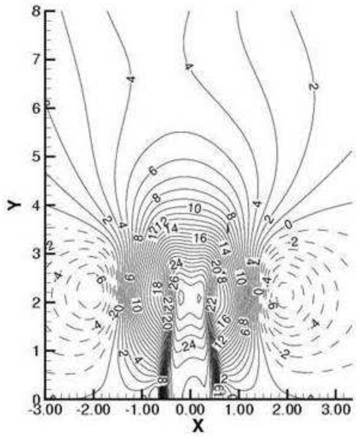

(a) NASA-tlns3d-sa

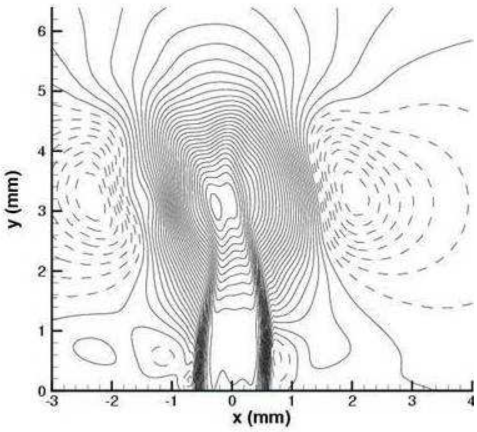

(b) NCAT-quasi1d

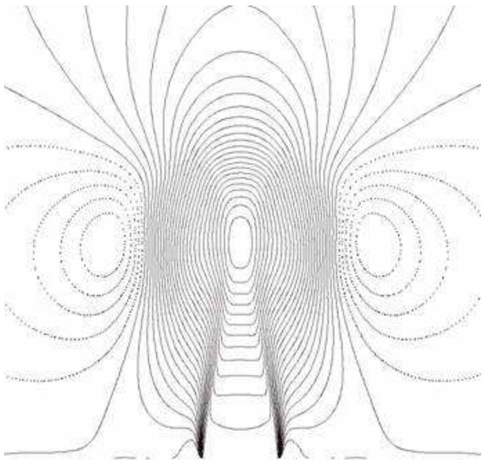

(c) POITIERS-satume-ke0.25f

Figure A.8: Phase-averaged streamwise velocity contours at 90° taken from the CFD validation workshop.

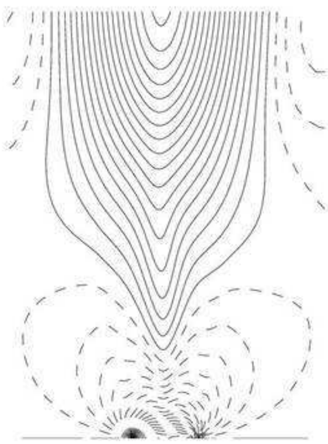

(a) ONERA-flu3m-2d-sa

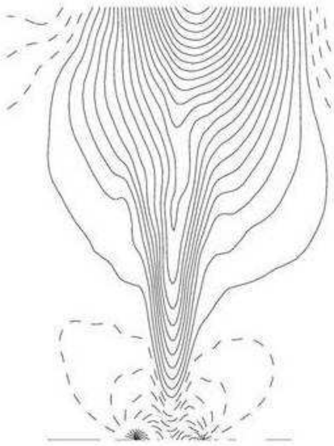

(b) ONERA-flu3m-les

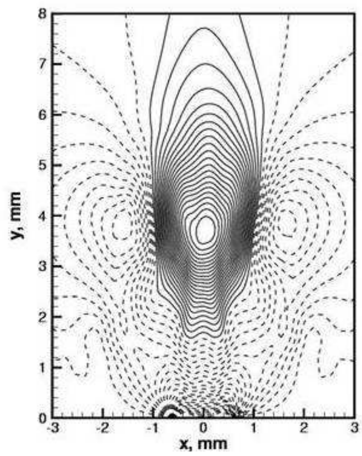

(c) GWU-ns-lam

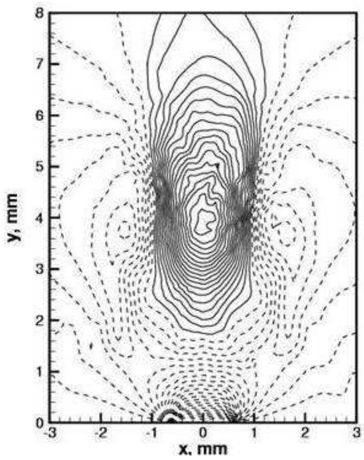

(d) GWU-ns-lam(3d)

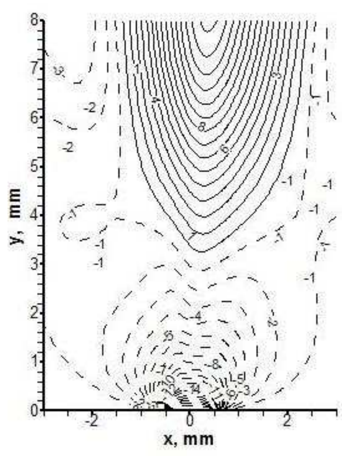

(e) WASHU-wind-sa

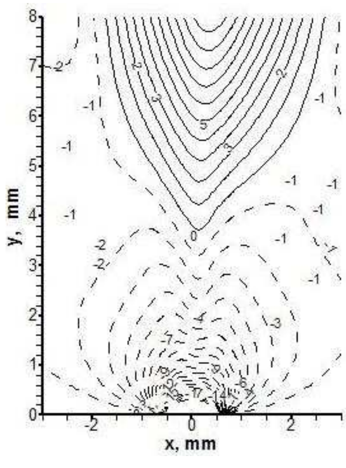

(f) WASHU-wind-sst/les

Figure A.9: Phase-averaged streamwise velocity contours at 225° taken from the CFD validation workshop.

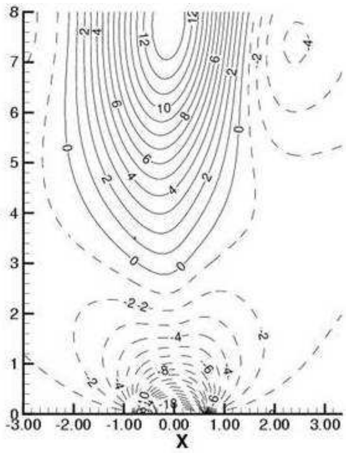

(a) NASA-tlns3d-sa

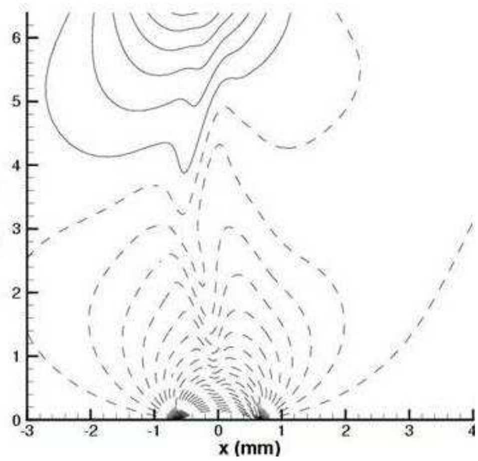

(b) NCAT-quasi1d

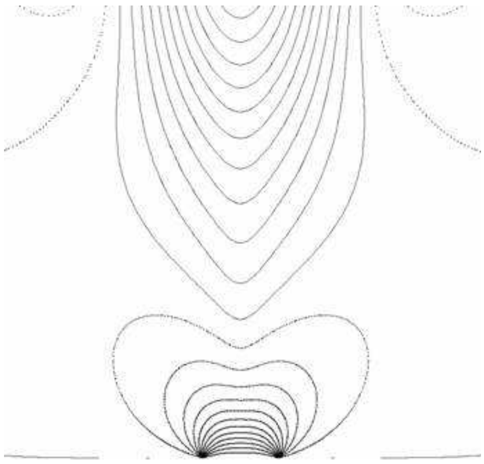

(c) POITIERS-satume-ke0.25f

Figure A.10: Phase-averaged streamwise velocity contours at 225° taken from the CFD validation workshop.

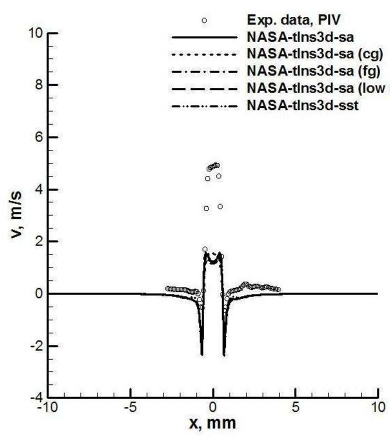

(a)

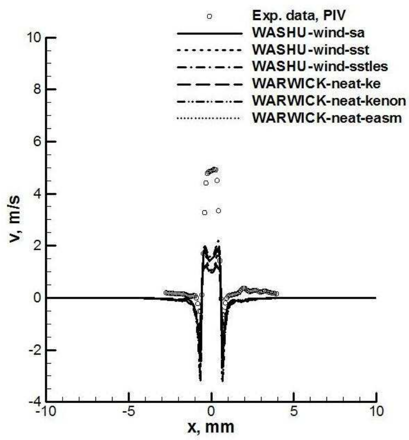

(b)

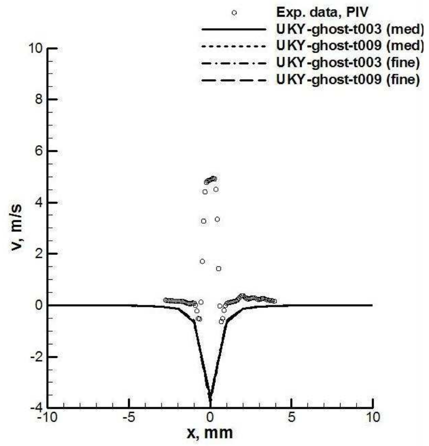

(c)

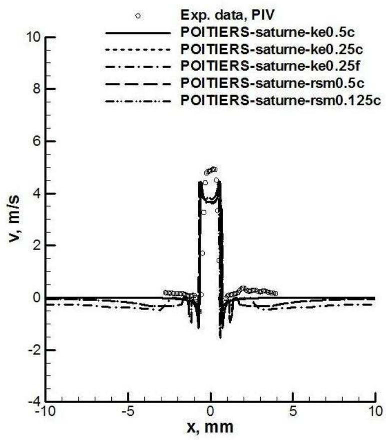

(d)

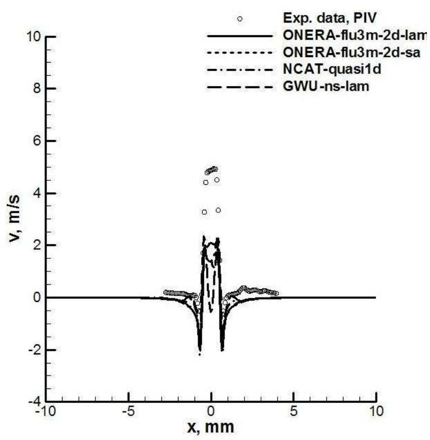

(e)

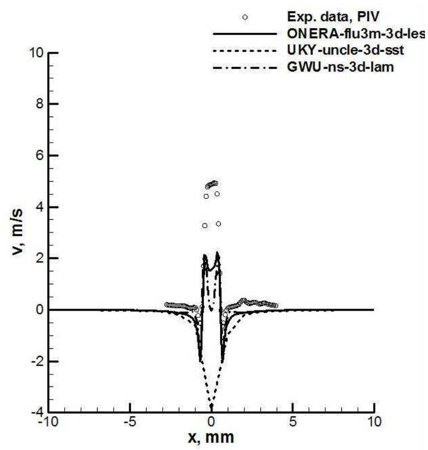

(f)

Figure A.11: Computed results from the CFD validation workshop of time-averaged streamwise velocity at 0.1mm above the slot exit.

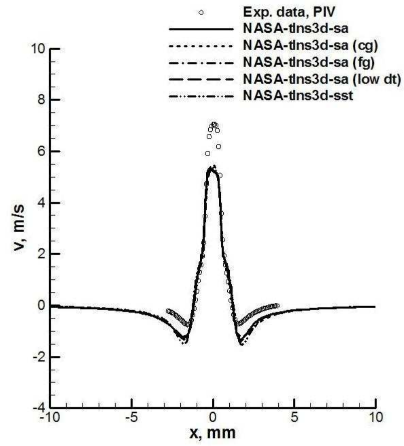

(a)

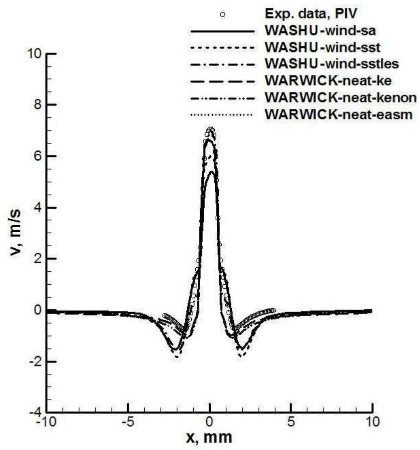

(b)

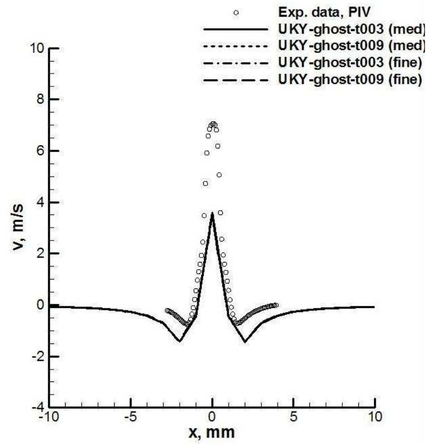

(c)

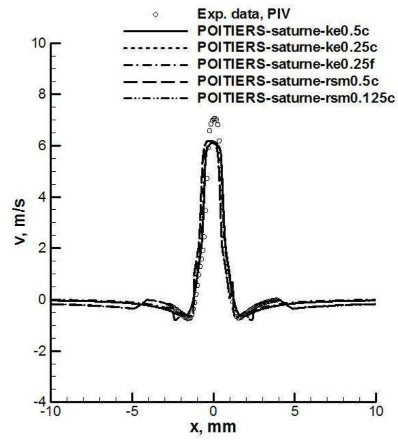

(d)

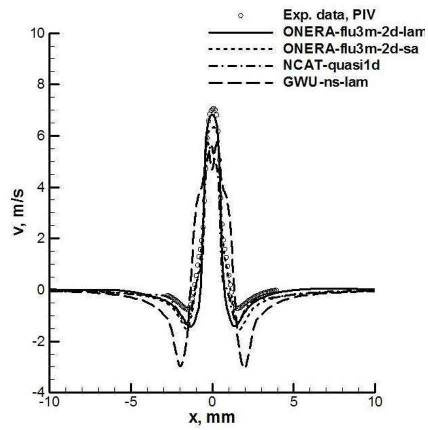

(e)

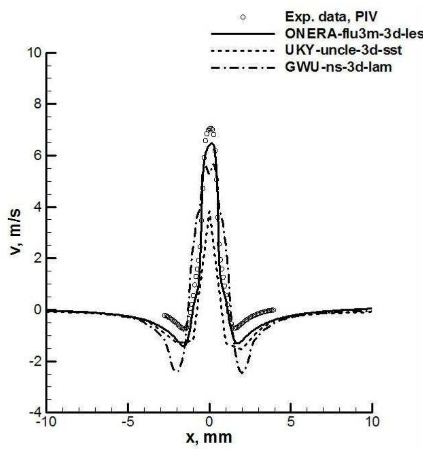

(f)

Figure A.12: Computed results from the CFD validation workshop of time-averaged streamwise velocity at 1mm above the slot exit.

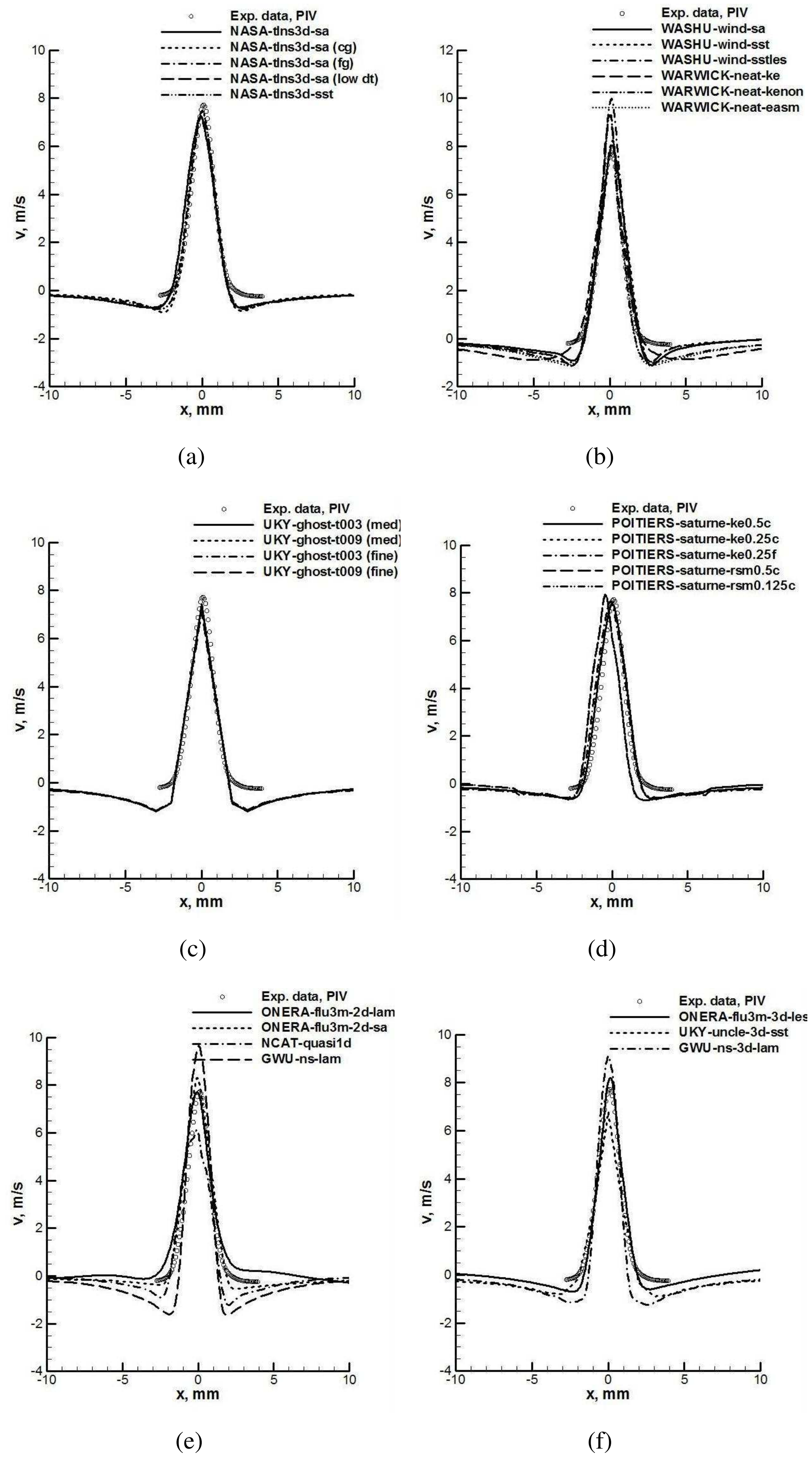

Figure A.13: Computed results from the CFD validation workshop of time-averaged streamwise velocity at 4mm above the slot exit.

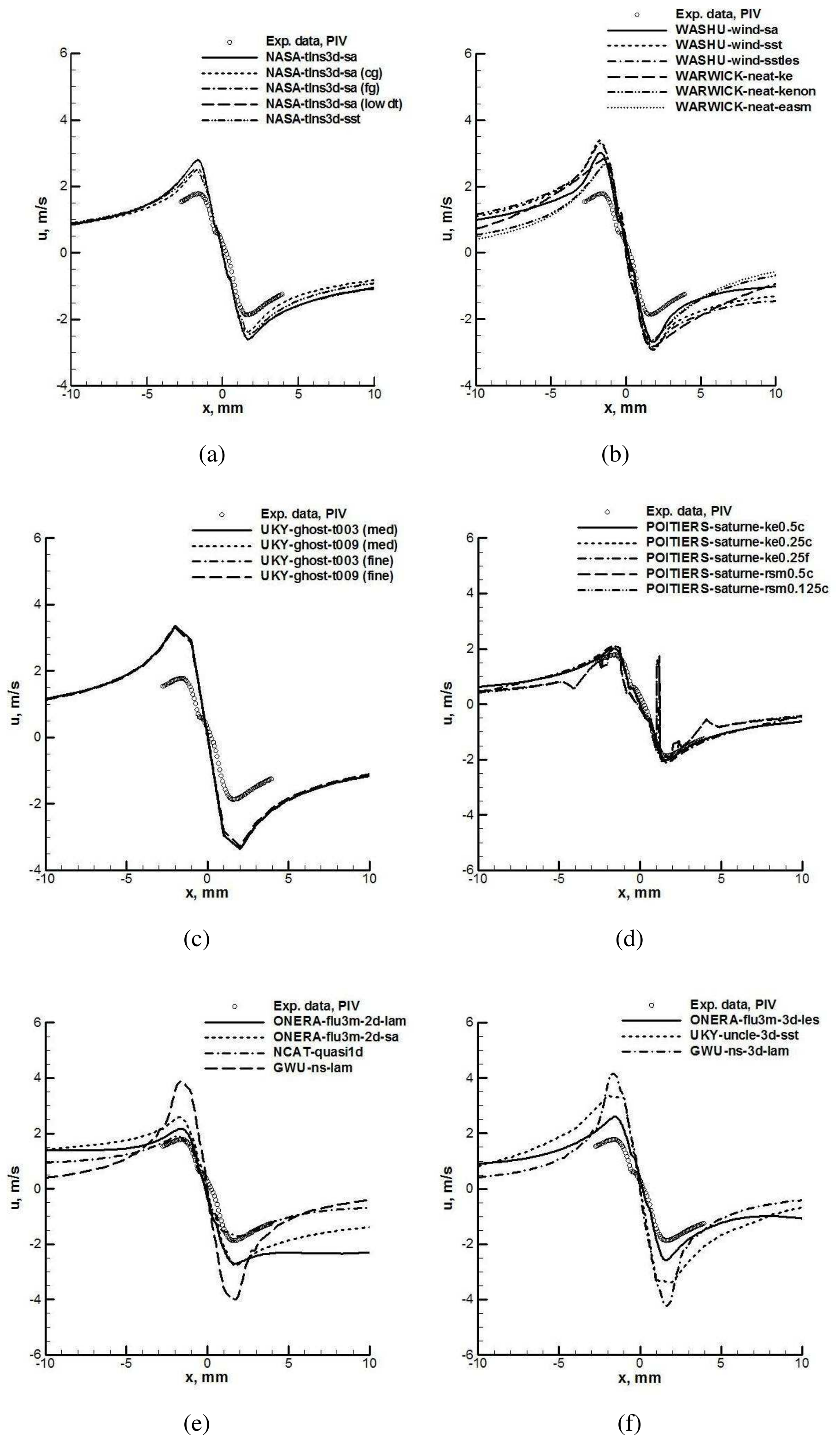

Figure A.14: Computed results from the CFD validation workshop of time-averaged cross-streamwise velocity at 1mm above the slot exit.

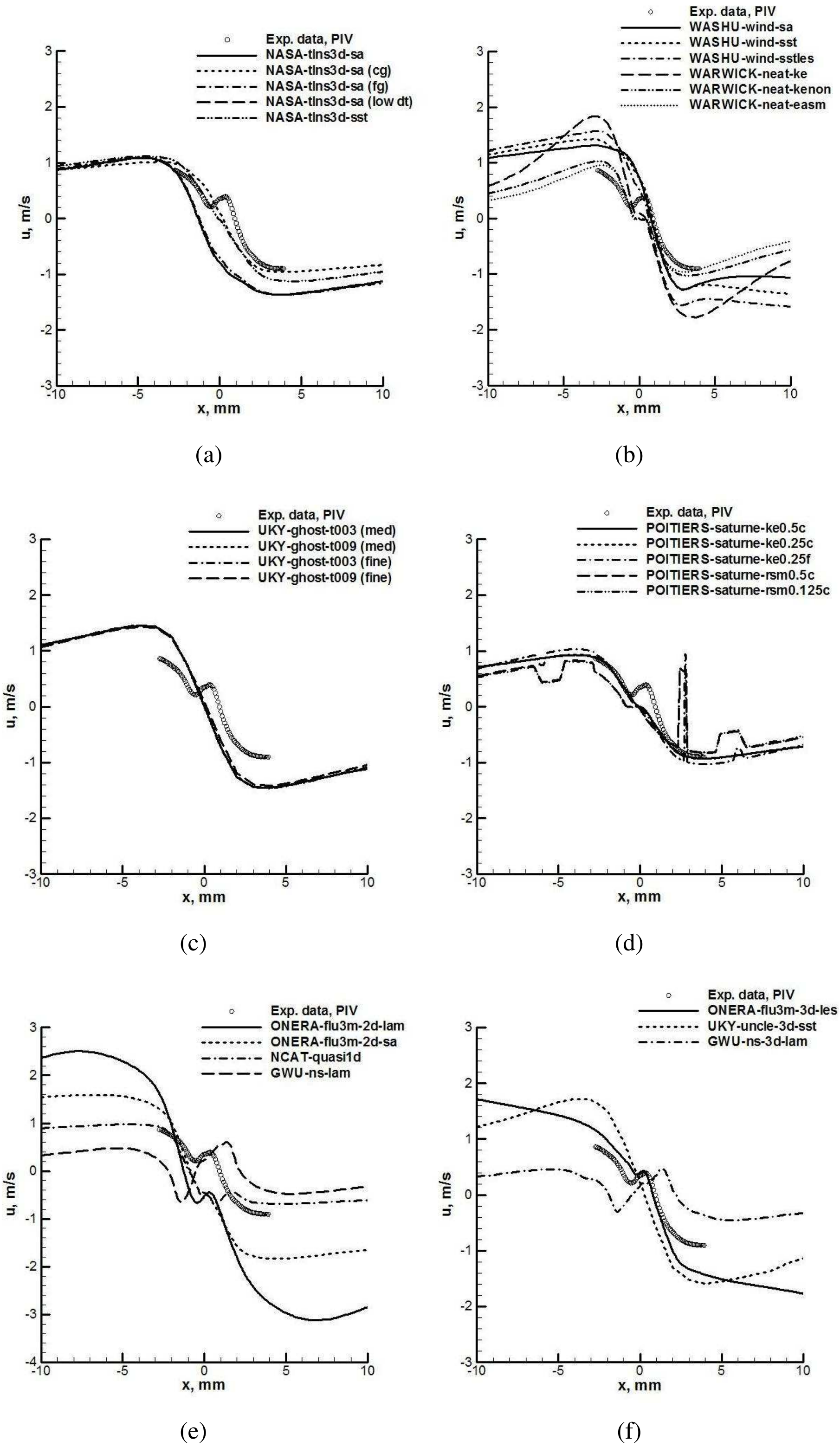

Figure A.15: Computed results from the CFD validation workshop of time-averaged cross-streamwise velocity at 4mm above the slot exit.